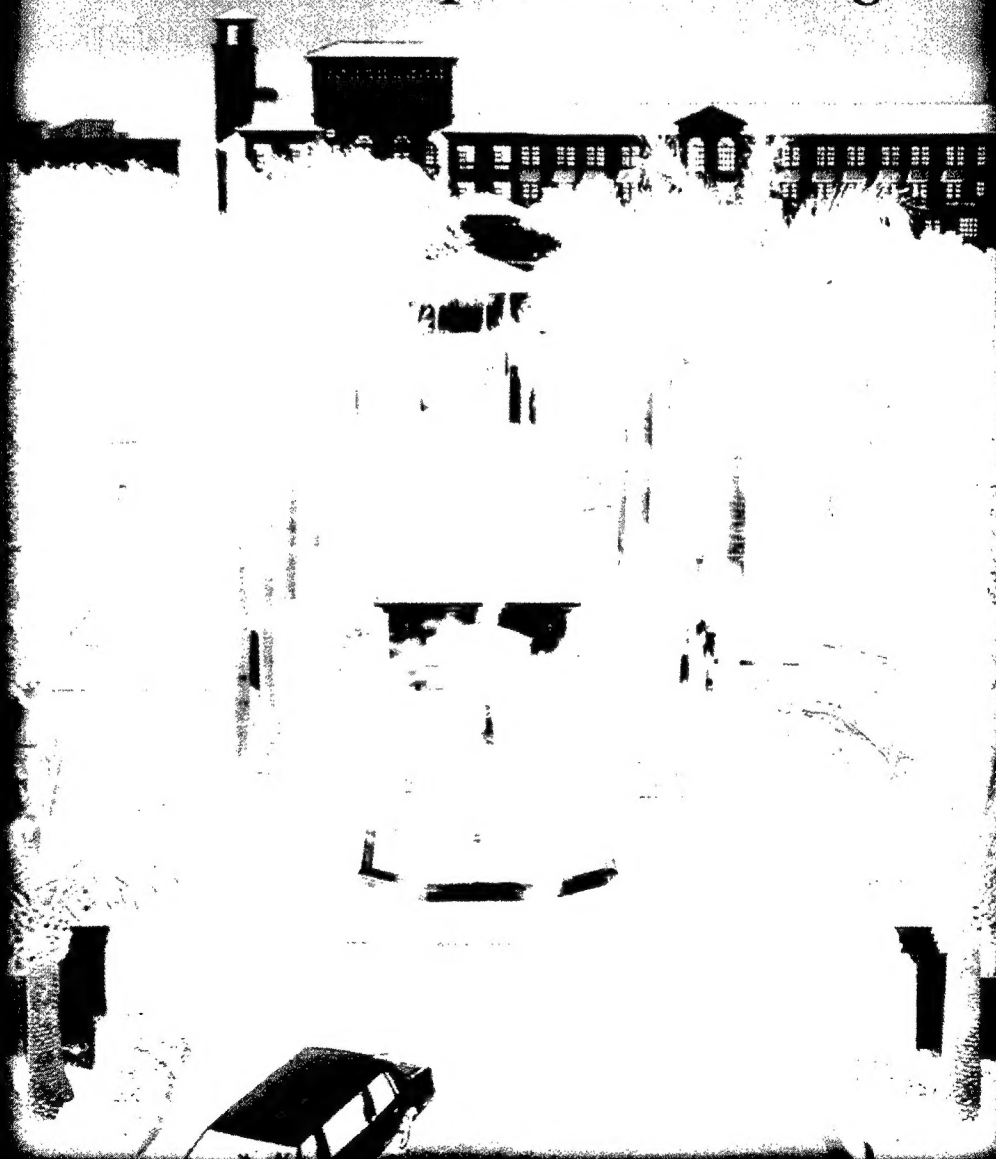# 2000 Digest of the LEOS Summer Topical Meetings

Electronic-Enhanced Optics
Optical Sensing in Semiconductor Manufacturing
Electro-Optics in Space
Broadband Optical Networks

2000 IEEE/LEOS
Summer Topical Meetings

24-28 July 2000,
Turnberry Isle Resort & Club,
Aventura, FL

IEEE Catalog #00TH8497   ISBN #0-7803-6252-7
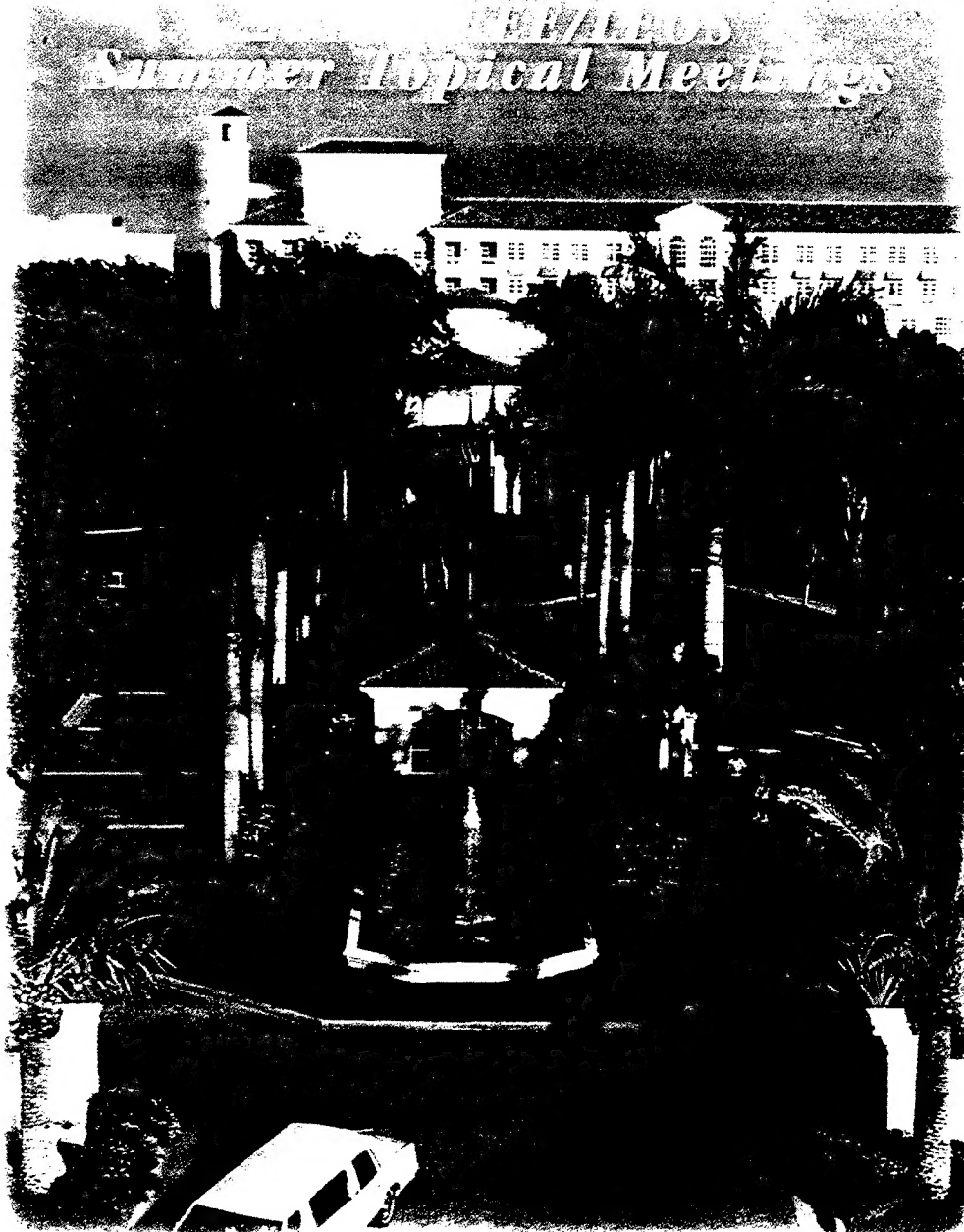
2000 Digest of the
LEOS Summer Topical Meetings

Electronic-Enhanced Optics
Optical Sensing in Semiconductor Manufacturing
Electro-Optics in Space
Broadband Optical Networks

ARO 41491.1-PH-CF

20001122 094

24-28 July 2000,
Turnberry Isle Resort & Club,
Aventura, FL

IEEE Catalog #00TH8497   ISBN #0-7803-6252-7

REPORT DOCUMENTATION PAGE

Form Approved
OMB NO. 0704-0188

1. AGENCY USE ONLY (Leave Blank)	2. REPORT DATE - 2000	3. REPORT TYPE AND DATES COVERED Final Report

4. TITLE AND SUBTITLE

2000 IEEE/LEOS Summer Topical Meeting-Electronic-Enhanced Optics

5. FUNDING NUMBERS

DAAD19-00-1-0468

6. AUTHOR(S)
Paul Shumate, principal investigator

7. PERFORMING ORGANIZATION NAME(S) AND ADDRESS(ES)
IEEE Lasers and Electro-Optics Society
445 Hoes Lane
P.O. Box 1331
Piscataway, NJ 08855

8. PERFORMING ORGANIZATION REPORT NUMBER

9. SPONSORING / MONITORING AGENCY NAME(S) AND ADDRESS(ES)

U. S. Army Research Office
P.O. Box 12211
Research Triangle Park, NC 27709-2211

10. SPONSORING / MONITORING AGENCY REPORT NUMBER

ARO 41491.1-PH-CF

11. SUPPLEMENTARY NOTES
The views, opinions and/or findings contained in this report are those of the author(s) and should not be construed as an official Department of the Army position, policy or decision, unless so designated by other documentation.

12 a. DISTRIBUTION / AVAILABILITY STATEMENT

Approved for public release; distribution unlimited.

12 b. DISTRIBUTION CODE

13. ABSTRACT (Maximum 200 words)

. The 2000 IEEE/LEOS Summer Topical Meeting - Electronic Enhanced Optics was held 24-26 July 2000 at the Turnberry Isle Resort & Club, Aventura, Florida. The purpose of the meeting was to facilitate information exchange between the various technical communities impacted by the integration of electronic circuitry with optical devices and systems. The three-day meeting included the following topics: Devices, Structures, and Circuits; Architectures and Modeling; Integration and Packaging; and System Demonstrations and Applications. The format included both invited and submitted talks. The conference was highly relevant to a number of Army topics to include imaging, photonic interconnects, and communication systems.

14. SUBJECT TERMS

15. NUMBER OF PAGES

16. PRICE CODE

17. SECURITY CLASSIFICATION OR REPORT UNCLASSIFIED	18. SECURITY CLASSIFICATION ON THIS PAGE UNCLASSIFIED	19. SECURITY CLASSIFICATION OF ABSTRACT UNCLASSIFIED	20. LIMITATION OF ABSTRACT UL

2000 Digest of the LEOS Summer Topical Meetings

Electronic-Enhanced Optics
Optical Sensing in Semiconductor Manufacturing
Electro-Optics in Space
Broadband Optical Networks
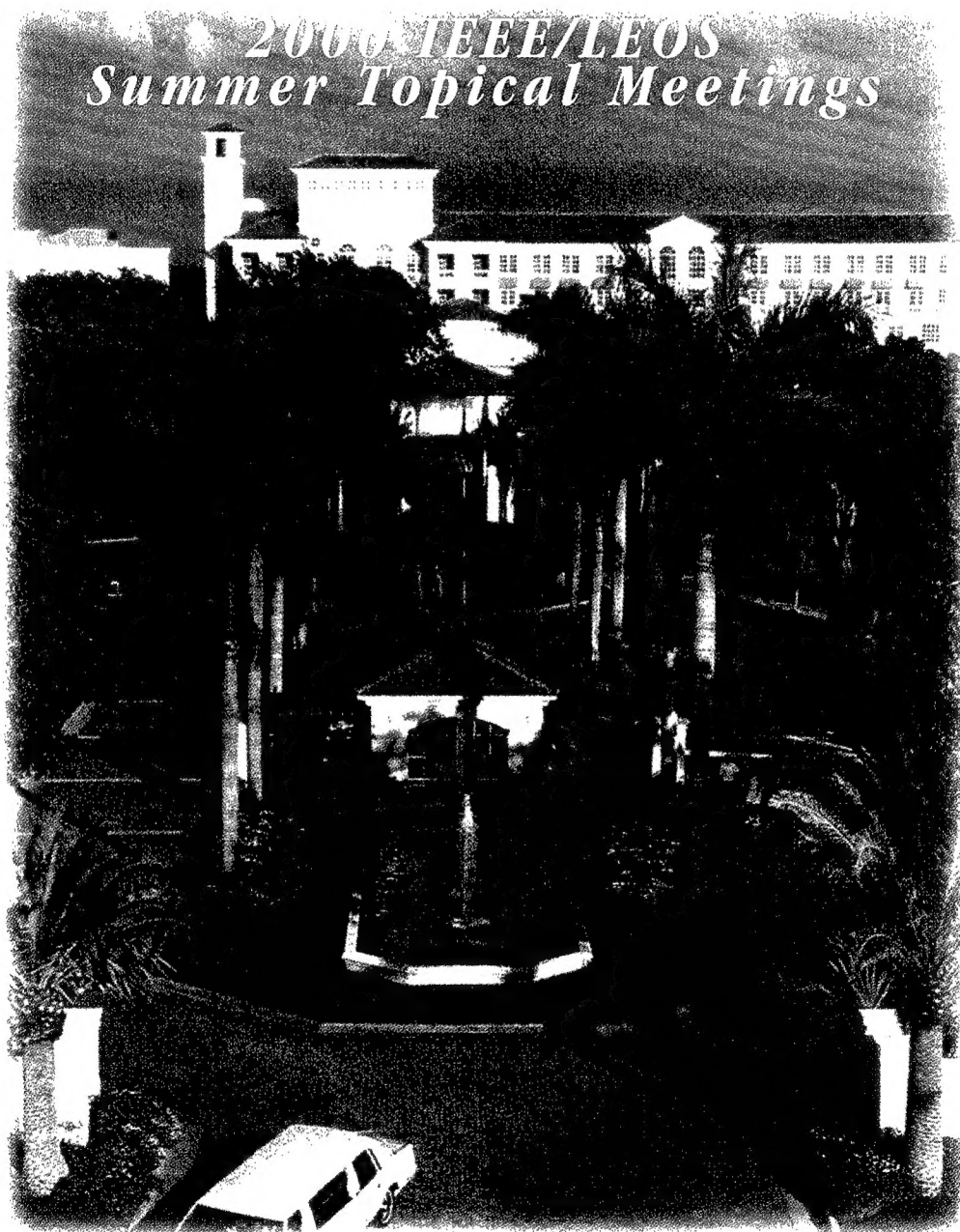
24-28 July 2000,
Turnberry Isle Resort & Club,
Aventura, FL

IEEE Catalog #00TH8497   ISBN #0-7803-6252-7

ACKNOWLEDGEMENT

The Conference Committee would like to thank the following companies
for their sponsorship of the
2000 IEEE/LEOS Summer Topical Meetings:

The Boeing Company

EPI MBE Products Group

Oriel

2000 IEEE/LEOS
Summer Topical Meeting

24 - 26 July 2000

Electronic-Enhanced Optics

Turnberry Isle Resort & Club
Aventura, FL

Electronic-Enhanced Optics

Chair:

Barry Shoop, *United States Military Academy*, West Point, NY

Technical Program Committee:

H.S. Hinton, *University of Kansas*, Lawrence, KS
N.M. Jokerst, *Georgia Institute of Technology*, Atlanta, GA
F. Kiamilev, *University of Delaware*, Newark, DE
C. B. Kuznia, *University of Southern California*, Los Angeles, CA
D.V. Plant, *McGill University*, Montreal, QC, Canada
I. Underwood, *University of Edinburgh*, Scotland, UK
C. DeCusatis, *IBM Corporation*, Poughkeepsie, NY
F.B. McCormick, *MODE*, Albuquerque, NM

Wednesday, 26 July 2000

Electronic-Enhanced Optics

Monday, 24 July 2000

MA1:   Enabling Technologies I
MA2:   Enabling Technologies II
MA3:   Integration Technology
MA4:   Systems and Demonstrators

Monday Missing Papers

MA3.1   "High Performance Computing Using Heterogeneously Integrated Silicon and III-V Optoelectronic Devices" J. Trezza, *Sanders, A Lockheed Martin Company, Nashua, NH, USA.*

HIGH SPEED CMOS IMAGING

E. Fossum, A. Krymski

Photobit Corporation
135 N Los Robles Ave, 7th Floor, Pasadena, CA, 91101
E-mail: fossum@photobit.com

High speed imaging has been undergoing very revolutionary changes. Just recently CCDs, having spent more than 3 decades of development and spending many hundreds of millions of dollars, were hard pressed to reach the milestone of 250 kilo-pixels at 1000 frames per second. A typical high speed CCD camera is a computer rack size box, filled with many components: multiple power supplies, pulse generators and drivers, ADCs etc., consuming tens of Watts of power. Comparatively, high speed CMOS sensors are just getting started (the first sensor for high speed was designed only about two years ago), but have already exceeded this data throughput with 4,1 Mega-pixels at 240 FPS, and progress is continuing so rapidly that no one can predict what will be possible in say two years.

This paper analyzes basic architectural features of CMOS digital imagers, presents the history of their development, and gives examples of high-speed CMOS APS implementation.

Photodiode image sensors with MOS scanning circuits were known from mid 60s, however, they were not embraced commercially because of poor performance and large pixel size (for that time) relative to that of the CCD. In the early 90-s CMOS sensors re-emerged as a low-cost, low-power alternative to CCDs and because one could integrate various signal and image processing blocks such as amplifiers, ADCs, circuits for color processing and data compression, standard TV and computer I/O interfaces on the same chip [1]. CMOS technology is now making a breakthrough on two fronts: sensors for computers and cell phones on the low-end, and ultra high speed, large format imaging on the high-end .

A typical CMOS APS (active pixel sensor) contains 3 NMOS transistors in it. Although this allows a very compact implementation, the sensor lacks parallel acquisition of the image data, a feature often important in high speed imaging. The alternative is a pixel that contains an analog memory and is called SNAP: shuttered-node active pixel. This approach will also be addressed within this presentation.

The readout of all pixels in one row is usually done in parallel. This parallelism potentially allows very high speed of data readout. An important issue is how the data is multiplexed into the output pad (pads). Multiplexing of digital data (only 1

or 0) is much simpler than passing of analog data, so the data from the pixel must be digitized prior to the readout. It is then straightforward to read the digital data through a wide (8, 10, or 16 bit) bus. In the presentation, different architecture readouts and ADCs are considered. We found the column-parallel ADC architecture extremely efficient when implementing large format high speed image sensors. This approach is feasible for large format because the ADCs occupy a noticeable area, so it would not be as suitable for realization of CIF-VGA format sensors operating at regular 30-60 Frames/s speed.

Another architectural feature that allows high speed operation is pipelining. It is essential that the readout of the digitized data is done at the same time as pixel readout and A-to-D conversion. While this may sound trivial, but in the practical implementation, care must be taken to eliminate the crosstalk between noisy digital data paths and sensitive analog nodes.

The following high speed CMOS APS were designed recently:

1. 1024x1024 500 Frames/s CMOS APS with rolling shutter and 10 um pixels [2]
2. 2368x1728 240 Frames/s CMOS APS with rolling shutter and 7 um pixels
3. 1280x 1024 600 frames/s CMOS APS with SNAP 12 um pixel.

The achieved performance will be outlined in the presentation and sample images captured by cameras built using the sensors will be demonstrated.

To conclude, we considered a number of CMOS APS architectures and demonstrated that CMOS technology is very suitable for the realization of high speed electronic cameras. Such a technology yields low power (~0.5 W for the sensor), a compactness unachievable with CCDs, and reliability. The future for CMOS technology in high speed imaging is bright.

References:

1. Fossum, E.R. , "CMOS Image Sensors: Electronic Camera on a Chip", IEDM Tech Dig., pp.17-25, Dec. 1995.
2. A. Krymski et.al, A High Speed, 500 Frames/s, 1024x1024 CMOS Active Pixel Sensor", 1999 Symp. on VLSI Circuits, pp.137-138, 1999

MULTICHANNEL COMPUTER GENERATED HOLOGRAMS

M. A. Araiza-Esquivel and S. Guel-Sandoval

Instituto de Investigación en Comunicación Optica (IICO), Universidad Autónoma de San Luis Potosí (UASLP), A. Obregón 64, San Luis Potosí, S.L.P. 78000, México

1. INTRODUCTION

Detour phase computer generated holograms were designated more than 30 years ago[1,2], however they still remain under research due to their interesting characteristics. In the late years many researchers have proposed several multiplexing methods[3-5], using detour holograms, where they have been able to perform an image reconstruction in various diffraction orders

As a new approach, in this work we propose handling two or three flat partial objects (FPO) (sections of a whole flat object), that will be stored in a hologram, in such a way that an image addition is carried out with the recovering being in the same or different direction and same diffraction order. The used FPO's can be parts of a larger one, so a direct application of this method is to reunite as a whole, several flat partial images (FPI) from corresponding FPO's.

2. CODIFICATION TECHNIQUE

Fig. 1 shows various cell designs, each of size $\delta v \times \delta v$, with coordinates $(m\delta v, n\delta v)$ where up to three rectangles are used, with the purpose of increasing the amount of information codified in the hologram. In next paragraph, first cell characteristics and equations are given. The others are only mentioned, since their treatment is similar, however results are shown with all cells included.

$$(a) \qquad (b) \qquad (c) \qquad (d)$$
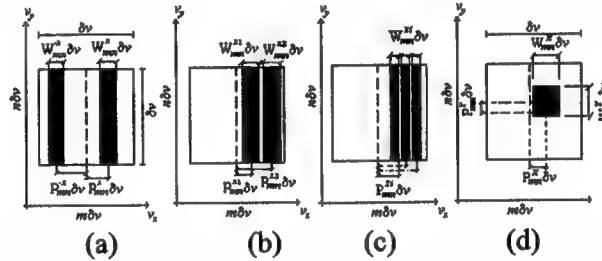
Figure 1. Cells' structure for binary holograms. Parameters W and P, with indices (m, n), codify amplitude and phase, respectively. The upper indices identify FPO's.

Cell in Fig. 1(a) allows codifying up to 4 free parameters. Each rectangle's width is defined: $W_{mn}^X \delta v$ and $W_{mn}^{-X} \delta v$, and lateral changes are introduced by variables: $P_{mn}^X \delta v$ and $P_{mn}^{-X} \delta v$, with constant height. Our purpose is to codify two flat objects: one $u_X(x,y)$, with parameters $W_{mn}^X \delta v$ and $P_{mn}^X \delta v$, and another $u_{-X}(x,y)$, with parameters $W_{mn}^{-X} \delta v$ and $P_{mn}^{-X} \delta v$. Both images will be obtained in the diffraction order ± 1. The letters $-X$ and X are used to identify different flat objects.

The binary amplitude transmittance H of the holograms can be written as:

$$H(v_x, v_y) = \sum_{m,n} \left\{ rect\left[\frac{v_x - m\delta v - P_{mn}^X \delta v}{W_{mn}^X \delta v}\right] rect\left[\frac{v_y - n\delta v}{\delta v}\right] + rect\left[\frac{v_x - m\delta v + P_{mn}^{-X} \delta v}{W_{mn}^{-X} \delta v}\right] rect\left[\frac{v_y - n\delta v}{\delta v}\right] \right\} \quad (1)$$

Each value (m, n) refers to a cell. The *rect* function is defined only horizontally, since in the vertical direction the *rect* function is constant and equal to δv for all n, so it can be neglected. Then at the output plane, the field distribution $h(x, y)$ appears as the inverse Fourier transform (IFT) of $H(v_x, v_y)$ as:

$$h(x,y) = \sum_{m,n} \left\{ \left(x\delta v W_{mn}^X \pi\right) sinc\left(x\delta v W_{mn}^X \pi\right) exp\left[2i\pi x\left(m + P_{mn}^X\right)\delta v\right] + \left(x\delta v W_{mn}^{-X} \pi\right) sinc\left(x\delta v W_{mn}^{-X} \pi\right) exp\left[2i\pi x\left(m - P_{mn}^{-X}\right)\delta v\right] \right\} \quad (2)$$

Besides it is desired that the complex amplitude $h(x, y)$ describes the images $u^X(x,y)$ and $u^{-X}(x,y)$. After some approximation, the equation above is reduced to:

$$sen\left(\pi W_{mn}^{X}\right)= A_{mn}^{X} \qquad\qquad \varphi_{mn}^{X} = 2\pi P_{mn}^{X}$$
$$sen\left(\pi W_{mn}^{-X}\right)= A_{mn}^{-X} \qquad\qquad \varphi_{mn}^{-X} = -2\pi P_{mn}^{-X} \qquad\qquad (3)$$
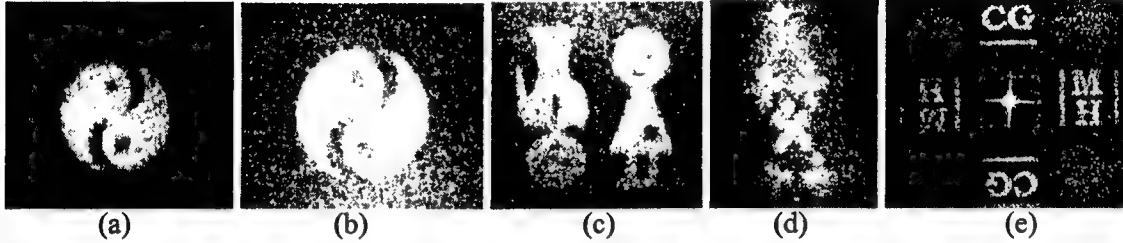
In this way it is possible to reconstruct both images in the same order, as we can see next.

3. EXPERIMENTAL RESULTS AND CONCLUSIONS

Fig. 2 shows different groups of FPO's used to generate several holograms. Results are shown in figure 3 and discussed in text below:

Figure 2. Flat partial Objects.

Figure 3. Reconstructed images. (a) Using Fig. 1(a) and couple of FPO's Fig. 2(a); (b) Fig. 1(b) and Fig. 2(a); (c) Fig. 1(a) and Fig. 2(b) manipulating some instruction; (d) Fig. 1(c) and Fig. 2(c); (e) Fig. 1(d) and Fig. 2(d).

Results show it is possible to reconstruct a whole image of two or three FPO's which are codified separately and maintained independent during codification. The hologram thus works as a multiplexing system capable of encoding two or three separated channels of information.

The method has been designated as: image addition by multiplexed computer generated holograms (IAMCGH). This IAMCGH method can be considered, as a different approach for a system to codify information by sections, to be recuperated latter as a whole. The cell dimensions limit the maximum number of rectangles used and consequently the number of FPO's that can be codified. For the time being up to three FPO's have been recorded. An additional characteristic of the IAMCGH method is that it makes possible to recuperate the FPO's images in the same or different directions. The authors acknowledge Prof. A. W. Lohmann for their suggestions and encouraging comments. Besides, one of the authors (MAE) acknowledges CONACYT (Mexico) for providing financial partial support for this work. We also acknowledge J. Nieto for providing technical support.

4. REFERENCES

1. B. R. Brown and A. W. Lohmann, "Complex spatial filtering with binary masks", Appl. Opt. **5**, 967-969 (1966).
2. A. W. Lohmann and D. P. Paris, "Binary Fraunhofer Holograms Generated by Computer", Appl. Opt. **6**, 1739-1748 (1967).
3. D. Mendlovic and I. Kiryuschev, "Two-channel computer-generated hologram and its application for optical correlation", Optics Commun. **116**, 322-325 (1995).
4. D. Mendlovic, "Double-multiplexed computer-generated holograms", Appl. Opt. **35**, 3887-3890 (1996).
5. R. ChaoHong, Z. Jin and G. WenQi, "Four-channel self-focus computer generated hologram", Appl. Opt. **36**, 8844-8847 (1997).

Polarisation-induced beating in Spatial Light Modulator Optical Switches

Hsiao-Hua Chu, Melanie J. Holmes

Department of Electronic Engineering, King's College London, Strand, London WC2R 2LS, U.K.
E-mails: hsiao-hua.chu@kcl.ac.uk, melanie.j.holmes@kcl.ac.uk

Abstract   We report, for the first time, results of a full polarisation analysis of SLM-based switches, taking into account all diffraction orders. Although the switch efficiency is dominated by a polarisation-independent term, we discover polarisation dependent beating effects with the residual zero order.

Introduction   Spatial light modulators (SLMs) are an attractive option for beam-steering optical switches due to the rapid response time of the liquid crystal, the potential for multicasting, and the lack of moving parts. The aim of our research is to design a beam-steering terminal for network protection in submarine networks. Previous results have been reported in [1].

Polarisation dependent analysis   The basic operation of such a switch has been reported in [2], and uses phase modulation applied by a ferroelectric liquid crystal SLM to steer an incident beam into the selected output waveguide. In practice, the effect of the phase modulation is to diffract the beam incident on the SLM into a number of reflected beams, each corresponding to a different diffraction order of the phase modulation. Only one of these diffraction orders is created intentionally; the others are unwanted. The selected diffraction order carries the message stream into the required output waveguide, while the unwanted diffraction orders lead to crosstalk and backreflection. On arriving at the launch end of the waveguide, the tails of the beams in the unwanted diffraction orders will couple into their nearest port, and lead to crosstalk.

The beam leaving the fibre is approximated to be Gaussian, and for arbitrary elliptical polarisation field, is therefore expressed as $Ein(x,y) = (Ex\hat{\underline{x}} + Eye^{i\delta}\hat{\underline{y}})\exp[-(x^2+y^2)/w_0^2]$, where $\hat{\underline{x}}$ and $\hat{\underline{y}}$ are unit vectors, defined to be parallel and perpendicular, respectively, to the axis of the FLC cone. Previously, the switching efficiency into first and higher diffraction orders has been shown to be polarisation-independent [3], with the result of non-ideal SLM cell thickness and tilt angle being the creation of a residual zero order. We have carried out a full polarisation analysis of the coupling efficiency and discovered polarisation-dependent beating effects. The field incident on the SLM is proportional to the Fourier transform of the electric field and may be calculated from diffraction theory. The beam incident on the SLM passes through a cover glass, a layer of birefringent liquid crystal, is reflected from a mirror pixel and then passes back through the liquid crystal and cover glass. This propagation through the SLM may be represented in the form of a Jones matrix. Therefore, the field leaving the SLM depends on the FLC tilt angle, θ, and the cell property (retardation) Γ, where $\Gamma = 2\pi\Delta n t/\lambda$; t is the thickness of the liquid crystal, Δn is the refractive index difference between the fast and slow axis of the liquid crystal.

In normal operation, the main terms in our result are that the coupling efficiency is given by: $\eta = \eta_0 + \eta_1 + \eta_b$, where η_0 is the expected coupling efficiency of the power in the first diffraction order (as in [3]): $\eta_0 = \alpha_l^2(a1^2+b1^2)/4$, where $a1$ and $b1$ are the real and imaginary first-order Fourier series coefficients of the periodic phase modulation applied by the SLM, and $\alpha_l = \sin 2\theta \sin \Gamma$ is the modulating coefficient. η_1 represents the power coupled in from the evanescent tail of the beam directed into the residual zero order: $\eta_1 = (\alpha_{0r}^2 + \alpha_{0i}^2)q^2$, where $\alpha_{0i} = \cos 2\theta \sin \Gamma$ and $\alpha_{0r} = \cos \Gamma$ are the non-modulating real and imaginary coefficients caused by the residual zero order, and $q = \exp[-d^2/(2w_0^2)]$ and we have set the output waveguide position, d, to be optimised to receive a first order. The polarisation-dependent term, η_b, is given by:

7

$$\eta_b = \frac{2ExEy}{Ex^2 + Ey^2}\alpha_i(\alpha_{0i}\sin\delta - \alpha_{0r}\cos\delta)[b1q + (b0 + b2)q^2]\qquad(1)$$

where $b0$, $b1$ and $b2$, are the zeroth, first and second order imaginary Fourier series coefficients of the periodic phase modulation applied to the SLM. In steady-state operation these zero and second orders would be very weak, so this term would be negligible. However, they may become significant intermittently, as the hologram is scrolled across the SLM, in order to maintain DC balance [2]. What is surprising about this result (and we have checked it several times) is that the result depends only on the imaginary Fourier series coefficients. In principle, then, the effect could be avoided by making the phase modulation have even symmetry about the centre of the hologram. However, in practice the hologram pattern must be scrolled to maintain DC balancing of the pixels. As the pattern is scrolled across then $|a1|$ will fall to zero and $|b1|$ will become maximised, at a value of up to $2/\pi$ for the most efficient hologram patterns.

The worst-case fractional polarisation-dependent fluctuation, η_b/η_0, is plotted in the >figure, for a tilt angle, θ, of 36°, and for values of retardation Γ that are ideal, and in error by 20% to 40% of the ideal value. The results are plotted as a function of the waveguide offset from the output position of the zero order, d, and assuming a spot-size, w_0 of 5.1 μm. This figure has two sets of curves grouped together: the upper group (labelled PI) shows the polarisation-dependent power fluctuations, while the lower group of curves in the figure (labelled RZ) shows the expected crosstalk from the residual zero order, given by η_1/η_0. These results show that for significant errors in cell thickness, and for offsets of 5μm or more away from the output position of the residual zero order, the polarisation-dependent fluctuation becomes larger than the expected power in the received signal.
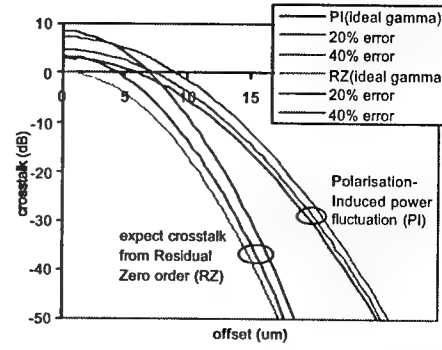
It may be shown that the worst-case polarisation-dependent fluctuation is given by $(\eta_b/\eta_0)_{WORST\text{-}CASE} = \pm2\sqrt{\eta_1/\eta_0}$. Hence when the expected crosstalk from the residual zero-order is −30 dB, the polarisation-dependent fluctuation would be −12 dB. Therefore, in order to avoid significant temporal fluctuations as the polarisation state changes, and as the hologram pattern is scrolled across the SLM, these effects should be taken into account when beam-steering SLM-based switches are designed For an ideal SLM, the residual zero order would be absent, and so the polarisation-dependent beating would also disappear.

Conclusions We report, for the first time, results of a full polarisation analysis of the switch, taking into account all diffraction orders. We discover a strong polarisation dependent beating between the first order and residual zero order, and weaker polarisation-dependent beating with the zero and second orders from the hologram (phase modulation) pattern. This beating results in significant power fluctuations in output channels located close to the residual zero order, and should be taken into account in future designs of beam-steering optical switches using ferroelectric SLMs.

4. References

[1] H H Chu, M J Holmes, 'Design issues in compact optical switches using spatial light modulators', IEE Colloquium on multiwavelength optical networks: devices, systems and networks implementations, June, 1998

[2] W A Crossland et al, 'Beam-steering optical switches using LCOS the ROSES demonstrator', submitted to IEEE/LEOS Summer Topical Meeting on Electronic Enhanced Optics, July 2000

[3] S T Warr, R J Mears, 'Polarisation insensitive operation of ferroelectric liquid crystal devis', Electronics Letters, Vol.31 No.9, April 1995

Monolithic InGaAs/InGaAsP Electro-Absorption Intensity Modulator Fabricated Using Low Energy Arsenic Ion Implantation Induced Intermixing

S.L. Ng*, H.S. Lim, B.S. Ooi, Y.L. Lam, Y. Zhou, Y.C. Chan
Photonics Research Group, School of Electrical and Electronic Engineering
Nanyang Technological University, Singapore
*Fax: 65-7912687 Telp: 65-7906319 e-mail: eslng@ntu.edu.sg

V. Aimez, J. Beauvais and J. Beerens[†]
Centre de recherche sur les propriétés électroniques des matériaux avancés,
Département de Génie Électrique et Génie Informatique, and [†]Département de physique,
Université de Sherbrooke, Sherbrooke, Québec, Canada J1K 2R1

In view of the increasing demand for greater communication capacity, the bit rate for long haul communication has been rising alarmingly over the years. This has led to explosive growth for high speed, large bandwidth light-wave technology in carrying the vast amounts of data reliably, efficiently and cost effectively in long haul communication systems [1,2,3]. Consequently, this has motivated the optical communication technology moving towards monolithic integration of light source and modulator devices operating at 1.55 um, as the integration provides advantages such as improved performance, reliability and cost reduction [4]. Integrated modulator with semiconductor lasers seems to be a potential candidate in high-density wavelength division multiplexing systems [5]. One of the main advantages of the integrated modulator is to reduce frequency chirping, resulted from the direct modulation of lasers, hence expanding the system bandwidth [5,6].

In this paper, 10-channel monolithic multiple wavelength electro-absorption (EA) modulators have been fabricated onto a single chip using a one-step quantum well intermixing technique based on arsenic (As^{++}) ion implantation through a graded thickness silicon dioxide mask [7]. Each individual modulator has a dimension of 400 x 500 μm^2, 50 μm width of active window, 500 μm cavity length and 20 μm width of isolation trench. The EA intensity modulators were characterized at room temperature using end-fire-coupling technique. Samples used in this study had a InGaAs/InGaAsP multiple quantum well (MQW – five quantum wells) laser structure grown by metal-organic vapor phase epitaxy and were of the form of a stepped graded index (GRIN) hetero-structure.

Photo-current measurements from 0.0 V to 9.0 V bias were performed by end-fire coupling a single-mode laser source into the quantum-well active region. A tunable semiconductor laser, with wavelength tunability ranging from 1500 nm to 1580 nm, was used in this measurement. Figure 1 shows the photo-current absorption for the EA modulators with wavelength, which have undergone intermixing that resulted blue wavelength shifting of 0 nm (channel 1), 24 nm (channel 6), 33 nm (channel 7) and 46 nm channel (8), respectively. Note that the band-edge of channels 9 and 10 cannot be determined due to the limitation of the tunable laser source. Figure 2 shows the photo-current spectra of the intermixed modulator (channel 6) under 0.0 - 9.0 V reverse bias. Figures 1 and 2 resemble optical absorption profile for quantum well structure. From Figure 1, it can be observed that the photo-current absorption curves have been blue-shifted to different degrees across the single chip. Only band-edges from 6, out of 10, channels have been measured. The band-edges of the quantum well are approximately found to be 1558 nm (channel 1), 1556 nm (channel 2), 1553 nm (channel 3), 1534 nm (channel 6), 1525 nm (channel 7) and 1512 nm (channel 8).

Although there is no clear exciton peak observed, behaviors relating to the light and heavy holes transitions are still relatively distinguishable (Figure 1). For the intermixed samples, these behaviors become more poorly defined as the degree of intermixing increases, i.e. as the quantum well profile becomes parabolic after intermixing. Figure 2 shows that the absorption increases to longer wavelengths in the consequence of the broadening of the absorption edge, due to the Franz-Keldysh (FK) effect. Since the exciton peaks under 0 V bias (Figure 1) are not clearly resolved, it is not sure whether there is any quantum-confined Stark effect (QCSE) [8]. However, it is still believed that good intermixed and un-intermixed EA modulator could be fabricated using this technique.

The intermixed EA modulator at channel 6 (ie band-edge of 1534 nm) was then reverse biased to assess the modulation depth and the voltage swing. The tunable laser source was set to 1555 nm, i.e. below the absorption

edge, for this measurement. A modulation depth of as high as –8 dB with voltage swing of –7.5 V has been observed.
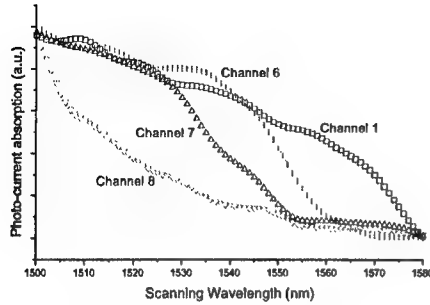

Figure 1 Photo-current absorption for modulators, with energy band-gap shifted by 0 nm (channel 1), 24 nm (channel 6), 33 nm (channel 7) and 46 nm (channel 8) under no bias.
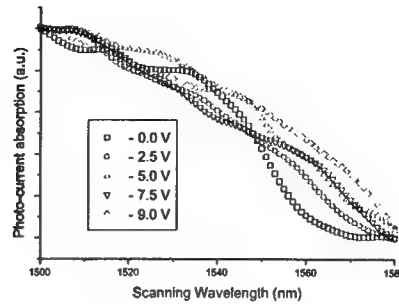

Figure 2 Photo-current absorption for modulator, with energy band-gap shifted by 24nm (channel 6) under 0.0 – 9.0 V bias.

Multiple wavelength selective channel electro-absorption (EA) intensity modulators have been successfully fabricated on the single chip using a one-step QWI process. A modulation depth of as high as –8 dB with voltage swing of –7.5 V has been measured.

References

[1]   J. Singh, "Semiconductor Optoelectronics : Physics and Technology", McGRAW-HILL Int. Ed., 1995, Singapore.
[2]   T.L Koch and Uziel Koren, "Semiconductor Photonic Integrated Circuits:, IEEE Journal of Quantum Electronic, Vol. 27, No.3 1991, pp 641-653.
[3]   K. Shimomura and S. Arai, "Semiconductor Waveguide Optical Switches and Modulators", Fibre Integrated Optics, Vo. 13, pp 65-100.
[4]   S. Charbonneau, E.S. Koteles, P.J. Poole, J.J. He, G.C. Aers, H. Haysom, M. Buchanan, Y. Feng, A. Delage, F.Yang, M. Davies, R.D. Goldberg, P.G. Piva, and I.V. Mitchell, "Photonic integrated circuits fabricated using ion implantation", J. Select. Topics Quant. Electron. 4, vol. 4, pp 772-793, 1998
[5]   H. Takeuchi, K. Kasaya and K. Oe, "Low-Switching-Voltage InGaAsP/InP Waveguide Interferometric Modulator for Integrated Optics", IEEE Photonics Technology Letters, vol. 1, No. 8, pp 227-229, 1989.
[6]   F. Koyama and K. Iga, "Frequency Chirping in External Modulators", Journal of Lightwave Technology, Vol. 6, No. 1, 1988, pp 87-93.
[7]   H.S. Lim, "Photonics Integration of InGaAs-InGaAsP Laser Using Low Energy Implantation Induced Quantum Well Intermixing", M. Eng. Thesis, School of Electrical and Electronic Engineering, Nanyang Technological University, Singapore, 2000.
[8]   A. McKee, C.J. McLean, G. Lullo, A.C. Bryce, R.M. De La Rue, J.H. Marsh and C.C Button, "Monolithic Integration in InGaAs-InGaAsP Multiple Quantum-Well Structures Using Laser Intermixing", J. Quantum Electronics, 33, No. 1, pp. 45-54, 1997.

Enhanced Imaging Arrays Using a
Sigma Delta ADC in Si CMOS for Each Array Pixel

Martin A. Brooke
School of Electrical and Computer Engineering
Georgia Institute of Technology
Atlanta, Georgia 30332

Abstract

Recently we have demonstrated a compact current input oversampling modulator for a scalable high frame rate focal plane arrays [1] that enable frame rates over than 100kfps operating in continuous imaging mode. All the circuits including data lines and detectors were laid-out to fit into 125umX125um space using 0.8um CMOS technology. This compact converter also provides improvement in noise filtering performance over imagers that use capacitance at each pixel to convert detector current to voltage. This technique may allow noisy detectors to be used at high temperatures with good image quality.

1. Introduction

Current imaging systems implemented using charge-coupled device (CCD) technology with off-chip analog-to-digital data converters are limited in the amount of detector noise they can filter this causes problems with noise at high frame rates [2] or with noisy detectors (e.g. IR detectors) Focal-plane-array (FPA) technology [3] can reduce the noise added to the detector noise at each pixel by eliminating long analog signal paths, however if a capacitor is used to convert detector current to voltage, or a charge packet, at each pixel, this capacitor "samples" the noise in the detector before each readout permanently embedding it with the signal.

Recently to overcome the speed limitations of the conventional readout systems, we have developed fully parallel readout systems which need a compact ADC for each pixel [4][5]. Due to the small Si area available, a compact ADC with high speed and large dynamic range is necessary. A current input oversampling modulator was found to be a very compact candidate for this imaging application because it is immune to component mismatch, and through subsequent digital filtering of the output signals, a tradeoff between dynamic range and frame rate can be achieved. In addition, the digital filtering can remove high frequency noise from the image data, resulting in an improved signal to noise ratio for the ADC-based system.

2. Current input oversampling modulator

Modern short-channel CMOS processes offer a speed performance which far exceeds the requirements of most imaging systems. Since shorter channel lengths will be available in the future, this speed advantage will be further improved; however, accuracy and component matching are expected to become worse. It could be a serious problem for the fully parallel FPA readout system because there are thousands of ADCs working simultaneously, and needing good uniformity to get a good image. Hence, it is desirable to trade off speed for accuracy, and obtain accuracy advantages at the cost of speed reductions in the focal-plane-array ADCs. One of the ADC's which trade off speed for accuracy is oversampling ADC which is designed in this paper

3.1 Circuit and simulation results

Figure 1 shows the schematic of the combined modulator circuits. The output of the current buffer is connected to the D/A converter and integrator. The current integrator is implemented with a capacitor. The last stage is a comparator, which compares the integrator voltage and reference voltage then makes a one bit output data stream [6]. The comparator output is also fed back to the DAC to control the feedback current which makes the comparator output average track the input value.
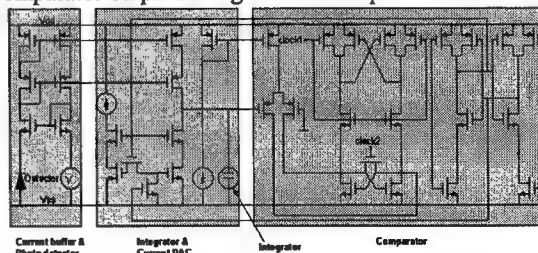

Figure 1. Current input oversampling modulator

Figure 2 shows SPICE simulation results with 50kHz 2uA sinusoidal input. Figure 2(a) shows the integrator voltage variation and the modulator output. The power density function (PDF) of the output code is shown in Figure 2(b). Since this spectrum is of a digital 1 bit

signal, the plot of the PDF shows that most of the digitization noise has been shifted to frequencies higher than the signal frequency. This will occur provided that the ADC operating frequency is much higher than the signal frequency (oversampling). Thus we can digitized the detector current, and almost arbitrarily reduce the amount of noise added in the digitization process by oversampling at higher and higher rates and then filtering out the high frequency noise with a DSP process (such as the FFT used to obtain Figure 2(b)).
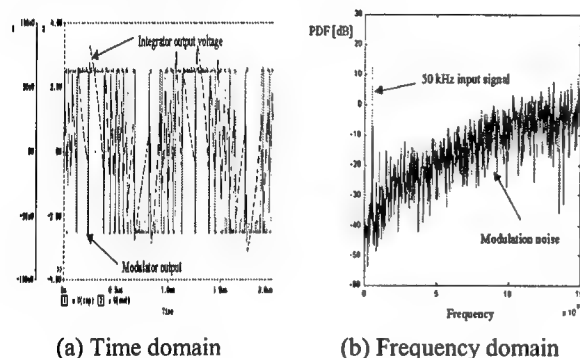

(a) Time domain   (b) Frequency domain

Figure 2. Simulation results

3.3 Fabrication and Test Results

Figure 3 shows a layout and photomicrograph of the modulator circuits for FPA pixels. An 8x8 focal-plane-array system was tested using a 100 MHz system clock which means each pixel operates at 1.56MHz.
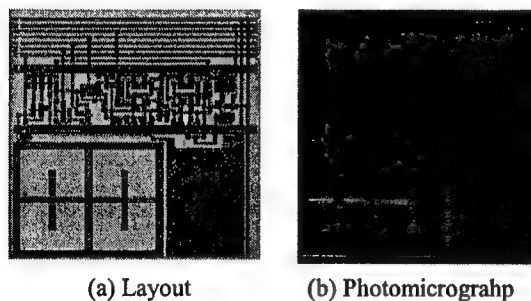

(a) Layout   (b) Photomicrograhp

Figure 3. Modulator Layout and photomicrograph

Figure 4(a) shows the frequency response of the system. The noise is modulated and the in-band noise is decreased. Figure 4(b) shows a purely simulated result from the Matlab for comparison.
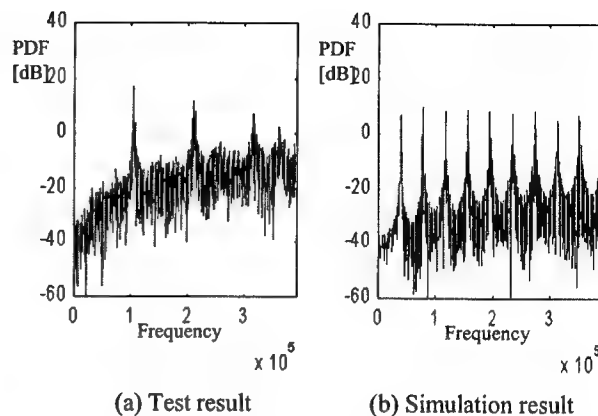

(a) Test result   (b) Simulation result

Figure 4. PDF responses of the modulator

There are many pattern noises in the ideal simulation which can be removed by adding a white noise. Test results have less pattern noise because there are many noise sources which dither the input signal [7]. From the simulation and test results, it is not possible to distinguish the system noise from the quantization noise. Which means at an oversampling ration of 4096 no noticeable noise is added by our hardware. Thus only detector noise in the signal band would remain after filtering.

6. References

[1] Youngjoong Joo, Martin A. Brooke "Compact Current Input Oversampling Modulator Design for a Scalable High Frame Rate Focal Plane Arrays," *ISCAS 2000 Conf Publ* Geneva, Switzerland, May, 2000.

[2] B. T. Turko, G. J. Yates, N. S. King, " Processing of multiport CCD video signals at very high frame rates," *Proc. SPIE Int. Soc. Opt Eng.*, vol. 2549, pp. 11-15, 1995.

[3] Z. Zhou, B. Pain, R. Panicacci, B. Mansoorian, J. Nakamura, E. R. Fossum, "On-Focal-Plane ADC: Recent Progress at JPL," *Proceedings of SPIE - The International Society for Optical Engineering*, vol. 2745, pp. 111-122, 1996.

[4] Y. Joo, S. Fike, K. S. Chung, M. A. Brooke, N. M. Jokerst, D. S. Wills, " Application of Massively Parallel Processors to Real Time Processing of High Speed Images," *MPPOI*, pp.96-100, 1997.

[5] Y. Joo, J. Park, M. Thomas, K. Chung, M. Brooke, N. Jokerst, D. Wills, "Smart CMOS Focal Plane Arrays: A Si CMOS detector array and sigma delta analog to digital converter imaging system," *IEEE Journal of Selected Topics in Quantum Electronics*, vol. 5, no. 2, pp.296-305, 1999.

[6] G. M. Yin, F. Op't Eynde, W. Sansen, "A high-speed CMOS comparator with 8-b resolution," *IEEE J. of Solid-State Circuits*, vol. 27, no. 2, pp.208-211, February 1992.

[7] J. C. Candy, G. C. Temes, "A tutorial discussion of the oversampling method for A/D and D/A conversion," *Proceedings - IEEE International Symposium on Circuits and Systems*, vol. 2, pp. 910-913, 1990.

Characterization and Performance Evaluation of CMOS Based Photodetectors

Sunil S. Konanki and Fred R. Beyette Jr.

University of Cincinnati
Department of ECECS
PO Box 210030
Cincinnati OH, 45221-0030
beyette@ececs.uc.edu

ABSTRACT

The design, characterization and evaluation of silicon photodetectors suitable for smart pixel based applications are presented. Several different CMOS based photodetector structures are presented including p-n junction detectors and bipolar phototransistors.

SUMMARY

Photodetectors a fundamental component necessary for the implementation of photonic information processing systems.[1-2] In addition to the ability to detect optical signals, it is often desirable to have a photodetector structure that can monolithically integrated with CMOS logic circuitry.[3] In this paper we report on the design, characterization and performance evaluation of silicon photodetectors that can be fabricated within the technology constraints of a standard 1.2μm CMOS fabrication process.

PHOTODETECTOR DESIGN

In this study, p-n junction photodiodes are implemented using a P+ diffusion to N-well and N-well to P-type substrate resulting in a very fast shallow p-n photodiode and a slow n-p photodiodes respectively. The phototransistor is implemented using a P+ diffusion in an N-well to form the emitter and base regions. The P-type substrate(which is grounded in the n-well CMOS process) acts as the lightly doped collector region. Figure 1 shows a cross-sectional view of a typical photodetector structure.
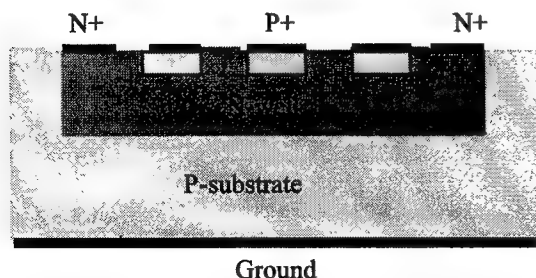
N+   P+   N+

P-substrate

Ground

Figure 2 Cross-section of a typical photodetector.

PHOTODETECTOR PERFORMANCE

Simulation results indicate that the dark currents for the photo diodes and the phototransistor are very low (on the order of pico amps). Both photodiode and phototransistor configurations can be biased over the range of bias potentials common in digital logic circuits. Placing the p side at a lower potential than the n side biases the photodiodes. This is relatively straightforward for most circuit designs especially for the well to substrate diode where the p-substrate is normally tied to the lowest bias potential on the chip. In addition to using the photodiodes independently, it is possible to combined the operation of both photodiodes by biasing the n-well to positive potential and grounding the P+ diffusion and the P-substrate.

The phototransistor is biased in a floating base configuration. In this configuration, transistor action in the device amplifies the photogenerated current, which acts as a base current in the transistor structure.

Figure 2 shows the simulated photocurrent as a function of optical intensity for each individual photodetector illuminated with a 600nm light source. As in the figure, transistor action increase the photocurrent in the PNP phototransistor by a factor of ~100.

Photo currents for different models at 600nm

Current in A/micron

1.00E-05
1.00E-06
1.00E-07
1.00E-08
1.00E-09
1.00E-10
1.00E-11
1.00E-12
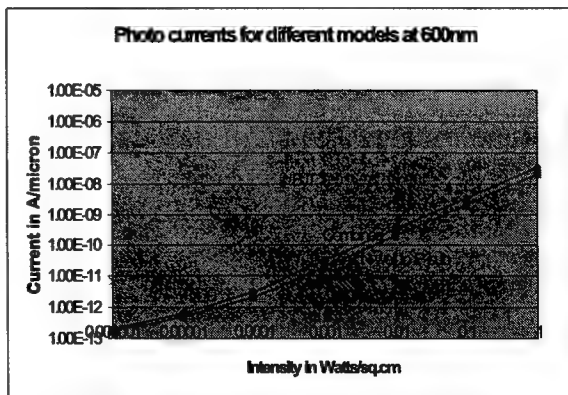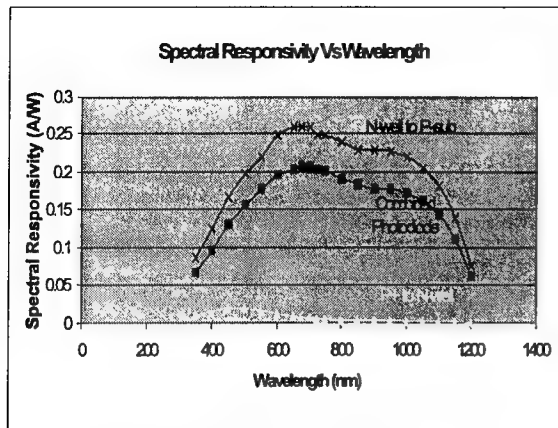1.00E-13

Intensity in Watts/sq.cm

Figure 1. Simulated photocurrents as a function optical intensity for 600 nm light.

Figure 3. Simulated Spectral Responsivity as a function of wavelength for the photodiode structures.

As shown in figure 3, the spectral responsivity of the well to substrate photodiode increases as the wavelength is increased from λ=300nm to 650nm where it reaches a maximum at ~0.27A/W. As wavelength is further increased beyond 675 nm, the responsivity of the photodiode drops due to a decrease in absorption in the active (space charge) region of the photodiode.

As shown in the figure, the spectral responsivity of the P+ to well photodiode is significantly lower than the well to substrate photodiode. This is due to the shallow nature of the pn junction (i.e. as the wavelength increases, a larger fraction of the light is absorbed deep in the substrate where it can not be collected by the P+ to Well diode). Thus, the P+ to Well photodiode has a maximum responsivity at 450nm.

Simulated transient analysis of these photodetectors shows that the P+ to well photodiode is very fast with very small rise and fall times (on the order of pico seconds). The rise time of the well to substrate and the combined photodiodes is very small in the order of pico seconds but the fall time is fairly large around 85ns. This is explained by the long lifetime for photogenerated carriers deep inside the substrate. The rise time of the phototransistor is around 30µs and fall time 75µs. The fall time is large compared to the rise time as the collector is the large substrate and hence carrier lifetime affects the transistor shut off.

CURRENT STATUS

Results shown in this paper are simulated results generated with the commercial 2d material/device simulation package MEDICI. Structures similar to those simulated have been produced in a CMOS layout. These test structures have been sent for fabrication through the MOSIS foundry service. Devices are due back for testing in April 2000. Based on the evaluation of these test device, comparison between simulation results and actual device performance will be presented during the summer of 2000.

CONCLUSIONS

In this paper we have demonstrated and characterized photodetectors suitable for smart pixel applications. Based on 1) the compatibility with CMOS fabrication processes, 2) the ability to detect small power optical signals 3) the ability to directly interface with the conventional electronic logic circuits, we believe that these photodetectors can be successfully used in the designed photonic information processing systems based on photonic VLSI device technologies.

REFERENCES

[1] J.Tang, S.Konanki, B.Seshadri, B.K.Lee, R. C.J.Chi, A.J.Steckl, F.R.Beyette Jr, "CMOS Photodetectors/Receivers for Smart-Pixel Based Photonic Systems", Accepted for presentation at the Proceedings of SPIE – Aug 00, San Diego, CA.

[2] F.R.Beyette Jr, J.Tang, B.Seshadri and S. Konanki, "CMOS based photodetectors and photoreceivers for smart optical memory interface devices", Presented at SPIE Annual Meeting, Denver, Colorado, July 1999.

[3] J.Tang, B.Seshadri, K.N.Naughton, B.K.Lee, R.C.J.Chi, A.J.Steckl and F.R.Beyette Jr. "CMOS Based Photoreceiver Arrays for Page-Oriented Optical Storage Access", Submitted to IEEE Photon. Tech Lett.

Frequency Locking of Micromachined Tunable VCSELs to External Wavelength Selective Filters.

W. A. Martin, C-C. Lin

Solid State and Photonics Lab, Paul G. Allen Center for Integrated Systems, Rm. 328, Stanford, CA 94305
Phone: (650) 725-6913, Fax: (650) 723-4659, email: wayne@snow.Stanford.edu

F. Sugihwo

Communication Optics Research Laboratory, Agilent Laboratories, 3500 Deer Creek Road, Palo Alto, CA 94304

J. S. Harris, Jr.

Solid State and Photonics Lab, Paul G. Allen Center for Integrated Systems, Rm. 328, Stanford, CA 94305

Abstract: Frequency locking and tracking of a micromachined tunable VCSEL to an external spectrometer over a 7 nm range is demonstrated. Frequency locking to channels in an arrayed waveguide grating is needed for WDM systems.

1. Introduction

Wavelength division multiplexing is vastly increasing the capacity of installed fiber and increasing the market for fiber optic communications systems. However to enable fiber -to-the-desktop and fiber-to-the-home a low-cost integrated wavelength tunable transceiver must be available. Arrayed waveguide gratings (AWG) provide the integrated multichannel wavelength selective filter and micromachined vertical cavity photonic devices provide the tunable sources and detectors needed for a WDM transceiver. The WDM transceiver needs to be able to transmit and receive on any wavelength, which requires a method of frequency locking the tunable devices to the passband of a channel in the AWG.

Using our micromachined tunable vertical cavity lasers (MTV CSELs) [1-3] we have demonstrated frequency locking and tracking to an external spectrometer over a 7 nm range. The tuning range is limited by the voltage required to tune the membrane exceeding the output voltage range of the op -amps used in the frequenc y locked loop (FLL) electronics. The current devices were made in the optimized process so their tuning voltage is abnormally high and a new process run would allow the tuning range to be limited by the operation of the MTVCSEL ~30 nm.

2. Frequency Locking

The method for frequency locking to the slope of the wavelength passband is shown in figure 1.
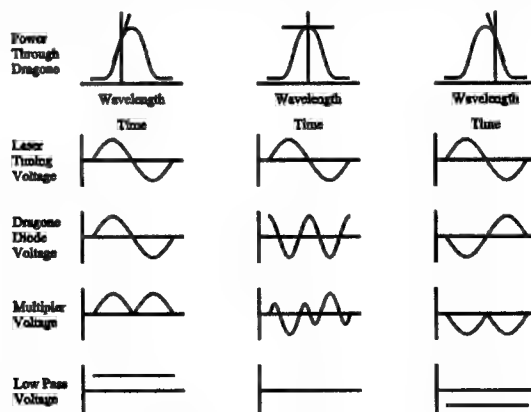

Fig. 1. Concept for frequency locking to a wavelength passband

A small sinusoidal dither signal is added to the DC bias of the tuning membrane and causes a slight variation in the wavelength of the laser, which is converted to an intensity variation by an external wavelength filter. The

intensity variation is measured with a photodiode and multiplied by the original sinusoid in o rder to detect the relative phase, which is set by the local slope of the wavelength passband. Feedback with an integrator can then follow the slope to the peak of the passband. A block diagram of the FLL system is shown in figure 2.
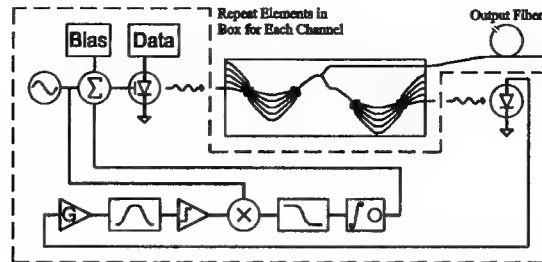

Fig. 2. Block diagram of FLL system

In order for the system to be stable under all laser modulation schemes and changes in the laser output power and coupling efficiency versus tuning the FLL uses adaptive gain. The basic design is a form of th e externally excited adaptive loop, which has been analyzed by Horowitz [4]. The current design is stable for 30 dB of gain variation.

3. Measurements

After fabricating the MTVCSELs a custom built on wafer probing system is used to measure their lasing a nd tuning characteristics. A microscope objective collimates the backside laser emission, which is routed to a beamsplitter and then to a fiber coupler and the spectrometer. The fiber -coupled emission is connected to either an optical spectrum analyzer or a scanning Fabry-Perot to measure the output spectrum.

The MTVCSEL tuning voltage is shown in figure 3 for different spectrometer settings when the system is frequency locked.
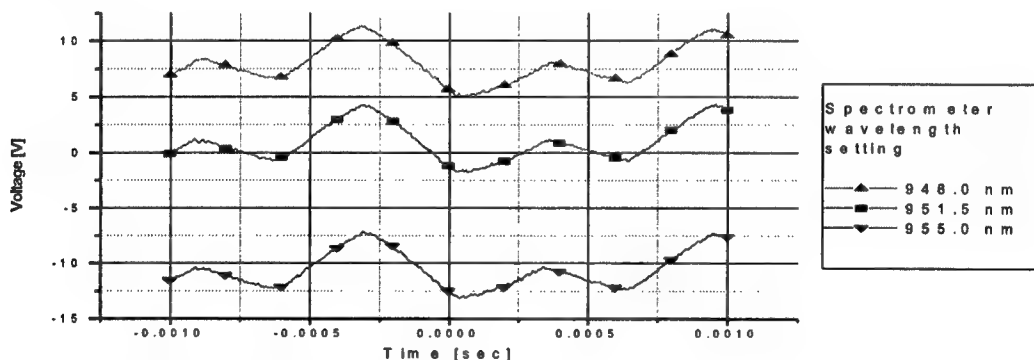

Fig. 3. VCSEL tuning voltage versus time for different spectrometer settings

The amplitude of the dither signal is large in this example because the conversion gain of the multiplier is too low. Increasing the amplitude of the reference sinusoidal input will correct this and allow the dither amplitude to be decreased, which will clean up the optical spectrum which is presently about 600 GHz (2 nm) wide. The excessive width is likely caused by the device going into multimode operation due to excessive excitation of the membrane. The typical FWHM of th e laser linewidth is about 3 GHz (10 pm) when the membrane bias is not modulated.

3. References

[1] F. Sugihwo, M. C. Larson, J. S. Harris, Jr., "Micromachined widely tunable vertical cavity laser diodes," JMEMS, 7, 48-55 (1998).
[2] F. Sugihwo, M. Larson, C-C. Lin, W. A. Martin, and J. S. Harris, Jr., "Micromachined Tunable Vertical Cavity Laser with a 25nm Wavelength Range," Proceedings of the 55th Annual Device Research Conference, (Institute of Electrical and Electronics Engineers, New York, 1997), pp. 108-10.
[3] W. Martin, F. Sugihwo, J. S. Harris, Jr., "Frequency Locking of a Micromachined Tunable VCSEL for WDM optical interconnects," Digest of the OSA Annual Meeting / ILS-XIII, (Optical Society of America, Washington, D.C., 1997), pp. 112.
[4] I. M. Horowitz, J. W. Smay, A. Shapiro, "A Synthesis Theory for the Externally Excited Adaptive System," TAC, 19, 101-107 (1974)

High-sensitivity 1-Gb/s CMOS receiver integrated with a III-V photodiode by wafer-bonding

Tatsushi Nakahara, Hiroyuki Tsuda, Kouta Tateno, Noboru Ishihara, and Chikara Amano

NTT Photonics Laboratories

3-1 Morinosato-Wakamiya, Atsugi, Kanagawa, 243-0198, Japan

e-mail: nak@aecl.ntt.co.jp

Low-cost silicon photoreceivers are useful in telecommunications- and optical interconnection-systems. CMOS receivers are especially attractive because of their low power and ease of integration with CMOS-VLSI systems. 1-Gb/s monolithic CMOS receivers integrating silicon photodiodes (PDs) in the conventional CMOS process have been developed [1][2]. Hybrid receivers integrating III-V PDs with CMOS have also been fabricated using either the flip-chip bonding technique [3] or the polyimide wafer-bonding technique we developed [4]. However, the monolithic receivers operate at only 0.85-μm wavelength and require a high supply voltage of over 10 V for the PD. All of the reported hybrid receivers also operate at only 0.85 μm, despite the fact that hybrid integration allows a variety of device combinations. Furthermore, none of the reported CMOS photoreceivers have achieved a sensitivity below −10 dBm at 1Gb/s.

We have developed wafer-bonded hybrid receiver using 0.5-μm CMOS that operates with a single 3.3-V supply voltage. The receiver circuit is small and simple, has high sensitivity and a broad bandwidth, and operates at either 0.85 or 1.55 μm due to the direct attachment of the III-V PD without parasitic capacitance.

Figure 1 is a circuit diagram of the CMOS receiver, which consists of the III-V PD, two amplifier stages, and an off-chip driver. The first stage is a transimpedance amplifier made of a simple inverter and a feedback resistor (R_f). Because the parasitic capacitance on the PD is below 10 fF [4], the gate width of the first-stage transistor can be small, and R_f can be set as high as 5kΩ when the front-end of the receiver has a bandwidth of over 1 GHz. Such a large R_f leads to not only low noise, i.e. high sensitivity, but also high gain. The small size and high gain of the first stage allows the use of a second-stage voltage amplifier made also of a simple, small-sized inverter. The off-chip driver consists of two inverters, both with a feedback resistor. The driver is designed to have a bandwidth of over 1 GHz, zero voltage gain, and a 50-Ω output impedance. The gate width of each transistor is shown in the figure. The gates are gradually widened so that capacitive charging time does not limit the bandwidth. The voltage supply lines are divided into four sections so that the amplified output signal is not fed back to the sensitive input part through the lines.

Figure 2 is a photograph of the receiver. A GaAs PD is attached to the CMOS circuit by means of the polyimide wafer-bonding, which is followed by mesa-etching of the PD and interconnection process. As can be seen, the area is small because the CMOS circuit is simple and neither bonding wires nor large pads are needed to connect the CMOS to the PD. The PD, without an AR-coating, showed a photoresponsivity of 0.42 A/W and a dark current below 10 pA @ 5 V. Figure 3 is a measured eye diagram for the GaAs-PD/CMOS receiver operating at 1 Gb/s when optical input has −26.4-dBm average power and 0.85-μm wavelength. The input was 2^{15}-1 PRBS signal, and the electric output off chip was directly monitored. For the measurements, all four voltage supply lines were connected to a single 3.3-V source. A good eye opening is observed. The O/E conversion efficiency is about 10000 V/W, corresponding to a transimpedance gain of about 25kΩ. Figure 4 plots bit error rates (BERs). At 10^{-10} BER, minimum input sensitivities are −29.7 and -27.1 dBm for bit rates of 622 Mb/s and 1 Gb/s, respectively. Dynamic ranges are 21.7 and 19.0 dB, respectively. The receiver operated error free at up to 1.3 Gb/s with total power consumption below 30 mW. The measurement results are summarized in Table 1.

We hybridized InGaAs PDs in almost the same manner as the GaAs PDs. The measurement results using 1.55-μm light are also summarized in Table 1. The sensitivities are a little worse than those for the 0.85-μm receiver. This is attributed to high contact resistance and a fairly large dark current of 100 nA.

In conclusion, a GaAs or InGaAs photodiode was attached to a 0.5-µm CMOS receiver circuit by a polyimide wafer-bonding technique. The circuit is simple and small, and has high sensitivity and a broad bandwidth due to the low parasitic capacitance on the photodiode. The receiver operates with a single 3.3-V supply voltage at either 0.85 or 1.55 µm and achieves −27.1-dBm sensitivity at 1 Gb/s.

References

[1] T. K. Woodward and A. V. Krishnamoorthy, "1 Gbit/s CMOS photoreceiver with integrated detector operating at 850 nm," Electron. Lett., 34, (12), 1252-1253 (1998).

[2] C. L. Schow, et. al, "A Monolithically Integrated 1-Gb/s Silicon Photoreceiver," IEEE Photon. Technol. Lett., 11, (1), 120-121 (1999)

[3] A. V. Krishnamoorthy, et. al.,"Operation of a single-ended 550 Mbit/s, 41 fJ, hybrid CMOS/MQW receiver-transmitter," Electron. Lett., 32, (8), 764-765 (1996).

[4] T. Nakahara, et. al., "Hybrid integration of GaAs pin-photodiodes with CMOS transimpedance amplifier circuits," Electron. Lett., 34, (13), 1352-1353 (1998).
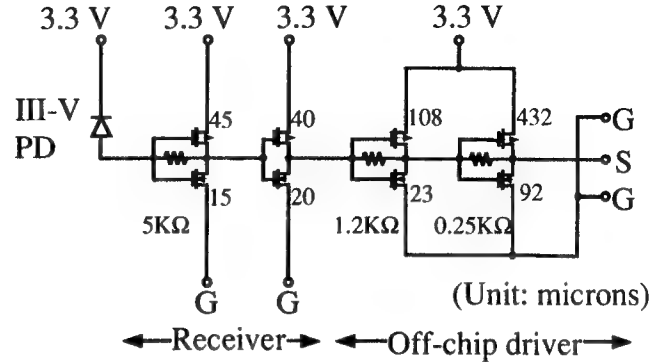
Fig.1 Circuit diagram of the CMOS receiver integrated with a III-V photodiode
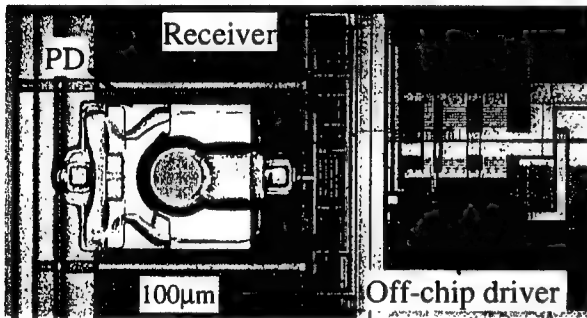
Fig.2 Photograph of the receiver

20 mV/div   500 ps/div
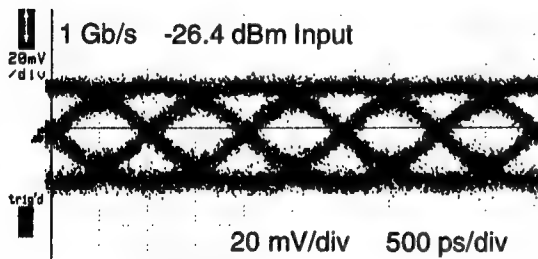
Fig.3 Eye diagram at 1 Gb/s
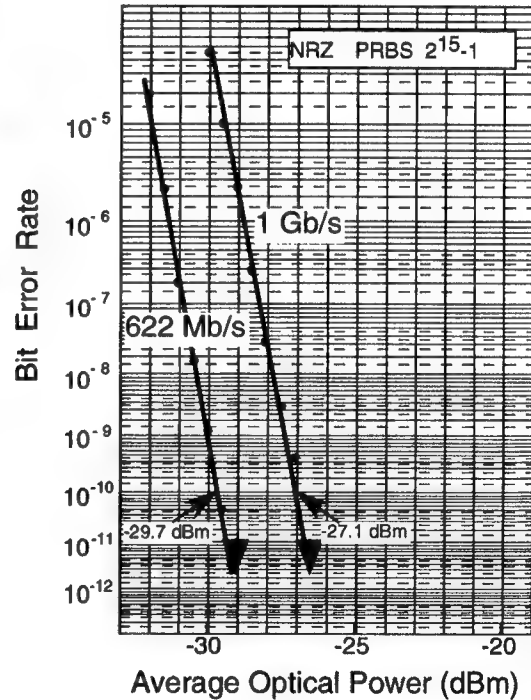
Fig.4 Bit error rates

Table 1 Measurement results   @10^{-10} BER

Photodiode				PD/CMOS Receiver			
Material	Diameter (µm)	Dark current	Responsi-vity (A/W)	Wavelength (µm)	Bit rate (NRZ b/s)	Sensitivity (dBm)	Dynamic range (dB)
GaAs	30	< 10 pA	0.42	0.85	622 M	-29.7	21.7
					1 G	-27.1	19.0
					1.3 G	-18.3	5.2
InGaAs	44	~100 nA	0.8	1.55	622 M	-28.4	18.7
					1 G	-25.3	14.7

18

Hybrid GaAs MQW Modulators and Detectors Flip-Chip Bonded to Silicon CMOS Circuitry

H. D. Chen[a], K. Liang[a], Q. M. Zeng[b], X. J. Li[b], Z. B. Chen[a], Y. Du[a], R. H. Wu[a]

[a] State Key Laboratory on Integrated Optoelectronics, Institute of Semiconductors
Chinese Academy of Sciences, Beijing 100083, China
hdchen@red.semi.ac.cn
[b] Hebei Semiconductor Research Institute, Shijiazhuang 050051, China

The two dimensional arrays of GaAs/AlGaAs multiple quantum well (MQW) modulators and detectors array flip-chip bonding[1] directly over state-of-the-art silicon VLSI can allow high speed electronic processing and high density optical input and output[2]. A modulator-based optoelectronic-VLSI (OE-VLSI) circuit technology has been developed at Bell Laboratories[3-6].

We demonstrated the hybrid integration of reflection-mode, surface-normal GaAs/AlGaAs multiple quantum well modulators and detectors array directly over 1μm silicon CMOS circuitry via flip-chip solder bonding. Some MQW devices were used as input-light detectors and others served as output-light modulators, which were designed for 850nm wavelength operation. The GaAs/AlGaAs multiple quantum well (MQW) structure was grown by molecular beam epitaxy. In order to increase the absorption of the intrinsic region, the period of quantum wells was chosen to be 90 pairs and decreased the thickness of AlGaAs barriers for decreasing for operation voltage.

We have fabricated 1×20 the modulators and detectors array for optoelectronic hybrid integrated module. The MQW device mesa was 60μm × 160μm in size and each was consisted of a 40μm×40μm P-pad and N-pad. The active region of the device was the P-pad which also serve as a reflector. The bump-bond pad sizes and optical windows sizes were 26μm×26μm. Indium was deposited on both GaAs chip and silicon chip for the solder. The circuits contain transimpedance receiver, switching nodes and modulator driver, as shown in Fig. 1. The receiver had four amplication stages, with the first being of the transimpedance amplifier and inverter-based amplifiers in the following three stages. The control signals of A-C used as selecting output light modulators addressed. The transimpedance receiver-transmitter circuit can be operated at 300MHz frequency.

The GaAs substrate was removed after the bonding to avoid excess absorption in the substrate. The etching of devices was stopped on the AlAs stop-etch layer, which had been placed between the GaAs substrate and the active devices layer. A key feature of hybrid integrated devices for flip-chip bonding and then GaAs substrate removal was the etching of outer mesas around the MQW devices. If the etching were not controlled well, it would cause to break and possibly damaging. In order to avoid this case, we developed the method which when the one terminal of MQW device mesas were exposed first during the etching process of GaAs substrate, the etching was stopped immediately, as show in Fig. 2. This method would allow large area of the wafer remain instead of small isolated mesas left and the exposed terminals of MQW devices were used as sign to mark their location. It did not bring more absorption in remain GaAs substrate since the wafer thickness was only few micron.

In fact, we get nearly the same reflection spectrum for the four devices at an array after flip-chip bonding and package, shown in Fig. 3. It is indicated the good optoelectronic uniformity of elements modulators and detectors array. Because of the strong exciton absorption, the reflectivity at wavelength 850nm is the minimum under zero field, it can be used as a photodetector in input windows. In other hand as light modulator in output window, increasing with an applied field, the MQW reflection modulator contains the effects of quantum confined Stark effect, which shows the shift of exciton peak and the change of the absorption coefficient in quantum well under applied electric field. Figure 4 shows the microspot reflectivity spectrum at zero and 5V biases of the MQW device after flip-chip bonding. When the operation wavelength is at 860nm, the low reflectivity at an applied voltage of 5V and the high reflectivity at 0V, and the contrast ratio is more than 1.2:1 for a 5V bias.

REFERENCES

1. K. W. Goossen, J. A. Walker, L. A. D'Asaro, S. P. Hui, B. Tseng, R. Leibenguth, D. Kossives, D. D. Bacon, D. Dahringer, L. M. F. Chirovsky, A. L. Lentine, D. A. B. Miller, *IEEE Photon. Technol. Lett.* , 1995, **7**, pp. 360-362.
2. H. S Hinton, *IEEE J. of Selected Topic in Quantum Electron.*, 1996, **2**(1), pp.14-23
3. A. V. Krishnamoorthy, and D. A. B. Miller, *IEEE J. of Selected Topic in Quantum Electron.*,1996, **2**, pp.55-76,
4. A. V. Krishnamoorthy, and K. W. Goossen, *International J. of Optoelectron.* , 1997, **11**(3), pp.181-198
5. A. L. Lentine, D. J. Reiley, R. A. Novotny, R. L. Morrison, J. M. Sasian, M. G. Beckman, D. B. Buchholz, S. J. Hinterlong, T. J. Cloonan, G. W. Richards, and F. B. McCormick, *Appl. Opt.* , 1997, **36**, pp. 1804-1814.
6. T. K. Woodward, A. V. Krishnamoorthy, *Electron. Lett.* ,1998, **34**(12), pp. 1252-1253.
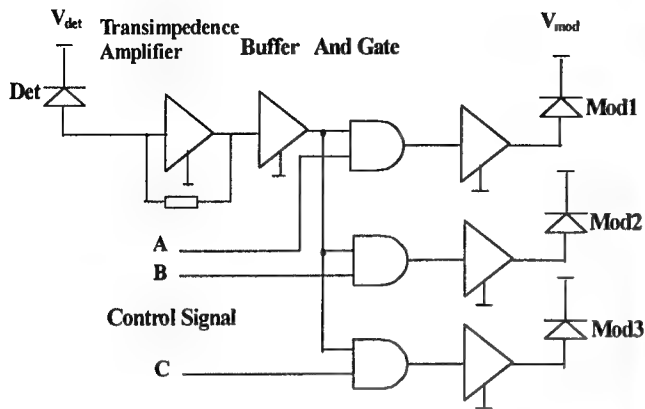
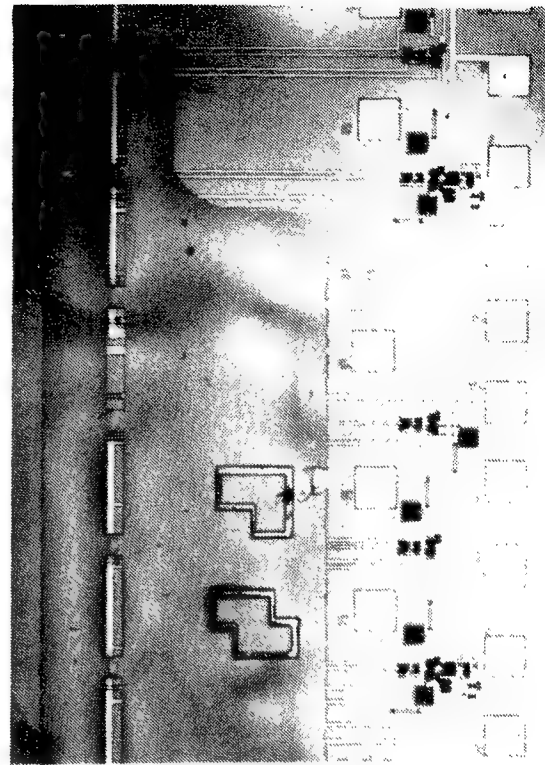Fig. 1. Schematic diagrams of a node in the hybrid circuit

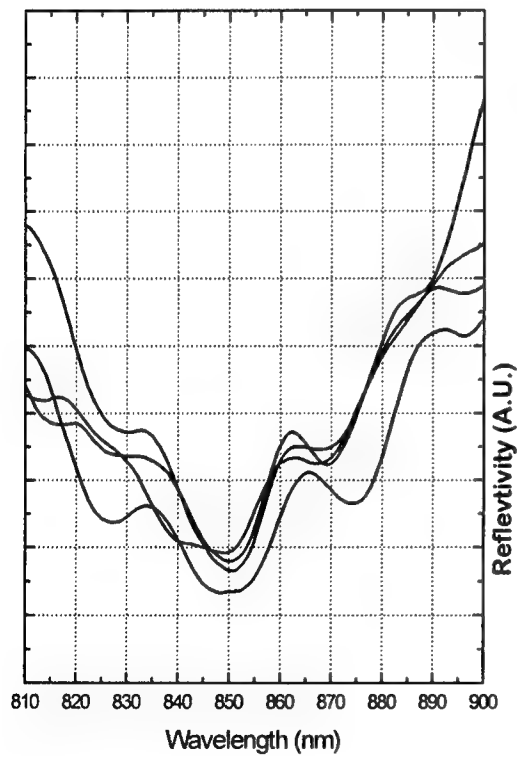Fig. 2. Microphotograph of the controlled etching substrate

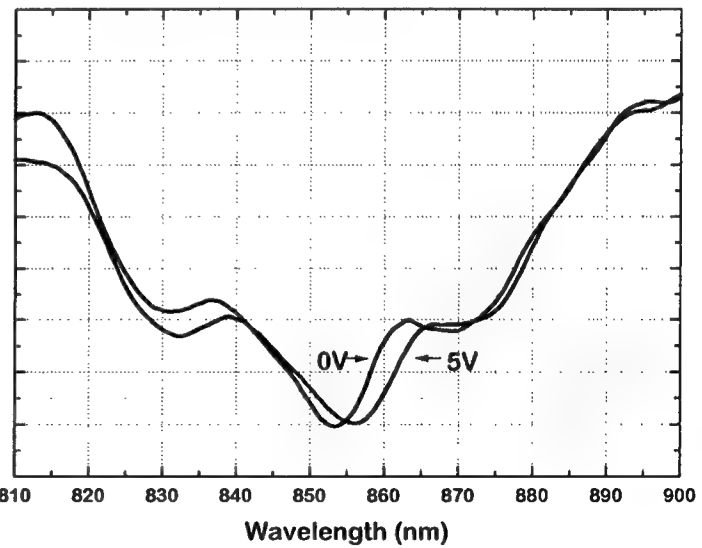Fig. 3 Reflection spectrum for the four devices at an array

Fig. 4 Reflectivity spectrum at 0V and 5V biases

Antiferroelectric Liquid Crystal on Silicon

I. Underwood[1], D.G.Vass[1], M.I. Newsam[1]
J.M. Oton[2], X. Quintana[2],
L. Chan[3], N Flannigan[3]
G Swedenkrans[4]
M Rampin[5]

[1] University of Edinburgh, Dept of Electronics & EE / Dept of Physics & Astronomy, The Kings Buildings, Mayfield Road, Edinburgh, EH9 3JL, Scotland
[2] Universidad Politecnica Madrid, Dept Tecnologia Fotonica, 7 Ramiro de Maeztu, Madrid 28040, Spain
[3] Micropix Technologies, 1 St David's Drive, Dalgety Bay, Dunfermline, Scotland, KY11 9PF
[4] Ericsson Saab Avionics AB, 32C Torshamnsgatan, Stockholm SE-16484, Sweden
[5] Seleco Italtel Multimedia SpA, 11 Viale Lino Zanussi, Pordenone, I-33170, Italy

Introduction

Liquid Crystal on Silicon (LCoS) is, by now, a relatively mature technology for the realization of silicon backplane based microdisplays and spatial light modulators. Most silicon backplane microdisplays utilise forms of nematic material and electro-optic effects which, while relatively slow switching, are capable of supporting grey levels and thereby field sequential color at video frame rates. The faster switching ferroelectric materials and electro-optic effects generally operate in a binary mode, so being capable of supporting bit-plane sequential color at video frame rates. We have explored the two combinations of

- tristate antiferroelectric liquid crystal on silicon, and
- thresholdless antiferroelectric (or V-shaped) liquid crystal on silicon.

Pixel count	1280x1024 (SXGA)
Pixel pitch	10um
Aperture ratio	$\geq 80\%$
Frame rate	≥ 60Hz full colour
Contrast ratio	$\geq 30:1$

Table 1. Outline target specification for MINDIS

The primary aim of our collaboration, entitled MINDIS (Miniature Information Display System) has been to characterise the suitability of such materials for use on reflective silicon backplanes and to design and evaluate an AFLCoS microdisplay whose outline target specification is shown in Table 1.
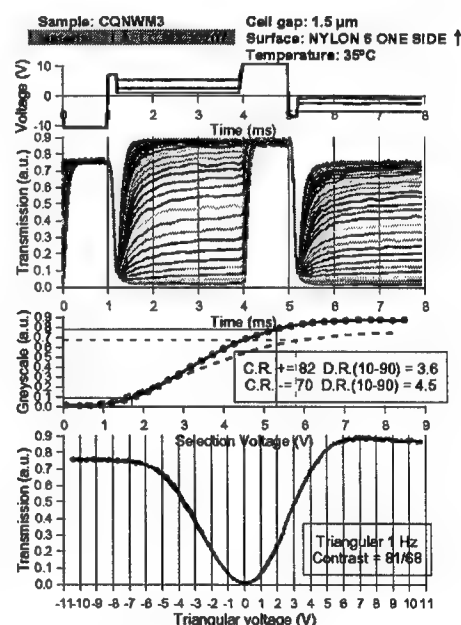
Figure 1. Example of results of AFLC material characterisation

Materials

Electro-optical characterization has been carried out on a number of candidate materials and a comparative evaluation made. DC and switching response have been measured *in reflection* as well as the effect of, for example, temperature and ageing. Figure 1 shows an example of such characterization. It should be noted that only amplitude (not phase) modulation has so far been explored.

Silicon backplane

A silicon backplane has been designed, fabricated and functionally tested successfully. It consists of an array of 1280x1024 pixels on a 10um pitch as indicated on Figure 2. The pixel circuit, Figure 3, is a 2-transistor design consisting of a PMOS analogue switch and a PMOS FET which stores charge on its gate.
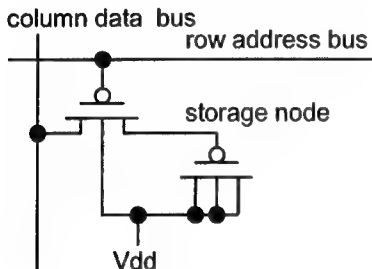
Figure 3. Pixel circuit

In order to minimise hardware design risk and retain maximum AFLC drive waveform flexibility, minimal peripheral circuitry has been included on the chip. Silicon wafers are currently undergoing in-house .

Drive scheme

A major undertaking within the project has been the design of appropriate driving waveforms for TSAFLC and V-shaped materials. Such drive schemes have to take into account both material and backplane issues. Several candidate waveforms have been developed and successfully tested on single pixel test structures using discrete drive circuits.

In order to maintain the flexibility to further optimise these waveforms under the constraints imposed by our SXGA backplane, a field programmable gate array (FPGA) based solution has been adopted for the prototype interface. The pixel driving waveform originates, in effect, from a fully programmable waveform generator.

Conclusions

TSAFLC and V-shaped materials have been shown to be physically, optically and electrically compatible with a CMOS active matrix backplane. They offer promise for silicon backplane based microdisplays and spatial light modulators. It should be noted that only amplitude (not phase) modulation has so far been explored.

Acknowledgements
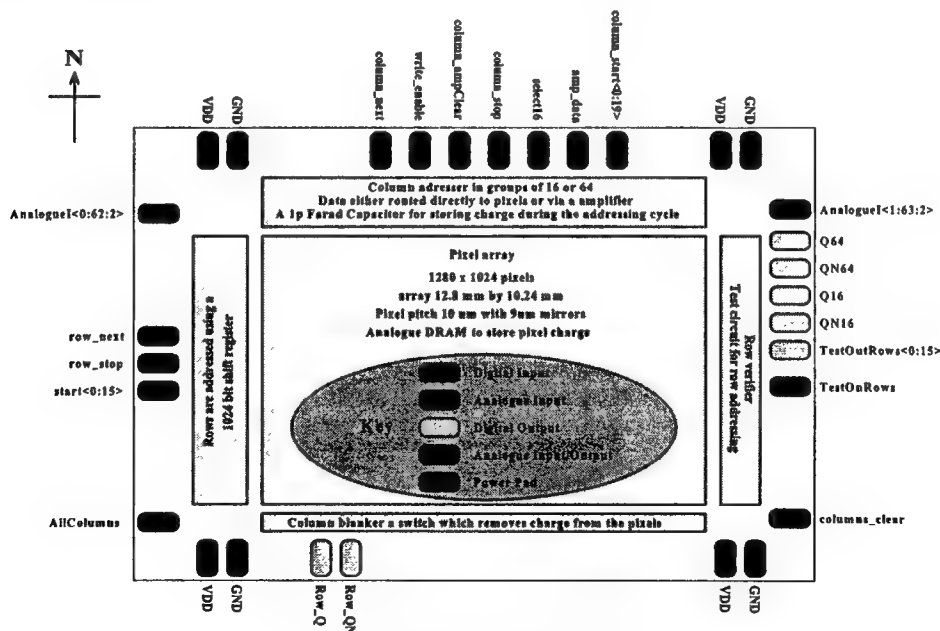
Figure 2 Backplane schematic

Alignment Tolerant Hybrid Photoreceivers Using Inverted MSMs

Michael Vrazel, Jae J. Chang, Martin Brooke, Nan M. Jokerst, Georgianna Dagnall, April Brown
School of Electrical and Computer Engineering, Georgia Institute of Technology
Atlanta, GA 30332, E-mail: mvrazel@ee.gatech.edu

The pervasive implementation of optical links, including fiber to the home and in-home fiber optic backbones, relies upon the cost reduction of optoelectronic interfaces. Highly alignment tolerant photoreceivers can reduce the packaging cost of optical links for applications, which include those mentioned above, by easing packaging constraints. Previously reported optical alignment tolerance measurements have been reported for speeds up to 3 kbps. To achieve a high level of optical alignment tolerance at higher speeds, a high responsivity, large area, low capacitance photodetector such as the inverted metal-semiconductor-metal (I-MSM) detector can produce excellent results. Herein, we report on the hybrid integration of a thin film large area (250×250 μm^2), low capacitance (0.43 pF), high responsivity (0.5 A/W, with no AR coating) InGaAs/InP I-MSM onto a Si CMOS differential receiver circuit. This integrated receiver (shown in Figure 1) demonstrated a bit-error-rate (BER) of 10^{-11} at 414 Mbps and 0.1×10^{-10} at 480 Mbps. The alignment tolerance of this receiver has been modeled and measured at 200 Mbps, and the theoretical results correspond quite well to experimental data.

Photodetector speed in an integrated receiver is limited by either the RC time constant of the device or the transit times of photogenerated carriers within the device. In order to integrate highly alignment tolerant receivers, large area photodetectors are desired; however, the input capacitance to the receiver must be minimized. PIN photodiodes are a common choice for integration onto receivers due to their high responsivities [1,2]. However, these devices have a large capacitance per unit area that ultimately limits detector size and alignment tolerance for a desired data rate. Conventional (C-) MSMs have a low capacitance per unit area, but these detectors have responsivities much lower than those of PINs due to shadowing from the interdigitated electrodes on the top of the device. By inverting the MSM – essentially flipping a C-MSM upside down so the electrodes are on the bottom of the device and removing the substrate – this tradeoff between large area and high responsivity is eliminated with only a minimal sacrifice of device transient response [3].

The I-MSM integrated onto the receiver shown in Figure 1 was fabricated from a wafer grown by molecular beam epitaxy (MBE) with the following nominally undoped layer structure: 400 A InAlAs cap layer, 500 A graded layer, 7400 A InGaAs layer, 500 A graded layer, 400 A InAlAs, 2000 A stop etch layer, and InP substrate. Ti/Au (250 A/2250 A) electrodes and contact pads were deposited via a liftoff process. The electrodes were 2 μm wide and had 5 μm spacings. The contact pads were 250 μm wide and 40 μm long. Mesas were defined by standard photolithography, and the devices were mesa etched down to the InGaAs stop etch layer. The MSMs were then embedded in a protective Apiezon W wax coating, and the substrate and stop etch layer were removed. The encapsulated devices were then bonded to a transparent Mylar® transfer diaphragm, and the wax was removed. At this point, the metal electrodes and contact pads of the MSMs were exposed as the bonding surface, and the bottoms of the devices were bonded to the diaphragm. Such an arrangement facilitated the MSM inversion process during integration.
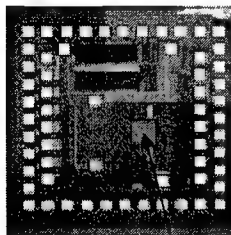
Figure 1 – InGaAs/InP I-MSM integrated onto Si CMOS differential receiver circuit.

The differential Si CMOS receiver circuit was fabricated at the MOSIS foundry. It consisted of a fully differential current mode input, current to voltage conversion, and voltage gain stages. Ti/Pt/Au (250 A/250A/2500 A) integration pads were deposited onto the circuit. The Ti acted as an adhesion layer, and Pt was used as a diffusion barrier. The exposed device contact pads were used to metal-metal bond an individual detector to the integration pads on the receiver circuit, resulting in fingers on the bottom of the MSM device. A polyimide coating was spun onto the integrated circuit and cured at 200 °C in order to promote the adhesion of the detector to the circuit. The polyimide was subsequently removed using a dry etch. The integrated circuit was then wire bonded to a printed circuit board for testing.

The performance of the integrated receiver was tested using a Fabry-Perot laser pigtailed to a single-mode optical fiber. A BER transmitter was used to drive the laser with a pseudorandom pattern. The pigtailed fiber was coupled via FC connectors to a single-mode fiber patch cord that was cleaved on the opposite end. The cleaved end of the fiber was positioned over the integrated receiver using an XYZ

translation stage. The mode field diameter of this fiber was given by the manufacturer as 9.3 μm. A Keithley Source-Measure Unit (SMU) biased the I-MSM. Photocurrent as a function of fiber to detector misalignment was measured at 200 Mbps.

The integrated receiver was modeled and tested for two types of alignment tolerance. Longitudinal alignment tolerance refers to receiver performance as a function of the separation between the surface of the photodetector and that of the emitting source. Transverse alignment tolerance describes the receiver performance as a function of the off-axis separation between the center of the source and the center of the detector.

A Gaussian intensity distribution was assumed as a first-order approximation to the beam emitted from the cleaved fiber. In order to estimate the power coupled from the fiber to the detector, the intensity of the Gaussian beam was integrated over the area of the I-MSM to calculate the percentage of power coupled from the fiber to the detector as a function of longitudinal separation. To predict the coupling efficiency under lateral misalignments (with 1 mm longitudinal separation), the limits of integration were appropriately adjusted to effect a transverse separation between the centers of the fiber and detector. Because the device is inverted, carriers can be excited in the areas of the InGaAs absorbing region that lie directly above the metal contact pads. This has the effect of extending one dimension of the 250x250 μm^2 detecting area by 2 diffusion lengths. Electron diffusion length within the InGaAs was calculated to be ~20 μm based on the assumption of an electron mobility of ~10000 cm ^{2}/Vs and an electron lifetime of 16.7 ns (as described in [4]).

Measured photocurrent was used to calculate power coupled from the fiber to the detector. These experimental results as well as the theoretical predictions for coupled power as a function of longitudinal and transverse separation are compared in Figures 2 and 3. The experimental data in Figure 3 was taken with 1 mm of separation between the fiber and the detector. Experimental and theoretical data in both figures have been normalized to optimal fiber-detector alignment. The discrepancy between the theoretical curve and the experimental data near the 1mm separation mark in Figure 2 may be a result of simplifying the emitted beam to a Gaussian or of the transient response of the I-MSM to excitation by a 200 Mbps pseudorandom signal. The discrepancy in Figure 2 accounts for the discrepancies in the peaks shown in Figure 3 since the latter figure was evaluated at a longitudinal separation of 1 mm.
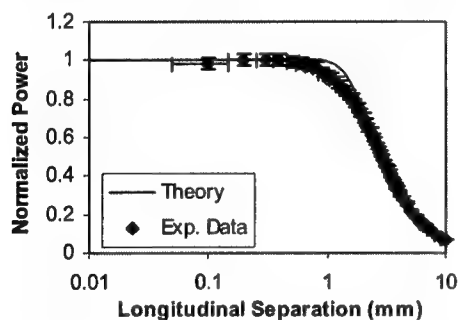
Figure 2 – Longitudinal alignment tolerance   Figure 3 – Transverse alignment tolerance
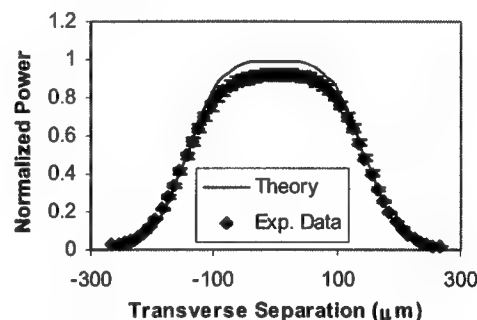
Thin film large area I-MSMs have been integrated onto Si CMOS circuits. These integrated receivers have demonstrated highly alignment tolerant operation at 200 Mbps. Measured alignment tolerance of the receiver corresponded quite well to the performance predicted by theory.

Acknowledgments

References

[1] T. Nakahara, H. Tsuda, K. Tateno, S. Matsuo, and T. Kurokawa, "Hybrid integration of smart pixels by using polyimide bonding: demonstration of a GaAs p-i-n photodiode/CMOS receiver," *IEEE Journal of Selected Topics in Quantum Electronics*, vol. 5 no. 2, pp. 209-216, 1999.

[2] Hsu, S., King, O., Johnson, F., Hryniewicz, J., Chen, Y., Stone, D., "InGaAs pin detector array integrated with AlGaAs/GaAs grating demultiplexer by total internal reflector," *Electronics Letters*, vol. 35, no. 15, pp. 1248-1249, 1999.

[3] Vendier, O., Jokerst, N., Leavitt, R., "Thin-Film Inverted MSM Photodetectors," *IEEE Photonics Technology Letters*, vol. 8, no.2, pp.266-268, 1996.

[4] Juodkazis, S., Petrauskas, M., Quacha, A., and Willander, M., "Charge carrier recombination and diffusion in InGaAs(P) epitaxial layers," *Physica Status Solidi A*, vol. 140, no. 2, pp. 439-443, 1993.

Integrated Opto-VLSI Mobile Multimedia Communicator

Kamran Eshraghian

Centre for Very High Speed Microelectronic Systems
Edith Cowan University
100 Joondalup Drive, Western Australia 6027
k.eshraghian@cowan.edu.au

"It is difficult to say what is impossible, for the dream of yesterday is the hope of today and the reality of tomorrow." Robert H Goddard.

Mobile communications technology has made significant progress from the 1970/80's first generation providing analog voice-only services, to the 1980/90's second generation enabling digital voice and data services. The next generation will be heralded by truly personal communication systems, which are expected to incorporate a high degree of multimedia functionality (voice and data, images, and video), mobility (portable low power devices, heterogeneous networks, roaming), and flexibility (scalability, multiple access, intelligence). Thus, the new generation of personal interactive mobile multimedia mobile communication (M^3C) demand highly compact low power devices capable of image capture and display as well as low bit rate coding and transmission. The new design concept based upon integration of optics with that of electronics has facilitated the realisation of a novel *Intelligent Pixel Array* (IPA) architecture to create a real-time implementation of forward and inverse wavelet transform (WT) for image capture, in-situ processing and display.

The processor consists of an array of Intelligent Pixel (IP) processing elements, as illustrated schematically in Figure 1. Each element of the array incorporates three components: (a) a photo-detector (PD) with associated analogue to digital converter (ADC) for the conversion of the incident light. (b) embedded processor for implementation of parallel video codec algorithm. (c) a liquid crystal display for the conversion of the decoded incoming video stream to an optical output for display. To carry out the required video coding the IP array is used to emulate a mesh network of processing elements such that the inherent parallelism and interconnectivity of the architecture is fully exploited.

Figure 1. Intelligent Pixel processor
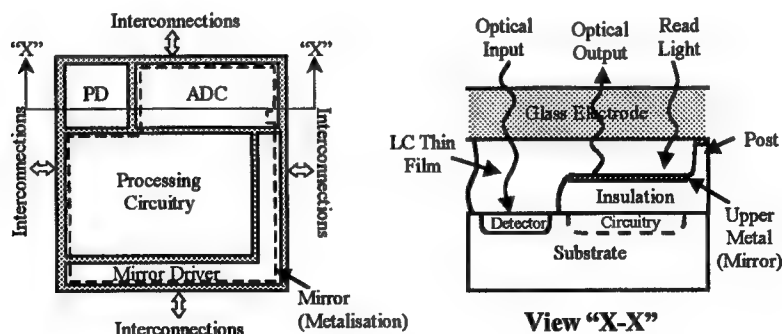
A wavelet transformation is essentially a sub-band decomposition that segments an image into a number of frequency domains at different scales. A complete two-dimensional decomposition can be calculated by sequential convolution of the rows and columns of an image with a pair of suitably chosen quadrature mirror filters (QMFs) followed by half rate sub-sampling at each scale. For a VLSI

implementation 1-D FIR filters can be used for these convolutions. Suitably chosen wavelet basis functions are used to derive the filter coefficients. The transform coefficients, y_i, are thus obtained by convolving the pixel input values, x_i, with the coefficients, w_s, of an FIR filter of length L:

$$y_i = \sum_{s=1}^{L} x_{i-s} w_s \qquad (1)$$

This convolution can be computed by scaling the image coefficients with each of the filter coefficients and accumulating the sum of these products in each pixel. This operation is performed very efficiently on the IP array as the mesh network of processing elements allows all of the convolutions in one plane to be carried out in parallel. In addition, adoption of binary representable filters allows the convolution operations necessary for the computation of the discrete wavelet transform (DWT) to be carried out using integer arithmetic only. A complete multi-scale DWT can thus be computed on the IP array using a single bit-serial adder accumulator along with two additional registers to store the current frame for left and right shifting. The approach facilitates decomposition at any scale with the same time complexity. The advantage of the algorithm is that at the end of the transform the coefficients are ordered together into wavelet blocks facilitating embedded mapping of the Zerotree Entropy Coder(ZTE) within the IP array.

Figure 2 outlines the logical architecture necessary to carry out the DWT using a symmetric binary representable wavelet filter. Due to the limited space available within the IPs all arithmetic operations are performed in a bit-serial fashion.
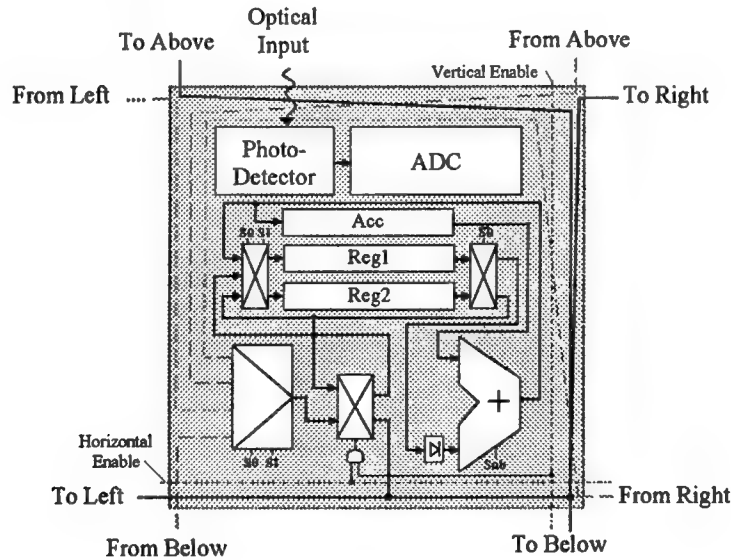
Figure 2. Logical architecture within each pixel for computation of the DWT

The massively parallel nature of the IP array enables the architecture to operate in real-time at very high frame-rates. A complete three-scale forward wavelet transformation followed by ZTE coding can be performed in less than 300 clock cycles irrespective of image size. The algorithm is completely symmetric so that the inverse transform, necessary for displaying an image from remote site, is simply carried out in reverse.

The IP is capable of real-time very-low-bit-rate video coding with performance comparable to other state-of-the-art codecs. Integration of optics with that of VLSI technology (Opto-VLSI) has provided important foundation for realisation of new generations of Systems-on-Silicon (SoS).

Latency study of an optical area I/O enhanced FPGA with 256 optical channels per CMOS IC.

R. Bockstaele(a), M. Brunfaut(b), J. Depreitere(b), W. Meeus(b), J. M. Van Campenhout(b), H. Melchior(c), R. Annen(c), P. Zenklusen(c), L. Vanwassenhove(a), J. Hall(d), A. Neyer(e), B. Wittmann(e), P. Heremans(f), J. Van Koetsem(g), R. King(h), H. Thienpont(j), R. Baets(a)

(a)University of Ghent - IMEC, Department of Information Technology (INTEC), St Pietersnieuwstraat 41, B-9000 Gent, Belgium. Tel +23 9 264 3445, Fax +32 9 264 3593, email : rbock@intec.rug.ac.be

Introduction

In this paper, a detailed theoretical and experimental analysis of the latency of optical interconnects in a FPGA system is presented. The optical link consists of a CMOS integrated driver, an flip-chip mounted RCLED coupled to a small-core POF, InGaAs detectors and CMOS integrated receiver, comparators and amplifiers.

The optically interconnected FPGA system

FPGAs are electronic components that can be programmed to implement arbitrary electronic designs. As programming can be done in-situ and repeatedly, FPGAs are being applied in rapidly growing numbers in a large variety of applications. But FPGAs are frequently plagued by a lack of interconnect capabilities. Multi-FPGA systems in particular suffer from the lack of inter-chip interconnect capability. Optoelectronic area-I/O for multi-FPGA systems would offer a definite advantage in terms of interconnect capability. They provide a viable substitute and extension of the electrical interconnect system in multi-FPGA systems[1].

A small-scale optoelectronic FPGA is currently being realised and will be used in a three-chip demonstrator system as test bed for these concepts. The full-custom CMOS FPGA circuit is an 8 x 8 array of simple configurable logic blocks (a 4-bit function table, one flip-flop), interconnected by a programmable 6 x 6 switch matrix fabric. The switch matrices, traditionally responsible for the on-chip interconnections, have now been extended to include the off-chip optical interconnections. The optical components consist of two 8 x 8 source arrays (either RCLEDs or VCSELs) and two 8 x 8 InP detector arrays, which are flip-chip bonded to the CMOS circuit and actually overlay part of the CMOS circuits. Electronic driving and receiving circuits are realised as part of the CMOS FPGA chip, and are intermixed with the digital circuits [2].
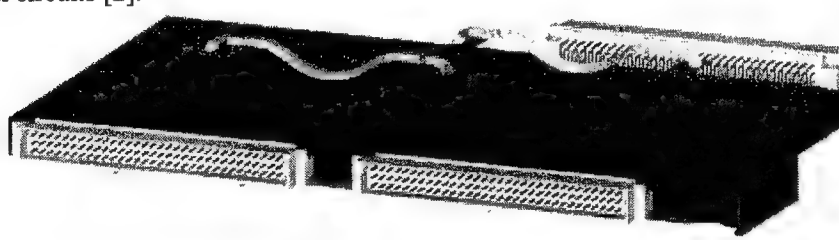
Fig 1 : picture of the optically interconnect FPGA demonstrator

Each of the 256 optical channels is designed to operate at an information rate of 80 Mbit/s, a typical data rate for high-end commercial FPGAs. To ensure reliable communication over so many parallel channels in a noisy digital environment, AC-coupled communication with Manchester coded data is used in the design. Hence, the information rate of 80 Mbits/s requires a signalling rate of 160 Mbaud. The optical pathways between the FPGA chips and their neighbouring chips are two removable 8 x 16 POF ribbons. The CMOS FPGA chips containing approx. 165,000 transistors on a 6.3 mm x 8.3 mm area have been fabricated in the AMS three metal 0.6 um technology.

Results and discussion

The latency of the complete optical link is simulated, using Cadence and a large-signal model for the RCLED. The detector is presented by a capacitor. The latency is defined as the time difference between the input signal and the moment a signal reaches 50% of its static value. Fig 2 shows the calculated latency of the link, at different stages. The rise latency of the RCLED is larger compared to its fall latency. This is in

agreement with theoretical calculations : the delay can be calculated from the rate-equations, and is given by :

$$t_{0 \to 50\%} = \sqrt{\frac{qV}{BI}} \operatorname{arctan} h \frac{1}{\sqrt{2}} \approx 0.88 \sqrt{\frac{qV}{BI}} \text{ and } t_{100 \to 50\%} = \left(\sqrt{2} - 1\right)\sqrt{\frac{qV}{BI}} \approx 0.42 \sqrt{\frac{qV}{BI}}$$

The fall latency of the receiver is larger compared to its rise latency. This effect is explained in fig. 3. The reference level of the comparator (which is generated using a low-frequency filter) is smaller than the mean value of the peak-to-peak signal. Fig 4 shows the total latency of the link, as function of the drive current. The rise latency decreases as function of the drive current, due to the shorter LED and receiver delay (because of the larger current density in the LED and the larger detector current). However, the fall latency increases, in spite of the smaller RCLED delay at larger current densities. This increase of the latency in the receiver - as explained above - overcompensates the shorter delay in the LED.
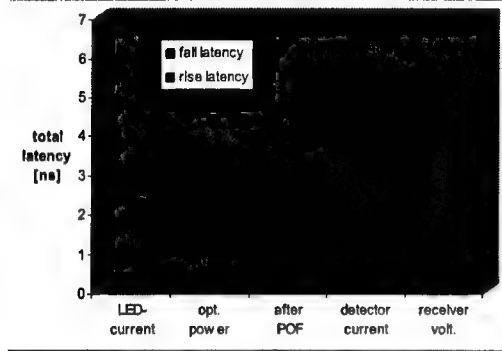
Fig 2 : calculated latency of the optical link.
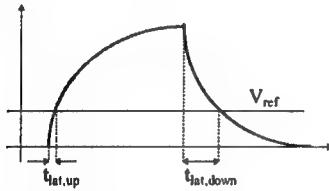
Fig 3 : influence of reference level on the latency
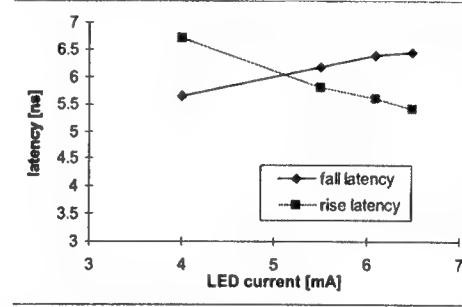
Fig 4 : calculated overall latency of the optical link.
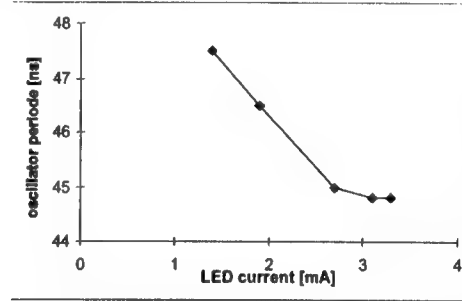
Fig 5 : measured period of the ring oscillator

Finally, measurements have been carried out on the demonstrator. The FPGA was programmed to act as a ring oscillator, and the frequency of the oscillator was measured. This frequency is inverse proportional to the delay of the ring. It was found that the maximal frequency is about 22 MHz, corresponding to a 45 ns period (see fig 5), and a 22ns round trip (including the optical and the electrical path). More simulations on the complete optical link (including the complete electrical and optical path) were in agreement with the measurement. As a conclusion, it was found that the overall delay the optical path (including drivers and receivers) is about 5 to 6 ns. The pure optical delay (the time-of-flight though the fibre) is only a small part of it. The main part of this delay is generated in the LED switching and in the receiver.

Acknowledgement

REFERENCES :
[1] J. Van Campenhout et al : "Optics and the CMOS interconnection problem", Int Journ Opto, 1998, Vol 12 no 4, p 145-154
[2] R. Bockstaele et al : "Realization and Characterisation of 8x8 Resonant Cavity LED Arrays Mounted onto CMOS Drivers for POF-Based Interchip Interconnections", IEEE JQSTE Vol 5 No 2 (1999)

Beam Steering Optical Switches using LCOS: The 'ROSES' Demonstrator

W. A. Crossland, I. G. Manolis, M. M. Redmond, K. L. Tan, T. D. Wilkinson [1],

[1] Cambridge University Engineering Department, Trumpington Street, Cambridge, CB2 1PZ

H. H. Chu, J. Croucher, V. A. Handerek, M. J. Holmes, T. Parker [2],

[2] Dept of Electrical and Electronic Engineering, Kings College London, WC2R 2LS

I. G. Bonas, B. Robertson, S. T. Warr [3]

[3] Thomas Swan and Co Ltd, Crookhall, Consett, Co Durham DH8 7ND

R. Franklin, C. Stace, H. J. White [4],

[4]BAe Systems, Filton, Bristol   BS12 7QW

R. A. Woolley [5]

[5] CRL, Dawley Road, Hayes, Middlesex UB3 1HH

G. Henshall [6],

[6] Nortel Telecommunications, London Road, Harlow, Essex CM17 9NA

The increasing deployment of optic networks is now reaching a point where major simplifications and cost reduction can occur by the use of scalable optically transparent switches. In the following paper the design, assembly and performance of a prototype 1 ×8 reconfigurable holographic free-space switch is described [1]. Central to the switch fabric is a ferroelectric liquid crystal (FLC) on silicon spatial light modulator (SLM) [2] deposited with a 540×1 array of planar mirror strips. The input and output ports to the switch are fabricated as a linear array of silica planar waveguides connected to single-mode fibres. The waveguide array and the single Fourier transform lens for the 2 f holographic replay system are housed in an opto-mechanical mount to provide stability. The switch operates at 1.55 μm wavelength and has a designed optical bandwidth of >60 nm.
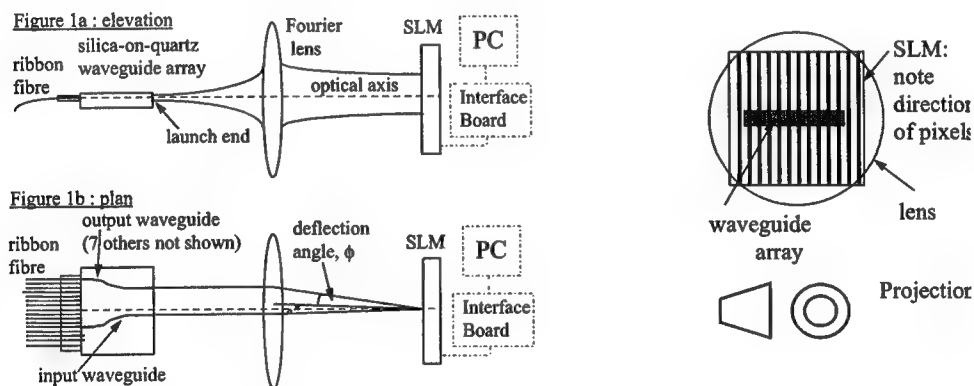
Figure 1: Operation of the ROSES 1x8 holographic routing switch.

The primary aim of the ROSES project was to develop the technology required to implement a large scale NxN holographic routing switch. As a first step towards this goal, a prototype polarisation independent [3,4] linear 1x8 fibre optic routing switch was developed. The switch was designed to take a signal beam from a single mode fibre, and dynamically route it to one of eight single-mode output fibres. The switch is shown schematically in figure 1, and consists of four main components: a waveguide array providing spatial fan-in to and from the input and output fibres, a Fourier lens, a reflective binary-phase ferroelectric liquid crystal silicon backplane SLM that acts as a beam-steering element, and a custom interface board.

The basic operation of the switch is as follows: the optical signal is launched down the input fibre, and couples via the ribbon fibre into the input waveguide, from where it propagates to the launch end of the waveguide array, and is collimated (figure 1a) by the Fourier lens onto the SLM. The SLM consists of a linear array of 540 pixellated electrodes, each 18 μm by 6mm, with a 2 μm dead space between the pixels. The SLM acts like a polarization

independent phase-only diffraction grating [3,4] with a tuneable period and pattern, creating a deflection angle, ϕ, of the reflected beam, as shown in figure 1b: this figure shows the path of the centre of each beam. By controlling the deflection angle, the beam may be made to return to a selected point on the waveguide array, from where the signal propagates across the waveguide array and into the ribbon fibre and output fibre. The deflection angle depends on the phase modulation pattern (the hologram), which is downloaded from a PC via the custom interface board to SRAM circuitry integrated with the pixels. The hologram patterns were calculated using Fourier series analysis under the constraint of suppressing crosstalk and backreflection from unwanted diffraction orders to target levels of -20 dB, and -40 dB respectively. The number of pixels used to display the phase modulation was chosen to be sufficient to avoid excess crosstalk and insertion loss penalties due to clipping of the tails of the beam incident on the SLM. The theoretical diffraction efficiency of the holograms varies between 4 dB and 4.8 dB: 4 dB of this is inherent to binary-phase modulation, while the 0.8 dB variation is the loss penalty resulting from modifications to the pattern in order to suppress crosstalk from unwanted diffraction orders. Additionally, in order to maintain DC balancing without severe interruption of the optical signal, the hologram pattern was scrolled (one pixel at a time) across the SLM. The waveguide array was designed to maximise the wavelength range of the system. Custom optomechanics were used to align and control the relative positions of all optical components.

In order to minimize the insertion loss through the switch, the optimum liquid crystal tilt angle is 45 degrees. For the switch demonstration we used CDRR8, an organosiloxane based experimental compound with the phase sequence:- I-(57)-Sc*-(room temp) and a tilt angle of 34 degrees at room temperature. The diffraction efficiency of this first SLM specifically designed for phase modulation was measured to be 8.0 ±0.2%, (11.0±0.1dB): this value includes loss penalties due to non-ideal tilt angle (0.7 dB), dead space (0.9 dB) and cell thickness error, from which the predicted insertion loss for the switch is 14.4 ±0.4dB, including connector loss, waveguide loss and lens aberrations.

The switch performance was tested by aligning the waveguide array to maximize the signal diffracted into the output channels, while simultaneously minimizing the crosstalk between channels. The SLM was then configured to direct light into each of the output channels in turn, and power measurements made to determine the full 8×8 crosstalk matrix. The measured insertion loss of the switch was 16.9 ±0.5 dB. The excess 2.5 ±0.1 dB loss is due to non-optimum alignment, increased aberrations introduced by misalignment, and beam distortion due to a non-uniform curvature of the SLM.

The signal-to-peak noise crosstalk varied between a worst case figure of -19.1dB to optical isolations as high as –40.5dB. These results are extremely promising, as the target crosstalk figure was –20dB and the theoretical worst crosstalk figure was calculated to be -21.0dB, assuming perfect alignment. The wavelength response of the switch was measured and on the outermost channel a worst-case insertion loss variation of 4dB was found over a 60nm range centred on 1550 µm. Finally, the back reflection from the switch was investigated and a worst case value of –35.1dB was measured.

The ROSES project has brought together the current technology in SLMs, free-space opto-mechanics and in techniques for designing waveguides and computer-generated phase holograms. The first integrated 1 ×N switch using reconfigurable phase holograms has been built in a form suitable for system trials, and to a specification that would enable it to be used in the target applications. The 16.9 dB insertion loss and -19.1 dB isolation were obtained without the need to precisely control each switching element. Significant improvements in these figures can be expected. In the former case by optimising the FLC switching angle and thickness, and in the latter by reducing aberrations. The same spatial light modulators and hardware principles are capable of extension to significantly larger switches.

References
1) D. C. O'Brien et al, "Dynamic holographic interconnects that use ferroelectric liquid crystal spatial light modulators", *Appl. Opt.*, **33**, 14, pp. 2795-2803, 1994.
2) N. Collings et al, "Evolutionary development of advanced liquid crystal spatial light modulator", *Appl. Opt.*, **28**, 22, pp 4720-4747, 1989.
3) M. J. O'Callaghan and M. A. Handschy, "Diffractive ferroelectric liquid-crystal shutters for unpolarized light", *Optics Letters*, **16**, 10, pp. 770-772, 1991.
4) S.T. Warr and R. J. Mears, "Polarization insensitive operation of ferroelectric liquid crystal crossbar devices", *Electronic Letters*, **31**, pp. 714-716, 1995.

Optical Comparator based on FLC LCOS technology.

T.D. Wilkinson, N. New and W.A. Crossland

Cambridge University, Engineering Department
Trumpington St, Cambridge CB2 1PZ, UK
tdw@eng.cam.ac.uk

SLMs based on Ferroelectric Liquid Crystals (FLCs) offer a potentially cheap and fast technology for optical systems, however, they are limited by their binary modulation. An efficient JTC can be implemented with FLC SLMs, if the 1/f or two pass architecture is used[1]. More importantly, the 1/f system can be made into a very powerful yet optically simple processor when it is implemented with a liquid crystal over silicon (LCOS) binary phase modulator[2].
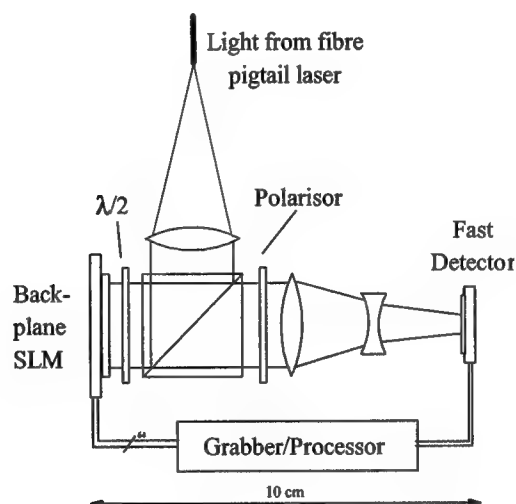

Figure 1. Schematic of the binary phase-only 1/f JTC using LCOS

Recently, this architecture has developed around an in-house SLM based on FLC over silicon technology, known as the fast bitplane SLM (FBP-SLM)[3]. This device has 320x240 unplanarised pixels on a 34μm pitch and is capable of binary phase modulation at rates in excess of 10 000 frames per second. The much smaller pixel pitch of the FBP-SLM compared to the transmissive devices used previously, allows a much more compact optical system to be built as in Figure 1. The fast detector array in Figure 1 is currently a standard CCD camera, with two possible options in the near future. The first is a much faster CMOS array whilst the second is a custom designed silicon VLSI smart detector array. The basic unit has been tested as a bench based compact system using similar mounts as the previous system. The overall footprint was 200x200mm, most of which was due to the optical mounts for the components. A more compact has also been made using the optical rail/cage system and results from this will be shown at the conference, along with demonstrations of the applications outlined in the following sections.

A very important observation is that the traditional 1/f JTC can be used as a 'recogniser' or comparator, where the reference image is unknown or unspecified. This completely reverses the role of the correlator and opens up a whole plethora of applications that revolve around object tracking and motion analysis. Rather than having a pre-defined target or reference image, the input is made up from a sequence of frames from a video source. One elegant scenario is when a correlator is used to compare sequential frames in a video stream a production line. In such an application, the current frame is the unknown and the previous frame is the 'reference'. Events that occur from frame to frame can now easily be tracked. This is outlined in the simple yet very powerful example of Figure 2. Here we are implementing an industrial inspection system. The current frame and previous frame are synchronised with the progress of objects through the system (in this example, roadsigns). If the sequence does not change, then the output correlations remain from frame to frame, however, when a change occurs (in this example a rotated roadsign), then the correlation between frames is interrupted. Moreover, the cycle of distortion can be detected by looking at the sequence of disturbances about the first detected defect.
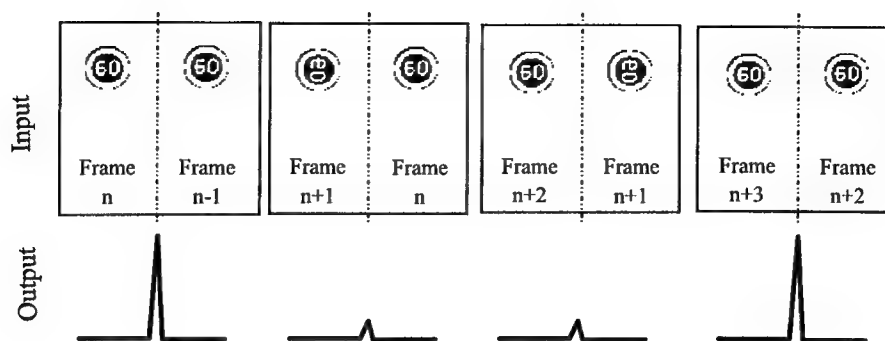
Figure 2. Example application for an optical recogniser.

Even gradual distortions in the object can be picked up by correlating over multiples of frames to look for small changes. Most importantly, the whole process is done without ever knowing anything about the object being inspected. This application is being tested experimentally as part of an investigation into applications and markets of this technology. One area that is being tested in the inspection of labels on a production line. The issue here is to detect missing or distorted letters in the names printed onto labels in a production process.

It is also possible to use the optical comparator for motion estimation and tracking. In this case, the current and previous frames are compared to see if there has been any motion between frames. The previous frame is broken into a number of smaller segments, which may or may not be overlapping as shown in Figure 3. Each separate segment is then correlated with the whole current frame at a rate much higher then the video stream rate.
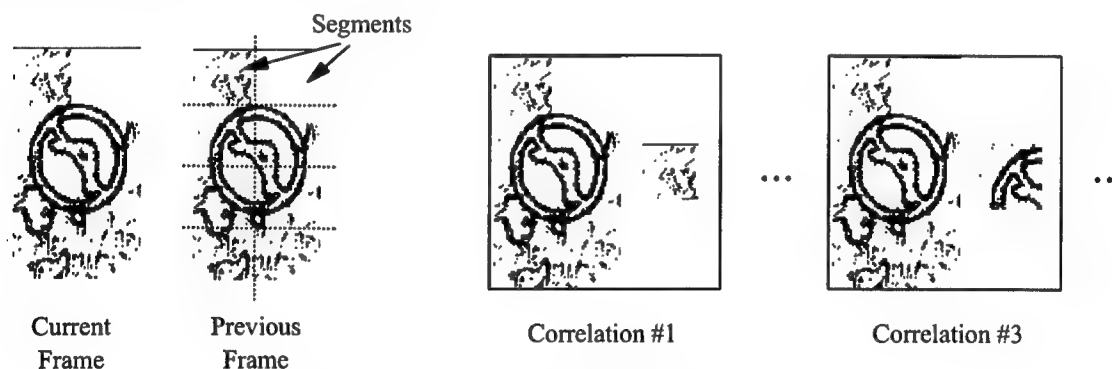
Figure 3. Basic concept or motion estimation with the recogniser.

The motion of each segment can then be plotted based on the motion of the correlation peaks within a particular sector in the output plane. From this, an idea of motion between frames can be derived and this motion information is totally independent of the objects in the frame. Such a process is vital in security, crowd density and traffic monitoring systems as events often are signalled by abnormal motion. A more adventurous and longer term application of this concept is in generating motion vectors for MPEG-2 compression systems. With a 640x512 pixel comparator running at 10^4 frames per second, it would be possible to obtain motion information in real-time

[1]   J.L. Horner and C.K. Makekau, "Two focal length optical correlator ", *Applied Optics,* **28**(24), 1989, pp5199-5201
[2]   T. D. Wilkinson and V. Kapsalis, "The binary phase-only 1/f joint transform correlator using an FLC SLM", *Ferroelectrics*, **213**, 1998, pp241-247.
[3]   W. A. Crossland, T. D. Wilkinson, T. M. Coker, T. C. B. Yu and M. Stanley, "The fast bitplane SLM: a new FLC on silicon SLM designed for high yield and low cost manufacturability", *OSA TOPS: Spatial Light Modulators*, **14**, 1997, p102.

Electronic-Enhanced Optics

Tuesday, 25 July 2000

TuA1:   Optical Interconnects and Networking I
TuA2:   Optical Interconnects and Networking II

Optoelectronic Interconnections for High Throughput Networks and Pipeline Signal Processing

Alexander A. Sawchuk and Charles B. Kuznia
Signal and Image Processing Institute; University of Southern California
3740 McClintock Avenue; Los Angeles, CA 90089-2564
Tel: 213-740-4622 Fax: 213-740-4651 email: sawchuk@sipi.usc.edu

1. Introduction

We describe the concept and experimental implementation of a smart pixel (SP) system for networking and image/video processing based on digital optoelectronic (DO) technology. DO technology enables 2-D optical data transfer to and from VLSI chips at a throughputs of >1 Tb/s, with very low latency (<10 ns) and very high speed (>500 Mb/s) on each of many (>100) parallel data channels. Figure 1 shows this system concept, called Transpar-TR (Translucent Smart Pixel Array-Token-Ring) [1]-[3].

The Transpar-TR is configured as a photonic ring network that transfers digital data

Figure 1. Transpar-TR ring network. Optical parallel data packets transfer data between nodes on parallel optical channels.

using three-dimensional optical parallel data packets (OPDPs). Similar to most packet based networking schemes on serial interconnect links, the OPDPs contain data payload and source/destination node address information. The data pipe between nodes consists of a 2-D array of optical links each operating at on-chip clock rates. This data pipe between nodes is designed to accommodate the sum of all other smaller data pipes entering the network from individual nodes, thus this system is an example of a 'firehose' architecture [4]. Our goal is to demonstrate two features unique to SP systems: networking with 2-D spatial parallel channels and 2-D parallel pipeline image and video processing for applications such as compression and tracking.

2. Transpar-TR Description

Figure 2 shows the detail of two Transpar-TR nodes. Each node contains a field programmable gate array (FPGA) logic chip, a transimpedance amplifier (TIA) receiver chip, and a single chip (fabricated by Honeywell) containing an interlaced 4 x 4 array of vertical cavity surface emitting laser (VCSEL) sources and 4 x 4 array of metal-semiconductor-metal (MSM) detectors on a 250 μm x 250 μm grid. The FPGAs are programmed to implement the smart pixel circuitry, which includes data processing and networking functions. The FPGA's reconfigurablity allows testing of several system concepts [5]. The FPGA also is capable of directly driving the output VCSELs. The TIA receiver chip was designed by us and provides amplification of the detected optical signals so they can drive the FPGA logic. We have tested the optical links in this system to 100 Mbps, the results are shown in Fig. 3.
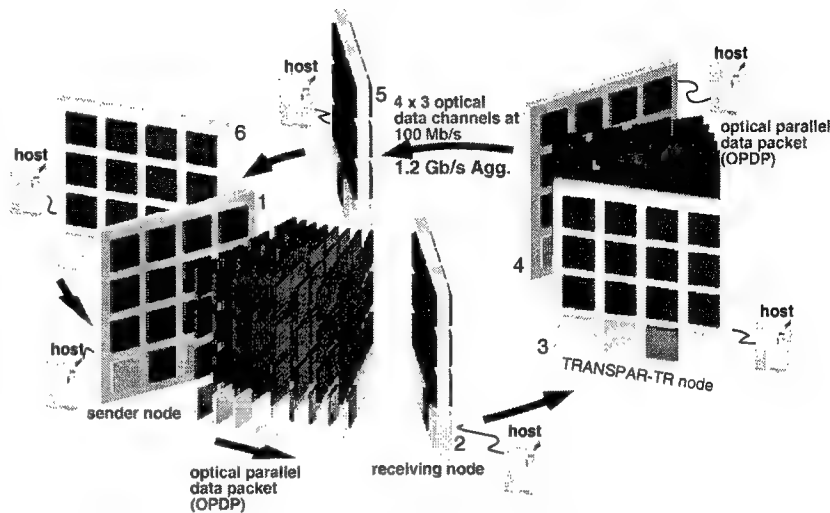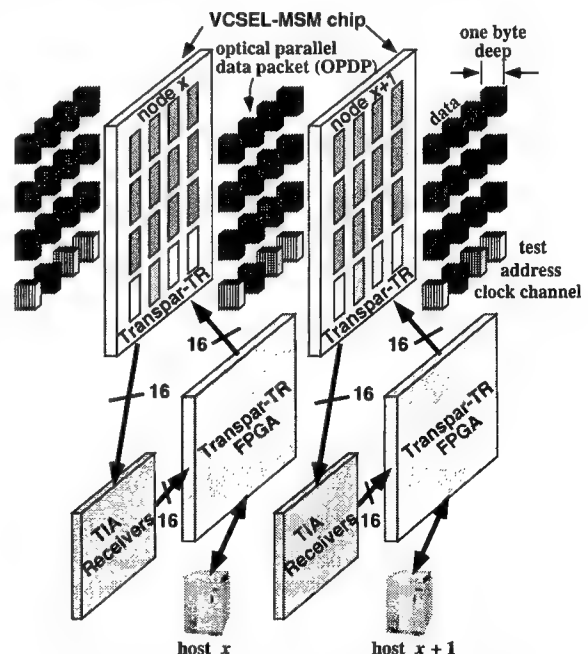

Figure 2. Modular Transpar-TR FPGA node.

In Transpar-TR, each OPDP consists of a 4 x 4 spatial array of eight bit bytes that are transmitted from the VCSELs over eight clock cycles. Twelve of these sixteen channels are reserved for data, one contains destination address information, one is a clock channel, and two are reserved for testing purposes.

In anticipation of crosstalk problems between VCSEL and MSM signals, we developed a novel slotted token-ring protocol for an N node (N even)

Figure 3. 100 Mbps operation (left) and resulting eye diagram (right). The bottom trace in the voltage driving the VCSEL whose optical output enters an MSM receiver. The middle trace is the receiver chip output.

Transpar-TR which allows collision free, high throughput network operation and avoids simultaneous VCSEL-MSM operations. In this scheme, each node waits for a 'ready to receive' signal from the next node before transmitting an optical packet. Packets are received and re-transmitted at each node as they traverse the network. Using this technique, the handshaking protocol allows packets from alternate network nodes to occupy the network concurrently (as shown in Fig. 1). Thus $N/2$ nodes transmit simultaneously. A transmit queue and a receive queue are included to bridge the ultra fast optical network and relatively lower speed of the electrical smart pixel array processors, and minimize packet loss. Due to the parallel transmission of address and data packets, the processing latency is minimized, which differs from generic token-ring networks.

Transpar-TR uses a Honeywell VCSEL-MSM smart pixel supplied by the DARPA-sponsored foundry project operated by the CO-OP program at George-Mason University (co-op.gmu.edu/vcsel) [6]. The Altera FPGA, VCSEL-MSM chip, and a driver chip designed by our group is mounted on a four layer printed circuit board (PCB). The board is connected to a host computer using a high speed digital interface connector.

3. Conclusions

We view this system as a first step toward the development of an integrated smart pixel having active sources. The PCB integration of Transpar-TR components has several disadvantages compared to monolithic or flip-chip optoelectronic integration [7]. Perhaps the biggest drawback is parasitic inductance and capacitance of the PCB that make detecting low current MSM signals difficult. However, one advantage of system modularity is that each component can be individually tested and characterized before system integration.

4. Acknowledgments

5. References

1. C.-H. Chen, B. Hoanca, C.B. Kuznia, A.A. Sawchuk and J.-M. Wu, "TRANslucent Smart Pixel ARray (TRANSPAR) Chips for High Throughput Networks and SIMD Signal Processing," *IEEE Journal of Selected Topics in Quantum Electronics*, vol. 5, pp. 316-329, (1999), (invited paper).
2. C.B. Kuznia, C.-H. Chen, B. Hoanca, L. Zhang, D. Pansatiankul, J.-M. Wu, and A.A. Sawchuk, "Modular System Demonstrator for Hybrid VCSEL/MSM Smart Pixel Networking, *Optics in Computing*, OSA Technical Digest, pp. 156-158, Optical Society of America, Washington, DC, 1999.
3. C.-H. Chen, B. Hoanca, C.B. Kuznia, D. Pansatiankul, L. Zhang and A.A. Sawchuk, "Modulator and VCSEL-MSM Smart Pixels for Parallel Pipeline Networking and Signal Processing," in *18th Congress of the International Commission for Optics: Optics for the Next Millennium, Proc. SPIE*, vol. 3749, pp. 241-242, 1999.
4. A.V. Krishnamoorthy and D.A.B. Miller, "Firehose Architectures for Free-Space Optically Interconnected VLSI Circuits," *J. Parallel and Distributed Computing*, vol. 41, 109-114 (1997).
5. T.H. Szymanski, M. Saint-Laurent, V. Tyan, A. Au and B. Supmonchai, "Field Programmable Logic Devices with Optical Input-Output, *Applied Optics*, vol. 39, pp. 721-732, 2000.
6. M.K. Hibbs-Brenner, Y. Liu, R. Morgan and J. Lehman, "VCSEL/MSM Detector Smart Pixel Arrays," *Proc. IEEE Summer Topical Meeting on Smart Pixels*, Monterey, CA, pp. 3-4, July, 1998.
7. A.V. Krishnamoorthy and K.W. Goossen, "Progress in Optoelectronic-VLSI Smart Pixel Technology Based On GaAs/AlGaAs MQW Modulators," *International Journal of Optoelectronics*, vol. 11, pp. 181-198, 1997.
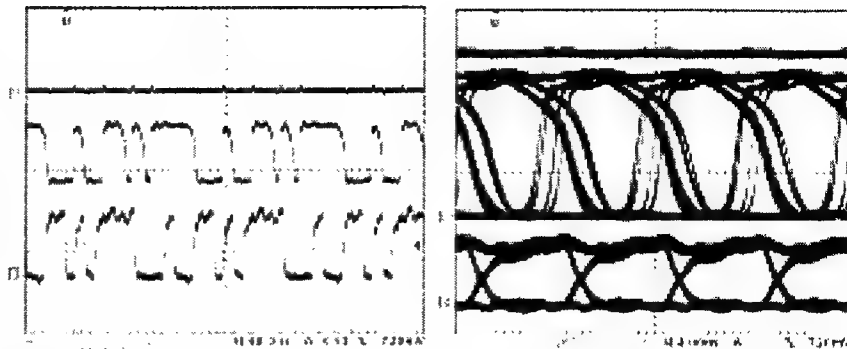
Circuit Boards with Integrated Optical Interconnects – Technology, Modeling, and Application Examples

Dr. E. Strake, Robert Bosch GmbH, Dept. FV/SLD-Hi, Robert-Bosch-Str. 200, D-31139 Hildesheim, Germany

Dr. D. Krabe, Fraunhofer Institute IZM, Dept. PCB Packaging, Gustav-Meyer-Allee 25, D-13355 Berlin, Germany

Summary

The continuing rapid progress in micro system technologies, micro electronics, and packaging techniques strongly impacts developments and applications in many technical fields like computer and information technology or signal transmission systems. Often, signal transmission throughput falls back behind local processing speed on chip level and thus builds a bottleneck limiting overall system performance. In all these areas, growing demands regarding signal transmission bandwidth, insusceptibility against electromagnetic interference and also cost effectiveness require novel solutions for interconnection techniques.

Optical signal paths using fibers or waveguides represent promising solutions, since they are inherently insensitive against high frequency and electrostatic fields and at the same time provide very large bandwidths. Optical fibers have been introduced as standard transmission media in wide area networks for years and also represent the state-of-the-art for high performance local area networks. Even in networking between locally distributed electronic modules of in-vehicle systems plastic optical fibers are utilized as high performance transmission media. In order to push the advantages of optical signal transmission further into the short haul range of PCB or module level, cost efficient solutions have to be found for the realization of optical interconnections.

The contribution presents concepts, technologies, and first results for novel hybrid electrical/optical circuit boards which extend the conventional setup of existing electrical printed circuit boards by incorporating additional layers with optical waveguide structures. A major aspect of the inclusion of optically functional layers into conventional circuit boards is the requirement of maximum compatibility with existing board fabrication and assembly techniques. Any substantial change in board fabrication and assembly parameters has to be avoided in order to obtain the desired cost efficiency.

Thermal and mechanical load during board lamination and component soldering processes dictate the use of highly thermally stable transparent polymers. The desired compatibility with mechanical tolerances of existing board fabrication and component placement techniques can be well achieved with optical multimode waveguide structures having core cross sections in the range of, e.g., $(50\mu m)^2$ to $(100\ \mu m)^2$. Multimode waveguide structures have been fabricated in different polymer materials using hot embossing. The formation of waveguides was achieved by filling the embossed channel structures with a core material of larger refractive index compared to the substrate material. Among other materials, we used commercially available optical adhesives for this step. An over-cladding consisting of the same material as the substrate finally seals the waveguide core structures. With a typical in-

dex difference between core and cladding materials of approximately 0.03, a numerical aperture of 0.3 results.

The optical transmission properties of multimode waveguides can be adequately modeled by ray optical methods (ray tracing) rather than field theoretical approaches (FEM, FDM or BPM) due to the very large number of propagating modes. A realistic description of light propagation in these waveguides has to include mode coupling phenomena induced by waveguide irregularities like a finite core surface roughness, which is inevitably introduced by any fabrication process. These waveguide deformations lead to mode coupling, which in turn has a strong effect on signal propagation of the entire optical interconnect. The resulting transient behaviour is of special importance for short haul interconnects like board-integrated waveguides. In order to realistically model these properties, scattering effects have been included into a ray tracing algorithm using a perturbation description of angular scattering intensity distributions.

Different approaches for the coupling between optical emitters and receivers and waveguides are compared. A first concept is based on reflecting facets at the waveguide ends combined with optoelectronic components mounted with their axes orthogonal with respect to the waveguide axes. A second approach uses butt coupling, in order to minimize axial offsets responsible for beam widening. This is especially important at the detector side, where a large waveguide numerical aperture leads to a large beam divergence, thus limiting cross talk supression between neighbour channels. First results of realized hybrid electrical/optical boards with mounted optoelectronics (VCSEL emitter and PIN-detector array components) are reported.

Examples are presented showing the potential of board-integrated optical interconnects for applications like in-vehicle multimedia optical bus systems.

Simulation of interchip interconnections based on Resonant Cavity LEDs, Plastic Optical Fibres and CMOS interface circuits.

R. Bockstaele, R. Baets
University of Ghent - IMEC, Department of Information Technology (INTEC), St Pietersnieuwstraat 41,
B-9000 Gent, Belgium. Tel +32 9 264 3445, Fax +32 9 264 3593, email : rbock@intec.rug.ac.be

Introduction

This paper presents a LabView-based interchip electro-optical parallel interconnect simulator. Such links are a possible solution for the interconnect bottleneck in future digital systems. The links and their characteristics are quite different from the traditional long distance optical links : the components should be small, low-cost, temperature-insensitive and simple; and the latency (the overall signal delay) and power dissipation must be kept under control. This simulator focusses inb particular on the modelling of the Resonant Cavity LED (RCLED), and the performance analysis.

Description of the link

The parallel interchip optical link studied in this paper consists of CMOS integrated drivers, an 8x8 array of RCLED flipchip mounted on the CMOS chip, coupled to a POF (Plastic Optical Fibre), an InGaAs detector and CMOS integrated receiver and amplifier. There is no optical power control loop, nor time regeneration circuits included. The optical link is currently built, in the framework of the European OIIC project. The simulator is implemented in LabView, allowing an easy integration of different calculation techniques and an easy user interface. The modelling of all subcomponents is shortly discussed hereafter.

The electrical model of the driver and the RCLED.

The driver consists of CMOS integrated buffer stages and a driving transistor. The driving transistor is modelled by a current source and a parasitic capacitance. The carrier concentration in the RCLED active layer as a function of time is calculated by solving the RCLED rate equations. From the carrier concentration, the voltage drop across the RCLED is calculated. This allows to calculate the power dissipation.
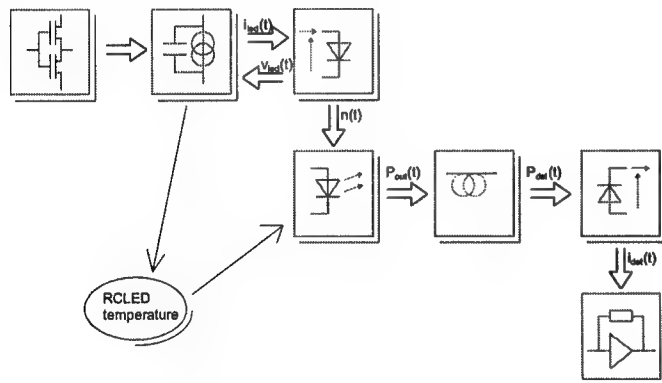
Figure 1 : schematic representation of the link.
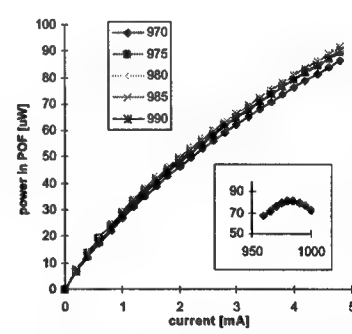
Fig 2 : calculated PI curves of RCLED coupled to POF, as function of the detuning

The optical model of the RCLED and coupling to POF fibre

An RCLED has an increased extraction efficiency compared to standard LEDs : the intrinsic spontaneous emission pattern is enhanced by the microcavity effect. In this simulation tool, the temperature and current dependent extraction efficiency is calculated from the cavity parameters.

$$\eta_{extr,POF} = \eta_{extr,POF,nocav} \cdot enh_{cav} = \frac{NA_{POF}^2}{2n_{sub}^2} \int_{int \, r\_spectr} enh(\lambda)d\lambda$$

The temperature of the flipchip mounted RCLED is calculated from the ambient temperature and the power dissipation in the driver. This results in a decreased internal quantum efficiency and a decreased enhancement. The coupling efficiency from the LED to the POF fibre is calculated, taking into account the lateral misalignment. Fig 2 shows the fibre coupled power of a 15 um RCLED, taking into account the saturation effect. The influence of the cavity tuning is shown in the inset. The absorption in the POF is included, but no dispersion effects are taken into account (negligible because of the short fibre length, typically 30 cm).

The detector and receiver

The detector is modelled by its diameter, responsivity and its junction capacitance. The receiver is a transimpedance amplifier, with a capacitive load. The response of the receiver is described by its linear differential equation, which is solved by an Euler method. From the time domain trace, an eye-diagram is constructed. An input current noise source is added to calculate the BER and SNR. The noise is assumed to be gaussian distributed, and its rms-value is given by the standard expression [2].
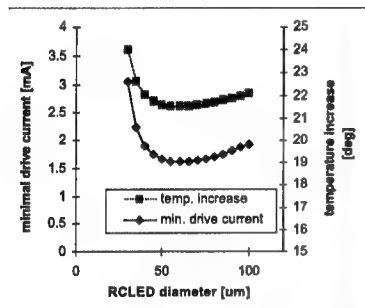
Fig 3 : min drive current of RCLED, as function of device diameter

Figuur 3
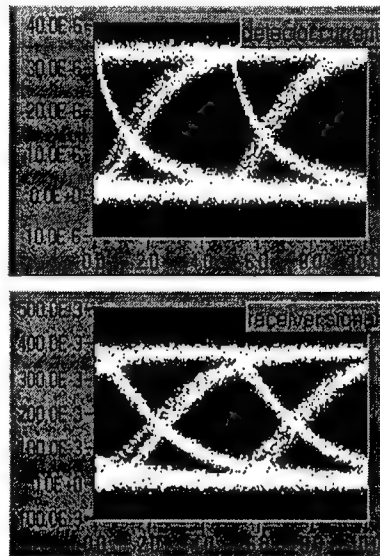
Fig 4 : calculated eye-diagram of optical link.
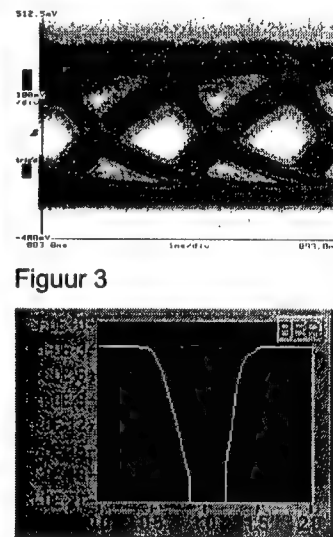
Fig 5 : calculated BER of optical link.

Discussion of the simulation results

First, an optical link using 120um core diameterPOF is studied. Fig 3 shows the minimal drive current to achieve a 15uA detector current, and the corresponding temperature increase in the RCLED (including the driver heating) as function of the RCLED diameter. The optimal diameter is in-between 45 and 80 um. Next, optical links using a 62 um POF are studied. Fig 4 shows a calculated eye-diagram of a link with a 30um diameter RCLED and driven by 3 mA current pulses at 200 MBps. The corresponding BER as function of the sampling time is shown in fig 5. There is clearly a wide time margin.

In conclusion, a simulation tools for RCLED-POF-CMOS based interconnection links is presented. This tools allows us to study the thermal and speed properties of the complete link. Good agreement between experiments and simulations was found.

Acknowledgements

References

[1] R. Bockstaele et al : "Realisation and Characterisation of 8x8 Resonant Cavity LED Arrays Mounted onto CMOS Drivers for POF-Based Interchip Interconnections", IEEE JQSTE Vol 5 No 2 (1999)

[2] S. Alexander : "Optical Communication Receiver Design" SPIE Optical Engineering Press

Optoelectronics for Multi-Terabit Intelligent Wavelength Division Multiplexing Networks

Casimer DeCusatis
IBM Corporation
2455 South Road MS P343, Poughkeepsie, NY 12601

With the explosive growth in fiber optic communication networks has come a wide range of opportunities for electronic enhanced optical systems (1). This paper describes some of the opportunities for electronic enhancement of fiber optic systems, and present some new results of device evaluations in this area. Recent standards efforts have turned their attention to data transmission rates of 10 gigabit/second and above for a single data link. This is being driven by a number of factors, including new industry standards efforts from the IEEE, ANSI, and Infiniband Trade Association (2). Serial transceivers for 10 gigabit/second have been demonstrated, but present problems dealing with signal integrity between CMOS logic chips and the optical physical layer. One proposal is to integrate the 10 Gigabit serialze/deserialize function and data encode/decode function into the media access layer as a single CMOS ASIC, while an eye opener function and media dependent input/output interface would be implemented as a hybrid of silicon germanium (SiGe) and gallium arsenide (GaAs) technologies. We have helped develop new SiGe manufacturing processes such as ultra-high vacuum chemical vapor deposition which allow integration of SiGe with standard CMOS circuitry to form BiCMOS devices using sub-0.5 micron designs and standard 200 mm wafer substrates. For example (3), SiGe cross point switches have been demonstrated with 17 x 17 channels capable of 3.2 gigabit/second data rates while requiring only 3.3 V and dissipating only 3.7 W of power. SiGe transimpedance amplifiers designed for 10 gigabit links have exhibited 3 Ghz bandwidth with 280 nA room mean square noise, sensitivity down to 19 microamps, and power consumption as low as 470 mW.

This growing demand for channel bandwidth has also driven the acceptance of dense wavelength division multiplexing (DWDM). As data rates approach OC-768, multiple SONET-based overlay networks are evolving into a service transparent DWDM structure, with features such as protection switching, optical add/drop, and quality of service pushed to the edge of the network. There is a clearly emerging trend towards elimination of the ATM and SONET layers, and towards the direct transmission of IP over DWDM. This new model requires the DWDM layer to assume many of the traditional functions associated with ATM over SONET. Different implementations have been proposed; for example, the Optical Internetworking model allows the IP switching/routing layer to operate at the same data rates as the DWDM equipment and serve as a centralized point of pure IP network management. A complimentary viewpoint known as the "intelligent optical network" maintains that IP switches/routers can't provide the wavelength switching, service provisioning and rapid path restoration functions required by larger networks, and these functions best reside in the optical layer. Such devices would either be integrated with or interface with existing DWDM equipment, and would provide the above functions in addition to handling the details of signal transport. Both types of intelligent networking offer the advantage of bandwidth management, protection switch events within the maximum SONET switch time of 50 ms or better, and scalabilty to terabit network bandwidth. Furthermore, there are a number of proposals to more closely integrate the electrical and optical domains by linking IP data packets directly to DWDM optical wavelengths, so that the optical network can take

some advantage of the intelligence imbedded in IP traffic. For example, the Optical Domain Service Interconnect (ODSI) coalition seeks to define common control interfaces between the physical and IP MAC layers based on derivatives of the Internet Engineering Task Force Multi-Protocol Label Switching (MPLS). ODSI proposes control plane standards for layer 1 and 2 which must be met by both DWDM equipment and broadband IP switches/routers. A complimentary effort called Multi-Protocol Lambda Switching has been made by the IETF itself to link optical cross-connects and gigabit routers through a Layer 3 switching methodology on top of the ODSI protocols.

IBM has recently introduced the 2029 Fiber Saver, a DWDM solution designed to accommodate future intelligent network requirements (4). The 2029 offers 80 gigabytes of managed bandwidth, and is compatible with long-haul networks using 10 gigabit links which can scale the aggregate network bandwidth to over 6.5 terabytes. The DWDM electronics incorporates data retiming, reshaping, and regeneration, protection switching, and in-band management into the edge of a protocol independent, self-healing, fault tolerant, dual counter rotating ring network. These features have been tested by constructing a fully protected DWDM network which included two IBM G5 Enterprise Servers (capacity of 1600 MIPS each) in a 40 km Parallel Sysplex architecture including 4 sysplex timers and 4 intersystem channel coupling links; four FICON channels, each carrying a time division multiplex of 4 ESCON channels through a 9032-5 ESCON Director driving an IBM 3945 automated tape library with 10 terabytes storage at a distance of 70 km; and a 500 user Gigabit Ethernet LAN which spanned a 35 km hubbed ring interconnected with a Cisco Catalyst 5000 router. This network operated error free (extrapolated to 10^{-15} bit error rate) over a 4 week test period, with 99.999 % availability of end user applications even when single points of failure were deliberately introduced into the testbed.

References

1) Handbook of Fiber Optic Data Communication, C. DeCusatis, E. Maass, D. Clement, and R. Lasky, editors, Academic Press, N.Y. (1998); also C. DeCusatis, "Optical data communication: fundamentals and future directions", Opt. Eng. vol. 37, p. 3082-3099 (December 1998)

2) see IEEE 802.3z higher speed discussion group (10 Gigabit/second Ethernet) at http://grouper.ieee.org/groups/802/3/10G_study/public/ or see Infiniband trade association at http://www.connectedpc.com/design/servers/future_server_io/link_spec.htm

3) J. Ebentier and K. Prentiss, "silicon germanium for network systems design", Integrated Communication Design vol. 1, no. 3, p. 19-20 (Nov. 1999); or see http://www.icdmag.com; also D.L. Harame and B.S. Meyerson, "The history and future of SiGe mixed signal technology at IBM", to be published, special issue on SiGe in IEEE Trans. Elec. Devices (May 2000); also see http://www.chips.ibm.com/bluelogic/showcase/sige/

4) C. DeCusatis and P. Das, "Subrate multiplexing using time and code division multiple access in dense wavelength division multiplexing networks", Proc. SPIE Workshop on Optical Networks, Dallas Texas, Jan. 31-Feb. 1, 2000

Modeling of Highly Multimodal Optical Interconnects
for Time Domain Analysis

A. Himmler, E. Griese, J. Schrage
Siemens AG IC C-LAB, Fürstenallee 11, 33102 Paderborn, Germany
Thomas Bierhoff, Amir Wallrabenstein
University of Paderborn, Electrical Engineering/C-LAB, Fürstenallee 11, 33102 Paderborn, Germany
G. Mrozynski
University of Paderborn, Electrical Engineering, Warburger Straße 100, 33098 Paderborn, Germany

The design of high performance computing and telecommunication switching equipment requires very accurately the knowledge of signal integrity and timing behavior of all intrasystem and intersystem interconnects (i.e. chip-to-chip, board-to-board, cabinet-to-cabinet). In order to predict and optimize the signal transfer properties the use of computational methods is inevitable during the system design process. For modeling and simulating the physical behaviour of electrical interconnects very accurate models and comfortable software tools are available. But comparable models and tools supporting the design of optical interconnects do not exist.

The integration of optical interconnects into electronic systems results in hybrid electrical-optical interconnects (Fig. 1). To design such systems the physical behaviour of the electrical and optical parts has to be modeled. The latter one requires the consideration of the technological given facts typical for the addressed interconnection level (component-, module-, and system level) in order to select appropriate numerical methods and simulation models. In case of guided wave optics the interconnection level characteristical dimensions determine whether the optical singlemode or multimode technology is applicable.
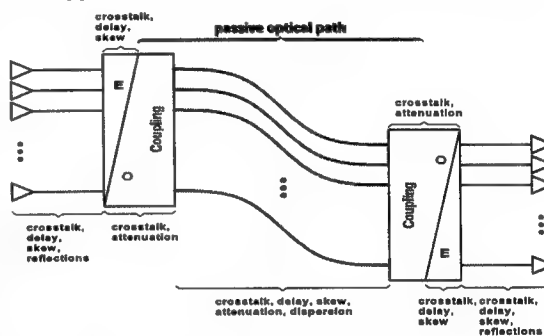
Figure 1: Hybrid electrical-optical interconnect [2]

For interconnects on board level and between boards and cabinets multimode waveguides are the appropriate solution due to their relaxed tolerance requirements compared to singlemode technology. On printed circuit boards only multimode waveguides with cross sectional dimensions comparable to those of microstrip lines lead to an acceptable technology (Fig. 2). This, of course, has a significant influence on the modeling and simulation methodology. Singlemode interconnects can be modeled by well known numerical methods (e. g. FEM, BPM), but these methods are not applicable to optical waveguides with more than 1000 propagating modes, where additionally manufacturing caused roughness of the waveguide surfaces has to be considered. For this reason only methods based on geometrical optics (ray tracing) can be applied.

Figure 2: Electrical printed circuit board with optical multimode waveguides [2]

The modeling of the overall optical path requires models of the optical transmitters (VCSEL) and receivers (photodiode) suitable for the ray tracing analysis of the optical waveguides. To represent the emission of the optical source the emitted beam is discretized in angular domain in order to get a finite number of initial rays. At the end of the passive optical path a reference plane is defined which includes the sensitive area of the photodiode. Equivalent to the modeling of the laser the photodiode is also discretized to model a location and angular dependent sensitivity. In case of ideal waveguide boundaries every initial ray would hit exactly one sub-area but in case of rough surfaces every initial ray is able to contribute to the

illumination of all sub-areas. To model the transmission characteristics of the overall optical path a multiport (Fig. 3) with N inputs, M outputs, and time dependent transfer functions $h_{nm}(t)$ can be defined. The N inputs and M outputs represent the steradian segments A_n of the laser beam and the sub-areas B_m of the photodiode, respectively. The transfer functions $h_{nm}(t)$ characterize the transfer behaviour of the optical waveguide in respect of the optical power emitted into the nth spatial angular element. These functions are time dependent to take mode dispersion as well as mode coupling caused by surface roughnesses and waveguide inhomogenities into account. Their numerical determination can be performed by a ray tracing algorithm which is able to take surface roughnesses of waveguides into account [1].

Figure 3: Multiport representation of an optical multimode interconnect

The functions $h_{nm}(t)$ cannot be computed directly, but its integral $\Psi_{nm}(t) = \int h_{nm}(t)\,dt$ being the step response of the corresponding optical path. Taking into account the physical behaviour of wave propagation and the ray tracing modeling approach some important properties of $\Psi_{nm}(t)$ can be derived.

- $\Psi_{nm}(t)$ is zero before t_1, determined by the finite propagation velocity of light.

$$\Psi_{nm}(t) = 0, \quad t < t_1 \tag{1}$$

- $\Psi_{nm}(t)$ is constant and positive after the time t_2, mainly determined by the mode dispersion.

$$\Psi_{nm}(t) = \text{const.} > 0, \quad t > t_2 \tag{2}$$

- $\Psi_{nm}(t)$ is monotonical rising during $t_1 \leq t \leq t_2$.

$$\frac{\Psi_{nm}(t)}{dt} = h_{nm}(t) \geq 0, \quad t_1 \leq t \leq t_2 \tag{3}$$

To use these functions, which are only given by a finite set of discrete points, for time domain simulations, an appropriate approximation should be introduced in order to avoid discrete convolution algorithms leading to extremely high and unacceptable computation times. Due to the fundamental properties of $\Psi_{nm}(t)$ an approximation by a sum of weighted and delayed decreasing exponential functions of the kind $w\,(1 - e^{-ct})$ is proposed. This approach enables the application of recursive convolution algorithms leading to very accurate results and short computation times [4]. The described modeling methodology is validated by analyzing a slab waveguide, whose transmission characteristics can be determined very accurately applying the Coupled Power Theory [3].

Figure 4: Normalized power distribution of all 41 guided modes of a slab waveguide (height $100\mu m$) with surface roughnesses after a propagation length of 10 cm and an excitation of the 20st guided mode calculated by the Coupled Power Theory and the extended ray tracing technique

[1] Th. Bierhoff, A. Wallrabenstein, A. Himmler, E. Griese, and G. Mrozynski, G., "An approach to model wave propagation in highly multimodal optical waveguides with rough surfaces", in *Proc. X. International Symposium on Theoretical Electrical Engineering (ISTET'99)*, pp. 515 – 520, Magdeburg, Germany, Sept. 1999.

[2] E. Griese. "Parallel optical interconnects for high performance printed circuit boards", in *Proc. 6th. International Conference on Parallel Interconnects*, pp. 173–183, Anchorage, Alaska (USA), Oct. 1999.

[3] D. Marcuse, *Theory of Dielectric Optical Waveguides*, Academic Press, New York, 1972.

[4] M. Ramme, E. Griese, M. Kurten, "Fast simulation method for a transient analysis of lossy coupled transmission lines using a semi-analytical recursive convolution procedure", in *Proceedings of 1997 IEEE International Symposium on Electromagnetic Compatibility*, pp. 277 – 282, Austin, Texas (USA), 1997.

Optical Waveguide Taps on Silicon CMOS Circuits

V. E. Stenger and F. R. Beyette Jr.

University of Cincinnati
Department of ECECS
PO Box 210030
Cincinnati OH 45221-0030
vstenger@ececs.uc.edu or beyette@ececs.uc.edu

ABSTRACT

A CMOS compatible integrated optic waveguide tap technology is proposed which has potential for high electrical and optical bandwidth. The technology encompasses grating couplers and mode-controlled optical detection to realize low-loss, wavelength-selective taps.

ABSTRACT

As processor and RAM speeds approach the GigaHertz regime, it is becoming more difficult to realize efficient, high-density, metal interconnects at the board and multi-chip levels. The high carrier bandwidth and parallelism of optical interconnects make them a good candidate for interconnection of electronic gate technologies. The parallelism of optical signals has been largely exploited in the form of local and long haul fiber communications networks. Others have proposed or demonstrated various optical distribution schemes at the board and chip levels. [1-3] To properly exploit the large optical carrier bandwidths, optoelectronic interconnects must also include high-speed optoelectronic conversion for receivers, and high-speed electro-optic modulation for transmitters. For this work, the receiver portion of the optical interconnect problem is addressed. In particular, a practical solution based on standard CMOS and integrated optic polymer waveguide technology is proposed. Optical signals are distributed proportionately over a series of taps (Fig. 1a), or are split up by wavelength via grating couplers (Fig. 1b).
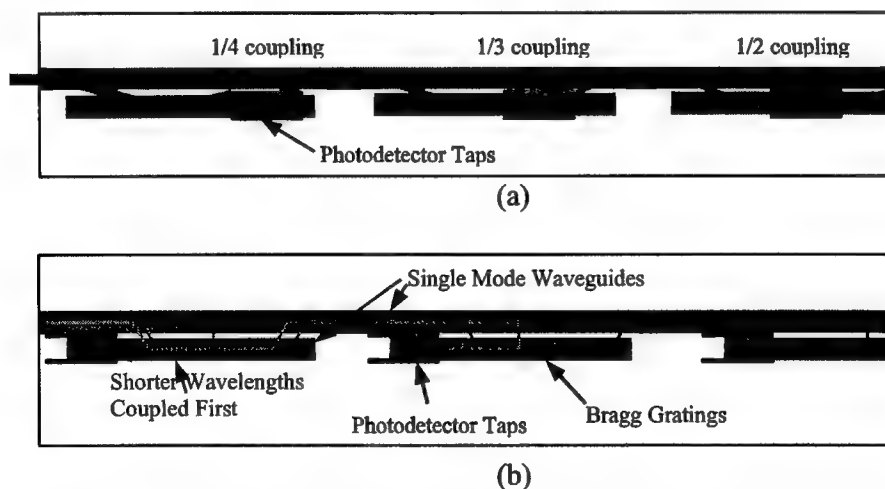
Figure. 1: Top view of optical signals being routed to multiple points on a chip or circuit board. (a) Distribution of one signal with equal power detection at each tap, and (b) division by wavelength, where each light color represents an additional wavelength or bit signal.

The advantage of optics is already apparent in Figure. 1b, in that multiple signals can appear as different wavelengths on the same optical "trace". The colors are selected based on the Bragg grating pitch at each tap device. In both Figure 1 cases, the optical signals are converted to electrical ones via high-speed traveling-wave photodetectors. These photodetectors are based on standard CMOS structures, and do not introduce any new complications to the processing. The optical waveguides are made from polymer materials in the interest of

economy of processing and of planarization requirements. The basic structure for the traveling wave photodetector tap device is shown in Figure 2. The idea behind a traveling wave structure is that the optical signal and induced electrical signals are matched in velocity along the respective optical and electrical guides. High gain, speed, and power handling can be achieved with such designs.
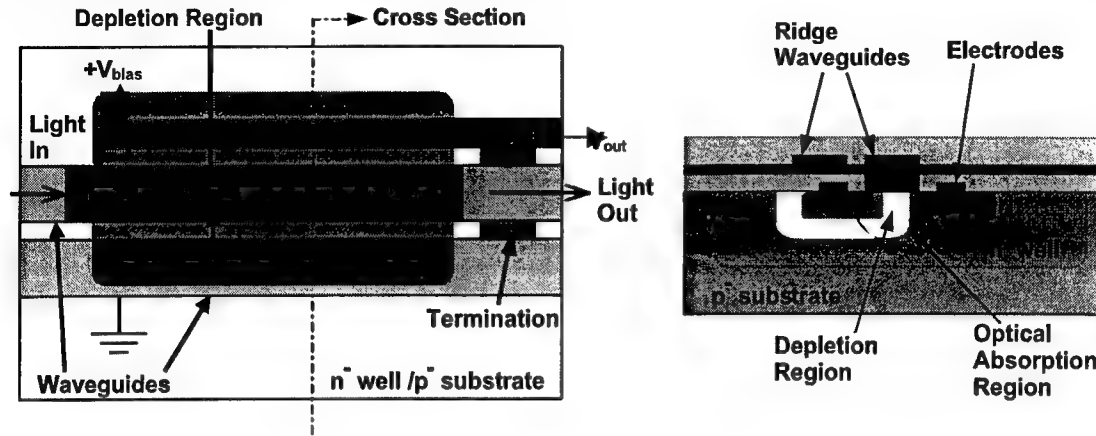
Figure 2: Detailed top and cross sectional views of the tap design. Note the high-speed traveling wave design for the photodetector for high speed optical to electrical conversion.

A key feature of the tap technology is that a series of taps is fashioned in such a way that losses are minimized. This is accomplished by transporting the light in "single-mode" between taps. The tap section itself is multimode in the vertical (y) direction, such that light propagates in a well-defined pattern toward the detector/substrate region without scattering loss. For a certain tap length, the light oscillates back to a profile, which can couple efficiently into the exit guide. This is shown in the figure 3 below.

Figure 3: Side view cross section of the optical tap, showing multimode oscillation

To date, basic structures have been simulated using BeamProp waveguide optics design software with promising results. Typical structure parameters are 1 µm HMDS upper and lower claddings, 1µm Polycarbisol core layer with a 0.1µm ridge, and tap lengths in the 20 µm regime. Grating coupler lengths are in the 0.3 to 0.5 mm regime to ensure good wavelength selectivity. Fabrication of test structures is currently underway.

REFERENCES

[1] S.K. Tewksbury and L.A. Hornak, "Optical Clock Distribution in Electronic Systems", J. VLSI Signal Processing, No. 16, pp. 225-246, 1997

[2] A.V. Krishnamoorthy and K.W.Goossen, "Optoelectronic-VLSI: Photonics Integrated with VLSI Circuits", IEEE J. Sel. Topics Quantum Electronics, Vol. 4, No. 6, pp. 899-912, Nov/Dec 1998

[3] T.K.Woodward and A.V. Krishnamoorthy, "1-Gb/s Integrated Optical Detectors and Receivers in Commercial CMOS Technologies", IEEE J. Sel. Topics in Quant. Elect., Vol. 5, No.2, pp 146-156, March/April 1999

An Optimal Distribution of Interconnections and Computations for Optically Interconnected Parallel Processing Systems

Makoto Naruse and Masatoshi Ishikawa
Department of Mathematical Engineering and Information Physics,
Graduate School of Engineering, University of Tokyo
7-3-1 Hongo, Bunkyo-ku, Tokyo 113-8656, Japan E-mail: naruse@k2.t.u-tokyo.ac.jp

This paper shows how to distribute given algorithms onto processing systems composed of several numbers of optoelectronic LSI (OE-LSI) chips and optical interconnections so that the potential capability of the physical layer enhanced by the optical technologies are utilized.

1 Introduction

This paper is theoretically approaching an optimal algorithm design method for optically interconnected parallel processing systems in a systematic way to utilize the enhancement of the physical layer capabilities supported by optoelectronic LSI (OE-LSI) or free-space optical interconnects. The method could be adapted to OCULAR-II [1] which is a hierarchical parallel optoelectronic system to yields its best performance.
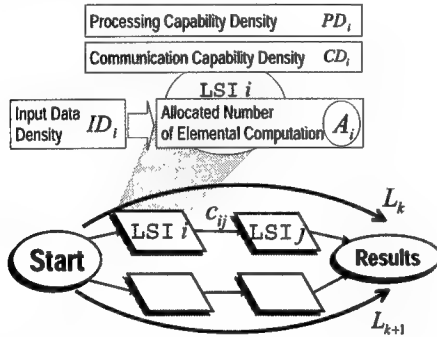

Fig. 1 The System Model: Each LSI has numerical indexes.

2 Model of Optically Interconnected Systems

A time frame to perform a computation written by $y = f(x_1, x_2)$ is composed of (1) the cost to transfer a variable to a chip, which we call "**Elemental Interconnect**": t_c, and (2) the cost to execute a computation, namely the "**Elemental Computation**": t_p. Based on the roadmaps of semiconductor and optical interconnects technologies[2][3], the transmission delay of interconnection is being reduced and will be comparable to that of the instruction cycles on a chip, which is evaluated as $t_c \sim t_p$. In addition to the temporal properties, the capabilities supplied by parallel optical devices should be represented as features per unit space and unit time to clearly exploit the spatially dense channels and the possible high-speed off-chip clock frequency.

Here we define two indexes that represent the potential capability of OE-LSI: (1) **Communication Capability Density** (CD_i) : Product of the number of I/O channels per unit area of LSI i and the frequency of individual channels. Here, i is the index of a LSI in a entire system, (2) **Processing Capability Density** (PD_i) : Product of the number of transistors per unit area of LSI i and the frequency of individual transistor.

In addition, free-space optics provides flexibilities for the data transfer pathways such as fan-out, fan-in,

or reconfigurable interconnection topologies. To represent interconnection flexibility, a matrix $M = \{m_{ij}\}$ called an Interconnection Matrix is defined to represent the connectivity among OE-LSIs where the existence of connections between LSI i and j is indicated by $m_{ij} = 1$ and no connection is expressed by $m_{ij} = 0$.

Picking up all the Elemental Interconnects and Elemental Computations contained in a given application, if some portion of Elemental Interconnects or Elemental Computations can be performed simultaneously, total latency will be reduced. To numerically discuss the optimal algorithm, let the amount of the Elemental Interconnect given to a unit area of an OE-LSI specified by index i during a unit time be "Input Density", denoted by ID_i, and let A_i being the number of the Elemental Computation allocated to LSI i.

Using above defined quantities, the required amount of latency to perform a given application is given by the **Effective Processing Time** which is

$$\max_k \left[\sum_{(i,j) \in L_k} \left\{ c_{ij} \cdot \frac{ID_j}{CD_j} \cdot t_c + \frac{A_j}{PD_j} \cdot t_p \right\} \right], \quad (1)$$

suppose that the area of every LSI in the system is equal to unit area, CD_j and PD_j respectively means the maximum number of Elemental Interconnect and Elemental Computation that can be simultaneously done, and $c_{ij}t_c$ being latency between LSI i and j. Fig. 1 schematically shows the definitions of the numerical indexes that indicate the potential capability of the system.

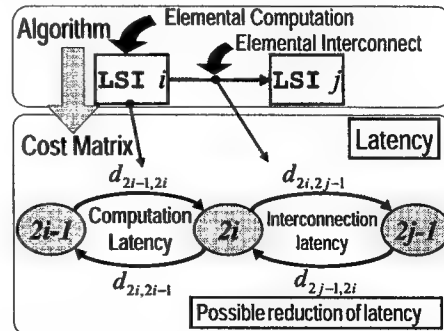

Fig. 2 The Assignment of Loads and the Definition of Cost Matrix.

3 Comprehensive Evaluation of Interconnect and Computation

As shown in eq. (1), bottlenecks could happen if excess loads of interconnect or computation are assigned

Table 1 The Definition of the Cost Matrix.

1. For every combination of $i \in 1, \cdots, N$, $j \in 1, \cdots, N$

   1) $\begin{cases} d_{2i-1,2i} = 1 & (0 \le A_i < PD_i) \\ d_{2i-1,2i} = \frac{A_i}{PD_i} + 1 & (A_i \ge PD_i) \end{cases}$

   2) $d_{2i,2i-1} = -\frac{A_i}{PD_j}$ $(A_i > 0)$

   3) $\begin{cases} d_{2i,2j-1} = c_{ij} & (m_{ij} = 1 \text{ and } 0 \le ID_j < CD_j) \\ d_{2i,2j-1} = c_{ij}\frac{ID_j}{CD_j} & (ID_j \ge CD_j) \end{cases}$

   4) $d_{2j-1,2i} = -c_{ij}\frac{ID_j}{CD_j}$ $(m_{ij} = 1 \text{ and } ID_j > 0)$

2. $i \in \{1, \cdots, N\}$
   $d_{2i,2N+1} = d_{2N+1,2i} = 0$
   (If the task assigned to LSI i is the final step of the given applications.)

3. Other elements are set to be infinity.

in some part of the system. Obtaining efficient computation procedure is corresponding to finding the best distribution of interconnects and computations that gives the shortest path between nodes depicted by "Start" and "Result" in Fig. 1.

In order to systematically derive the best way, a mathematical framework is introduced, which is named here as the **Cost Matrix**, for the representation of allocated computational loads at chips and interconnections in between. Fig. 2 shows the idea of the relationship between the load in the system and the element of the Cost Matrix. For an Elemental Computation assigned at LSI i, two nodes are defined, which are denoted by $2i - 1$ and $2i$, and the element of the Cost Matrix is given as the weight assigned to the arc between these two nodes, namely $d_{2i-1,2i}$, on the basis of the rule given in Table 1. As the same fashion, the Elemental Interconnect is also evaluated.

The weight allocated to reverse paths in the Cost Matrix, which is corresponding to the arc from $2i$ to $2i-1$ and from $2j-1$ to $2i$ in Fig. 2 take a critical role to obtain the optimum algorithm, by which possible reduction of the latency, if the task is cancelled at the corresponding processing node, is indicated.

3.1 Example

Suppose a system having three chips, each of which PD and CD being 1. The connections are specified by M shown in Fig. 3 (b). Let all of the Elemental Computation being allocated at LSI 2 whose number is 7, and they need an Elemental Interconnect from LSI 1. Then, the Cost Matrix is given by Fig. 3 (c). The arc between node i and j in Fig. 3(d) represents the (i, j)-element of the Cost Matrix.

4 Optimization Method: The Negative Closed Loop

Since the elements of the Cost Matrix could have negative values based on the definition of itself, there may be closed loops along which the summation of the elements results in a negative value. We call such loop a **Negative Closed Loop**.

The existence of Negative Closed Loops indicates the existence of more efficient algorithms than current one, by re-allocating some portion of Elemental Interconnect or Elemental Computation such that the negative value decreases along the closed loop. When the algorithm that minimizes eq. (1) is obtained, there are no Negative Closed Loops, which can be proofed by Network Flow theories[4].

In the example case, there is a Negative Closed Loop along nodes ④-③-②-⑤-⑥-⑦ whose summa-

tion of weight yields -5, as shown in Fig. 3(d). If some portion of the Elemental Computations is reassigned from LSI1 to LSI3 as shown in Fig. 4, then there is no Negative Closed Loop, which yields optimum algorithm for this problem.
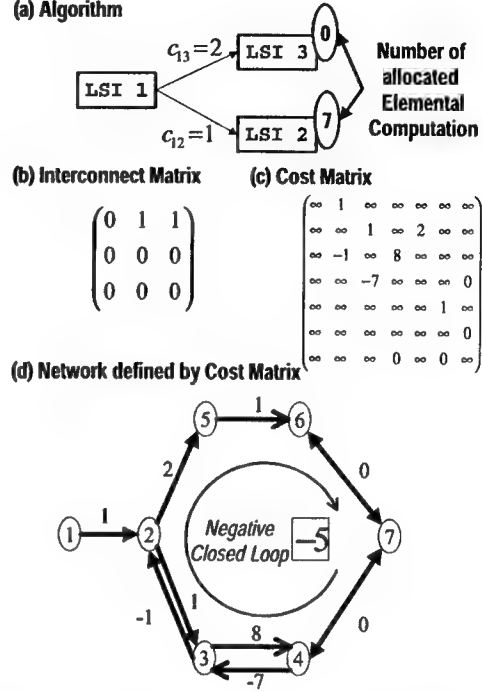
Fig. 3 Algorithm Formulation: Initial Status.
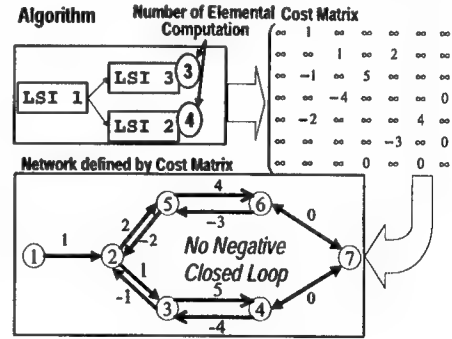
Fig. 4 Final Algorithm.

5 Conclusion

A method to obtain the processing and communication loads distribution that yields minimum processing time for a given application in a optically interconnected system has been shown considering the properties of the physical layer enhanced by optical technologies on the basis of a matrix-based mathematical framework.

References

1. N. McArdle et al., IEEE JSTQE, Vol.5, No.2, pp.250-260 (1999)
2. The National Technology Roadmap for Semiconductors, SIA, 1999.
3. Technology roadmap: Optoelectronic interconnects for integrated circuits, European Commission, 1998.
4. R. K.Ahuja et al., NETWORK FLOW, Prentice Hall, 1993.

Low-power short-distance optical interconnect using imaging fibre bundles and CMOS detectors

C. Rooman[1,2], M. Kuijk[1], D. Filkins[3], B. Dutta[2], R. Windisch[2], R. Vounckx[1], P. Heremans[2]

[1] University of Brussels V.U.B., department ETRO, Pleinlaan 2, B1050 Brussels, Belgium

[2] IMEC, Kapeldreef 75, B3001 Leuven, Belgium, tel ++32-16-281751, fax ++32-16-281501, email: rooman@imec.be

[3] Schott Fiber Optics, 122 Charlton Street, Southbridge, MA 01550-1960

Introduction and Description of the link

We report on the measured link performance of a novel parallel optical link that is to operate from CMOS chip to CMOS chip. The components of the optical link are shown in Figure 1 and briefly described below.

The optical channel is a 10-cm long imaging fibre bundle with 1.9 mm cross-section and open area ratio of 67%. The bundle is assembled from 7 µm fibres with numerical aperture of 1.

The light sources are a 2-dimensional array of 10 X 10 high-speed high-performance light-emitting diodes, called non-resonant cavity LEDs [1]. The LEDs have a diameter of 30 µm and are on a pitch of 100 µm in X and Y. The LED array is designed to be flip-chip mounted onto CMOS driver circuits, and the emission wavelength is 850 nm. To solve the problem that the GaAs substrate is not transparent at this wavelength, the original GaAs substrate is replaced by a fiber optic face plate [2], with square fibres of 5.4 µm with numerical aperture of 1.

Finally, the detectors and receivers in the system are standard CMOS detector-receiver cells, again arranged as an array on a pitch of 100 µm in X and Y. The detectors, called "Spatially Modulated Light Detector" [3] are designed to allow high-speed operation. Each detector is 50 µm X 50 µm, and its corresponding integrated receiver takes the remaining area in the 100 µm X 100 µm cell. The detector/receiver CMOS circuit was designed in 0.6 µm CMOS, and fabbed in a foundry.

Figure 1: Components of the proposed low-power short distance optical interconnect

Apart from the fibre optic face plate that serves as substrate for the LED array and the imaging fibre bundle, there is no optics in the system. In particular, there is no magnification/demagnification at the transition between the source array and the imaging fibre bundle, and no coupling optics at the entrance or exit of the imaging fibre bundle. The fibre is butt-coupled to the opto-electronic devices. The large numerical aperture of the face plate and the fibre bundle allows to capture and guide the light of the LEDs efficiently.

Measured link performance

Figure 2 shows the open eye diagram of an LED of the array (on fibre optic face plate) transmitted through the imaging fibre bundle at 1 Gbit/s. The measurement was done using a pseudo-random bit stream of $2^{23} - 1$ bits. It shows that the switching speed of the (small) LEDs used in this work allows Gbit/s optical transmission.

Figure 3 shows the digital eye diagram of the optical link including the LED on face plate, the imaging fibre bundle and the CMOS detector/receiver, at 300 Mbit/s. We checked that the detector, designed in 0.6 µm CMOS, operates at bit rates up to 600 Mbit/s. The transmission speed of the system is, today, limited by the receiver to 300 Mbit/s. Simulations show that a re-design in 0.25 µm should crank up this speed to over 1 Gbit/s per channel.

Figure 2 : Eye diagram of optical pulses transmitted through imaging fibre bundle
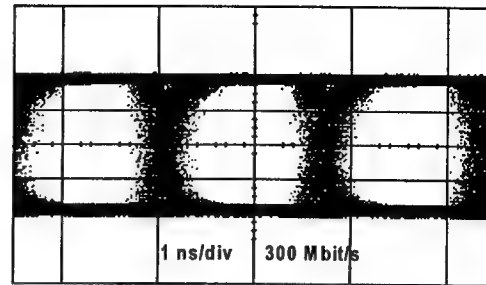
Figure 3 : Eye diagram of the system at 300 Mbit/s

Figure 4 shows the bit error rate versus optical power falling on the CMOS chip, at 250 Mbit/s and 300 Mbit/s, using a 2^{23}-1 pseudo-random bit stream. 10 µW average power (corresponding to –20 dbm) is seen to be sufficient at 300 Mbit/s to achieve a bit error rate of less than 10^{-12}.

In Table 1 is summarised the measured electrical power budget of the link. At 300 Mbit/s, the LED is driven at a drive current of 0.70 mA peak-to-peak. Since the CMOS driver circuit will draw this current from a power supply of 3.3 V, the average power dissipation in the LED + driver circuit will be close to 0.35 mA X 3.3 V = 1.15 mW. The power consumption of the CMOS detector/receiver was measured to be 2.8 mW. The total power consumption of a single link is therefore *only 4 mW*. In a parallel link between chips, where emitters and detector/receivers are evenly distributed over both chips, each opt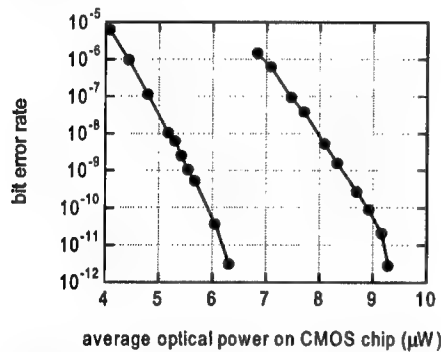ical I/O will therefore consume on average only 2 mW, and take up a space of merely 100 µm X 100 µm (in 0.6 µm CMOS, and scalable in newer CMOS generations).

Figure 4 : Bit error rate vs. average optical power for the link operating at 250 Mbit/s and 300 Mbit/s

Table 1 : Power budget of the link

Bit rate Mbit/s	required optical pow. µWatt	LED current mA	LED power consumption over 3.3 V mW	Det / Rec power consump. mW	avg. power consump. per chip mW
250	7	0.22	0.75	2.8	1.8
300	10	0.35	1.15	2.8	2.0

The power consumption and the density of the demonstrated optical link compares very favourably to competing electrical and optical solutions. For example, an electrical link consumes a power equal to CV^2. Here C consists of a fixed capacitance of about 10 pF plus a contribution proportional to the link length of at least 1 pF/cm. For 10 cm, the capacitance is therefore at least 20 pF. Even when switching over only 1 V, the electrical power consumption is more than 6 mWatt at 300 Mbit/s. When further increasing the link speed or length, the comparison is even more in favour of the optical alternative.

References

[1] R. Windisch et al., "Light-emitting diodes with 31% external quantum efficiency by outcoupling of lateral waveguide modes", Appl. Phys. Lett., Vol. 74, No 16, 1999.

[2] P. Heremans et al, "Thin-film 850-nm light emitters on fibre optic face plate", ECOC '99, Nice, France, Proc. pp. II-304/5, Sept. 1999

[3] D.Coppée et al., "Experimental study of the spatially-modulated light detector", *Stolid State Electronics,* vol. 43, pp.609-613, March 1999.

Acknowledgements

FAST AND ROBUST MEASUREMENT OF OPTICAL CHANNEL GAIN

Anders la Cour-Harbo, Jakob Stoustrup

Aalborg University
Department of Control Engineering
Fredrik Bajers Vej 7C
9220 Aalborg, Denmark
alc@control.auc.dk, jakob@control.auc.dk

Lars F. Villemoes

Royal Institute of Technology
Department of Mathematics
100 44 Stockholm, Sweden
larsv@math.kth.se

ABSTRACT

We present a numerically stable and computational simple method for fast and robust measurement of optical channel gain. By transmitting adaptively designed signals through the channel, good accuracy is possible even in severe noise conditions.

1. INTRODUCTION

The measuring of optical channel gains is a key element in many applications. Measuring channel gains means determining the change in intensity when a signal is transmitted from an emitter to a receiver. A well-known and simple application is an automatic door, which responds whenever a person is reflecting the emitted signal, and thereby significantly increasing the channel gain. Another example is measuring the thickness of paper. A more subtle example is determination of spatial position by comparing the intensities of a multitude of reflections from a single object. A typical way of making this type of measurements is emitting a simple signal, such as a harmonic or square wave signal, since they are both easily constructed and measured with analog electronics. Such solutions have two major disadvantages: The signals are sensitive to frequency located disturbances, and it is difficult to detect and avoid/neutralize such disturbances.

We propose a measuring method which is highly accurate in moderate noise conditions, and less accurate, but very robust, in severe noise conditions. This is achieved by using two closely related digital signal design algorithms; a "best case" and a "worst case" algorithm. The former is based on the wavelet transform (WT), while the latter is based on the Rudin-Shapiro transform (RST). They are both simple, numerically stable, and post-processing friendly making them ideal for implementation e.g. in a fixed point DSP. By introducing a signal processor it becomes possible to continuously redesign the signals for improved SNR, and thereby maintaining the accuracy in changing and/or severe noise conditions.

2. DESIGNING THE DIGITAL SIGNALS

The two design algorithms are based on the wavelet packet transform scheme; it is fast, numerically stable, works well in fixed point arithmetics, and has low program complexity.

The best case algorithm uses the classical WT to create signals which are near-orthogonal to expected noise occurrences, while the other algorithm uses the RST to create an all-spectrum signal, which by nature has low sensitivity with respect to time and frequency located noise occurrences. The difference is essentially that the WT algorithm "searches for holes" in the current noise, while the RST algorithm spreads information in time and frequency to reduce the impact of localized disturbances. The prefered method depends on the noise conditions. If there are easy-to-find holes in the noise, the former can provide very accurate measurements. If, however, the noise is difficult to define or is changing rapidly, the latter method provides lesser accurate, but more robust measurements.

A good introduction to the wavelet theory is Wickerhauser [6]. A mathematically rigorous treatment of the subject is given in Daubechies [3]. For more material on Rudin-Shapiro polynomials see Brillhart [1]

2.1. The wavelet transform

The WT based algorithm takes a simple, time localized signal (see figure 1 for an example), and inversely wavelet packet transform it, which results in a frequency localized signal. A typical maximum spread is also shown in figure 1. After transmission the signal is forwardly transformed to reproduce the original, now noisy simple signal, and by inner product with the "clean" original signal the transmission intensity (the channel gain) is determined. Since the original signal is completely known, it is also possible to obtain an estimated accuracy of the channel gain measurement. This is accomplished by taking inner product between the transmitted, transformed signal and a number of signals orthogonal to the original signal. If these quantities are small the transmission was most likely subject to only mild noise. This trick provides an easily calculated guideline to how much one can trust the current measurement. If each measurement is vital a number of signal restoration procedures (not further described here) can be applied. These also benefit from the complete knowledge of the original signal. Note that the small number of non-vanishing coefficients of the original signal in all cases significantly reduce the amount of calculations.

Because the transform is linear and has perfect reconstruction, it is also easy to make a good sample by sample estimation of the noise, which provides valuable information on any disturbances. This makes it possible to do real time adaptation of the signal. The mehtods combines the ability of the WT to produce predefined trade-offs between time and frequency information with the freedom in design of the original signal.
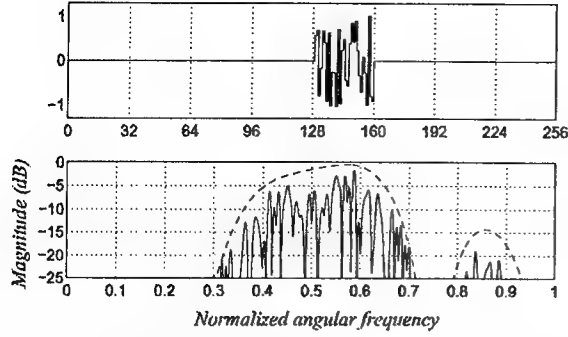
Figure 1: Uppermost a simple signal (here a sampled chirp). Below (in solid) the absolute value of the Fourier transform of the 3-scale inverse wavelet packet transform with symlets 6 [4]. The dashed curve shows the maximal frequency spreading for any (suitably normalized) signal with coefficients vanishing outside [128; 159].
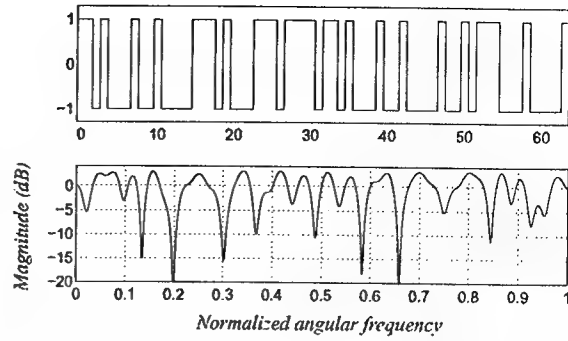
Figure 2: Uppermost is the result of applying the inverse Rudin-Shapiro transform to the 29th canonical basis vector of length 64. Below the frequency response (the absolute value of the corresponding $P_6(e^{i\xi})$ polynomial).

Thereby it is possible to adapt the method to virtually any type of noise, in particular disturbances with large temporal extent.

2.2. The Rudin-Shapiro transform

The RST is defined through a slightly extended version of the remarkable Rudin-Shapiro polynomials, introduced in 1951 by H. S. Shapiro in his master's thesis, and published in 1959 by Rudin [5]. Define the polynimals

$$P_{m+1}(z) = P_m(z) + (-1)^{\delta_m} z^{2^m} Q_m(z), \quad P_0 = 1$$
$$Q_{m+1}(z) = P_m(z) - (-1)^{\delta_m} z^{2^m} Q_m(z), \quad Q_0 = 1 \quad (1)$$

with $\delta_m \in \{0, 1\}$. It immediate follows that for all $|z| = 1$

$$|P_{m+1}|^2 + |Q_{m+1}|^2 = 2|P_m|^2 + 2|Q_m|^2 = 2^{m+2}.$$

Consequently,

$$\max_{\xi} |P_m(e^{i\xi})| \leq \sqrt{2} \|P_m(e^{i\xi})\|_2, \quad (2)$$

guaranteeing a certain flatness of the polynomials. A construction similar to (1) is found in Byrnes [2]. The coefficients of the polynomials can also be constructed with the Rudin-Shapiro transform, which is really a modified wavelet packet Haar transform. Define the unitary transform $\mathbf{H}_n : \mathbb{R}^{2^n} \mapsto \mathbb{R}^{2^n}, n \geq 1$, as

$$\begin{bmatrix} y_k \\ y_{k+2^{n-1}} \end{bmatrix} = \frac{1}{\sqrt{2}} \begin{bmatrix} 1 & (-1)^k \\ 1 & -(-1)^k \end{bmatrix} \begin{bmatrix} x_{2k} \\ x_{2k+1} \end{bmatrix}$$

for $k = 0, \ldots, 2^{n-1} - 1$ when mapping $\mathbf{x}$ to $\mathbf{y}$. Then, with $\mathring{\mathbf{H}}_n$ being the inverse of $\mathbf{H}_n$,

$$\hat{\mathbf{H}} \stackrel{\text{def}}{=} \prod_{n=1}^{N} \begin{bmatrix} \mathring{\mathbf{H}}_n & & 0 \\ & \ddots & \\ 0 & & \mathring{\mathbf{H}}_n \end{bmatrix}_{2^N \times 2^N}$$

transforms the canonical basis for $\mathbb{R}^{2^N}$ into the coefficients of the 2^N possible $P_N(z)$'s. Hence these coefficients constitutes an orthonormal basis, which not only consists of only ± 1, but

also, due to (2), has a remarkable frequency response. In figure 2 is an example of such a basis element and its frequency response. The RST based algorithm is applied in much the same way as the WT method. A simple signal is inversely transformed prior to transmission. This will produce an all-spectrum signal. Upon transmission the signal is forwardly transformed yielding the original, simple signal with noise. The post-processing is equivalent to that of the WT method.

3. CONCLUSION

Two computationally simple and numerically robust algorithms for measuring optical channel gains were presented. One of the algorithms provides excellent accuracy in moderate noise conditions, while the other has reduced, but very robust, accuracy even in severe noise conditions. Combining the two algorithms, either by applying the most suitable one, or jointly in two parallel systems, is easy due to their similar program and computational structure, and the result is a versatile optical channel gain method. The low complexity and numerical stability of the wavelet packet transform scheme and of the post-processing (mainly inner products) also makes this approach fast and suitable for low cost hardware implementation. For the commercial aspects of these methods, please refer to www.beamcontrol.com.

4. REFERENCES

[1] J. Brillhart. On the Rudin-Shapiro polynomials. *Duke Math. J.*, 40:335–353, 1973.

[2] J. S. Byrnes. Quadrature Mirror Filters, Low Crest Factor Arrays, Functions Achieving Optimal Uncertainty Principle Bounds, and Complete Orthonormal Sequences – A Unified Approach. *App. and Comp. Harm. Anal.*, 1:261–266, 1994.

[3] I. Daubechies. *Ten Lectures on Wavelets*. SIAM, 1992.

[4] I. Daubechies. Orthonormal bases of compactly supported wavelets. II. Variations on a theme. *SIAM J. Math. Anal.*, 24(2):499–519, 1993.

[5] W. Rudin. Some theorems on Fourier coefficients. *Proc. Amer. Math. Soc.*, 10:855–859, 1959.

[6] M.V. Wickerhauser. *Adapted Wavelet Analysis from Theory to Software*. A K Peters, May 1994.

52

Electronic-Enhanced Optics

Wednesday, 26 July 2000

WA1:   Electronically-Enhanced Imaging Systems
WA2:   Architectures and Applications

Unconventional Vision Sensors

Shree K. Nayar
Department of Computer Science
Columbia University
New York, New York

What can be perceived by a human or computed by a machine from an image is
fundamentally restricted by the captured data. Current imaging systems are limited in
spatial resolution, field of view, and dynamic range. In this talk, we present new vision
sensors that provide unconventional forms of visual information. The first part of the talk
focuses on the use of catadioptrics (lenses and mirrors) for capturing unusually large
fields of view. We describe several methods for obtaining single viewpoint and multi-
viewpoint images. The second part of the talk addresses the problem of acquiring high
dynamic range images using a low dynamic range detector. We present two approaches
for extracting the desired extra bits at each pixel; the first one uses multiple images while
the second uses just a single image. Several interactive demonstrations of our results will
be shown. These results have implications for digital imaging, immersive imaging, image
based rendering, 3D scene modeling, and advanced interfaces.

Design of a Smart Pixel Multispectral Imaging Array
Using 3D Stacked Thin Film Detectors on Si CMOS Circuits

K. Lee, S. Seo, S. Huang, Y. Joo, William A. Doolittle, S. Fike, N. Jokerst, M. Brooke, A.Brown
School of Electrical and Computer Engineering, Georgia Institute of Technology, Atlanta, GA 30332-0250
J.E. Jensen, T.J. de Lyon HRL Laboratories, 3011 Malibu Canyon Rd., Malibu, CA 90265-4799

Multispectral imagers have been widely investigated for their application to target recognition, particularly in clutter [1,2], industrial gas pollutant monitoring [3], and biomedical imaging [4]. For example, target recognition is a difficult task with passive detection of small targets embedded in infrared image data. This difficulty arises because in most cases the target exhibits only slight variation in temperature from the background clutter. When image data at multiple wavelengths is collected, the data can be processed to cancel the background clutter and improve the detectability of targets [1,2]. Many methods have been used to realize multispectral imaging, however, each has some significant difficulties [3,4] which can be resolved by using co-located detectors stacked in 3D on top of image processing circuitry [5,6,7].

Information processing using digital Si CMOS circuits is currently ubiquitous due to the increasing level of complexity of information processing demands and capabilities. Leveraging the high level of Si signal processing complexity by creating "smart" systems that use Si circuitry with enhanced added functions is an attractive system option. The most effective value-added components to add to Si CMOS are those that can be independently optimized, compromising neither the performance of the value-added devices nor the Si CMOS circuits. Herein, we discuss the design of a "smart" multispectral imaging system which can be fabricated with independently optimized detector arrays and Si CMOS circuits, which are stacked in three dimensions on top of one another for complete physical registration of the multispectral image. This smart multispectral imager, described herein, utilizes the heterogeneous integration of thin film GaN (UV), MCT (MWIR), and Si CMOS circuitry to create an outstanding example of the power of heterogeneous integration for enhancing optical systems using electronic signal processing capabilities.

The smart multispectral imager realizes the full registration of multicolor images through the integration of multiple stacked co-located detectors onto Si CMOS analog to digital converter (ADC) circuitry, as illustrated (not to scale) in Figure 1. A foundry digital Si CMOS array of sigma delta ADCs, shown in a photomicrograph in Figure 2, serves as the integration host substrate. These Si CMOS ADCs consist of one dedicated converter per image pixel, and the circuits have been optimized for low noise transfer of data off of the focal plane, using per pixel digitization and filtering methods which can also be used to trade off frame rate and resolution. The GaN UV MSM and MCT MWIR pn photodetectors are independently grown and optimized, and are designed for thin film processing, integration, and stacking using metal/metal bonding. This process is illustrated in Figure 3.
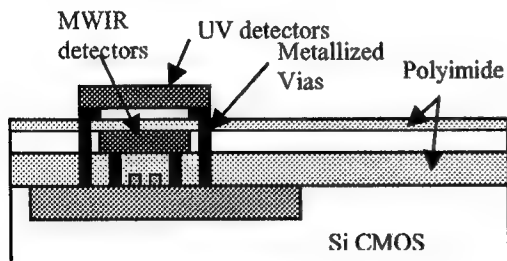

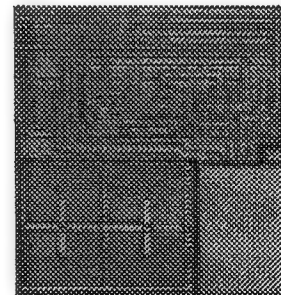Figure 1. Schematic of integrated multispectral imaging array using 3D stacked detectors.

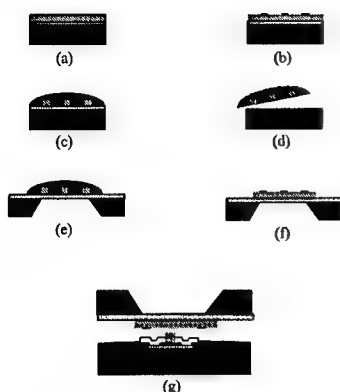Figure 2. Photomicrograph of Si CMOS ADC circuit fabricated through MOSIS.

Figure 3. Thin film integration process.

In this integration process, a stop etch layer is grown lattice matched between the detector epilayers and the growth substrate (a). This stop etch layer can be removed, and does not degrade device performance. The devices are mesa etched for pixellization (a partial mesa etch for arrays, to maintain spatial registration during subsequent bonding processes) (b), and the devices are protected from the substrate removal etchant by a handling layer such as Apeizon W (c). The substrate is removed using a wet etch which selectively etches the substrate and not the stop etch layer (d), and the stop etch layer, with another etchant, can then be removed if necessary. The devices are then bonded to a transfer diaphragm (e, f), and are aligned and bonded to the host substrate (g) [5,6].

To realize these thin film photodetectors, the MCT MWIR pn detectors are grown on SOI, and the GaN UV photodetectors are grown on lithium gallate. These structures enable the selective chemical removal of the growth substrate, as illustrated in Figure 3, with details in the presentation. To integrate the Si CMOS host substrate circuit, it is planarized and isolated with polyimide, cured, vias are cut to the Si CMOS contact pads using a reactive ion etcher (RIE), and the vias are metallized for contact to the MCT (bottom layer) photodetectors. Note that the original top metallization of the photodetectors is inverted in the transfer process, and the devices are thus metal/metal bonded to the Si CMOS circuit, resulting in an excellent mechanical and electrical bond. As an example of this type of thin film detector array integration, Figure 4 is a photomicrograph of an 8x8 array of thin film GaAs P-i-N detectors bonded directly on top of Si CMOS circuits [7].

(a)   (b)   (c)   (d)
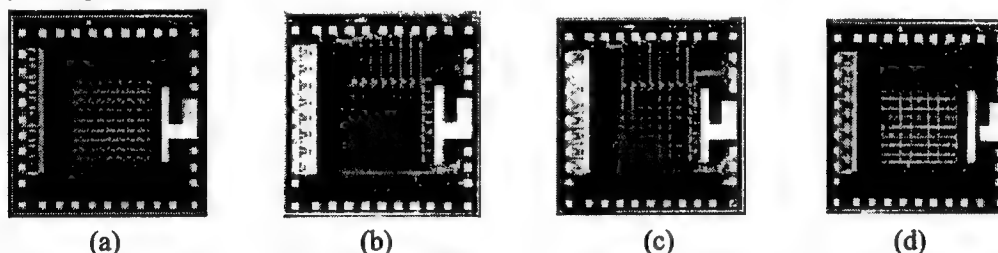
Figure 4. Photomicrographs of 8x8 integrated array: (a) Si CMOS circuit; (b) thin film P-i-N detectors bonded to planarized/via cut/metallized circuit; (c) interstitial layer removed; (d) planarization/isolation, top via, and top metal contact completed.

Since the MCT MWIR detectors are only microns thick, they can be planarized with polyimide or BCB with subsequent top contact metallization (which can be utilized as a shared contact with the GaN). To fully separate the MCT and GaN contacts, the MCT top contacts can be isolated with polyimide and the top MSM contact metallization for the GaN UV photodetector array deposited. Next, the GaN thin film MSM detectors are bonded, with contacts facing down to the metallized MCT array, thus completing the imaging array. Processing details and projected performance of the integrated multispectral imaging array will be discussed in the presentation.

[1] L. Hoff, J. Zeider, C. Yerkes, *SPIE Signal and Data Processing of Small Targets*, vol. 1698, pp. 100-114, 1992.
[2] L.E. Hoff, J.R. Evans, and L.E. Bunney, *NOSC TR 1404*, Dec. 1990.
[3] F. Lopez, J. deFrutos, A. Gonzalez, A. Navarro, *Sensors and Actuators B*, vol. 6, pp. 170-175, 1992.
[4] R. Williams, J. Sanders, R. Driggers, C. Halford, *Proceedings. IEEE Southeastcon '92*, vol. 1, pp. 291-294, April 1992.
[5] C. Camperi-Ginestet, M. Hargis, N. Jokerst, M. Allen, *IEEE Phot. Tech. Lett*, Vol.3, No.12, pp.1123-1126, Dec., 1991.
[6] N. Jokerst, M. Brooke, O. Vendier, S. Wilkinson, S. Fike, M. Lee, E. Twyford, J. Cross, B. Buchanan, S. Wills, *IEEE Trans. On Comp., Pack., and Manfuac. Tech., Part B*, Vol.19, No.1, Feb.1996, □□□□.
[7] S. Fike, B. Buchanan, N. M. Jokerst, M. Brooke, T. Morris, S. DeWeerth, *IEEE Phot. Tech. Lett*, Vol.7, No.10, pp.1168-1170, Oct. 1995.

A Novel Photoreceiver Array with Near Field Resolution Capability

Bharath Seshadri, Jainjing Tang, Irving Chyr, Andrew J. Steckl, and Fred R. Beyette Jr.

University of Cincinnati
Department. of ECECS
PO Box 210030
Cincinnati, OH 45221-0030 USA
beyette@ececs.uc.edu

Abstract

A photoreceiver array is presented that exploits the features of near field optics to provide sub-nanometer spatial resolution. Comprised of a photonic CMOS photoreceiver chip and a MEMS based aperture array, the near-field photoreceiver array is implemented using standard fabrication techniques.

Summary

It has been suggested that ultra high-density optical storage devices could be realized by storing data in patterns with spatial coordinates below the far-field resolution limit.[1] While the ability to write data on these fine dimensions has been shown, the ability to read data with sub-lambda spatial resolution has proven problematic. This is especially true for memory systems that require page-oriented memory access.

In this paper we describe a novel photoreceiver array technology that exploits the features of near field optics[2] to provide sub-nanometer resolution capabilities. Specifically, each optical input window in the array uses a sub-wavelength aperture to diffract evanescent waves into the silicon based detector of a high gain photoreceiver circuit. With this aperture structure, it is possible to transform evanescent waves with high spatial frequencies (on the order of the wave number of the evanescent waves) into lower frequency waves that propagate (with out evanescent decay) into the photodetector structure.[2]

Implemented with a photonic CMOS photoreceiver array and a silicon micro machined aperture array, our approach is based on standard fabrication processes. The near-field photoreceiver array consists of a 5x5 CMOS based photoreceiver array. Each individual photoreceiver module consists of a silicon based photodetector, a multistage current amplifier and a thresholding circuit that allows the photoreceiver sensitivity to be tuned over a wide range of optical power levels.[3] As suggested by the circuit diagram shown in figure 1, the entire photoreceiver module (including the PNP phototransistor) is based on a conventional CMOS device technology. Our current version of the photoreceiver chip has been fabricated through the MOSIS foundry service using a 1.2 µm CMOS device technology.
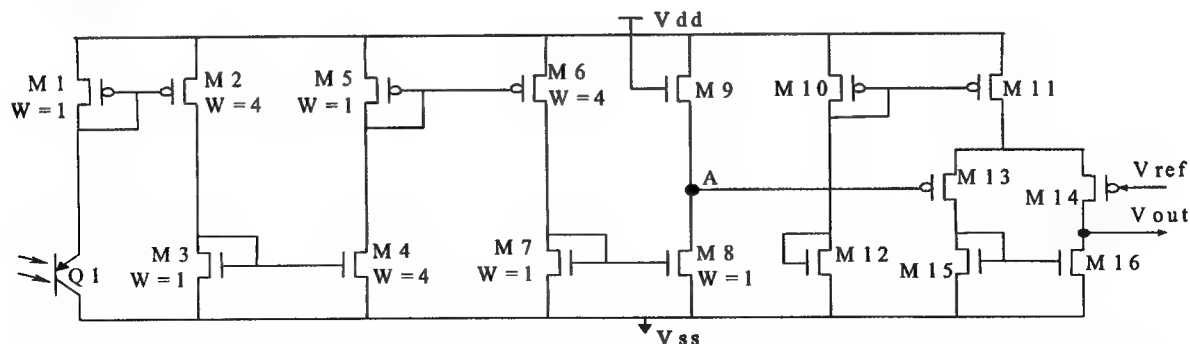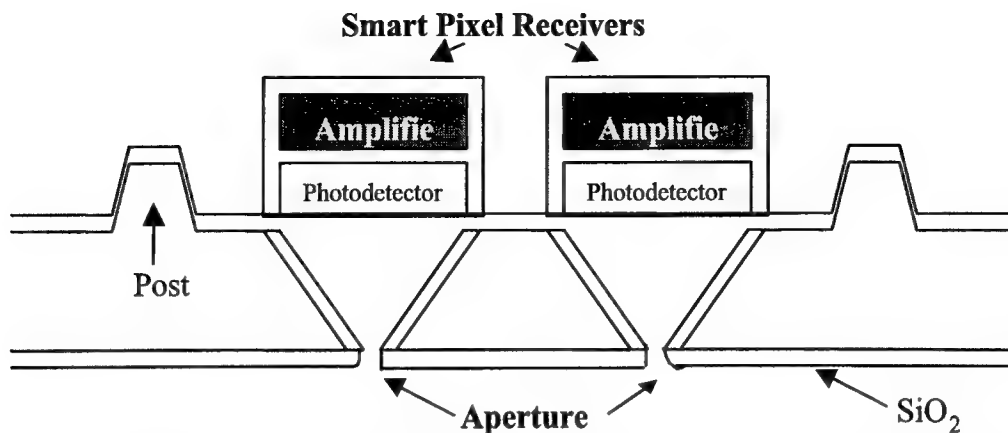

Figure 1 Circuit diagram for the CMOS based photoreceiver module. The phototransistor is implemented with a p+ emitter region implant in an N-well base region. The p-type substrate acts as the collector region in the resulting pnp transistor structure.

Smart Pixel Receivers

Amplifie	Amplifie
Photodetector	Photodetector

Post

Aperture

SiO₂

Figure 2   Cross section of the near field photoreceiver array showing the photoreceiver chip and the micro-machined aperture array.

While the photoreceiver circuit is an important component of our device technology, the aperture array is the fundamental component designed to enable data detection with near-field resolution. Using micro-machining technology pioneered for fabrication of micro electro-mechanical systems (MEMS), the aperture array is realized by etching Silicon with a KOH/IPA etching solution. This anisotropic etch step is used to machine via like structures through to a SiO_2 film on the back side of a thinned Silicon substrate. Finally, sub-micron sized apertures are milled through the SiO_2 film using a commercial focused ion beam milling system.

After independent fabrication of the photoreceiver array and the aperture array, the near-field photoreceiver array is completed by mechanically joining the two components. Figure 2 shows a composite view of the completed structure. As indicated in the figure, mechanical alignment features must be included on both the CMOS chip and the aperture array to ensure proper x/y alignment of the aperture array with respect to the photodetectors in the photoreceiver array. For the aperture chip, anisotropic etching is used to define a set of 4 posts on the top surface of the aperture array. Due to the fast off axis etching of pyramidal corner feature in Silicon, proper etching of the post structures requires the inclusion of corner compensation techniques[4] in the photolithography mask design. For the CMOS chip, pit features are etched into the CMOS photoreceiver chip using a post fabrication, anisotropic etching procedure on the packaged CMOS chips. Note that fabrication of these features requires the inclusion of openings through to the CMOS chip substrate. These "Open" features have been defined in the VLSI CAD tool as a composite layer comprised of existing oxide via layers.[5]

In this paper we present a detailed description of both the photoreceiver circuit and the aperture array fabrication method. Independent characterization of both the photoreceiver circuit and the aperture array will be included. Finally, the individual components are packaged together and the expected near-field resolution is quantified.

REFERENCES

[1] E. Betzig, J. K. Trautman, R. Wolfe, E. M. Gyorgy, P. L. Finn, M. H. Kryder and C. H. Chang, "Near-Field Magneto-Optics and High Density Data Storage", Appl. Phys. Lett., Vol. 61, pp. 142-144, July 1992.

[2] M. A. Paesler and P. J. Moyer, *Near-Field Optics: Theory, Instrumentation and Applications,* John Wiley & Sons, Inc., 1996.

[3] J.Tang, B.Seshadri, K.N.Naughton, B.K.Lee,R.C.J.Chi,A.J.Steckl and F.R.Beyette Jr., "CMOS based Photoreceiver Arrays for Page-Oriented Optical Storage Access", Submitted to IEEE Photon. Tech. Lett.

[4] B. Puers and W. Wansen, "Compensation Structures for Convex Corner Micromachining in Silicon", Sensors and Actuators, Vol. A21-A23, pp. 1036-1041, 1990.

[5] J. C. Marshall, M. Parameswaran, M. E. Zaghloul and M. Gaitan, "High-Level CAD Melds Micromachined Devices with Foundries", IEEE Circuits and Devices Vol. 8, No. 6. pp. 10-17, November 1992.

Artificial Retinal Prosthesis to Restore Vision for the Blind

Wentai Liu, Ph.D. (wentai@eos.ncsu.edu and http://www.ece.ncsu.edu/retina)
Department of Electrical & Computer Engineering, EGRC Building, North Carolina State University
Raleigh, NC 27695-7914

Mark S. Humayun, M.D., Ph.D. (mhumayun@jhmi.edu and http://www.irp.jhu.edu)
Wilmer Ophthalmological Institute, Johns Hopkins University, Baltimore, MD 21287

Introduction

Blindness robs millions of individuals of the keen sense of vision, leaving them in perpetual darkness. Several groups around the world are evaluating the feasibility of creating visual perception by electrical stimulation of the remaining retinal neurons in patients blinded by photoreceptor loss [1-5]. Artificial vision as provided by the prosthetic system of a multiple-unit artificial retina chipset *(MARC)* implanted within the eye holds a promise to restore useful vision to a large subset of patients who are blind from retinal disorders. The system would have an external camera (mounted in a glasses frame) to acquire an image and convert it into an electrical signal. This signal would be wirelessly transmitted to an implanted chip, which would electrically stimulate the non-degenerated cells of the retina. The pattern of electrical stimulation would be controlled to produce the perception of an image. Hence, the sense of vision could be partially restored with such an implantable electronic device.

The human eye with its nearly 100 million photoreceptors is a complex system that allows us to enjoy high resolution imagery full of colors. The system functions when light is focused by the cornea and crystalline lens within the eye on to the retina, a delicate tissue that lines the inside of the eye ball. The retina is highly structured, composed of multiple cell layers, each with a specific function. The photoreceptor cell layer captures light energy and converts it into electrochemical signals. These signals then excite bipolar cells located in the second layer of neurons in the retina. The bipolar cells subsequently transmit the signal to retinal ganglion cells whose axons collectively form the optic nerve that connects the retina to the visual centers of the brain. Other cells such as the horizontal and amacrine cells form connections between neurons within a layer, adding to the computational power of the retinal network of neurons. This biological neural network is a sophisticated image processor, capable of compressing information from 100 million photoreceptors into 1 million retinal ganglion cells.

Patients blind from retinitis pigmentosa (RP) and age-related macular degeneration (AMD), 2 prevalent retinal disorders, could regain vision with *MARC* is developed. AMD is the leading cause of blindness in individuals 60 years or older, with 200,000 eyes left legally blind each year. RP has an incidence of 1 in 4,000 and in the US alone afflicts 100,000 people. Currently, no treatment exists for either RP or AMD. We have shown that in these diseases despite near total loss of the photoreceptors, the remaining retinal neurons remain intact. Is there a way to jump-start these remaining awaiting neurons and thus create the sensation of vision?

Experiments

In 15 blind human volunteers tested, we have shown that the remaining neurons in a non-seeing eye can be activated by an electrical signal, resulting in the perception of light. The human tests were performed in an operating room, where, under local anesthesia, different custom-built stimulating microelectrode arrays were placed into the eye of a blind subject and positioned near the retina. Then patterns of electrical signals, generated by an external computer, were applied to the retina via the electrode arrays. The subjects were asked to describe the resultant perceptions. At first, we were concerned and unsure whether we could create one small spot of light that would correspond to the retinal area being stimulated. Once we were able to get patients to see one discrete spot of light localized to the retinal area being stimulated, the next question that needed to be answered was could we create an image by eliciting the perception of multiple spots of light (i.e., akin to how a dot-matrix printer creates images)? Could the brain make sense of more than one artificial signal at a time or would the spots of light merge into an incoherent blur? Using a 25-electrode array, we stimulated at first rows and columns of electrodes and then patterns of electrodes outlining a large letter or simple geometric shapes such as a rectangle. In all our experiments it took several minutes before the patient could confidently identify the artificially created spot of light. Once they recognized the first dot of light they made quick progress. As expected, the 25-electrode array provided poor resolution, however, it was sufficient for all the patients tested to date to see forms such as a large letter and simple geometric shape.

Progress Results

Our human tests have also demonstrated that the artificial vision created by controlled electrical stimulation of the retina has color. Patients have seen yellow, green and blue dots of light although as of yet we do not have a firm understanding on how to reliably elicit seeing one color over another. We could also set the stimulation frequency at a sufficiently high rate so that the perceptions would not flicker like a strobe light but instead appear continuous. Our results from tests in blind human volunteers demonstrate that form vision is possible using controlled pattern electrical stimulation of the retina. In order to determine the degree of visual acuity that is possible with such an approach, an implantable *MARC* is currently being developed so that the patient can become accustomed to processing a new type of visual input.

Concomitant with the human tests, we have been engineering a *MARC*, a completely implantable system capable of creating hundreds of individual spots of light. Specifically, we had to develop a chip that would be small enough to be placed within the eye and yet could stimulate the retina through a large number of electrodes. The retinal stimulation pulse has to excite the neurons but not damage them. To date, we have developed a chip that is 4x4 mm and can stimulate 100 electrodes with a safe and effective charge. This represents a first generation chip and the design of a 625-channel stimulator is progressing. Other system components are also under development. A prototype image acquisition using miniature CMOS camera and image processing system using a VLSI image processing board has been built. Wireless communication electronics using a radio frequency link has been developed and it can supply the required data transmission rate and power coupling. Stimulating electrode materials are being tested to assess their ability to withstand corrosion within the eye.

Of equivalent importance to the engineering development of the device is the biological testing that will show that a retinal implant is well tolerated in the eye. Although intraocular retinal surgical procedures are commonly performed there is no precedence to attaching a device to the delicate, paper-thin retina. The device could tear the retina, cause intraocular bleeding, or dislodge because of eye movements. We have used metal alloy tacks approved by the FDA for intraocular use to secure the implant. In animal experiments to date, the implants have remained affixed to the retina through 11 months and caused no structural of functional damage. Experiments in progress will examine the effects of electrical stimulation on the retina.

Conclusion

The artificial retinal prosthesis is a complex project, bridging the fields of optics, microelectronics, retinal surgery, electrophysiology, and psychophysics. Our team consists of medical doctors, scientists, and engineers each of who brings a unique and necessary experience that will enable the development of the retinal prosthesis system. The initial human tests and engineering developments have generated a great deal of excitement not only in the scientific community but also in the mainstream media. Moreover, because of the quality of our research team and the decade of work that we have invested developing *MARC*, we believe that the first prototype human implant *MARC* will be available in 2-3 years. And while the implantation of a retinal prosthesis would be a significant achievement, it would mark only the start of more research. Expected advances in microelectronics will allow more sophisticated implants. Image processing algorithms will enhance the electronically created perception. The implications of this research may extend beyond this immediate project, as contributions are made to the overall field of chronically implanted prosthetic devices, telemetric monitoring and control, and hermetic packaging. The observations and clinical and engineering experiments performed should lend insight into the actual functioning of the human retina. The feedback gained by these studies should provide a vehicle for further understanding of the retinal/vision/perception process.

References

[1] M. S. Humayun, E. de Juan, J. Weiland, et al., "Pattern electrical stimulation of the human retina," Vision Research, pp. 2569-2576, vol. 39, 1999

[2] W. Liu, M. Humayun, E. de Juan, et al., "Retinal prosthesis to benefit the visual impaired," in *Intelligent System and Techniques in Rehabilitation Engineering*, N. Teodorescu,(Ed), CRC Press, Chapter 2, 2000

[3] J. Wyatt, and J. Rizzio, "Ocular implants for the blind," IEEE Spectrum, pp. 47-53, 1996

[4] A. Chow et al., "The subretinal microphotodiode array retinal prosthesis," Ophthalmic Res. Pp. 195-198, 1998

[5] E. Zrenner, A. Stett, et al. "Can subretinal microphotodiodes successfully replace degenerated photoreceptors?" Vision Research, pp. 2555-2567, 1999

OPTICS COUPLED WITH ELECTRONICS ENABLES IMAGING SYSTEMS WITH PREVOUSLY IMPOSSIBLE PERFORMANCE

W. Thomas Cathey*[+], Edward R. Dowski[+], Gregory E. Johnson*[+], Robert H. Cormack[+], and Hans B. Wach*

The potential advantages of jointly designing a combined optical/digital imaging system have long been known.[1] Only recently, however, have several demonstrations of this been done. These include extending the depth of focus of an imaging system,[2,3,4] aberration invariance,[5,6] passive ranging,[7,8] wide-spectrum imaging, and high-performance single-lens imaging. Progress in designing special optical/digital imaging systems should greatly accelerate with the advent of new design software.

Progress in many applications where misfocus and a range of focus is involved was stimulated by the recognition that the optical transfer function (OTF) of an imaging system can be seen over a region of misfocus in a single plot that is mathematically equivalent to Woodward's ambiguity function.[9][10] Woodward's function can be used to easily visualize the OTF of a one-dimensional imaging system over a large range of misfocus values. This has allowed the mathematical lore that was developed for radar to be used in the analysis and design of imaging systems that use or discard misfocus information. The extension of the depth of focus of an imaging system is an example where the misfocus or depth information is discarded.[2,3,4] In this case, the optical portion of the system is modified so that the OTF of the image acquisition system (the optics) changes very little with misfocus. So, rather than having drastically changing OTFs with nulls at different locations for different portions of an extended object, the OTF essentially does not change and has no nulls. The output of the optical portion of the system, the "intermediate image", is detected and processed to obtain the final image. The digital processing is object independent and, because the OTF is unchanging, independent of object location. The image resolution is unaffected. However, the resulting OTF has spatial frequency regions where the response is lower than the in-focus unaltered system. Consequently, there is a signal-to-noise (S/N) loss in the final image of an extended-depth-of-focus (EDF) imaging system in comparison to a conventional in-focus image. The S/N loss is proportional to the increase in the depth of field.

EDF imaging systems are invariant to misfocus-type aberrations such as lateral chromatic aberration and curvature of field. For example, if red, blue, and green focus in different planes, and each focus is extended, the three focal planes become thick blocks, and overlap. Hence, there is an overlap region where all three colors are in focus.[5,6] Similarly, a curved thin focal surface in curvature becomes a thick arc into which a flat detector array can be fitted.

Hybrid optical/digital imaging systems with an extended depth of field have been used in image-based barcode readers, label readers, and in microscopes.[11,12]

Two types of passive ranging systems have been developed. One is based on range estimation and the modification of the optical portion of the system to have an OTF with periodically spaced zeros.[7] The period of these zeros changes with misfocus, and the application

of spectral estimation to a cluster of pixels that detect a portion of the scene will give an estimate of the misfocus, and hence, the range. The trade-off is that the lateral resolution is reduced. A disadvantage of this approach is that if there are two objects, or an object with parts at several ranges, the system will give a range estimate is a weighted average of the several ranges.

The other approach is to modify the optics so that there is a peak in the OTF as a function of misfocus or range.[8] This peak moves with misfocus, or position of the object. In this case, several range "bins" are created by detecting the energy that lies in the bins. This provides a range detection technique that can detect several objects at different ranges within the portion of the scene that corresponds to the cluster of pixels being processed. Again, the lateral resolution is compromised.

New optical/digital design tools have been developed that are a combination of traditional ray tracing programs to model the optics and custom software to model the interaction between the optics and digital processing. These tools allow both the optics and digital processing portions of the imaging system to be designed and optimized simultaneously.

[1] W. T. Cathey, B. R. Frieden, W. T. Rhodes and C. K. Rushforth, "Image Gathering and Processing for Enhanced Resolution," J. Opt. Soc. Am., Vol. A 1, pp. 241-249 (1984).

[2] E. R. Dowski and W. T. Cathey, "Extended Depth of Field Through Wavefront Coding," Applied Optics, Vol. 34, pp. 1859 - 1866 (1995).

[3] J. van der Gracht, E. R. Dowski, W. T. Cathey, and J. P. Bowen, "Aspheric Optical Elements for Extended Depth-of-Field Imaging" Proc. SPIE, vol. 2537, pp. 279-288 (1995).

[4] Sara C. Bradburn, W. T. Cathey, and E. R. Dowski, "Realizations of Focus Invariance in Optical-Digital Systems with Wave-Front Coding," Applied Optics, Vol. 36, pp. 9157 - 9166 (1997).

[5] E. R. Dowski, Jr., S. C. Bradburn, and W. T. Cathey, "Aberration invariant optical/digital incoherent systems," Japan Optical Review, Vol. 3, Dec. 1996.

[6] Hans Wach, E. R. Dowski, and W. T. Cathey, "Control of chromatic focal shift through wave-front coding," Applied Optics, Vol. 37, pp. 5359 - 5367 (1998).

[7] E. R. Dowski and W. T. Cathey, "Single-Lens, Single-Image, Incoherent Passive Ranging Systems," Applied Optics, Vol. 33, pp. 6762 - 6773 (1994).

[8] Gregory E. Johnson, Edward R. Dowski and W. T. Cathey, "Passive ranging through wavefront coding: information and application," accepted for publication in Applied Optics.

[9] "P. M. Woodward, *Probability and Information Theory with Applications to Radar* (Permagon, New York, 1953).

[10] "K.-H. Brenner, A. Lohmann, and J. Ojeda-Castañeda, "The ambiguity function as a polar display of the OTF," Opt. Commun. 44, 323-326 (1983).

[11] Sara C. Tucker, W. Thomas Cathey, and Edward R. Dowski, Jr., "Extended depth of field and aberration control for inexpensive digital microscope systems

[12] Carol J. Cogswell, M. R. Arnison, W. T. Cathey, E. R. Dowski, and Sara C. Tucker "A new generation, fast 3D fluorescence microscope using wavefront coding optics," Microscopical Society of America's Conf. on Microscopy and Microanalysis '99, Portland, Oregon, 1 - 5 August 1999.

A Fully-Connected, Distributed Mesh Feedback Architecture for Photonic A/D Conversion

B. L. Shoop, P. K. Das, E. K. Ressler, R. W. Sadowski, G. P. Dudevoir, and A. H. Sayles.
Photonics Research Center and Department of Electrical Engineering and Computer Science
MADN-PRC, United States Military Academy, West Point, New York 10996
Barry-Shoop@usma.edu

Analog to digital (A/D) conversion is an important component in any system, which must sense the natural environment and process that information using digital techniques. Because of the difficulty in achieving both high-resolution and high-speed A/D converters, this A/D interface has been and continues to be a barrier to the realization of high-performance systems. Photonic approaches to A/D conversion provide many advantages including high-speed sampling sources with extremely low clock jitter, ultra-fast nonlinear optical device switching, decoupling of the sampled and sampling signals when the sampled signal is electronic and the sampling signal is optical, and the inherent parallelism that optics provides. Here we report a new approach to photonic A/D conversion using a distributed neural network, oversampling techniques, and a smart pixel hardware implementation. In this approach, the input signal is first sampled at a rate higher than that required by the Nyquist criterion and then presented spatially as the input to a two-dimensional error diffusion neural network consisting of M ×N neurons, each representing a pixel in the image space. The neural network processes the input oversampled analog image and produces an M×N pixel binary or halftoned output image. By design of the neural network, this halftoned output image is an optimum representation of the input analog signal. Upon convergence, the neural network minimizes an energy function representing the frequency-weighted squared error between the input analog image and the output halftoned image. Decimation and low-pass filtering techniques, common to classic one-dimensional oversampling A/D converters, digitally sum and average the M×N pixel output binary image using high-speed digital electronic circuitry. By employing a two-dimensional smart pixel neural approach to oversampling A/D conversion, each pixel constitutes a simple oversampling modulator thereby producing a distributed A/D architecture, shown in Figure 1. Spectral noise shaping across the array diffuses quantization error thereby improving overall signal-to-noise ratio (SNR) performance. Here, each quantizer within the network is embedded in a fully-connected, distributed mesh feedback loop which spectrally shapes the overall quantization noise thereby significantly reducing the effects of component mismatch typically associated with parallel or channelized A/D approaches. The two-dimensional neural array provides higher aggregate bit rates which can extend the useful bandwidth of photonic-based, oversampling A/D converters.

Figure 1. Fully-connected, distributed oversampling A/D converter architecture.

The performance of this distributed approach to A/D conversion can be described in several different ways. The SNR can be shown to be

$$SQNR_{max}(M,N) = \frac{3}{2} \cdot \frac{2N+1}{\pi^{2N}} \cdot M^{2N+1},\tag{1}$$

where M is the oversampling ratio and N is the order of the error diffusion filter. This equation describes the performance of an Nth-order oversampling modulator, part of an oversampling A/D converter. The difference here is that the oversampling ratio is proportional to the output image size and therefore can be larger than classic oversampling ratios. Component mismatch effect tolerance can be quantified by considering the error diffusion neural network performance under these conditions. As an example, the effect of threshold mismatch across the array can be characterized as a modification to the neural network energy function according to

$$E = (\mathbf{y} - \mathbf{x})^T \mathbf{A}(\mathbf{y} - \mathbf{x}) + \mathbf{e}_t^T \mathbf{A}^{-1} \mathbf{e}_t - 2\mathbf{e}_t^T (\mathbf{y} - \mathbf{x}),\tag{2}$$
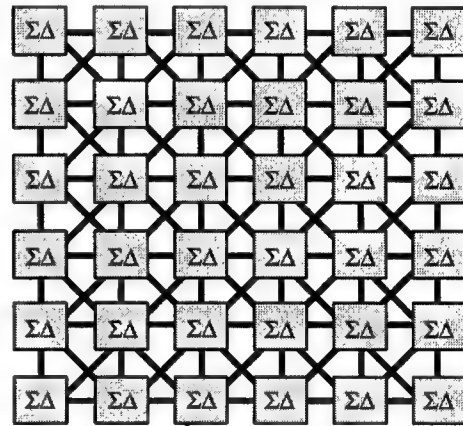
where ε_t is a vector containing the threshold mismatch of the array. This first term in Eq. (2) is the same as in the original error diffusion neural network. The last two terms are contributions from threshold mismatch. The matrix **A** is derived from the error diffusion filter weights and has high-pass spectral characteristics. Eq. (2) demonstrates that the contribution of the threshold mismatch to performance is spectrally-shaped by the error diffusion filter thereby reducing the overall impact.

In contrast to the majority of current smart pixel research, the architecture reported here is a mixed signal application of smart pixel technology. The optoelectronic circuitry for a proof-of-concept 5 ×5 error diffusion neural network was implemented in 0.5 μm silicon CMOS technology requiring the functionality of one-bit quantization, subtraction, neuron-to-neuron weighting and interconnection, and optical input and output. Figure 2 shows the circuitry associated with a single neuron of this error diffusion neural network implemented using CMOS-SEED smart pixel technology. Here, the one-bit quantizer is implemented using a wide-range transconductance amplifier operated in the subthreshold regime. The slope of this sigmoidal function was carefully designed by matching MOSFET transistors to meet the convergence criteria and the nonlinear dynamics of the error diffusion neural network. All state variables in this circuit are represented as currents and therefore the subtraction functionality was implemented using current summation techniques at specified nodes. The error weighting and distribution circuitry for the 5 ×5 array was implemented in silicon circuitry by designing and matching the width-to-length ratios of both the individual and stage-to-stage MOSFET transistors. Bi-directional error currents were implemented to provide the circuitry and the network with fully-symmetric performance. Optical input and output to each neuron was implemented using SEED multiple quantum well (MQW) modulators. The input MQW is reverse-biased and functions as an optical detector while the output optical binary signal is produced using a forward biased MQW, which provides photoemission through electroluminescence.
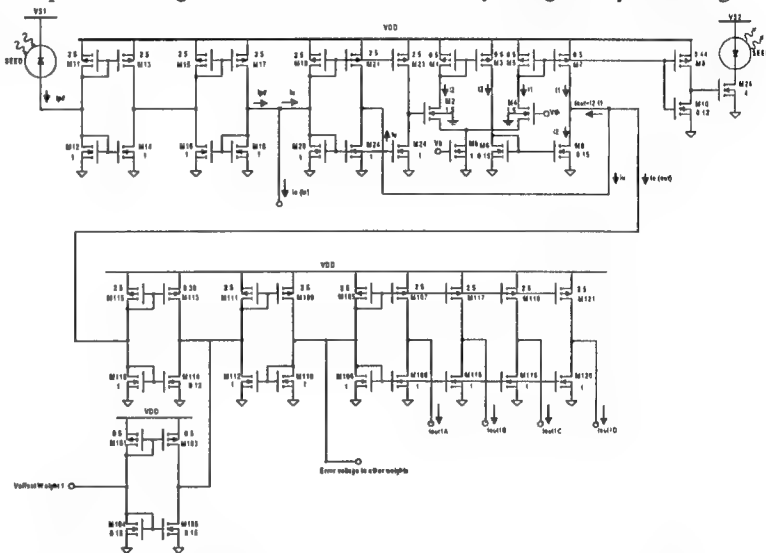

Figure 2. Circuit diagram of a single neuron and a single error weight of a 5×5 CMOS-SEED error diffusion neural network smart pixel architecture.

The central neuron of the smart pixel array consists of approximately 160 transistors while the complete 5 ×5 array accounts for over 3600 transistors. The central neuron is interconnected to the surrounding 24 neurons in the 5x5 array using a fixed interconnect and weighting scheme. SPICE simulations of each of the functional components as well as the complete 5 ×5 nonlinear dynamical neural network were performed using transistor parameters extracted from a previous 0.5 μm MOSIS foundry run and have verified both functional operation as well as overall network performance. Individual component functionality was experimentally characterized and dynamic operation of the full 5x5 neural array was also experimentally characterized. Figure 3 shows a CCD image of the operational array under 50% gray-scale condition. Dynamic stimulus of single and multiple neurons was also conducted and demonstrated correct error diffusion and network operation.
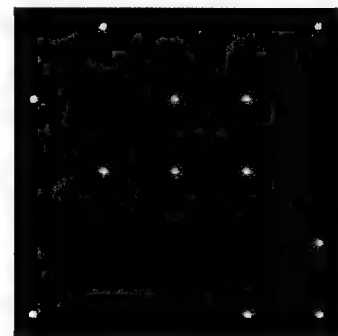

Figure 3. CCD image of 5×5 smart pixel array under 50% gray-scale conditions.

A Configurable Architecture for Smart Pixel Research

J. F. Cantin and F. R. Beyette Jr.

University of Cincinnati
Department of ECECS
PO Box 210030
Cincinnati OH, 45221-0030
beyette@ececs.uc.edu

ABSTRACT

We proposed a general purpose, smart pixel based photonic information processing architecture comprised of RISC processing pixels and a reconfigurable micro instruction store. Implemented with a photonic VLSI technology the device is suitable for prototyping photonic information processing systems.

SUMMARY

In the past decade, the development of smart-pixel device technologies has fueled the promise for information processing systems that would merge the areas of optical imaging and information processing.[1] As illustrated by the development of data processing systems, [2,3] application of smart pixel technology has gone beyond the design of smart image processing systems. Currently, the trend is towards the development of photonic VLSI technologies that combine the massive parallelism and high data transfer rates associated with photonic device and the high density, reliable and cost effective information processing capabilities associated with CMOS logic circuitry.[4]

While photonic VLSI chips enable unprecedented functionality, designing devices with integrated optical and electronic components is not trivial. Beyond providing functionality, optimization of chip performance requires consideration of several factors including: information loss associated with the conversion between the two forms of energy, the disparity between optical and electronic switching speeds, and the size mismatch between optoelectronic devices and CMOS transistors. Often individual pixel space is constrained by the need to fit a large array of pixels onto a single chip.

For these reasons and others, smart-pixel systems based on photonic VLSI devices are typically implemented as custom designed ASIC's that are well optimized for a target application. This approach can produce component designs that offer superior performance and efficiency over conventional processors and software. However, the design and implementation of these special purpose chips can also be very time consuming and costly. Thus, custom designed photonic VLSI systems are not well suited for photonic test-bed systems where information processing algorithms and system architectures can be refined through the use of a rapid prototyping research and experimentation environment.

To overcome these difficulties, we have proposed a generic information processing architecture based on smart pixel concepts implemented in a photonic VLSI device technology. We will refer to this architecture as CASPR (Configurable Architecture for Smart Pixel Research).

Conceptually, the CASPR architecture is comprised of an array of small, optically accessible, reduced instruction set computer (RISC), pixels that are controlled through a user programmable instruction set that is stored on the CASPR chip. Thus, the CASPR architecture provides a generically programmable smart pixel environment that can be configured for a variety of photonic information processing applications. Further, the CASPR design is simple enough that a large pixel array can fit on a single CMOS chip.

As shown in Figure 1, each CASPR processing cell contains a photodetector for receiving data, some storage in the form of registers or RAM, a simple ALU and a network interface to facilitate communications outside of the pixel. Each smart pixel element can perform computations on the data in its internal storage, the data received from other pixels and/or the optical data sampled through the photoreceiver. The network interface allows pixels to communicate and pass data in a number of ways, in addition to allowing a host computer to issue instructions to designated cells. Thus, each cell (or pixel) can receive data optically and process that data with the help of the other cells in the array.

The processing elements are controlled in a partitionable-SIMD fashion that dose not restrict all cells to execution of the same instruction. Rather, we relax that restriction of
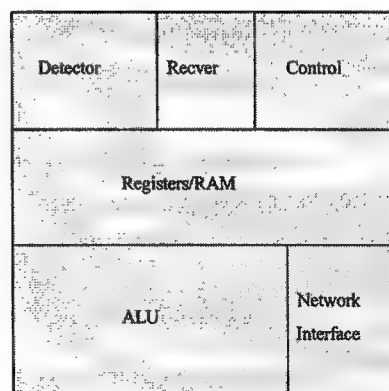

Figure 1 Block Diagram of a CASPR smart pixel. These devices can be tiled to form and array of generically programmable smart pixel based photonic information processing system.

conventional SIMD architectures[5] by allowing instructions from the host computer to be directed at specific cells or collections of cells based on a simple addressing scheme. Sending commands to the entire array can perform vector operations, while sending commands to selected cells (via an address and a mask) allows for different control paths between cells. Predication allows any given cell to ignore certain instructions based on its current state. Predication of instructions provides a simple form of conditional execution, without the need for multiple instruction streams.

To further improve flexibility, the instruction set visible to the host computer is not defined by the architecture [6]. A programmable control store (implemented as a cache) is located on each CASPR chip to map incoming instructions to control signals (an expanded microinstruction format) before broadcasting them to all the cells within. The contents of the control store can be configured such that the user can define and optimize an instruction set for the application of interest. This allows the encoding of instructions such that the CASPR chip can serve as a real-time prototyping device while using the same interface as a more specialized device. Further, the instruction set can be reconfigured during execution time to add specialized instructions as needed [7].

The advantages of the proposed architecture are generality, and flexibility. Devices that implement this architecture are not optimized for a single application, rather a set of applications ranging from optical computing to optical storage and communication. Specifically, any task that involves receiving pages of digital data from an optical source, processing the data in parallel, and returning results to a host computer. By means of the host computer, the user can define an instruction set, and program the device for the desired task. Since it is possible to construct both optical detectors and logic circuits on one monolithic chip in a commercial CMOS process [2], CASPR devices can be developed for a minimal cost. Researchers can then use this device to rapidly prototype and test other designs (and the systems that incorporate them) without the effort and expense of developing an ASIC. The device can be reused as needed, and serve as a platform for prototyping a variety of smart-pixel devices.

Figure 2 illustrates a possible photonic system test-bed environment suitable for prototyping smart pixel based photonic information processing systems. In this configuration optical data is passed to the CASPR chip from either a page-oriented optical storage device or a spatial light modulator (SLM) that is controlled by a host computer. The CASPR chip processes the optical data along with data held in each pixel and produces electrical output signals that are passed into the electrical host computer. The host computer uses the electrical output signals from the CASPR chip to drive the SLM producing a new set of optical input data for the CASPR chip. Thus, figure 2 represents a recirculating photonic information processing architecture that would allow for the evaluation of a variety of data processing applications including data sorting, data filtering, and matrix manipulation systems. Finally, in a more generic implementation, the straight pass optical interconnect between the SLM and the CASPR chip could be replace with a more complex
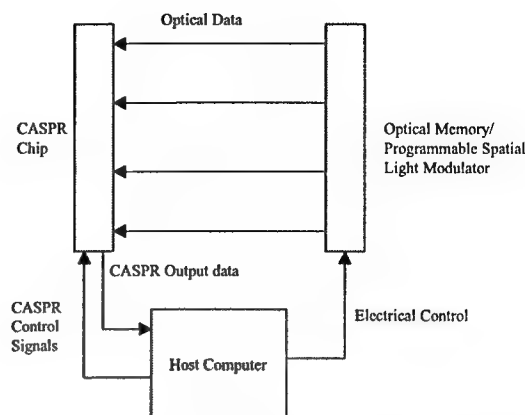

Figure 2 One possible prototyping environment suitable for evaluation of photonic information processing systems based on the CASPR chip.

interconnection network allowing for implementation/testing of more sophisticated photonic information processing systems.

In conclusion we have proposed a reconfigurable photonic information processing chip based on a photonic VLSI device technology. A test chip is currently being fabricated through the MOSIS CMOS foundry service. Details of the pixel design and operational results will be presented in the near future.

REFERENCES

[1] N. M. Jokerst and A. L. Lentine, "Introduction to the Special Issue on Smart Pixels", IEEE J. Selct. Topics in Quant. Elect., Vol. 2, No. 1, pp. 1-2, April 1996.

[2] F. R. Beyette, Jr. P. J. Stanko, S. A. Feld, P. A Mitkas, C. W. Wilmsen, K. M. Geib, and K. D. Choquette, "Demonstration and Performance of a CMOS/VCSEL Based Recirculating Sorter", Opt. Engineering, Vol. 37, No. 1, pp. 312-319, Jan. 1998.

[3] D. M. Chiarulli and S. P. Levitan. Optoelectronic-cache Memory System Architecture. Applied Optics, vol. 35, # 14, pp. 2449-2456, May 1996.

[4] H. Cat, M. Lee, B. Buchanan, D. S. Wills, M. Brooke, and N. M. Jokerst. Silicon VLSI Processing Architectures Incorporating Integrated Optoelectronic Devices. *Proceedings of the 16th Conference on Advanced Research in VLSI*, pp. 17-27, Chapel Hill, North Carolina, Mar. 1995.

[5] K. Kreeger and A. Kaufman. PAVLOV: A Programmable Architecture for Volume Processing. *Proceedings of the 1998 Workshop on Graphics Hardware*, pp. 77-85, Lisbon, Portugal, Aug. 1998. ACM.

[6] A. Huang and E.H. Kim, ReRISC: A Reconfigurable Reduced Instruction Set Computer. *Department of EECS, Massachusetts Institute of Technology, Cambridge.*

[7] M. Wirthlin and B. Hutchings, Sequencing Run-Time Reconfigured Hardware with Software. Proceedings of the 1996 ACM Fourth International Symposium on Field-programmable Gate Arrays, 1996, Page 122.

A Partitioning Scheme for Optoelectronic Neural Networks

T. D. Wagner, D. A. Nash, J. R. S. Blair, E. K. Ressler, B. L. Shoop
Department of Electrical Engineering and Computer Science
Photonics Research Center
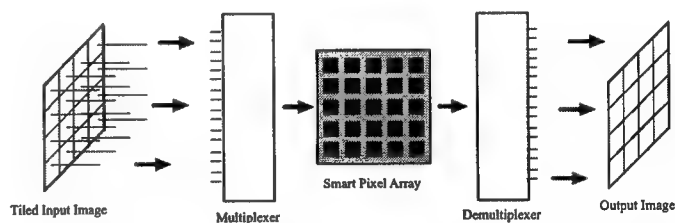MADN-EECS, United States Military Academy, West Point, NY 10996
Tommy-Wagner@usma.edu

Digital image halftoning, often referred to as spatial dithering, is the transformation of a continuous-tone input image into a binary-valued output image. Digital halftoning is particularly important to applications such as laser printing, bilevel displays, xerography, and facsimile. Error diffusion is an important class of digital halftoning transformations in which the error associated with a single pixel is diffused within a local region for the purpose of improving overall halftoning quality. Classical error diffusion algorithms are unidirectional and consequently introduce visually objectionable artifacts in the halftoned images. Recently, a fully symmetric approach to error diffusion based on a neural network has been investigated and implemented.[1] This new approach to halftoning has demonstrated improved halftone quality over other existing algorithms. The limitation in this approach is the speed of convergence of the neural network for reasonably-sized images. As a result, hardware architectures of this error diffusion network (EDN) are being investigated which provide sufficient switching speed and connectivity to generate real-time halftone images.

Smart pixel technology provides a promising technological alternative for the implementation of the EDN because optical input, electronic processing, and optical output are integrated in a single array. While current smart pixel technology could support 256×256 array sizes, it is of interest to investigate partitioning approaches which use smaller physical array sizes to achieve the same functionality and performance as larger arrays. One approach to this partitioning is to divide a large image into smaller sub-images, multiplex these sub-images into a small smart pixel EDN, and then demultiplex the partitions into the resulting full-sized image. This concept is shown graphically in Figure 1.

There are a number of conceivable approaches to the partitioning of the image. Simple tiling, in which the input image is segmented into N sub-images, each being processed independently of the other, produces undesirable artifacts in the resulting halftones. Figure 2(a) demonstrates this result. Like other neural networks, the EDN requires interconnections to neighboring pixels to accomplish the halftoning. Since there is no tile-to-tile communication, the error diffusion region is restricted and the diffusion to neighboring tiles is lost. The result is the visually objectionable horizontal and vertical banding seen in Figure 2(a).

Figure 1. Partitioning approach to error diffusion halftoning using a smart pixel array.

In research reported elsewhere, several alternatives to simple tiling were investigated.[2] The method that was found to be most successful was to constrain the pixels along the outside of a tile as it was being halftoned. The values used as constraints were the values of the pixels that resulted from halftoning neighboring tiles. For example, once the tile in the upper-left corner of an image has been halftoned, the tile immediately to the right was selected. Instead of constructing a tile of the same dimensions, the horizontal dimension was increased to include a band of pixels from the previously halftoned tile to the left. That band was fixed, or not allowed to change as the EDN halftoning of the second tile proceeded. This tied the result of halftoning the second tile to the the completed halftone of the first tile. Except for the constrained band, the smart pixels of the EDN were allowed to converge normally. Details of this technique's performance remain to be studied, but the initial results showed visually pleasing output from several different classes of input imagery. Figure 2(b) shows a result of this constrained tiling approach.

(a) Simple tiled halftone   (b) Constrained tiled halftone

Figure 2. Halftones produced by tiling.

This EDN approach to halftoning is an extension of work originally reported by Anastassiou.[3] He first defined a frequency-weighted mean square error distortion measure based on the frequency response of the human visual system and then showed that minimizing this metric was analogous to minimizing the energy function in a classical Hopfield-type neural network. In equilibrium, the error diffusion neural network satisfies $\mathbf{u} = \mathbf{W}(\mathbf{y} - \mathbf{u}) + \mathbf{x}$. For an $n \times m$ image, $\mathbf{W}$ is an $n^2 \times m^2$ sparse, nearly circu-

Figure 3. Equivalence of EDN(b) to Hopfield net(a).

lant matrix derived from the original $q \times q$ set of error diffusion weights $w_{i,j}$. An equivalence to the Hopfield network can be described by $\mathbf{u} = \mathbf{A}(\mathbf{W}\mathbf{y} + \mathbf{x})$, where $\mathbf{A} = (\mathbf{I} + \mathbf{W})^{-1}$. Effectively, the error diffusion network includes a pre-filtering of the input image $\mathbf{x}$ by the matrix $\mathbf{A}$ while still filtering the output image $\mathbf{y}$ but now with a new matrix, $\mathbf{AW}$. Consequently the EDN is equivalent to a certain class of Hopfield networks, as shown in Figure 3. The partitioning of large neural networks described here is potentially applicable to other applications of optoelectronic neural networks, notably signal processing[4] and pattern recognition.[5]
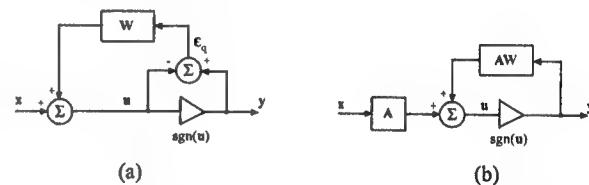
REFERENCES

1. E. K. Ressler and B. L. Shoop, "Analysis and design of error diffusion networks for digital halftoning," in *Proceedings of the 20th Army Science Conference*, pp. 267–271, (Norfolk, Virginia), June 1996.

2. J. R. S. Blair, T. D. Wagner, D. A. Nash, E. K. Ressler, B. L. Shoop, and T. J. Talty, "Partitioning schemes for use in a neural network for digital image halftoning," *Proc. of the SPIE, Applications and Science of Computational Intelligence III* **4055**, 2000.

3. D. Anastassiou, "Error diffusion coding for A/D conversion," *IEEE Trans. Circuits Syst.* **36**(9), pp. 1175–1186, 1989.

4. J. Hwang, S. Kung, M. Mahesan, and J. C. Principe, "The past, present, and future of neural networks for signal processing," *IEEE Signal Processing Magazine* **14**(6), pp. 28–48, 1997.

5. A. A. Sunao Kakizaki, Paul Horan, H. Sako, A. Saito, and F. Kugiya, "Optical implementation of a translation-invariant second-order neural network for multiple-pattern classification," *Applied Optics* **33**, pp. 8270–8280, December 1994.

Optoelectronic Page-Oriented Database Filter Based on a Single Chip Photonic VLSI Design

J. Tang, B. K. Lee, R. C. J. Chi, A. J. Steckl and F. R. Beyette Jr.

University of Cincinnati
Department. of ECECS
PO Box 210030
Cincinnati, OH 45221-0030 USA
beyette@ececs.uc.edu

ABSTRACT

A database filter suitable for accessing optical storage devices is presented. This photonic VLSI chip includes a smart pixel array that selects words matching a search criterion and control circuitry that interfaces the filter chip with an electronic host computer.

SUMMARY

The commercialization of CD ROM drives has clearly demonstrated the ability of optical storage devices to meet the current demand for archival data storage. However, with the continued expansion of electronic information resources, storage capacity requirements are expected to approach the terabit level for personal users and exceed the petabit level for database and data warehouse systems.[1] Further, many data intensive applications will continue to require real time data access rates. Thus, system designers for the next generation of archival storage system have the challenging task of providing storage capacities several orders of magnitude larger than existing systems while maintaining current data access times.
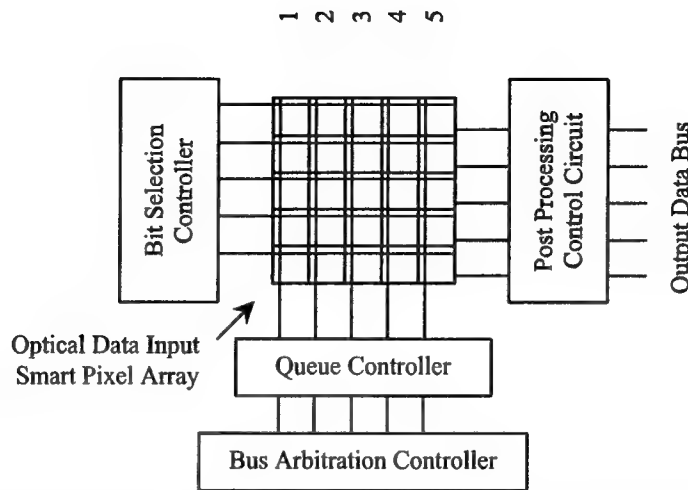
While considerable effort has been put toward the development of optical storage media capable of providing high capacity, volumetric data storage, relatively little work has been done to explore the technological barriers associated with providing page-oriented access to these memory devices. In particular, issues related to the bandwidth mismatch between a page-oriented optical memory and word-oriented electronic computer have not been addressed. More specifically, high capacity, high data rate, page-oriented optical storage devices do not address the bottle neck associated with getting data into the microprocessor of database management computer.
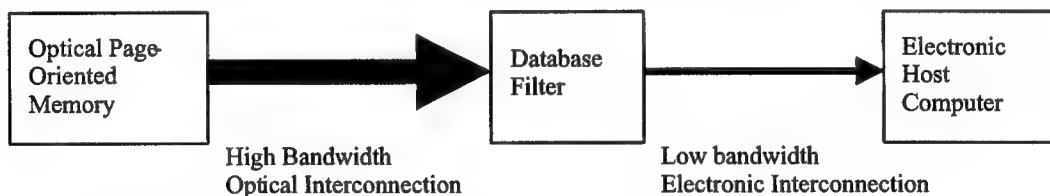
Figure 1 Block diagram of a database filter in the hierarchy of a memory access sub-system.

The concept of database filter has been suggested as a solution to this problem in database management systems.[2] As shown in Figure 1, a database filter is an optical memory interface device that accepts large bandwidth data from the page-oriented optical storage device, and produces word-oriented output at a data rate compatible with the electronic host computer. To accommodate the data rate mismatch between the storage device and the electronic host computer, the database filter preprocesses the optical input data by searching for words that match a user defined search criteria. Thus, the filter can pass only valid data along the low bandwidth connection to the electronic host.

Over the last few years, we have been developing smart read-head devices for large capacity, page-oriented optical storage systems.[3,4] Here we present the photonic VLSI design and initial circuit evaluations for our latest data filter design. Intended to function as a smart optical memory read head device, the database filter we present here

1 2 3 4 5

Bit Selection Controller

Post Processing Control Circuit

Output Data Bus

Optical Data Input
Smart Pixel Array

Queue Controller

Bus Arbitration Controller

Figure 2 Block digram of the optoelectronic database filter. The central grid area is a smart pixel array that accepts optical page-oriented data and executes the search operation. Valid data is held in the smart pixel array until access is granted to the external bus.

will extend the capabilities of conventional read head technology by including on-the-fly relational database processing integrated into the read head of a page-oriented optical memory system.

A conceptual view of the latest database filter design is shown in Figure 2. The Optical Data Input Smart Pixel Array reads optical data from a page-oriented optic storage device. Data is organized in this array with each column representing an individual word in the memory. Control signals provided by Bit Selection Controller allow each pixel to evaluate if its data bit matches the data selection criteria. The results from individual bit comparisons are summed along each word. If the result of the bit summation indicates that a word matches the selection criteria then the Data Queue Controller loads the word into an asynchronous data queue located in the smart pixel array. A Bus Arbitration Controller is used to control data flow between the individual word queues and the Post Processing Control Circuit. The Post Processing Control Circuit performs word based data manipulation operations including data projection and data formatting.

Based on a photonic VLSI device technology, our database filter monolithically integrates all necessary optoelectronic and logic components into a single CMOS chip that can be readily fabricated using standard VLSI fabrication facility. Thus, our data filter is, compact, readily integrated into optical storage read head designs, compatible with existing electronic device manufacturing technology and shares all of the reliability, uniformity, and manufacturability benefits associated with current electronic hardware.

In this paper we will present an evaluation of our latest smart pixel circuits and detail the performance of individual components of the database filter. Finally, we present our expectations for a 16x16 bit database filter currently under development.

REFERENCES:

[1] F. B. McCormick, "Optical MEMS potentials in optical storage", IEEE/LEOS Summer Topical Meeting on Optical MEMS, pp. 5-7, July 1998, Monterey CA.

[2] P. B. Berra, A. Ghafoor, P. A. Mitkas, S. J. Marcinkowski, and M. Guizani, "The impact of Optics on data and knowledge base systems", IEEE Transactions on Knowledge and Data Engineering, Vol. 2, No. 1, pp. 24-34, April 1996.

[3] J. Tang, B. Sheshadri, K. N. Naughton, B. K. Lee, R. C. J. Chi, A. J. Steckl and F. R. Beyette Jr., "CMOS Based Photoreceiver Arrays for Page-Oriented Optical Storage Access", submitted to IEEE Photon. Tech. Lett., January 2000.

[4] C. Kanyuck, M. Slutz, and F. R. Beyette Jr., "CMOS Based Optoelectronic Smart Pixel Array for Accessing Optical Page-Oriented Memories", IEEE/LEOS Summer Topical Meeting on Smart Pixels, pp. 37-38, July 1998, Monterey CA.

AUTHOR INDEX

Nakahara, T.	MA3.2	Sugihwo, F.	MA2.3
Naruse, M.	TuA2.3	Swedenkrans, G.	MA3.4
Nash, D.	WA2.4	Tan, K.	MA4.3
Nayar, S.	WA1.1	Tang, J.	WA1.3, WA2.5
New, N.	MA4.4	Tateno, K.	MA3.2
Newsam, M.	MA3.4	Thienpont, H.	MA4.2
Neyer, A.	MA4.2	Trezza, J.	MA3.1
Ng, S.	MA1.4	Tsuda, H.	MA3.2
Ooi, B.	MA1.4	Underwood, I.	MA3.4
Oton, J.	MA3.4	Vass, D.	MA3.4
Parker, T.	MA4.3	Van Campenhout, J.	MA4.2
Quintana, X.	MA3.4	Van Koetsem, J.	MA4.2
Rampin, M.	MA3.4	Vanwassenhove, L.	MA4.2
Redmond, M.	MA4.3	Villemoes, L.	TuA2.5
Ressler, E.	WA2.2, WA2.4	Vounckx, R.	TuA2.4
Robertson, B.	MA4.3	Vrazel, M.	MA3.5
Rooman, C.	TuA2.4	Wach, H.	WA2.1
Sadowski, R.	WA2.2	Wagner, T.	WA2.4
Sawchuk, A.	TuA1.1	Wallrabenstein, A.	TuA2.1
Sayles, A.	WA2.2	Warr, S.	MA4.3
Schrage, J.	TuA2.1	White, H.	MA4.3
Seo, S.-W.	WA1.2	Wilkinson, T.	MA4.3, MA4.4
Seshadri, B.	WA1.3	Windisch, R.	TuA2.4
Shoop, B.	WA2.2, WA2.4	Wittmann, B.	MA4.2
Stace, C.	MA4.3	Woolley, R.	MA4.3
Steckl, A.	WA1.3, WA2.5	Wu, R.	MA3.3
Stenger, V.	TuA2.2	Zeng, Q.	MA3.3
Strake, E.	TuA1.2	Zhou, Y.	MA1.4
Stoustrup, J.	TuA2.5	Zenklusen, P.	MA4.2

2000 IEEE/LEOS
Summer Topical Meeting

24 - 26 July 2000

Optical Sensing in
Semiconductor Manufacturing

Turnberry Isle Resort & Club
Aventura, FL

Optical Sensing in Semiconductor Manufacturing

Chair:

Kris Bertness, *NIST*, Boulder, CO

Technical Program Committee:

H. Anderson, *University of New Mexico*, Albuquerque, NM
J. Dadap, *Columbia University*, New York, NY
J.T. Hodges, *NIST*, Gaithersburg, MD
J.L. Lentz, *Lucent Technologies*, Breinigsville, PA
C.J. Miner, *Nortel Networks*, Ottawa, ON, Canada
C.J. Raymond, *Bio-Rad CD Systems*, Albuqueque, NM
R.N. Sacks, *Ohio State University*, Columbus, OH
W. Walecki, *Oriel Corporation*, Stratford, CT

TABLE OF CONTENTS

Monday, 24 July 2000

Tuesday, 25 July 2000

Wednesday, 26 July 2000

Optical Sensing in Semiconductor Manufacturing

Monday, 24 July 2000

MB1: Detection of Trace Impurities in Gases I
MB2: Detection of Trace Impurities in Gases II
MB3: Gas Diagnostics for Semiconductor Processing
MB4: Reflectance Monitoring

An IR tunable diode laser absorption spectrometer for trace humidity measurements at atmospheric pressure

CS Edwards[1], GP Barwood[1], P Gill[1], M Stevens[1], B Schirmer[2], R Benyon[3] and P Mackrodt[4]

[1]National Physical Laboratory, Queens Road, Teddington, Middx TW11 0LW
[2]University of Erlangen-Nürnberg, Cauerstrasse 4, D-91058 Erlangen, Germany
[3]Instituto Nacional de Tecnica Aerospacial, Ctra. a Ajalvir, km4, E-28850, Torrejon de Ardoz Spain
[4]Physikalisch-Technische Bundesanstalt, Bundesallee 100, D-38116 Braunschweig, Germany

Introduction

There is an increasing demand for the measurement of trace humidity in air at levels down to a few parts in 10^9 (ppb$_v$) at atmospheric pressure. This summary describes the development by a 6-member European collaboration of a diode laser absorption spectrometer capable of measuring trace humidity with an uncertainty of 5 ppb. The diode laser was a distributed feedback device, tuned to the 3,0,3 ← 2,0,2 rotation transition in the $v_1 + v_3$ vibrational band of water vapour at 1393 nm [1].

Three different spectroscopic techniques were investigated, namely wavelength modulation spectroscopy, single frequency modulation spectroscopy and two-tone frequency modulation spectroscopy (TTFMS). Of these methods, TTFMS combines the advantages of being the most sensitive technique and is relatively straightforward to implement. After a number of refinements to the optical layout, TTFMS features were obtained with no observable background interference effects. Figure 1 shows a scan with a signal to noise ratio on the strongest feature of 5600. This scan was obtained in 0.4 m of laboratory air at ambient pressure and humidity (≈50% relative humidity, equivalent to a concentration of 1.2×10^4 ppm).
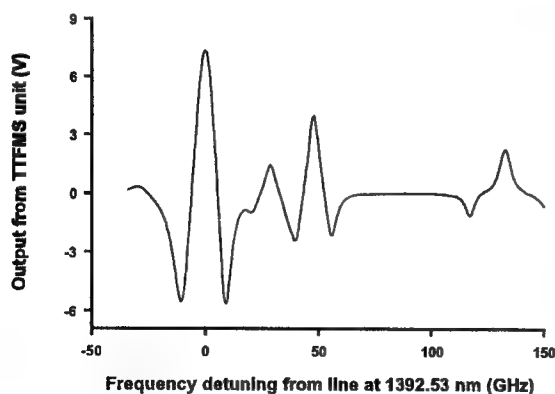
Figure 1: TTFMS spectrum obtained in 0.4 m of laboratory air at ambient humidity.

In order to provide a facility for trace humidity measurement, a multi-pass White cell was manufactured. The spectrometer design is shown in figure 2, and both free space and fibre pig-tailed versions of the input optics were built. The mirror separation in the cell was 0.25 m, and a 10-m optical path length was obtained by passing the beam 40 times through the cell. The peak TTFMS signal size varies linearly over a wide range of water vapour concentrations. This allows verification of the spectrometer in the region above 1 ppm where certified humidity measurement is possible. The TTFMS signal
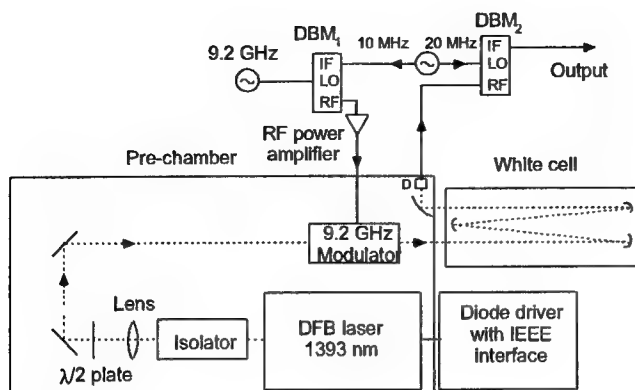
Figure 2: Diode laser spectrometer and multi-pass White cell. The diode laser driver was computer controlled.

size may then be extrapolated down. The spectrometer has currently undergone tests at the four humidity standard laboratories of the partners in the consortium [2].

The diode laser is computer-controlled via an IEEE interface and current-scanned over the absorption feature to determine the peak TTFMS signal. The TTMFS results were read by the computer via an analogue to digital input card. Multiple scans over the line were used and a curve fitting routine implemented in order to improve on the sensitivity and reproducibility. The software controls a voltage output from the PC which varies linearly with the water vapour concentration, with a reproducibility of 5 ppb. The concentration is also displayed on the screen and the data recorded as a function of time on disc.

Acknowledgement: The authors acknowledge the support of the European Union under contract SMT4-CT96-2125.
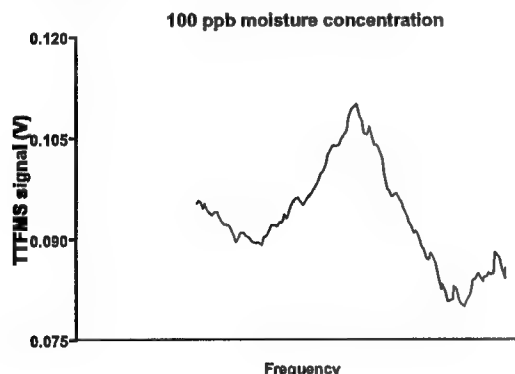
Figure 3: TTFMS signal from the ASTHMEG spectrometer at a 100 ppb water vapour concentration

References

1. CS Edwards, GP Barwood, P Gill, B Schirmer, H Venzke and A Melling, Applied Optics, 4699-4704 (1999) and references therein.
2. B Schirmer, H Venzke, A Melling, CS Edwards, P Gill, M Stevens, R Benyon, P Mackrodt, Measurement Science and Technology (accepted, 2000)

A Trace Gas Measurement Device Using Cavity Ring-Down Spectroscopy

Wen-Bin Yan, Yei Wo, MEECO, Inc., 250 Titus Avenue, Warrington, PA 18976
John Dudek, Paul Rabinowitz, Kevin Lehmann, Dept. of Chemistry, Princeton University,
Princeton, NJ 08544

Summary

Since 1995, MEECO, Inc., in collaboration with Professor Lehmann of Princeton
University, has been developing Cavity Ring-Down Spectroscopy (CRDS) for trace gas
measurement. This work provided the first demonstration that CRDS could be used with
highly attractive continuous wave (CW), semiconductor diode lasers. As a result,
Princeton University was awarded a patent that covers the use of any cw laser excitation
in CRDS. CW, single-mode semiconductor diode lasers make CRDS commercially
viable, thanks to their small size, low power requirements, long lifetime, monolithic
construction, and modest cost.

MEECO's first CRDS-based commercial product, MTO-1000 will be introduced mid-
2000. The initial target species for measurement is moisture, an important contaminant
in high-purity process gases used in the semiconductor industry. A critical factor in
achieving acceptable product yields with ever-smaller geometry chips is maintenance of
ultra-low contamination in semiconductor process gases. It has been established, for
instance, that moisture contamination levels of even a few parts per billion by volume
(ppb) can result in defects on silicon wafers. To offset the damages caused by the
presence of moisture in process gas lines, manufacturers call on gas suppliers to
guarantee moisture in semiconductor-grade gases at levels no greater than a few ppb.
Very few convenient analytical methods are presently available to measure residual water
vapor at such levels.

The basic operating principle of MTO-1000 is based on absorption spectroscopy, which
provides the most general spectroscopic method for detection of important trace
species. It is an absolute measurement method requiring no calibration. In the gas
phase, the spectrum of a molecular species consists of many sharp rotational lines that
provide high selectivity (a molecular 'fingerprint'). In a conventional absorption
measurement, the intensity of light transmitted through a sample is compared to the
transmission without the sample. The sensitivity and accuracy is often limited by the
amplitude noise of light sources and the detection system. CRDS, on the other hand, is
not affected by the laser noise because it only measures ring-down time. CRDS also
dramatically increases the sensitivity of absorption spectroscopy because its effective
absorption pathlength can be as long as 10^5 of the physical length of the cell.

The schematic of MTO-1000 is shown in Figure 1. With a one meter cavity and a 1.39
µm diode laser, we have measured ring-down time as long as 300 µs, which
corresponds to a pathlegth of 90 km. This device is capable of measuring 500 ppt of
moisture accurately in ultra-pure gases.

Through its new Tiger Optics subsidiary, MEECO is also developing this technology to measure a wide range of critical molecules, such as CO, NH_3, HF, HCl, CH_4. Future capabilities will be discussed in detail at the meeting.
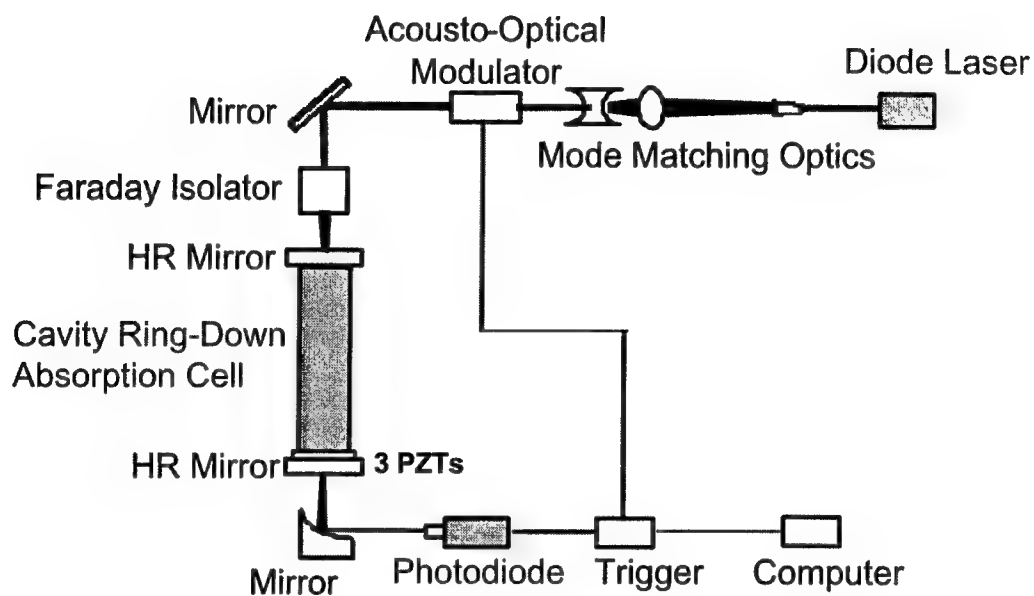
Figure 1. Schematic of MTO-1000

Application of Diode Laser Spectroscopy for Moisture Contamination Measurement in Semiconductor Processing

James McAndrew, Ronald Inman and Dmitry Znamnensky
Air Liquide
5230 S. East Ave.
Countryside, IL 60525
U.S.A.

Introduction

High purity of process atmospheres is usually considered critical to high yields in semiconductor processing. As device dimensions become smaller, purity demands increase, as manifested in the ppt (part-per-trillion) contamination levels now routinely required of carrier gases. In recent years, however, it has become clear that other sources of contamination, such as reactive gases, the process chamber and semiconductor wafers themselves, are more important. Tunable diode laser absorption spectroscopy (TDLAS) is extremely useful for such environments: As a spectroscopic technique that exposes only optical elements to the analyte, it is compatible with most matrices. In this work, we review some recent applications of this technique, both in the laboratory and in the wafer fab.

TDLAS has been applied to trace contamination measurement in high purity reactive gases – improving, for example, the achievable detection limit for H_2O in NH_3 from about 2 ppm (by FTIR) to 50 ppb – and to *in situ* monitoring in semiconductor process tools. *In situ* moisture monitoring enables improvements in overall equipment effectiveness (OEE) by reducing time spent on purging procedures. Moisture is an excellent indicator of atmospheric contamination, being perhaps the most difficult atmospheric impurity to remove. By measuring true contamination levels, rather than simply relying on pre-set timing, significant savings are achievable. In addition, non-product wafers for qualification and/or trouble-shooting can be reduced if the true system status is known.
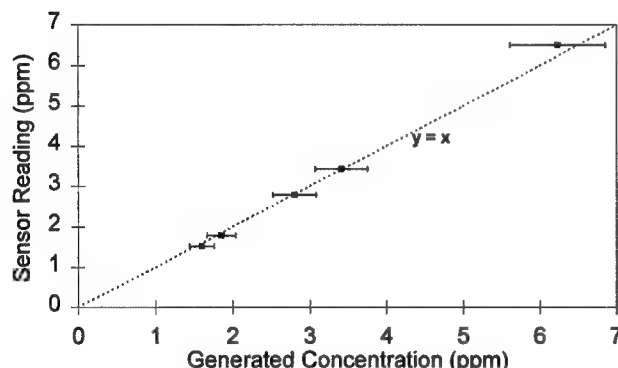
Figure 1: Calibration verification after 15 months on process tool

Air Liquide's TDLAS technology for moisture measurement in semiconductor gases and process atmospheres is now available commercially from SOPRA (Bois-Colombes, France), a manufacturer of optical instrumentation for semiconductor manufacturing and related industries.

TDLAS

Air Liquide selected TDLAS for development because it is a relatively well-established and robust technology already widely applied, not only in the laboratory, but also in numerous demanding field applications. It has been shown to be capable of delivering the ppb (part-per-billion) sensitivity levels required for semiconductor process gas monitoring. TDLAS does not demand extremely high mirror reflectivities as do intracavity laser and cavity ring-down spectroscopies, and is therefore less likely to display performance loss over time. To date we have focussed on the application of TDLAS to H_2O monitoring, but its application to other species is straightforward once a diode emitting at the appropriate

wavelength is available. As TDLAS becomes widely adopted, diodes that emit at wavelengths characteristic of most molecules of interest are expected to become available.

Because TDLAS is based upon absorption spectroscopy, the measurement is absolute and can be directly related to fundamental properties of the molecule of interest. In practice, it is often more convenient to quantify the response of the signal-processing electronics by direct comparison with a known moisture standard. The reliability of this procedure is illustrated in Figure 1. The sensor reading was verified after 15 months on a semiconductor process tool and found to be still in calibration within the accuracy of the moisture generator used. This chart is based upon a test such as that illustrated in Figure 2, in which various moisture levels are generated by varying the flow of pure gas over a permeation device. In this figure, the rapid response of the hygrometer is clearly illustrated.
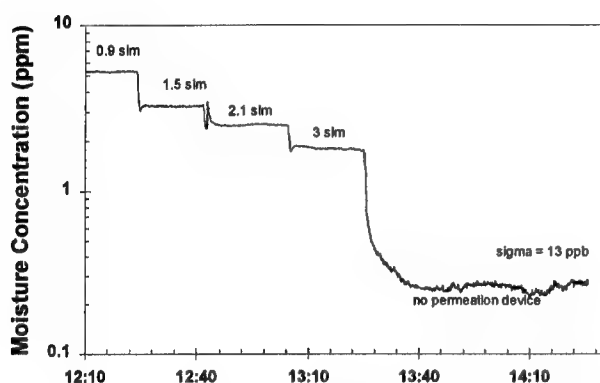
Figure 2:Response to varying moisture input

Applications

The application of TDLAS to a variety of semiconductor process environments, including RTP, CVD and etch, will be reviewed[1,2]. TDLAS has been demonstrated to be compatible with aggressive gases such as HCl, NH_3, SiH_2Cl_2, etc. and with strongly depositing atmospheres as in Si_3N_4 LPCVD[3]. In addition[4], it has been shown to be capable of trace moisture measurements to 50 ppb in pure NH_3 and to 10 ppb in a variety of corrosive gases including HCl. These applications will be discussed as will the key differences in approach required for *in situ* and for high-purity gas measurement.

Acknowledgements

References

1. *Progress in In Situ Contamination Control* J. McAndrew, Semiconductor International **21**(5) pp.71-78 (1998)
2. *Increasing Equipment Up-time through In Situ Moisture* Monitoring J.J.F. McAndrew, R.S. Inman, D. Znamensky, A. Haider, J. Brookshire, P. Gillespie, Solid State Technology **41**(8) (1998)
3. *In situ Measurement of Moisture Contamination Using Tunable Diode Laser Absorption Spectroscopy*, J. McAndrew, R. Inman, D. Znamensky, J.-M. Girard, G. Goltz and J.M. Flan, AEC/APC Symposium X, Vail Colorado Oct. 11- 16. P. 213. SEMATECH 1998.
4. *In-situ and on-line moisture monitoring in reactive gas environments* J. McAndrew, M. Bartolomey, J.-M. Girard, G. Goltz,and J.-M. Flan MICRO **18**(2) Feb. 2000.

Using CW-CRDS for Trace Gas Detection

John Dudek, Paul Rabinowitz, and Kevin K. Lehmann

Department of Chemistry, Princeton University, Princeton, New Jersey 08544

Wen-Bin Yan

Meeco Inc., 250 Titus Avenue, Warrington, PA 18976

Abstract

We have developed a technique to measure trace concentrations of gases in the near-infrared region using Continuous Wave Excitation Cavity Ring-down Spectroscopy (CW-CRDS). We have demonstrated that with a simple CW-CRDS system, trace amounts of moisture (water vapor) can be accurately detected.

Summary

Detection of trace gas species continues to be an important application of spectroscopy. Absorption spectroscopy is particularly attractive for such applications because of its high specificity, high speed of response, and absolute principle of calibration, based upon Beer's Law. The challenge is to reach ultrahigh sensitivity with this method in order to detect ultralow concentrations. Also, this method should be implemented in a way that is robust, compact, and of modest cost for a potential sensor. For the past several years, we have been using continuous wave (CW) Cavity Ring-down Spectroscopy [CW-CRDS] as a tool to meet this challenge. We have used this technique to measure trace concentrations of gases in the near infrared region because this region contains both vibrational overtone transitions and forbidden electronic transitions of many atmospherically important species. Our research has focused on investigating the properties of the cavity ring-down system in order to increase detection sensitivity of these atmospherically important species. Specifically, we are studying moisture detection at the parts per billion (ppb) to the parts per

trillion (ppt) range, shown in figure 1. We have obtained a detection limit of better than 1×10^{-11} cm^{-1} per root Hz for R $=0.999985$ reflectors which allows us to detect water at less than 10 ppb.

CW-CRDS method is limited to spectral regions where one can obtain high reflectivity dielectric mirrors, and there, only over spectral tuning ranges of a few percent for a single set of mirrors. To overcome these limitations, we have designed, constructed, and tested an astigmatic prism ring resonator which utilizes total internal reflection to achieve high reflectivity, a curved prism face for optical stability, and reflective coupling near Brewster's angle to provide controlled finesse of the resonator. We have measured the loss of this resonator, which includes scattering, diffraction, and stress induced birefringence, in the range between 470 nm to 1.6 μm and found good agreement with calculated values. The minimum loss per pass excluding coupling occurred at 900 nm and was $\approx 7 \times 10^{-5}$. It was mainly due to excessive diffraction resulting from an error in fabrication which we anticipate will be improved significantly in a new prism.
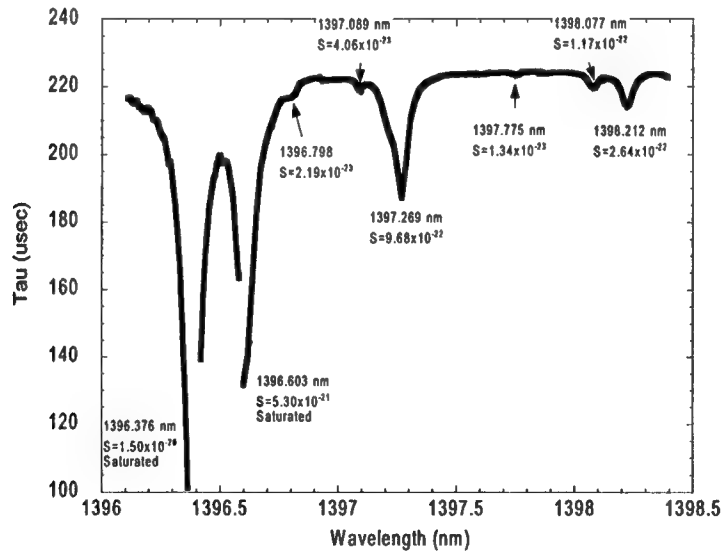
Figure 1: Moisture Scan from 1396.1 nm to 1398.4 nm at a concentration of 200 ppb.

TRACE MOISTURE DETECTION USING NEAR INFRARED DIODE LASERS

Chris Hovde

Southwest Sciences, Inc., Ohio Operations, 6837 Main Street, Cincinnati OH 45244

and Joel A. Silver

Southwest Sciences, Inc. 1570 Pacheco Street, Suite E-11, Santa Fe, NM 87505

The measurement of trace concentrations of water vapor is import in many industrial applications, especially semiconductor fabrication. A variety of methods exists for measuring water vapor at concentrations approaching one nmole/mole (one ppb). Optical methods include Fourier-transform spectrometry, intracavity laser absorption spectroscopy, and cavity ring-down spectroscopy. However, we have chosen to focus on wavelength modulation spectroscopy (WMS) as a practical method to achieve sufficient sensitivity.[1] WMS is a variation of transmission spectroscopy, and thus it shares the calibration benefits of other Beer's Law techniques. By rapidly modulating the laser wavelength, laser 1/f noise is avoided, so very small changes in laser power can be measured. When WMS is combined with a multiple pass absorption cell, ultra-sensitive detection of water vapor is possible, even when detecting H_2O using weaker overtone transitions with near-infrared InGaAsP diode lasers near 1392.5 nm. This approach has the desired combination of sensitivity and accuracy while enjoying the benefits of rugged communications-type diode lasers. Other researchers have employed similar techniques.[2,3]

The diode laser sensor measures the amount of water vapor by quantifying the absorbance of a single rotational line within a vibrational overtone band of water vapor. To measure the line profile, the laser drive current, and hence its wavelength or frequency v, is ramped once per minute over the absorption line and simultaneously modulated at frequency $f = 50$ kHz with a sine wave. The absorption signal as a function of ramp position is quantified by lock-in detection at twice the modulation frequency, $2f$. The water vapor concentration is determined by linear least squares fitting of the resulting spectrum using a theoretical model.

The sensor design is based on a sealed laser head connected to a Herriott multipass cell constructed from ultra-high vacuum stainless steel flanges sealed with copper gaskets. The sample pressure is maintained near 13.33 kPa (100 Torr), balancing signal strength while keeping the line shape sufficiently narrow so that the full shape $g(v)$ can be recorded within the wavelength scan range of the laser. The transmitted photocurrent is detected by an InGaAs photodiode; the *dc* and *2f* components of the photocurrent are separately amplified. To suppress étalons, the laser/lens assembly is mechanically vibrated[4] and a jitter modulation[5] is used.

For low moisture levels, the absorbed laser power is small, and a linear approximation to Beer's Law can be used. The *2f* component of the detected photocurrent is proportional to the transmitted laser power, line strength, path length, and water concentration (all of which are constant over the 20 μs modulation time scale), times the *2f* Fourier component of $g(v_m(t) + v_i)$ — the WMS spectral line shape $g_{WMS}(v_i)$. This linear relationship between the small absorbance signal and the line shape permits the use of linear least squares analysis to determine the best multiplier of the WMS line shape and thus the best estimate of the water concentration. The least squares model includes five vectors: a numerical WMS demodulated Voigt line shape $g_{WMS}(v)$, the derivative of this demodulated line shape $dg_{WMS}(v)/dv$, and three terms describing a quadratic baseline. The derivative term is used for locking the position of the peak within the scan.

Measurements using NIST Traceable Standards The diode laser moisture sensor was used in a series of calibration measurements against the new Low Frost-Point Humidity Generator (LFPG) at NIST.[6] The LFPG saturates an inert carrier gas stream with water vapor by flowing the gas over a plane surface of ice at fixed temperature and pressure. Its output can be predicted from thermodynamic principles and is independent of gas flow rate. The WMS instrument was calibrated in terms of the expected output of the LFPG by stepping the humidity generator through a series of set points ranging from 5 nmol/mol to

2.5 µmol/mol of water vapor in air (Fig. 1). Good agreement was obtained throughout this range, although outgassing within the laser sensor limited the accuracy at the lowest moisture levels.

The Allan variance provides a useful measure of the noise as a function of averaging time and shows that the resolution and minimum detectable concentration cannot be improved without limit simply by increasing the averaging time. Adopting a three sigma criterion for statistical significance (99.7% confidence level), the minimum detectable change in mole fraction of water vapor is ~0.2 nmol/mol for averaging times of ~20 min.

Figure 1. Calibration curve. Moisture as measured by the diode laser sensor vs. moisture supplied by the low frost point generator, showing good agreement throughout the range studied.

A useful figure-of-merit for comparing the performance of absorption measuring instruments is the noise equivalent absorptivity (NEA), defined here as the minimum detectable absorptivity per square root of the data acquisition rate. The WMS system NEA is $\approx 3.5*10^{-9}$ cm^{-1}/Hz$^{1/2}$. This NEA figure is equivalent to an absorbance of $2\cdot10^{-6}$ of the laser power. These figures compare favorably to those obtained with other sensitive absorption methods and are especially noteworthy in that they are based upon the rate at which entire line profiles are recorded and fit.

Conclusions Diode laser absolute moisture detection is sensitive, precise and accurate. Using a combination of methods to suppress étalons and achieve high signal/noise, a detection limit of ~0.2 nmol/mol can be achieved. The frost-point temperature equivalent to this detection limit is -117°C. The linearity of the instrument is excellent, exhibiting an error of only 1% at water concentrations in the µmol/mol range (frost points near -65° C), and this range could be improved by using the full exponential form of Beer's Law. The most significant limitation to the accuracy appears to be from outgassing within the sample region.

References

1. Hovde, C., *Extended Abstracts of the NIST/AVS Workshop*, Gaithersburg, MD, p. 47-48 (May 23-25, 1994).
2. Wu, S.-Q.; Morishita, J.-I.,; Masusaki, H.; Kimishima, T., *Anal. Chem.* **70**, 3315-3321 (1998) .
3. J. M. Girard and P. Mauvais, *Proc. ISSM'96, 5th Int. Symp. Semicond. Manuf.*, Ultra Clean Society, Tokyo, Japan 325-328, (1996).
4. Silver, J. A.; Stanton, A. C., *Appl. Opt.* **27**, 1914 (1988).
5. Cassidy, D. T.; Reid, J., *Appl. Phys. B* **29**, 279-285 (1982) .
6. Scace, G. E.; Huang, P. H.; Hodges, J. T.; Olson, D. A.; Whetstone, J. R. *1997 NCSL Workshop and Symposium,* Atlanta, GA (July 27-31, 1997) .

Trace Moisture Detection in Corrosive Gases Using Quadrupole Mass Spectroscopy

Hans Funke, Mark Raynor, Virginia Houlding
Matheson Tri-Gas
Advanced Technology Center

Terry Ramus, Scott Hein
Diablo Analytical, Inc.

Ralph Kirk
Advanced Technology Development, Inc.

An online analyzer for impurities in corrosive gases was developed using an HP-5973 MSD Quadrupole Mass Selective Detector equipped with customized data acquisition and gas sample inlet designed by Diablo Analytical, Inc. The instrument was evaluated for its ability to quantitatively analyze moisture and other impurities at the ppm level in HCl.

Figure 1: Sampling system
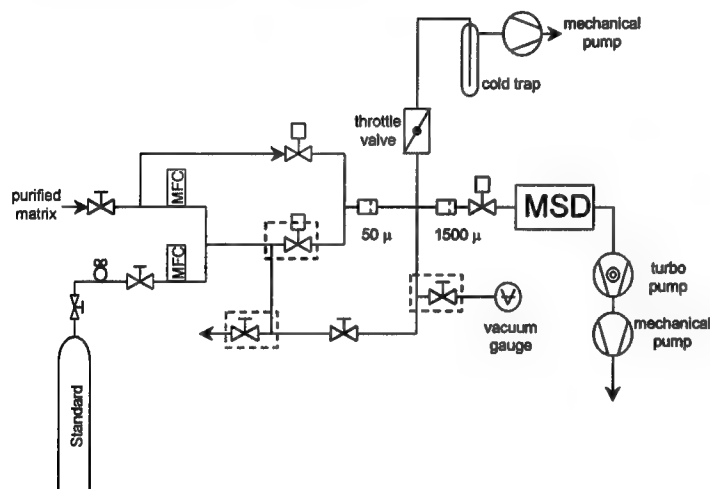
The sample gas is introduced at atmospheric pressure through a 50 micron orifice into a vacuum line system that is pressure controlled with a throttle valve and a mechanical pump to $\sim 10^{-1}$ torr. A sample stream is introduced through a 1500 micron orifice and an air actuated valve into the MS chamber for analysis (see Figure 1). The HP tuning algorithm was not applicable in the mass range of interest and manual tuning was required for high sensitivity.

Tests with ppm levels of oxygen in nitrogen and argon matrix demonstrated a very fast response to changing inlet concentrations (Figure 2). The instrument was sensitive to single digit ppm and sub ppm changes and calibration curves were linear. The sensitivity was a strong function of the matrix gas. The highest sensitivity was obtained in He whereas the heavier matrix gases decreased the sensitivity by about 1-2 orders magnitude.
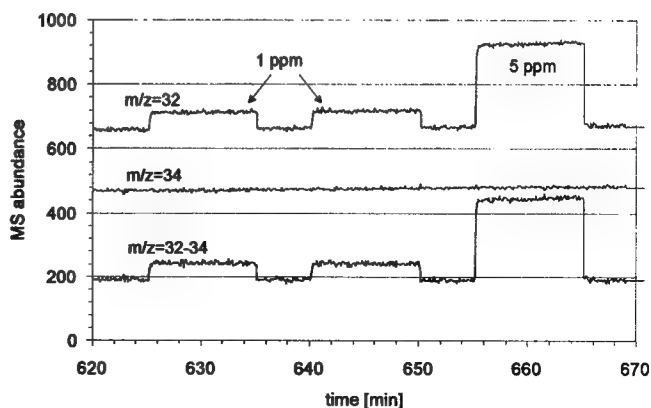
Figure 2: O$_2$ in N$_2$ matrix

Simiilar results were obtained in HCl matrix for moisture impurity. Moisture was measured at m/z=18+19. Figure 3 illustrates the response to moisture challenges of 11, 9, 7, 5, and 3 ppm. The quadrupole chamber did not show any visible corrosion during several weeks of study. The electron multiplier response, however, significantly decreased in the time frame of hours similar to the results in inert gases.
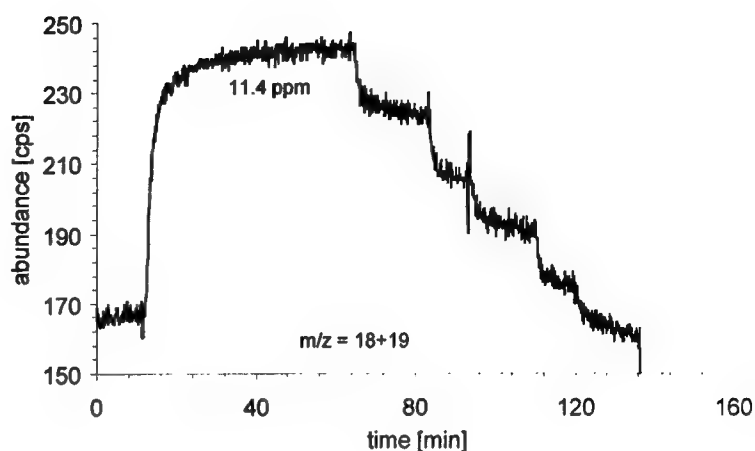
Figure 3: Moisture in HCl matrix (m/z=18+19)

Fe ions could be detected in HCl matrix in the mass range above 100 amu, possibly due to contamination of the source gas (Figure 4). Also, formation of Fe species in the source cannot be completely ruled out. For example, Ti species were detected in the gas phase with a TiN coated source, indicating that at least a fraction of the observed metal species stem from the source.
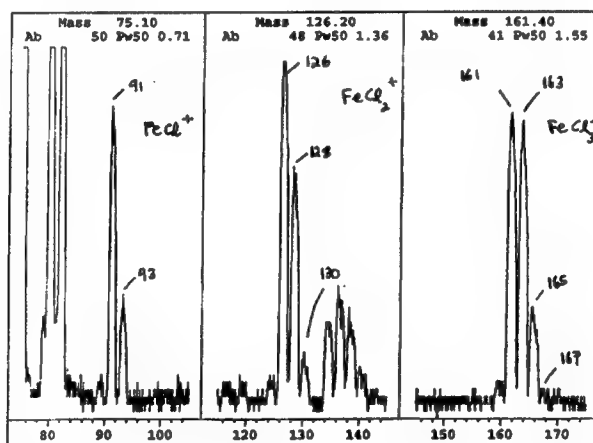
Figure 4: Iron chloride species detected in HCl matrix

Application of CW-CRDS to Monitor and Control Chemical Vapor Deposition

David S. Green,[a,b] John P. Looney,[b] Gary W. Rubloff [a]

a. *Institute for Systems Research, University of Maryland, College Park, MD 20742*

b. *National Institute of Standards and Technology, Process Measurements Division, Gaithersburg, MD 20899.*

ABSTRACT

Continuous wave excitation cavity ring-down spectroscopy (CW-CRDS) is being developed for real time chemical sensing of volatile CVD byproducts (e.g. HF, H_2O) and as a quantitative and robust metrology tool for advanced process control methodologies.

SUMMARY

Real-time metrology providing information on reactant depletion and product generation for process control during semiconductor manufacturing is needed to enhance productivity and reduce costs [1]. While there are many methods to characterize thin films, it can be difficult to characterize processes because no standardized measurement methods exist to quantify the effects of gas phase changes on film properties. We believe that continuous wave cavity ring-down spectroscopy (CW-CRDS) [2] holds potential in wafer state metrology for advanced process control, yield management, and quality assurance.

Optical sensors exploiting advances in diode lasers, coatings, and photonics can provide compact, rugged and reliable devices for *in situ* spectroscopic sensing. Absorption spectroscopy is attractive as a metrology method because it is species specific and quantitative. Process control becomes viable when gas phase observations are captured in real time and combined with a model incorporating the effect of process parameters.

Advantages of CRDS over conventional laser absorption spectroscopy include lower detection limits, and insensitivity to absorption by ambient species and to fluctuations in laser intensity and phase. Also, the sample volume in CRD systems can be made relatively small, thus providing good spatial resolution in the transverse direction and facilitating integration into process tools. Finally, CRD signals can be modeled with a relatively simple yet rigorous and accurate theory.

We are investigating the quantitative capabilities of CW-CRDS by targeting hydrogen fluoride, HF, and water vapor, H_2O. The former is a major byproduct occurring when excess fluorine (in the chamber and on surfaces) reacts with hydrogen-containing precursors. H_2O is important in fluorine process environments since it is the most common reactive impurity involved in gas phase and surface reactions leading to the formation of HF and other compounds. The capability to monitor the real-time evolution of HF in a process chamber will provide critical feedback used for system control. As a specific example, this has the potential to provide wafer state reaction information that is the basis for film thickness metrology in CVD systems.

In the first stage of this work, we are developing a bench-top CW-CRDS sensing platform to provide a prototype system that is compatible with semiconductor manufacturing applications. This prototype will be integrated with a commercial thermal CVD chamber that runs tungsten hexafluoride (WF_6) chemistries to deposit blanket tungsten films. The CRDS measurements will be used to characterize the limitations of quadrupole mass spectrometry measurements of HF and to provide wafer state reaction information that is the basis for film thickness metrology [3]. We anticipate that this effort will help drive the development of several aspects of CW-CRDS technology toward a reliable field-deployable system.

Unlike many other applications of CRDS emphasizing detection sensitivity, this study is not aimed at trace species for fault detection or contamination control but aims to monitor fluctuations in the concentration of

majority reaction byproducts of the CVD process for real-time control. Operating conditions in the commercial CVD chamber are typically 67 Pa pressure and 400 °C temperature. Feed gas consists of less than 10% WF_6 by volume and chemical conversion rates of 2% are typical. A mechanistic model for W-film growth specifies the stoichiometry of HF generated for each WF_6 consumed. Quantitative analysis of HF concentration can then be correlated to film thickness [3].

The test platform being developed incorporates a compact (nominally 25 cm) high finesse linear cavity encased in a stainless steel or anodized aluminum housing with O-ring seals and gas inlet and pump ports. Temperature control, upstream flow control, and downstream pressure control are being implemented. High quality dielectric-coated mirrors and custom mirrors with corrosion-resistant coatings are being examined. Pairs of high-reflectivity (99.995%) mirrors coated at 670 nm and 685 nm are selected for HF spectroscopy. Commercially available CW tunable diode lasers with nominal powers less than 30 mW and time averaged bandwidth of about 20 MHz are being used as the light sources to pump the ring-down cavity. An optical isolator is used to prevent feedback into the diode source. A spatial filter and a mode-matching lens are used to couple into a single mode of the ring-down cavity. In one embodiment, an acousto-optic modulator in conjunction with a gate and delay generator and a low noise fast photodiode receiver (monitoring the ring-down signal) are used to detect light build-up within the cavity and fast switching to induce the transient decay of light. The signals are digitized and processed on a personal computer.

Figure 1. Estimated Fractional Optical Loss Per Pass for HF absorption at 670 nm in a 25 cm cavity at 298K.

CW-CRDS can be used to probe numerous absorption transitions of HF and water vapor. The spectroscopic parameters of HF are known and the rotational structure is simplistic. The line strengths at room temperature for the strongest rotational features of the HF (0-4) vibrational band are estimated to be ~1.2×10^{-22} $cm^{-1}cm^2$/molecule at 298K using the data of Rimpel [4]. Calculated per pass losses in a 25 cm cavity are illustrated in Fig. 1. As indicated by this figure, for HF partial pressures greater than 1 Pa -10 Pa, optical losses of ~ 10^{-5} – 10^{-4} per pass are expected and should be readily observable. Number densities will be extracted from the ring-down signals and used as input parameters to numerical simulations of W deposition.

CRDS studies will be part of a larger view toward the impact of optical sensing in semiconductor manufacturing processes. We will use lessons learned from the CRDS experience as a stimulus for identifying and assessing the viability of different sensor-based approaches to wafer state metrology for control. We expect that the application itself will initiate new ideas in CRDS and more generally in optical absorption methods.

REFERENCES

1. ITRS99, International Technology Roadmap for Semiconductors, 1999 Edition, Semiconductor Industry Association, San Jose, CA, 1999.

2. D. Romanini, A.A.Kachanov, N. Sadeghi, F. Stoeckel "CW Cavity ring Down spectroscopy," *Chem. Phys. Lett.* **264**, 316 (1997).

3. T. Gougousi, Y. Xu, j.N. Kidder, Jr., G.W. Rubloff, and C.R.Tilford, "Process Diagnostics and Thickness Metrology using in-situ Mass Spectrometry for the Chemical Vapor Deposition of W from H_2/WF_6." *J. Vac. Sci. Technol. B* (in press).

4. G. Rimpel. "Linienstärken in der 4-0 und 5-0 Rotatinsschwingungsbande von Fluorwasserstoff." *Z. Naturforsch* **29A**, 588 (1974).

Plasma Diagnostics for Semiconductor Processing

Harold M. Anderson
Department of Chemical and Nuclear Engineering
University of New Mexico
209 Ferris Engineering Center
Albuquerque, NM 87131 USA

Frequency-modulated, infrared diode laser absorption spectroscopy (IRLAS) and full-spectrum CCD-based optical emission spectroscopy (OES) are two powerful new tools for plasma diagnostics. This presentation focuses on the use of these diagnostics in plasma etch processing used for semiconductor manufacturing. In particular, IRLAS is finding extensive use in measuring absolute concentrations of gas phase radicals formed in the oxide etch process performed with fluorocarbon high-density plasma (HDP) discharges. Knowledge of the absolute concentrations of reactant species (CF_x) and product species (SiF_x and COF_x) formed in trace amounts (10^{11}-10^{14} cm-3) during etching of oxide substrates is important for predicting the behavior of this complex plasma-surface interaction. These measurements are a critical element in a SEMATECH sponsored program for plasma etch model development, and are intended for validating computer simulation models of this complex process. Full-spectrum OES on the other hand is a more mature technology that is finding application in day-to-day semiconductor fab plasma processing operations like end-point and fault detection. With the development of CCD sensors and micro-machined diffraction gratings, it has been possible to build miniaturized spectrometers mounted on computer boards that allow rapid acquisition of the complete uv-visible optical emission spectrum of the plasma. Chemometric multivariate statistical analysis of this full-spectrum database in real time is made possible by integrating the spectrometer with a fast portable computer. In combination, these techniques have been shown to provide superior sensitivity for detecting process end-point in real-time and information for process fault detection. This capability is becoming more important to the semiconductor industry as the critical dimensions of the chip are approaching the extreme sub-micron ($\sim$0.1 μm) range and the exposed area of the thin film to be etched is dropping to under one-half percent of the wafer surface.

The discussion of IRLAS focuses on the ability to detect trace amounts of radical species important to the oxide etch process with only a single or double pass using frequency modulation second derivative (or 2f) spectroscopy. This aspect of the diagnostic tool design is critical since any plasma diagnostic must be non-perturbing to the plasma and be accomplished without radically altering the commercial etch tool chamber configuration. At best, commercial etch tools provide only one to two small diagnostic windows for viewing the plasma during operation. Practically speaking then, this limits the type of optical diagnostic data acquisition to emission or line-of-sight absorption. Also, since space in a semiconductor clean room is extremely expensive, the size or foot-print of the diagnostic tool must be compact. Solid-state diode lasers operating in the mid-IR range (3-12 μm) meet all these requirements and provide radical detection sensitivity down to number densities in the 10^{10}-10^{11} cm^{-3} range given a few passes through the plasma chamber (30-40 cm diameter) and 2f derivative spectroscopy. The diode laser in the system employed in this study is cooled in a compact liquid nitrogen dewar mounted on a compact portable optical board. Commercially available temperature and current

controllers along with a lock-in amplifier, oscilloscope and PC computer are all that are needed for data acquisition. Although not suited for routine day-to-day use in a semiconductor fab, this type of diagnostic tool has been used extensively for diagnostics studies of plasmas in semiconductor research facilities such as those found at SEMATECH, etch tool manufacturer development facilities and universities.

Much of this portion of the presentation will focus on diagnostics needed for the improving the performance of next generation, inductively coupled, low pressure HDP discharges that are being manufactured to meet the coming need for extreme sub-micron etching. The reactors typically operate with pressures in the 5-10 mTorr range and generate plasmas with densities in the high 10^{11} cm^{-3} range. Radicals, formed by electron impact dissociation, drive the important surface reactions even though their number densities are only in the 10^{12}-10^{14} cm^{-3} range. The CF$_x$ radicals used in oxide etching are extremely important to the process since they provide for the selectivity of the etch (i.e. the ability to stop etching the silicon underlying oxide film). This is one of the most critical etch steps in semiconductor manufacturing and is used to establish the contacts to IC devices. A thin (2-3 nm) CF$_x$ polymeric deposited film is shown to be crucial for regulating the etch during processing. Monitoring the concentrations of CF$_x$ radicals is in turn shown to be important to controlling the amount of polymer deposition.

The OES sensor discussion focuses on the advantages of full spectrum CCD-based optical emission spectroscopy (OES) over monochromator-based systems and the design of a compact computer integrated sensor known as the EP-2000 system now manufactured by Cetac Technologies. Traditionally, monochromator based systems have been used to determine endpoint by monitoring one or two strongly emitting wavelengths. For exposed open areas of <1.0%, a more sensitive approach is required for the next generation of chips. CCD array detector based systems can provide a wealth of spectral information from a variety of potentially useful gas phase emitting species. In the case of particularly challenging applications such as reverse mask shallow trench isolation (STI) and contact etches, utilization of the full optical emission spectrum has been shown to provide tangible benefits. Production facility results regarding these and other demanding applications will be presented. The talk will largely focus on oxide etching in AMAT MXP and AMAT HDP platforms. Evolving Window Factor Analysis (EWFA) and Multiple Curve Resolution (MCR) are the principal multivariate techniques used in the analysis. They allow one to dynamically track the principal components of the oxide etch process. EWFA is also shown to useful for automatic fault detection. MCR is used to depict the dynamic rate of formation (or depletion) of the principal chemical species in the plasma during the etch. By integrating the sensor within a computer and coupling the sensor to the plasma emission via optical fibers, one is able to collect and statistically analyze the full-spectrum data in a 1-2 hundred milliseconds. This allows for sampling at 5-10 Hz rate, which in terms of the oxide etch process is effectively real time. The compactness, ease of use, reliability and robustness of this type of optical sensor makes it extremely valuable to the semiconductor industry for day-to-day process control. Units are now in use at IBM, Motorola and other semiconductor manufacturing facilities.

In situ reflectance monitoring of epitaxial growth

William G. Breiland, Dept 1126 MS 0601
Sandia National Laboratories, Albuquerque, NM 87185-0601

Epitaxial growth of compound semiconductors is accomplished with Metal Organic Chemical Vapor Deposition (MOCVD) or Molecular Beam Epitaxy (MBE). In both these methods, many process variables must be precisely controlled to achieve the proper combination of layer thickness, chemical composition, lattice matching, and doping levels required by modern compound semiconductor devices. We have found that a simple and robust *in situ* monitor, normal incidence reflectance, has proven to be an indispensable tool for achieving stringent device requirements for epitaxial growth.
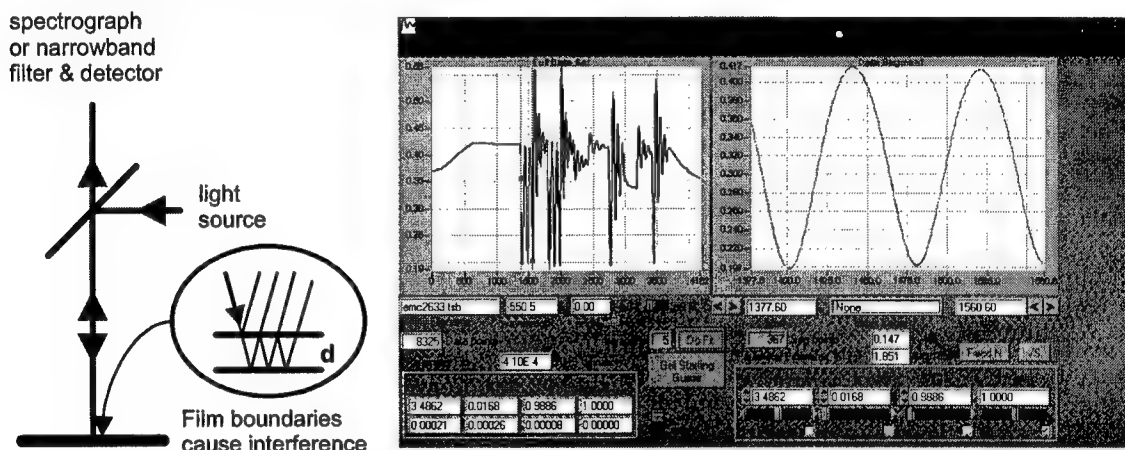
The schematic on the left of the figure above shows the reflectance experiment. Interference of light between interfaces of the thin films cause oscillations in the reflectance signal as the films are grown. The monitor requires only one window, polarization is not a factor, and the effects of wafer wobble can be minimized. The screen print on the right shows the interference data from a pre-growth calibration run. These data are analyzed using the ADVISOR (Analysis of Deposition Using Virtual Interfaces and Spectroscopic Optical Reflectance) method [1]. Growth rates for each bubbler source and for several doping conditions are determined to better than 1% accuracy. These numbers are fed to a model-based automated recipe generator that is used by the MOCVD tool to grow a device structure. Results of the usefulness of the ADVISOR approach are shown in the figures below.
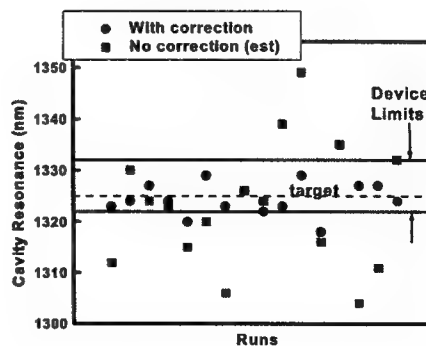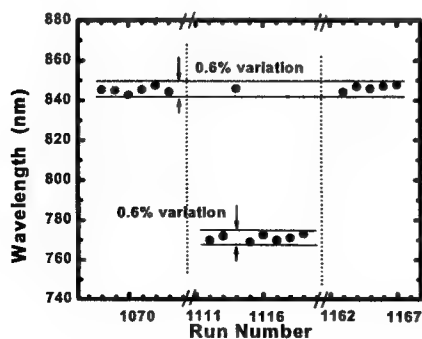
The left figure shows the reproducibility of the cavity wavelength values for 770 and 850 nm vertical cavity surface emitting laser (VCSEL) structures [2]. These devices consist of nearly 700 layers. The right figure shows the results of real-time process control during the MBE growth of a complicated reflectance modulator structure [3]. ADVISOR analysis was done on early layers to modify the deposition rates. Squares represent cavity wavelengths that would occur without correction. Circles represent the measured cavity wavelength with ADVISOR control. Note the large increase in device yield that was achieved with the in situ monitor.

(3QW) GaAsP-GaAs-GaAsSb Growth
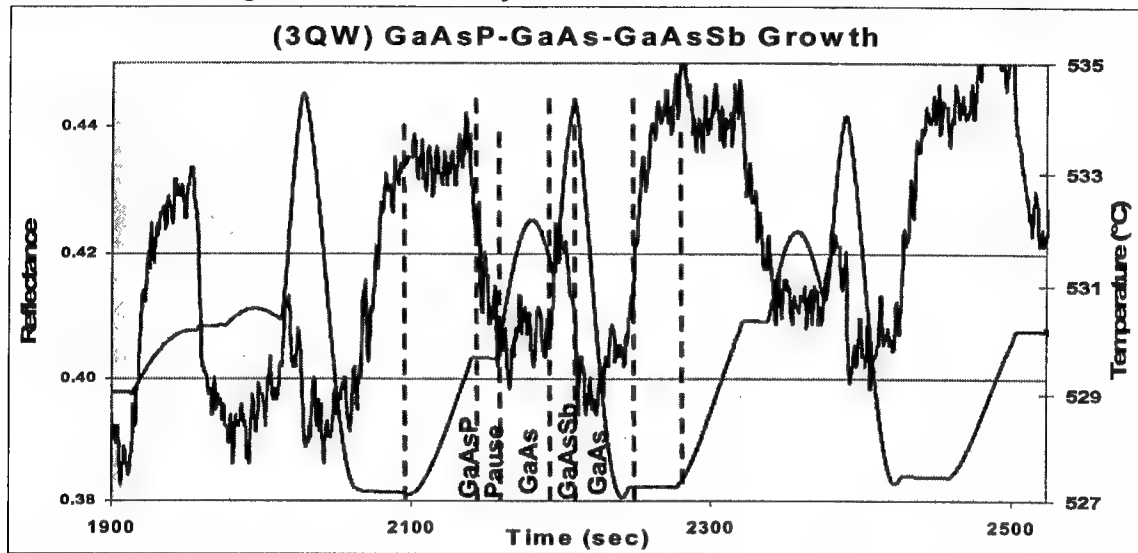
Normal incidence reflectance may also be used to determine surface temperatures during growth. A single-wavelength pyrometer will exhibit large (up to 100 °C) artifacts in temperature if it is not corrected for the change in emissivity that occurs during thin film growth. For smooth, flat, opaque surfaces, the emissivity is simply (1 − reflectance). An instrument that simultaneously records thermal emission and normal incidence reflectance may thus be used to perform emissivity-correcting pyrometry during thin film growth. The figure above shows a plot of reflectance at 550 nm (left scale, smooth data) superimposed on the 900 nm emissivity-corrected surface temperature (right scale, noisy data) [4]. Subtle temperature effects may be observed during the growth. For example, a pause was required between the GaAsP and GaAs layers. The figure reveals that the reason for this pause was to allow the system to recover to the 530 °C growth temperature. The figure also illustrates the high signal-to-noise that may be achieved with reflectance waveforms. The layer labeled "GaAsSb" is a 77 Å quantum well between 120 Å GaAs barriers.

Reflectance has also been used to monitor plasma etching on patterned wafers. Unlike many silicon-based etching processes, selective etch recipes are rare. It is thus useful to watch the time-reversed interference pattern evolve during an etch process in order to stop the etch at the correct interface or within the correct layer. Complications due to photoresist etching may be dealt with using digital filtering methods.

1. W.G. Breiland and K.P. Killeen, J. Appl. Phys. 78 (1995) 6726.
2. W. G. Breiland, H. Q. Hou, H. C. Chui, B. E. Hammons, J. Cryst. Growth, 174 (1997) 564
3. W. G. Breiland, H. Q. Hou, B. E. Hammons, and J. F. Klem, XXVIII SOTAPOCS Symposium, Electrochem. Soc. 1998.
4. A. Allerman, T. Harget, and W. G. Breiland, unpublished, (2000).

AlGaAs Composition Measurements from *In Situ* Optical Reflectance*

K. A. Bertness,** J. T. Armstrong, R. B. Marinenko, L. H. Robins, A. J. Paul, J. G. Pellegrino, P. M. Amirtharaj, D. Chandler-Horowitz, National Institute of Standards and Technology, **Mailstop 815.04, 325 Broadway, Boulder, CO 80303

We describe preliminary determinations of AlGaAs layer composition using *in situ* optical reflectance spectroscopy (ORS) data. Reflection high energy electron diffraction (RHEED) oscillations are used to independently determine the composition of the AlGaAs layers. The results are compared with *ex situ* measurements of photoluminescence (PL), photoreflectance (PR), x-ray rocking curves, and electron microprobe analysis (EMPA).   Although additional work is needed to refine the uncertainty estimates and reduce sources of error, we find that growth rate as measured by ORS agrees with RHEED oscillation data to within 2 %.   The ultimate goal of this project is to produce standard reference materials (SRMs) of certified alloy composition to mole-fraction uncertainty of 0.002 for a range of important III-V alloys.

ORS data was acquired by reflecting monochromatic light at near-normal incidence from a semiconductor wafer mounted in the growth chamber of a molecular beam epitaxy (MBE) system. The optical access window was heated to minimize deposits, particularly arsenic. Additional details have been published elsewhere.[1] Before each growth run, the AlAs, GaAs, and AlGaAs growth rates were measured separately using the monolayer oscillations in the intensity of the zero-order beam in the RHEED pattern. The Al mole fraction was calculated by dividing the AlAs growth rate by the sum of the AlAs and GaAs growth rates, resulting in an estimated uncertainty of 0.004 in the mole fraction. ORS does not measure the composition directly; however, the growth rate measurements from RHEED and ORS are based on independent physical processes. Over a large sample set, agreement between RHEED and ORS growth rates indicates that the composition determined by RHEED has persisted throughout the run. The index of refraction derived from ORS can also be used to derive composition, although our present data set is insufficient for accurate determinations.

Typical ORS data during growth of a thick $Al_{0.20}Ga_{0.80}$ As layer is shown in Fig. 1, along with a theoretical fit to the data using algorithms based on the virtual-substrate formalism.[2,3] The variables optimized by the fit are the index of refraction and absorption coefficient of the layer, the growth rate, the effective index and absorption coefficient of the underlying layers, and an overall reflectance scaling factor.
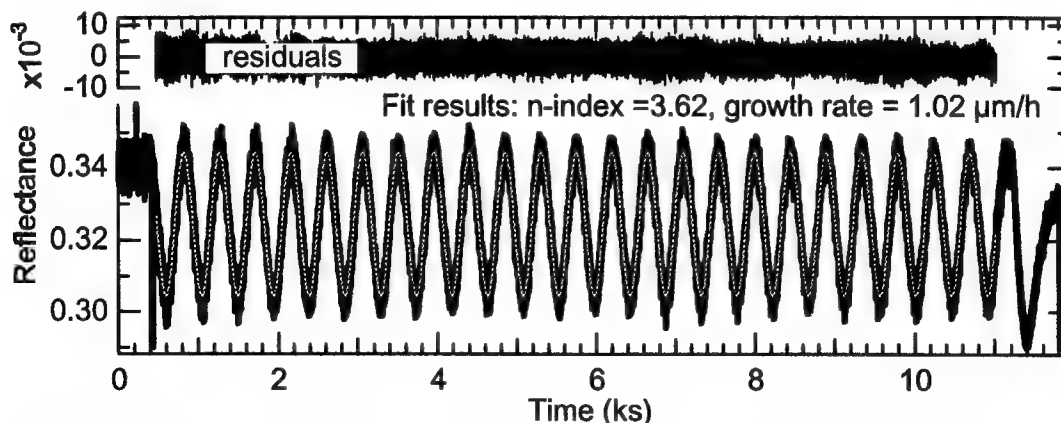
Fig. 1 Wafer reflectance (black) at 925 nm as a function of time during the growth of a layer of $Al_{0.20}Ga_{0.80}$ As at 595 °C. Also shown are the results of an optimized fit (gray) and fit residuals.

* Contribution of the National Institute of Standards and Technology and not subject to copyright.
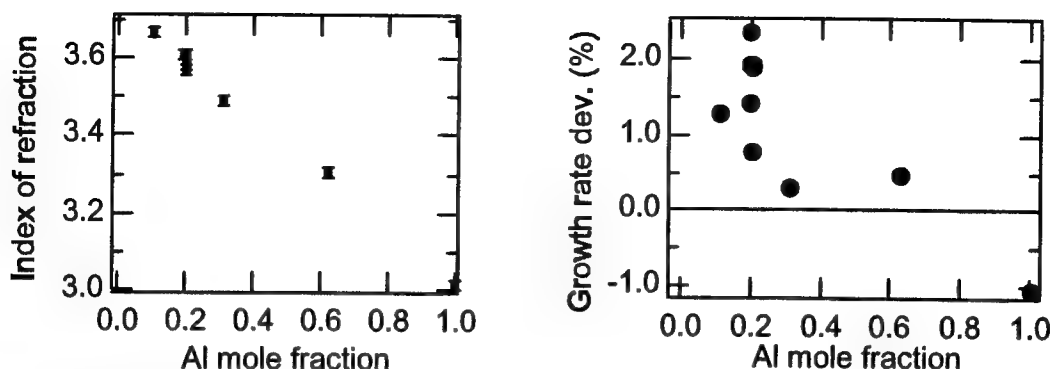
Fig. 2. Index of refraction and ORS growth rate deviation from RHEED oscillation growth rate for a series of layers with different Al mole fractions.

Fig. 2 summarizes two important layer properties derived for a number of growths with different Al composition. The growth rate determined from ORS fits was within 1.5 % of that from RHEED for all runs. There is a fairly large variation in the index derived for the set of runs with Al mole fraction near 0.20. Some variation originates with the difficulty the modeling encounters in distinguishing among changes in reflectance scaling, growth rate, and index of refraction. This set also comprises runs with different doping levels, doping types and growth temperatures (from 585 °C to 600 °C), all of which can alter the index. We expect that recent improvements to the calibration of the reflectance scale will allow reduction of the uncertainty.

In Fig. 3, we compare the *in situ* composition measurement results with the conventional *ex situ* measurement techniques of PL, PR, x-ray diffraction rocking curves, and EMPA. More specimens are needed to improve the statistical significance of the data, but in this preliminary set we see that the *in situ* measurements agree with each other well. The EMPA data were analyzed using procedures developed specifically for this project.[4]

References
1.   K. A. Bertness, R. K. Hickernell and S. P. Hays, *Mat. Res. Soc. Symp. Proc.* (MRS, Pittsburgh, 1999), vol. 570, p. 157.
2.   W. G. Breiland and K. P. Killeen, *J. Appl. Phys.* **78**, 6726 (1995).
3.   D. E. Aspnes, *J. Opt. Soc. Am. A* **10**, 974 (1993).
4.   J. T. Armstrong, *Microscopy and Microanalysis* **4 (suppl. 2)**, 226 (1998).
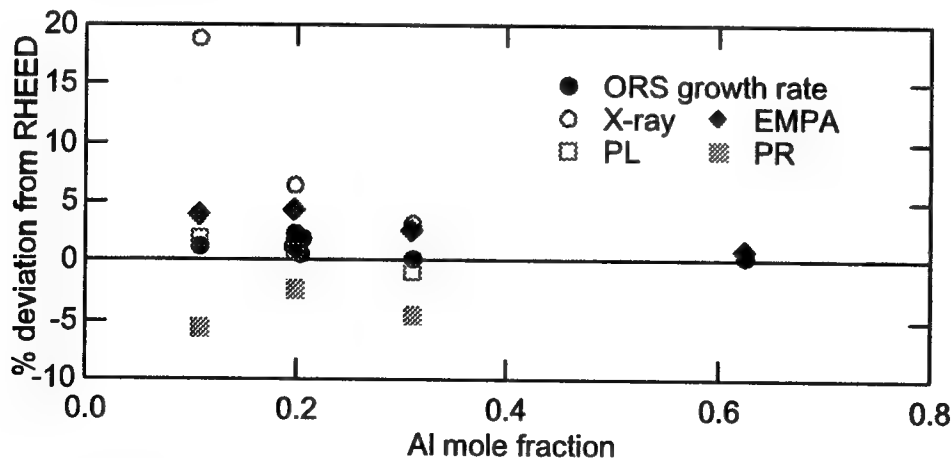
Fig 3.   Comparison of *in situ* and *ex situ* composition determinations.

Optical Sensing in Semiconductor Manufacturing

Tuesday, 25 July 2000

TuB1: Spectroscopic Ellipsometry and Reflectometry
TuB2: Epitaxial Growth Control
TuB3: Nonlinear Optics and Scatterometry
TuB4: Scatterometry

Real-Time Monitoring of Epitaxial Growth

D. E. Aspnes

Department of Physics, North Carolina State University, Raleigh, NC 27695-8202 USA

ABSTRACT: Optical probes not only provide information about microscopic mechanisms of epitaxy but have also been used for fully automatic sample-driven closed-loop feedback control of the growth of compositionally graded materials and structures.

The drive toward higher performance and increasing complexity in semiconductor devices, together with the trend toward chemical-beam deposition methods such as organometallic chemical vapor deposition (OMCVD) and chemical beam epitaxy (CBE), have provided strong incentives to develop a better understanding of growth processes and better methods of monitoring and even controlling epitaxial growth. Optical probes are of interest here because they are nondestructive, noninvasive, and function in relatively high-pressure ambients, including OMCVD where standard surface-analysis probes cannot be used.

A number of optical techniques, such as spectroscopic ellipsometry (SE), spectroscopic reflectometry (SR), surface photoabsorption (SPA), reflectance-difference (-anisotropy) spectroscopy (RDS/RAS), p-polarized reflection spectroscopy (PRS), laser light scattering (LLS), and second-harmonic generation (SHG) have been either refined or invented to overcome the intrinsic insensitivity of optical probes to surface conditions and meet the challenges presented by monitoring and control.[1,2] The surface-optical probes either rely on symmetry (RDS/RAS, LLS, SHG) or enhancement of surface sensitivity by operation at the Brewster (PRS) or pseudo-Brewster (SPA) angle to suppress the bulk response in favor of the surface component of the total reflected intensity.

However, the main practical considerations in growth and deposition involve layer thicknesses and compositions, which are bulk properties that can only be determined by bulk probes such as SR and SE. SR is well adapted to monitor and control deposition in optical thin-films technology, such as Bragg reflectors for vertical cavity surface-emitting lasers.[3] However, for control purposes one needs not average compositions but fluctuations of these compositions from target values, ideally of just-deposited material in a region where the thickness is ideally vanishingly small. These near-surface data have recently become available through the development of virtual-interface (V-I) theory.[4] Here, kinetic ellipsometric (KE) data and their derivative with respect to layer thickness are used to determine the dielectric response of near-surface material down to the monolayer (ML) level, even if nothing is known about the underlying material.

The potential effectiveness of various control strategies can be assessed by considering the four regions associated with epitaxy: the ambient, surface reaction layer (SRL), the near-surface region (NSR), and the bulk. The ambient consists of the carrier gas (if any) and the nutrient species providing the constituent elements to the growth surface, including possibly thermally cracked and pre-reacted species. The SRL contains both weakly (physisorbed) and strongly (chemisorbed) bound fractions. The NSR consists of the most recently deposited material, and its thickness is defined by instrument sensitivity. Since the ambient feeds the SRL and the SRL feeds the NSR, the nature of the SRL is determined by its interactions with both ambient and NSR. Although for control purposese information about all regions can be used to advantage, it is clear that the weakest and strongest links in the control process are those involving the ambient and near-surface regions, respectively. Control approaches based on wafer-state (SRL[5] and NSR[6-8]) measurements also have the advantages of bypassing the need to accurately measure process parameters and to model the intervening processes leading to species incorporation. In addition, they can automatically correct for small changes as they occur, and are portable, not being affected by the idiosyncracies of a particular reactor.

While monitoring provides useful information, the ultimate goal of real-time diagnostics is wafer-driven closed-loop feedback control of deposition. For structures such as VCSEL mirror stacks that are relatively thick optical films, this is equivalent to endpoint detection. Here, SR is adequate and even desirable, since reflectometers operating in the relative-reflectance mode are relatively simple devices and reflectance measurements require only normal-incidence optical access to the growth surface, minimizing the modifications needed to growth chambers. For composition control, especially involving sub-nm films, it is necessary to use SE, where both phase and amplitude are returned in a single measurement. However, spectroscopic ellipsometers are considerably more complicated than spectroscopic reflectometers, and non-normal-incidence optical access to the growth surface is required, generally requiring in turn modifications of growth chambers. The recent development of rotating-compensator SE systems, replacing the older rotating-analyzer and rotating-polarizer designs, eliminates the possibility of some systematic errors and allows for more compact configurations.[9]

Holding compositions constant is the least demanding version of wafer-driven closed-loop composition control, since averages can be taken over relatively large thicknesses. Using SE and the virtual-interface approach, InGaAs compositions have been held constant to within 0.1% in a multiwafer production OMCVD reactor.[10] Control of compositionally graded materials requires analysis of relatively thin layers, and precision is correspondingly less. The Bellcore group demonstrated ±3% precision in the growth of AlGaAs structures, where the composition was determined by analysis of the outermost 3 A of depositing material.[6] Control of continuously graded compositions has been demonstrated in SiGe and InGaP as well, but reported precisions are lower.[7,8]

The two groups who have grown symmetric compositionally graded structures under sample-driven closed-loop feedback control found that the flow of reactants at the end of the growth of such structures is different from that at the beginning.[6-8] For AlGaAs this was attributed to the gettering of triisobutylaluminum, whereas for InGaP structures the difference appeared to be due to the rate at which trimethylindium (a solid) is picked up by the carrier gas as it passes through the cell. It would obviously be difficult, if not impossible, to model such hysteresis effects. This indicates that the accuracy of a "virtual reactor", where the properties of a sample are predicted via computational models, must be limited at best.

REFERENCES
1. I. P. Herman, **Optical Diagnostics for Thin-Film Processing** (Academic, New York, 1996).
2. D. E. Aspnes and N. Dietz, Appl. Surface Science **130-132**, 367 (1998).
3. K. P. Killeen and W. G. Breiland, J. Electron. Mater. **23**, 179 (1994).
4. D. E. Aspnes, J. Opt. Soc. Am. **10**, 974 (1993).
5. N. Dietz, V. Woods, K. Ito, and I. Lauko, J. Vac. Sci. Technol. **A17**, 1300 (1999).
6. D. E. Aspnes, W. E. Quinn, M. C. Tamargo, M. A. A. Pudensi, S. A. Schwarz, M. J. S. P. Brasil, R. E. Nahory, and S. Gregory, Appl. Phys. Lett. **60**, 1244 (1992).
7. L. Mantese, K. Selinidis, P. T. Wilson, D. Lim, Y. Y. Jiang, J. G. Ekerdt, and M. C. Downer (to be published).
8. M. Ebert, K. A. Bell, S. D. Yoo, K. Flock, and D. E. Aspnes (to be published).
9. J. Opsal, J. Fanton, J. Chen, J. Leng, L. Wei, C. Uhrich, M. Senko, C. Zaiser, and D. E. Aspnes, Thin Solid Films **313-314**, 58 (1998).
10. A. G. Thompson, R. Karlicek, E. Armour, W. Kroll, P. Zawadzki, and R. A. Stall, III-Vs Review **9**, 12 (1996).

Spectroscopic Ellipsometry and Reflectometry: A User's Perspective

Harland G. Tompkins, Jeffrey H. Baker, Steven Smith, Diana Convey

Motorola Labs,
2100 E. Elliot Rd.
Tempe AZ 85284

We discuss how analytical tools in a characterization lab can be used to enhance metrology tools in a fab. The emphasis is on the interaction between a characterization lab and a wafer fab belonging to the same industrial company (as opposed to labs in academia, government labs, original equipment manufacturers, or the manufacturers of optical analytical or metrology tools). Specifically this work will deal with ex situ analysis rather than in situ metrology.

A metrology tool in a fab must be clean, fast, simple to operate, and must be able to measure small features. A classical example is a reflectometry tool.[1] On the other hand, a tool in a characterization lab can handle a much more complex sample, can take a significantly longer time for the analysis, and often has the luxury of using a blanket wafer. The analyst is also available for consulting with regard to optimum samples configuration in order to generate the information required. Our emphasis will be on using spectroscopic ellipsometry in a characterization lab to develop optical constants of unusual material so that this information can be used in a reflectometry tool in the fab.

As we begin, let us consider the reflectometry tool in its mode of operation where the lab interaction is *not* needed. For this example, which we will call Example #0, we consider the measurement of the thickness of well known materials such as thermal oxide, LPCVD nitride, or photoresist on a silicon wafer. The reflectometry spectrum is shown to the right. In this case, the spectrum has lots of structure, the index of refraction is well understood and the extinction coefficient is zero. There are no surprises here and the reflectometry tool must simply determine the thickness. No involvement from outside the fab is required. One simply pushes the button and gets the answer.
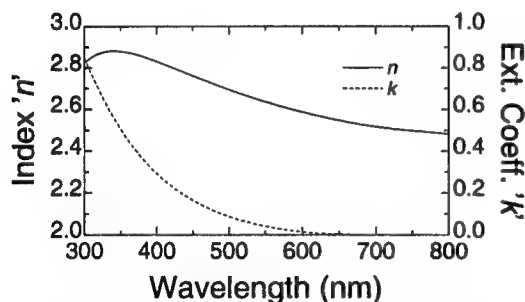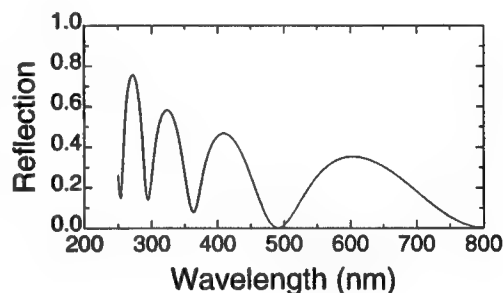
The next example, Example #1, is a situation where a small amount of interaction with a characterization lab is needed. Consider silicon-rich nitride. This might be deposited by either PECVD or LPCVD and the excess silicon is to be added either to control stress properties or to make an anti-reflective coating. The optical functions are shown at left. These are not fixed, as is the case for thermal oxide, but depend on how the material is fabricated. The function of the characterization lab is to determine the optical constants, usually with a variable-angle spectroscopic ellipsometer. A table of the optical constants are then generated and fed into the reflectometry tool in the fab. At that point, as long as the material is fabricated in the same manner, the metrology tool can be used in its normal mode, i.e. fast, simple. We would expect that the characterization lab would model the film using a dispersion equation such as the Cauchy equation, or with the slightly more complex Tauc-Lorentz equation.[2]

For the next example, Example #2, we consider a more complex issue. Optical techniques are not usually used to measure metal films. Historically, metal films have been thick enough to be opaque and if the light does not reach the lower interface, having more material does not change the measured quantity. Metal films with thicknesses less than 300Å are used in several applications, however, and in this thickness range, the films are not totally opaque and can be measured with an analytical or metrology tool. Examples of the use of thin metal films are for MRAM,[3] Flat Panel Displays, Advanced Lithography, etc.

The optical constants of metals depend on the fabrication methods; hence, one must determine the optical constants for the methods used rather than to use handbook values. The dispersion relationship for metal films often cannot be described easily with an equation and the values must be determined for each wavelength used. The difficulty is that for a single film, the problem is underdetermined and there are many combinations of thickness and optical constants with will give equally good fits to the measured data. One of the most powerful analysis methods in ellipsometry is to have several films of the same material, differing only in thickness. We asked the fabricator to deposit four films with target thicknesses in the range of 50 - 300Å. The ellipsometric spectra and resulting optical constants are shown below. Calculated values are also shown for zero thickness and opaque films.
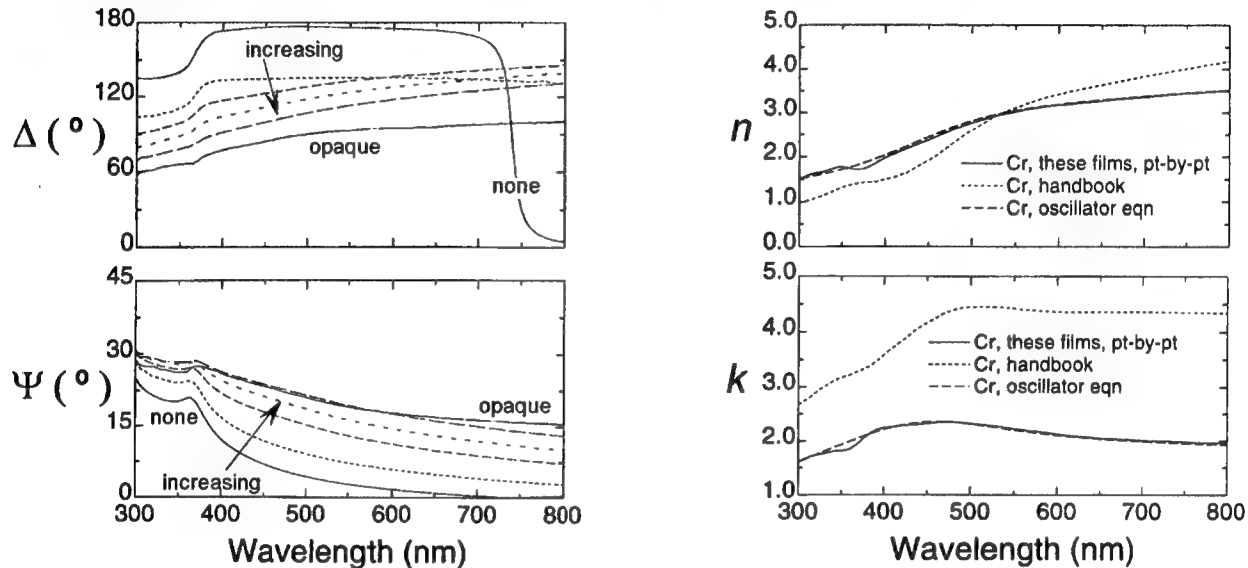
Following the analysis, the optical constants are formatted for the metrology tool and then used in the reflectometry mode. Note that whereas a dielectric film with thickness less than 100Å does not produce a response significantly different from no film, a metal film a few tens of angstroms will change the reflectometry response significantly.

As a final example, we show a possibility for quality control in a fab. Let us consider an amorphous carbon film deposited by PECVD with methane, a small amount of nitrogen, and argon. This material has very little hydrogen and no crystalline structure. As deposited, the carbon has primarily sp^3 bonding. When it is annealed, some of the bonding changes to sp^2. The resulting optical constants are shown to the right after annealing at temperatures ranging from 400 - 1000°C. The material was modeled using the Cauchy/Urbach dispersion equations. It is expected that in the fab, this measurement would be made with a spectroscopic ellipsometer with a fixed number of wavelengths using a CCD array. The function of the characterization lab would be to provide the seed parameters for a Cauchy analysis. The optical constants determined in the fab would be used for quality control of the annealed material.
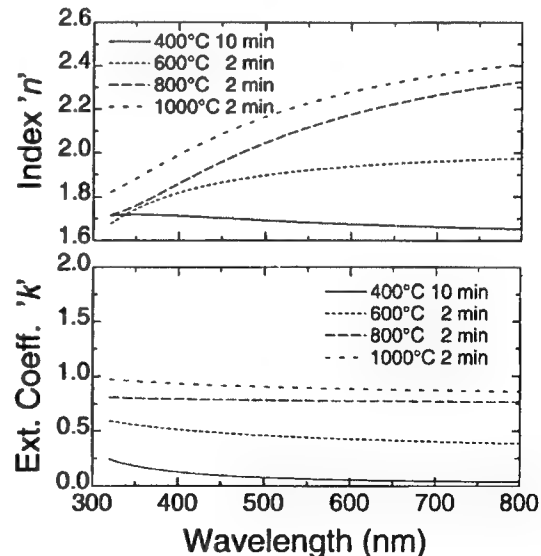
1. "Spectroscopic Ellipsometry and Reflectometry: A User's Guide", H. G. Tompkins and W. A. McGahan, John Wiley & Sons, New York (1999).
2. G. E. Jellison, Jr. and F. A. Modine, *Appl. Phys. Lett.*, **69**, 371 (1966), Erratum, *Appl. Pys. Lett*, **69**, 2137 (1996).
3. H. G. Tompkins, T. Zhu, and E. Chen, *J. Vac. Sci. & Technol. A*, **16**, 1297 (1998).

Optical Sensing Opportunities In Production MBE

Keith R. Evans and Steven P. Roth
IQE Incorporated
119 Technology Drive
Bethlehem, Pennsylvania 18015
Tel/Fax: 610-861-6930/5273
Email: kevans@iqep.com and sroth@iqep.com

MBE has grown from a fundamental research tool for investigating gas-solid interactions in the 1970's, to a basic R&D tool for developing advanced semiconductor device technologies in the 1980's, to a highly successful commercial manufacturing tool in the 1990's. The world market for III-V devices based on MBE and MOVPE wafers in 2000 is estimated to be nearly $9 billion. We estimate that nearly 1 million MBE wafers will be used in 2000 for a variety of commercial applications including those associated with optical data storage, mobile telephony, satellite communications, fiber optic communications, and wireless communications.

Success brings new challenges. The large and growing demand for MBE wafers required for current commercial applications and for development of future applications brings with it a concomitant need to better wafers more rapidly and more cheaply (hence the term "better, faster, cheaper"). Customers not only want low-priced high-quality wafers delivered on time; they want reduced delivery times, reduced wafer property variability, and continuous price reductions over time and volume. Additionally, as device and circuit designers strive to get greater performance from a given technology, there is a tendency to narrow wafer specification tolerances.

Standard new generation high volume MBE systems utilize optical sensors for platen position sensing and transport but not in growth parameter sensing. Still, standard new generation MBE systems provide significant benefits towards realizing better, faster, and cheaper wafers. Wafers are produced faster in large part because of the increased number of wafers grown at one time (higher throughput), and more cheaply because of reduced manpower needs (per wafer) and also because of higher yields (less scrap). Wafer platen transfers are automated thus minimizing human induced variations. Wafers are made "better" primarily due to reduced defects, improved flux stability, and improved uniformities. Such improvements brought about by new generation reactors are primarily due only to scaling up the size of the reactor. Defects are lower due to increased source substrate distance and modest improvements in source design. Increased flux stability results primarily from use of larger cells, which have larger thermal masses. Fluxes are still initially set using ion gauges together with flux vs. source thermocouple setpoint curves with thermocouple setpoints further adjusted based on ex-situ wafer characterization results. Calibration wafers and yielded device wafers (i.e., those that fall outside of wafer specification tolerances) add significant cost to the MBE wafer production effort.

Submitted to *Optical Sensing in Semiconductor Manufacturing*
Meeting of IEEE/LEOS 2000 Summer Topical Meetings

Product mix is an important variable in assessing opportunities for quality enhancement and cost reduction. When MBE production systems are used to produce different products within a campaign, it is necessary to calibrate and qualify the system for each new product lot upon completion of the growth of the last. The ability to move from product to product as efficiently as possible suggests a potentially greater role for optical sensors in a high product mix scenario.

Optical sensing has the potential to enable significant cost reduction and/or quality enhancement via: 1) the ability to impact wafer yield (number of wafers meeting customers spec divided by the total number of wafers grown), and 2) wafer throughput (rate of producing wafers that meet customer spec). Improvements in yield and throughput generally positively impact delivery times as well. Key technological and capacity issues that directly impact MBE process yield and throughput and for which optical sensors could play a role include:

- Vacuum integrity
- Reproducibility and reliability of source shutters
- Lateral and temporal variation in wafer temperature
- Substrate surface cleanliness, crystallinity, and morphology
- Operational efficiency of major heat removal mechanisms (e.g., water and LN2)
- Buildup of source materials and coupling with mechanical disturbances which could affect wafer defect formation via particulate generation
- Source flux compositional makeup including impurities
- Lateral and temporal variation in incident flux
- Source depletion

MBE wafer suppliers naturally focus cost reduction and quality enhancement efforts on opportunities for which the largest potential return on investment (ROI) exists; not all of such opportunities will benefit from optical sensing. To calculate ROI for sensor implementation, costs and benefits must be understood in detail. Detailed and accurate ROI calculations require access to MBE growth yield and throughput data taken under appropriately controlled conditions which most closely match those of the MBE production system under consideration and for the associated manufacturing scenario. Such data largely does not exist today for standard new generation MBE systems yet must be generated before ROI analysis can be completed. Each party - optical sensor supplier, MBE system supplier, and MBE wafer supplier – is motivated to understand the benefits of optical sensing. However, the costs of the underlying experiments are high and significant issues of intellectual property, confidentiality, and propriety are present, all of which present barriers to developing a useful ROI analysis. For these reasons it is proposed that a strategic partnership be formed between optical sensor supplier, MBE wafer supplier, and MBE system supplier, which balances issues of development, costs, intellectual property, confidentiality and propriety. Such a partnership provides a vehicle for carrying out maximally relevant experiments that in turn will lead to a cost benefit analysis that is appropriate for taking optimal decisions regarding implementation of optical sensors in next generation standard MBE production systems.

In Situ Raman Spectroscopic Characterization of Compound Semiconductor Free Carrier Concentration

J. E. Maslar
Chemical Science and Technology Laboratory, National Institute of Standards and Technology
100 Bureau Drive, Stop 8360
Gaithersburg, MD 20899-8360

C. A. Wang and D.C. Oakley
Lincoln Laboratory, Massachusetts Institute of Technology
244 Wood Street
Lexington, MA 02420-9108

Raman spectroscopy has been utilized with great success for *ex situ* characterization of III-V semiconductor epitaxial layers since it provides information about properties such as alloy composition, lattice mismatch, and crystallinity, as well as free carrier concentration and mobility.[1] However, it has been utilized infrequently for *in situ* characterization because of the low sensitivity, high cost, and large footprint of such systems. More recently, developments in detectors, filters, and laser technology now make Raman spectroscopy more attractive as an *in situ* probe. The objective of this work is to develop and evaluate Raman spectroscopy as an *in situ*, spatially resolved probe of compound semiconductor electrical properties for use in process monitoring and control.

In the first phase of this investigation, *ex situ* spectra of doped and undoped films of GaSb, GaAs, InGaAs, and InP were measured. Such semiconductor materials were selected because the different materials properties present different challenges in the interpretation of the Raman spectra. Spectra were generated in a near-backscattering geometry with radiation from argon and krypton ion lasers, appropriate holographic filters, a 0.46 m imaging spectrograph, and a back-illuminated, thermo-electrically cooled, charge coupled device camera. Figure 1 shows *ex situ* Raman spectra at room temperature of two InGaAs layers with carrier concentrations of 8×10^{17} cm^{-3} and 3×10^{18} cm^{-3} as determined by electrical measurements. The coupled phonon-plasmon mode is easily observed in each spectrum. The frequency of this mode increases with increasing free carrier concentration and provides the basis for optical determination of carrier concentration.

In contrast to Hall measurements, Raman spectroscopy does not require fabrication of electrical contacts and can be performed on conducting substrates. This latter aspect of Raman spectroscopy is particularly important when measuring carrier concentrations of materials for which semi-insulating substrates are difficult to obtain such as for GaSb. In this investigation, the carrier concentrations of doped GaSb on semi-insulating GaSb substrates were measured. This is significant because, while actual GaSb-based device structures are grown on GaSb substrates, test structures for GaSb carrier concentration and mobility measurements are grown on semi-insulating GaAs substrates. The assumption is made that the carrier concentration and mobility will be identical for layers of nominally identical dopant concentration regardless of substrate. Our Raman measurements show that this is not always the case.

In the second phase of this investigation, the effects of heating the films will be examined by making *in situ* measurements on selected well characterized epitaxial layers. The films, which have previously been grown, will be placed in an optically-accessible, vertical flow, rotating-disk thermal chemical vapor deposition reactor, and Raman spectra will be recorded from room temperature up to typical growth temperatures of around 600 °C. The reactor will be maintained under typical conditions for deposition, 150 torr of helium, although no growth will be performed.

[1]. B. Prévot and J. Wagner, "Raman Characterization of Semiconducting Materials and Related Structures," *Prog. Crystal Growth and Charact.* 1991, Vol. 22, pp. 245-319.
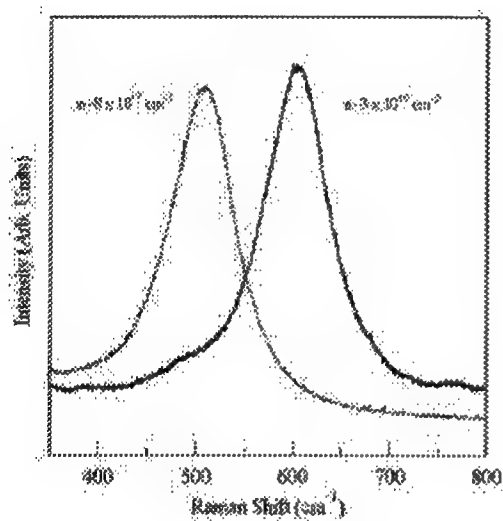
Figure 1. *Ex situ* Raman spectra at room temperature of two InGaAs layers with different free carrier concentrations.

TURNKEY INDUSTRIAL INSTRUMENTATION FOR FAST-RESPONSE, ON-LINE ANALYSIS OF PPB
IMPURITIES IN THE ELECTRONIC SEMICONDUCTOR GASES

Richard T. Meyer, Jorge E. Perez, and Shawn Strickland, CIC Photonics, Inc., 3825 Osuna Rd
NE, #6, Albuquerque, NM 87109, 505-343-9500, www.irgas.com

A totally integrated hardware and software gas analysis system, IRGAS™, is newly available to
the semiconductor process engineer to monitor the ppb quality level of the corrosive and toxic
cleaning and etching gases in real-time and on-line with process tools in a fab plant. The
IRGAS™ system is based upon an industrial-ruggedized FTIR spectrometer coupled with a
nickel-plated stainless-steel long-path-gas-cell containing stainless-steel mirrors coated with a
heavy-layer of reflective-gold over a thick-nickel substrate for chemical corrosion resistance. An
electronically-operated gas handling manifold, pumping system, and computer display package
are provided within a purgeable stainless-steel enclosure for user safety protection; see Figure 1.
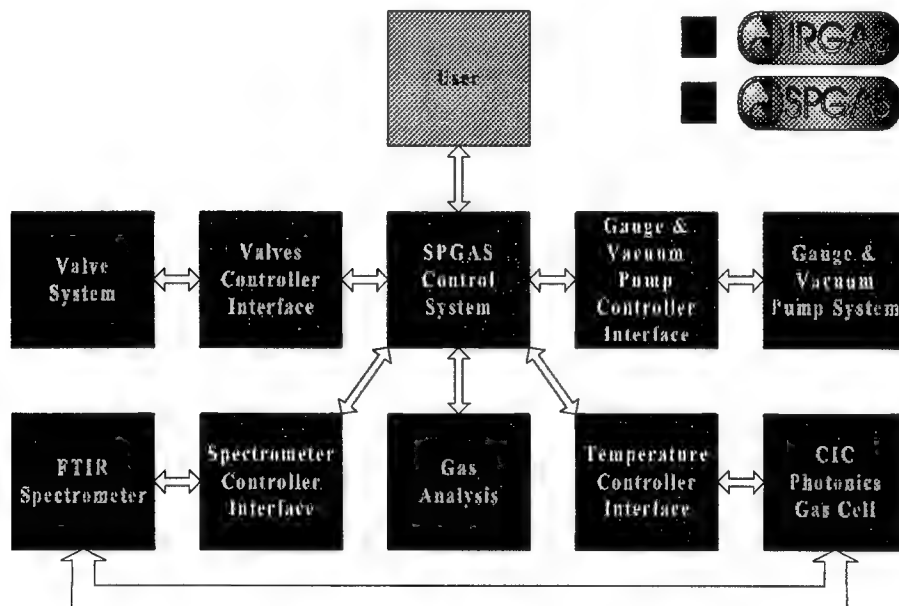
Figure 1 Block Diagram of IRGASTM System Components Managed by SPGAS™ Software

The SPGAS™ software provides both (1) total operational management of all hardware
components and (2) an innovative weighted multi-band, multi-component classical least squares
analysis of impurity gases from an on-board set of gas calibration data. The SPGAS™ permits
the process engineer to monitor any number of impurities simultaneously with preset ppb ranges
specified for normal, alert, and out-of-control indicators, alarms, or signals to a master computer;
see Figure 2 for a typical screen display. Both real-time and past-time readouts and records are
also available for gas cell temperature, pressure, and species concentrations.
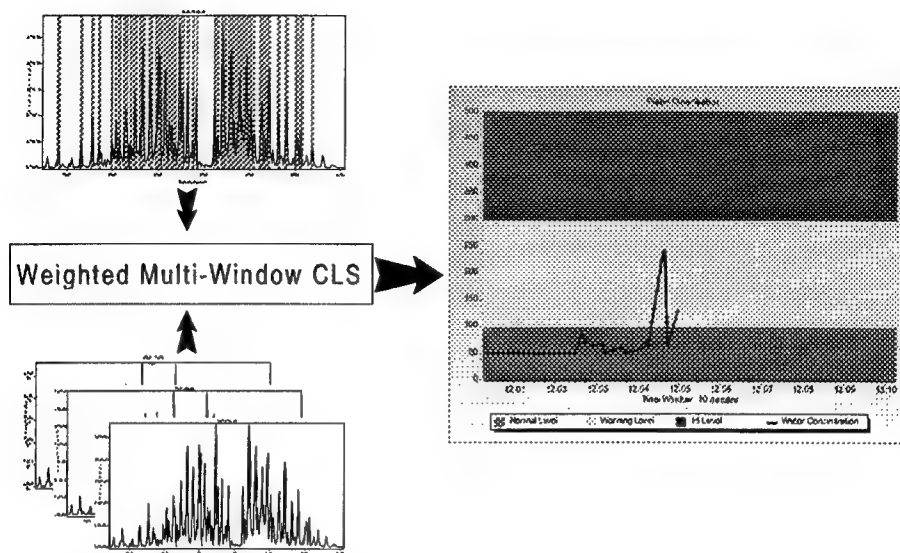
Figure 2 Functional Schematic of SPGAS™ Methodology for Impurity Gas Analysis

Also available is the SpectraStream™ algorithm set which provides for immediate early-detection of changes in impurity levels within seconds. This feature actually generates two time-lines of output from the FTIR spectrometer: the standard multi-scan analysis which generates low-noise data on the time-scale of several minutes and a unique scan-by-scan analysis which displays data within seconds of actual time. This fast-response feature enables the user to alter or stop a process operation before major losses of product occur. Figure 3 shows a simulation for the early detection of moisture as an impurity.
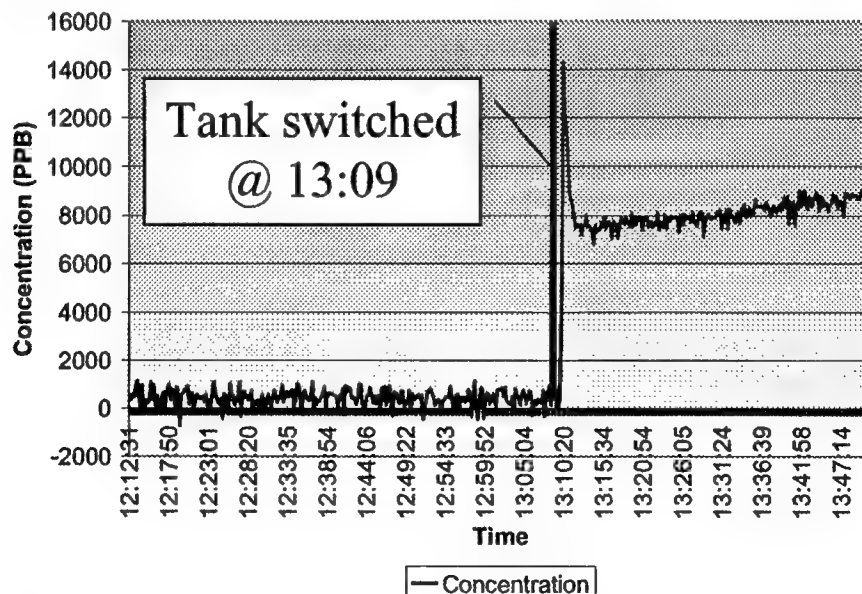
Figure 3 Illustration of Fast-Response Detection of Moisture by SpectraStream™

This turnkey system, which is available in four configurations, can be applied at multiple points of critical gas purity management within a semiconductor wafer manufacturing plant.

Nonlinear optics and spectroscopic ellipsometry as complementary sensors to monitor and control SiGe growth

L. Mantese[1], P.T. Wilson[1], K. Selinidis[2], D. Lim[1], Y. Jiang[1], J.D. Canterbury[1], J.G. Ekerdt[2], M.C. Downer[1]
[1]Department of Physics, University of Texas, Austin, TX 78712
[2]Department of Chemical Engineering, University of Texas, Austin, TX 78712

Due to their unique sensitivity to surfaces and interfaces, nonlinear optical techniques such as second harmonic (SH) and sum frequency generation (SFG) have emerged as powerful and highly versatile spectroscopic probes. With the recent availability of commercial, tunable, femtosecond laser systems, *in-situ*, real-time monitoring of the optical SH responses of Si(001) and SiGe(001) systems has become possible. Such investigations have included single-wavelength SHG monitoring of CVD growth chemistry, including H coverage and desorption at Si(001) in real-time [1,2]. Spectroscopic SH information around the E_1 region of Si has demonstrated adsorbate-specific sensitivity to ML coverages (Fig.1).
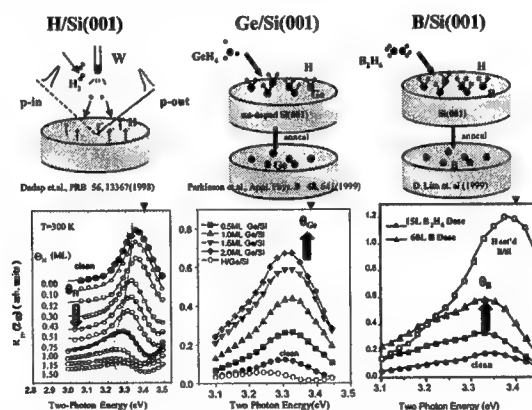
Figure 1. SH spectra of ML and sub ML-covered 2x1-Si(001).

The E_1 peak of Si shifts with increasing Ge composition, as observed in both SH spectra [3] and spectroscopic ellipsometry (SE). This information can be exploited for growth control, by calibrating the dielectric function of SiGe with Ge composition and using the virtual substrate approximation (VSA) developed by Aspnes [4,5]. Real-time growth control of compositionally-graded Si_xGe_{1-x} has been demonstrated using SE [6]. A similar approach is suggested by the sensitivity of SH to Ge composition (Fig. 2). However, the SH spectra acquired in several (~10) minutes by laser tuning are unacceptable for real-time growth applications. To overcome this problem, Wilson et al. [7] have developed a technique for rapid (~1 sec) spectroscopic detection of broadband SH spectra generated by a ~10 fs (~90 nm bandwidth) laser pulse. Real-time measurement and growth control using spectroscopic SH is thus feasible.

In addition, the SH responses of doped Si(001) samples have been investigated [8] and shown to be uniquely sensitive to bulk B doping. Upon *in-situ* B doping to ~5×10^{18}/cm^3, the SH signal increases by about five times and the peak blue shifts toward

3.4 eV. An issue of immediate technological concern that SH may prove able to address is Å-scale gate dielectric information. Erley and Daum's [9] SH results from
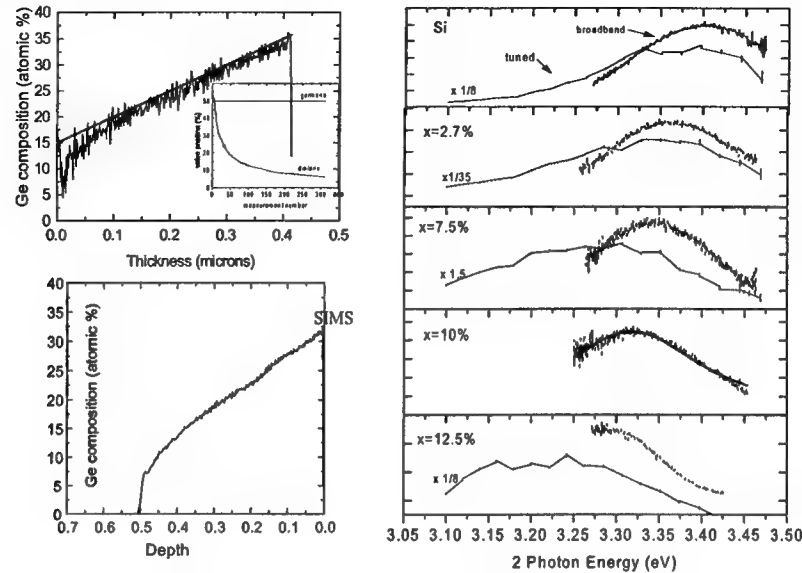
Figure 1. Left panels: Linear growth profile from 15% to 35% Ge composition using SE and VSA analysis with feedback control of the disilane valve. The inset corresponds to the disilane and germane valve positions during growth. The lower left panel shows corresponding post-growth SIMS data for verification. Right panels: SH responses of SiGe with increasing Ge composition. The thin-solid lineshapes were measured using a tuned laser output (acquisition time ~10 min) and the heavy-dashed lineshapes measured using a broadband laser source (acquisition time ~1sec)

SiO_2/Si surfaces show a strongly process-dependent response near 3.6-3.8 eV. A similar investigation of alternative, novel dielectrics using SFG is under investigation.

[1] J. I. Dadap, N.M. Russell, Z. Xu, X.F. Hu, O.A. Aktsipetrov, J.G. Ekerdt and M.C. Downer, *Phys. Rev. B* **56** (1997) 1.
[2] X.F. Hu, Z. Xu, D. Lim, M.C. Downer, P.S. Parkinson, B. Gong, G. Hess, and J.G. Ekerdt, *Appl. Phys. Lett.* **71** (1997) 1376.
[3] P. Parkinson, D. Lim, J. G. Ekerdt, and M. C. Downer, Appl. Phys. B **68** (1999) 1.
[4] D. E. Aspnes, W. E. Quinn, M. C. Tamargo, M. A. A. Pudensi, S. A. Schwarz, M. J. S. P. Brasil, R. E. Nahory and S. Gregory, *Appl. Phys. Lett.* **60**, (1992) 1244.
[5] D. E. Aspnes, *Jour. Opt. Soc. Am. A* **10** (1993) 974.
[6] L. Mantese, K. Selinidis, P.T. Wilson, D. Lim, Y. Jiang, J.G. Ekerdt and M.C. Downer, *Appl. Surf. Sci.* **154-155** (2000) 229.
[7] P.T. Wilson, Y. Jiang, O.A. Aktsipetrov, E.D. Mishina, and M.C. Downer, *Opt. Lett.* **24** (1999) 496.
[8] D. Lim, M.C. Downer, J.G. Ekerdt, N. Arzate, B.S. Mendoza, V.I. Gavrilenko and R.Q. Wu, *Phys. Rev. Lett.* (2000) in press.
[9] G. Erley and W. Daum, *Phys. Rev. B* **58** (1998) R1734.

SCATTEROMETRY APPLIED TO MICROELECTRONICS PROCESSING

John R. (Bob) McNeil
Center for High Technology Materials
Univ. of New Mexico
Albuquerque, NM 87131

In the manufacture of semiconductor devices, storage media, and in other areas, the creation of structures manufactured to pre-defined dimensional tolerances is required. It is therefore essential to have the ability to obtain a precise as well as accurate measurement of the dimensions of these manufactured structures. Precision refers to the ability to repeatedly obtain the same dimensional measurement while accuracy is concerned with the traceability of the measurement to a fundamental dimensional standard. Dimensional metrology of semiconductor structures has, to date, primarily been accomplished through the formation of an image of the structure. The image may be recorded, printed or displayed using a plethora of devices currently available for this purpose. The formation of an image requires the recording of the interaction of an incident radiation or probe with the object whose image is required.

This past decade has also seen the development of a non-imaging optical dimensional metrology technique known as scatterometry. Scatterometry is a non-destructive optical technique that records and analyzes changes in the intensity of light reflected from a periodic scattering surface. By measuring and analyzing the light diffracted from a patterned periodic sample, the dimensions of the sample itself can be measured. Scatterometry exploits the sensitivity of diffraction from a sample to changes in the line-shape of the sample. The use of an elementary sample illumination system, combined with a rigorous scattered signal analysis procedure presents a significant advantage over conventional metrology techniques. These will be discussed in detail in this paper.

Applications of scatterometry technique have included characterization of photomasks[1]; monitoring stepper focus[2] and dose[3]; and the photoresist post exposure bake process[4]; and even the characterization of three-dimensional features such as contact hole and DRAM arrays[5]. The most widely reported scatterometry data have been for measurements of developed photoresist and etched poly-Si gratings[6]. Like other optical metrologies, scatterometry measurements are rapid, non-destructive and highly repeatable.

Although the types of features mentioned above represent a considerable portion of a typical process, other types of materials, such as metal layers, are also commonly present, and are important to characterize. Recent scatterometry measurement data from metal layers will be presented; see Figure 1 below. The scatterometer used in this investigation was the so-called 2-Θ variety, where the scatter signature is obtained by measuring the diffraction efficiency of a particular order as the incident angle is varied. The analysis involved comparing the measured data to a library of theoretical scatter signatures (generated *a priori* from rigorous coupled wave theory) to find the best match. The scatterometer measurements agreed well with AFM measurements performed on the same samples. Details will be presented.

350 A TiN
6000 A AlC
250 A Ti
3000 A oxid

Si Substrate
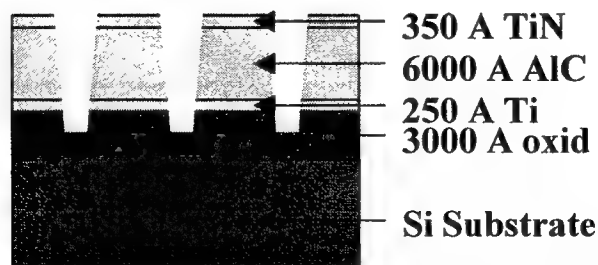
Figure 1. The post-etch and strip stack measured in this study. Note the etch process removes some of the oxide layer.

Another primary consideration of a metrology technique is the measurement repeatability. The scatterometer apparatus is simple, consisting of a laser or white light illumination arrangement and a simple detection arrangement. Because of this simplicity, the technique is inherently repeatable. This is illustrated below in Table 1 for the AlCu sample discussed.

Parameter name	Repeatability (6-sigma)	Reproducibility (6-sigma)	Precision (6-sigma)
Linewidth	0.13 nm	0.45 nm	0.47 nm
AlCu Thk	2.0 A	2.36 A	3.09 A
Etched Ox Thk	1.61 A	1.70 A	2.34 A
Unif Ox Thk	2.0 A	2.02 A	2.84 A

Table 1. Measurement precision data for the etched metal samples.

Measurement precision will also be discussed. Precision is dependent upon two issues: sensitivity of the measured quantity to changes in sample features, such as how the measured intensity changes with changes in line-width, and the measurement precision of the quantity being measured.. The latter is dependent on the particular scatterometer technique employed, and this will be discussed.

REFERENCES

1. S. M. Gaspar-Wilson, S. Naqvi, J. R. McNeil, H. Marchman, B. Johs, R. French, F. Kalk, "Metrology of etched quartz and chrome embedded phase shift gratings using scatterometry," *Integrated Circuit Metrology, Inspection and Process Control IX, Proc. SPIE 2439*, 1995.

2. L. M. Milner, K. P. Bishop, S. S. H. Naqvi, J. R. McNeil, "Stepper focus characterization using diffraction from latent images," *Journal of Vacuum Science and Technology B* 11(4), pp. 1258-1266, 1993.

3. K. C. Hickman, et al., "Use of diffraction from latent images to improve lithography control," *Journal of Vacuum Science and Technology B* 10(5), pp. 2259-2266, 1992.

4. J. Sturtevant et al, "Post exposure bake as a process-control parameter for chemically-amplified photoresist," *Proc. SPIE 1926*, pp. 106-114, 1993.

5. Z. R. Hatab, J. R. McNeil, S. S. H. Naqvi, "Sixteen-megabit dynamic random access memory trench depth characterization using two-dimensional diffraction analysis," *Journal of Vacuum Science and Technology B* 13(2), pp. 174-182, 1995.

6. C. J. Raymond, "Milestones and future directions in applications of optical scatterometry," *Proc SPIE CR72*, pp. 147-177, 1999.

Accuracy and Precision of Scatterometer Measurements Relative to Conventional CD Metrology

T. Hayes [*], R. Bowley [*], M. Littau [+], and C. Raymond [+]

[*] IBM Microelectronics Division, Essex Junction, VT 05452
[+] Bio-Rad CD Systems, Albuquerque, NM 87109

Abstract

Scatterometry is an emerging metrology technique for measuring critical dimensions (CD), profiles, and thicknesses within diffraction gratings printed on semiconductor film stacks. A 2θ scatterometer was used to measure diffraction gratings on two films stacks: 1) Front end of line logic gate stack, and 2) Resist on anti-reflective coating (ARC) on Silicon. The CD measurements of the scatterometer were compared to critical dimension scanning electron microscope (CD-SEM), atomic force microscope (AFM), and cross-section scanning electron microscope (X-SEM) measurements. The correlation between scatterometer and CD-SEM measurements was analyzed using the Mandel technique of Archie and Banke[1] where AFM and X-SEM measurements were used to characterize the "real" properties of the grating. Initial results indicated that the measured CD value by scatterometer and CD-SEM were linearly correlated with a sizeable offset. Further analysis of the correlation shows that the offset was pronounced at grating sidewall angles approaching 90°. The effect of sidewall angle on CD-SEM to scatterometer correlation and results for precision and accuracy on the scatterometer are discussed relative to in-line stepper focus control.

Summary

Semiconductor device performance is controlled by the critical dimension of features printed by lithographic and etch processes. Conventionally, the critical dimension scanning electron microscope (CD-SEM) is used for process control; however, the scatterometer is another technique that has recently become available. The two systems work on entirely different principles.

The CD-SEM uses a focused electron beam that is rastered over an area of interest, where by secondary and backscattered electrons are generated everywhere the beam imparts the sample[2]. The generated electrons are then collected, giving a waveform (1-D) or image (2-D) of intensity versus position which can be analyzed using different algorithms to extract critical dimensions[3]. The operating conditions of the CD-SEM are such that higher magnifications are used for critical dimension measurements; therefore, measurements are performed over small segments of device features.

The scatterometer works on the principle of light diffracted from an array of features.[4,5] At several angles the 2θ scatterometer measures the intensity of the 0th order diffraction intensity, which will vary depending on the film stack and diffraction grating spacing.[6] Rigorous modeling of the optical behavior of the grating as a function of angle can be used to predict the intensity profile for most film stacks and grating spacings. By comparing the measured intensities to the modeled data, film thickness, critical dimension, and sidewall profile information can be determined using the scatterometer. Due to the laser spot size and other optical considerations,

the scatterometer requires a large grating of 80μm x 120μm. Therefore, the reported measurements are an average over the entire grating array.

A wafer was constructed to evaluate the correlation between the CD-SEM and the scatterometer. Diffraction gratings were printed in UV-110 resist on a proprietary front end of line film stack. Gratings were printed with nominal linewidths of 150nm through 500nm at pitches of 2x, 2.5x and 3x. Each grating was printed at various focus and dose conditions using a Nikon 203b stepper system. Scatterometery measurements were made with the Bio-Rad CDS-2 system and compared to measurements taken on the AMAT 7830Si CD-SEM. CDS-2 and 7830Si measurements were linearly correlated with a regression yielding a slope of 1.07, y-intercept of −40.2nm and a correlation coefficient of 0.986; however, the poor correlation was dominated by measurements taken on features with near 90° sidewall angles. Figure 1 shows that the offset between the CD-SEM and scatterometer varies with sidewall angle, indicating that the two techniques interact differently with materials being measured. The sidewall angle dependence is linear between 86° and 90° and can therefore be extracted from the correlations. When sidewall angle information is accounted for the linear regression between systems is greatly improved, yielding a slope of 1.00, y-intercept of 9Å, and a correlation coefficient of 0.998. This effect is discussed relative to accuracy of critical dimension measurements.
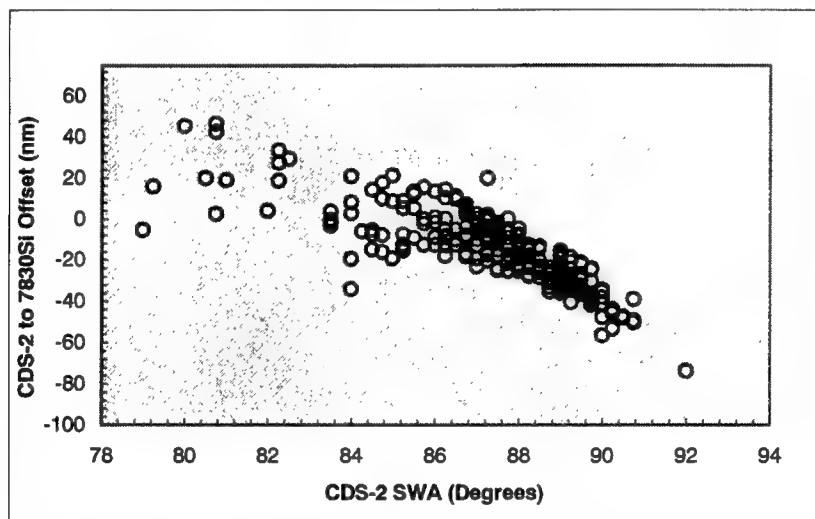
Figure 1. Plot of the difference in measured critical dimensions between the CDS-2 and 7830Si versus CDS-2 determined sidewall angle. The increase in magnitude of the offset with sidewall angle indicates that the two systems interact differently with near vertical sidewalls.

References

1. B. Banke and C. Archie, "Characteristics of Accuracy for CD Metrology,"Scanning Electron Microscopy: CDSEM, Proceedings of SPIE, Vol.3677.
2. J.I. Goldstein et al., Scanning Electron Microscopy and X-Ray Microanalysis, Plenum Press, New York, 1992.
3. M.T. Postek, in Handbook of Critical Dimension Metrology and Process Control, SPIE Optical Engineering Press, Washington, 1994, Vol. CR52, pg. 46-90.
4. D. Haliday and R. Resnik, Fundamentals of Physics, John Wiley & Sons, New York, 1988, pg. 935-940.
5. S. Sohail et al., "Scatterometery and the Simulation of Diffraction-Based Metrology, "Microlithography World, July/August/September 1993, pg. 5-16.
6. C. Raymond et al., "Multiparameter Grating Metrology Using Optical Scatterometery," J. Vac. Sci. Technol. B, 15(2), Mar/Apr 1997, pg. 361-368.

Polarized Light Scattering Techniques for Surface Wafer Inspection

Thomas A. Germer
Optical Technology Division
National Institute of Standards and Technology
100 Bureau Drive, Stop 8442
Gaithersburg, Maryland 20899-8442

Laser light scattering is used in semiconductor manufacturing to inspect product and process-witness wafers for particulate contaminants, defects, and roughness. Typically, a laser beam is focussed onto the wafer surface, and one or more large optics collect light scattered from the surface. As the laser beam is scanned over the wafer surface, background signal is associated with microroughness, while excursions from the background are associated with localized scattering sources, such as particles or subsurface defects. The use of multiple detectors allows some discrimination amongst different classes of light scattering events.

The polarization of scattered light carries with it information, which can substantially improve the ability of these instruments to characterize the light scattering sources. This information is often not fully utilized by these instruments. While the incident laser beam is usually polarized in a manner to accentuate a specific scattering source, analysis of polarization of the resulting scattered light is rarely performed. This summary will outline results, which have shown how the polarization can be used to identify scattering sources.

Light scattered by small amounts of roughness can be interpreted using first-order vector perturbation theory.[1] That theory predicts that the polarization is independent of the details of the surface height function, and that no depolarization occurs. That is, the differential Stokes vector power $d\mathbf{P}_s$ scattered per unit solid angle $d\Omega$ is given by[1]

$$\frac{d\mathbf{P}_s}{d\Omega} = \frac{16\pi^2}{\lambda^4} \cos\theta_i \cos^2\theta_s \ S(\mathbf{q})\mathbf{Q}\mathbf{P}_i \tag{1}$$

where λ is the wavelength of the probing light, θ_i is the incident polar angle, θ_s is the scattered polar angle, $S(\mathbf{q})$ is the power spectral density function of the surface height function, evaluated at surface wavevector $\mathbf{q}$, $\mathbf{Q}$ is a Mueller matrix, and $\mathbf{P}_i$ is the Stokes vector incident power. The Mueller matrix $\mathbf{Q}$ depends only upon the incident and scattering directions, the polarization of the incident light, and the optical constants of the material, and is non-depolarizing. The fact that roughness in the smooth surface limit does not depolarize light enables any scattering instrument to be insensitive to roughness by placing an appropriately aligned polarizer before each detector.[2] While the signal from a rough surface is virtually eliminated by the presence of the polarizers, that from other sources, be it from particulate contaminants or subsurface defects, is reduced by a much lower amount. Calculations of integrated scatter signals, comparing unpolarized detection with polarized roughness-blind detection, have yielded reductions of the minimum detectable diameter for small particles or subsurface defects of approximately a factor of two.[3]

Rough surface scatter not only contributes a background signal when no localized defects are present, but it also interferes with signals in the presence of defects. In any specific scattering direction, the signal when the laser beam is illuminating a particle is a result of the coherent sum of the fields from the particle itself and that from the residual roughness. Since the signals are added as fields, not intensities, a background signal whose intensity is only 1 % of the signal from the particle will contribute as much as 10 % to uncertainty of the net signal. With the polarized roughness-blind configuration, however, the signal measured by the instrument only includes contributions to the scatter from the particle, thereby reducing or eliminating the coherence noise caused by the roughness. This behavior substantially reduces uncertainties in measurements of scatter from standard diameter polystyrene latex spheres, as well as improves the characterization of unknown defects.

Many surfaces requiring inspection have dielectric layers deposited upon them. The scatter from such surfaces can be described as the sum of the scattered fields from the roughness of each interface.[4] Whether these materials depolarize the light or not is related to the degree of correlation between the roughness functions. When the layers are thin, their interfaces tend to be conformal, and the scattering is non-depolarizing. When this is the case, the method described above can successfully remove the entire roughness-induced signal. For thick layers, the roughness of each interface may not be conformal. This lack of interfacial conformity may yield some depolarization, limiting the ability for roughness-blind instrumentation to be fully roughness-blind. Any specific

interface, however, will contribute a polarized signal, so that roughness from a single interface can always be removed. A roughness-blind configuration can always be attained for a specific interface in a dielectric stack.

Eq. (1) has been used extensively to extract roughness functions $S(\mathbf{q})$ from angle-resolved light scattering measurement results. Interpreting such measurements in the presence of dielectric layers is difficult, requiring assumptions about the relative roughness levels and degree of correlation. Since the scatter polarization from two rough interfaces depends upon the roughness of each interface and the degree of correlation between the two interfaces, angle-resolved polarized light scattering can be used to characterize the roughness of two interfaces. Such measurements have been demonstrated with SiO_2 layers thermally grown on rough silicon and show the growth interface smoothening as the layer thickness is increased. [5]

Measurements of the polarization of light scattered by particulate contaminants can provide information about the size of those contaminants. Results using calibrated polystyrene latex spheres on silicon surfaces, [6] and on silicon surfaces with dielectric layers, [7] have shown that the polarization of the scattered light is a strong function of the size of the contaminants. While size of particulate contaminants is typically obtained by interpreting the intensity of the scattered light, the results can only be correlated to that scattered by calibration particles, which are typically polystyrene latex spheres. The results of theoretical calculations demonstrate that the factor that dominates the polarization of light scattered by small particulates is the mean distance the particle lies from the surface. [6,7] Application of these findings should substantially improve the ability for light scattering instruments to characterize real-world particulate contaminants.

References

1. D. E. Barrick, *Radar Cross Section Handbook*, (Plenum, New York, 1970).

2. T. A. Germer and C. C. Asmail, "Microroughness-blind hemispherical optical scatter instrument," United States Patent #6,034,776 (Mar. 7, 2000).

3. T. A. Germer, "Polarized Light Scattering and its Application to Microroughness, Particle, and Defect Detection," in *Characterization and Metrology for ULSI Technology,* D. G. Seiler, A. C. Diebold, W. M. Bullis, T. J. Shaffner, R. McDonald, and E. J. Walters, Eds., Proc. AIP **449**, 815-818 (1998).

4. J. M. Elson, "Multilayer-coated optics: guided-wave coupling and scattering by means of interface random roughness," J. Opt. Soc. Am. A **12**, 729-742 (1995).

5. T. A. Germer, "Measurement of roughness of two interfaces of a dielectric film by scattering ellipsometry," submitted for publication (2000).

6. L. Sung, G. W. Mulholland, and T. A. Germer, "Polarized light-scattering measurements of dielectric spheres upon a silicon surface," Opt. Lett. **24**, 866-868 (1999).

7. L. Sung, George W. Mulholland, and Thomas A. Germer, "Polarization of light scattered by spheres on a dielectric film," in *Rough Surface Scattering and Contamination,* P.-T. Chen, Z.-H. Gu, and A. A. Maradudin, Eds., Proc. SPIE, **3784**, 296-303 (1999).

Optical Sensing in Semiconductor Manufacturing

Wednesday, 26 July 2000

WB1:   Epitaxial Growth Control and Temperature
WB2:   Temperature

In-Situ Spectral Ellipsometry Monitoring/Control of MBE Growth

K. G. Eyink, W. T. Taferner , K. Mahalingam, D. L. Dorsey, S. Adams, Sensors and Survivability Directorate AFRL/MLPO Wright-Patterson AFB, OH 45433

Spectroscopic Ellipsometry (SE) has received considerable attention for semiconductor growth monitoring and control due to its ability to determine the thickness and composition of thin parallel layers. In this work, we report on the use of spectroscopic ellipsometry for monitoring and control of AlGaAs growth in molecular beam epitaxy. Knowledge of the optical constants as a function of composition and growth parameters is essential for modeling to be able to extract the composition and growth rate from measured SE data. For this work, we have used the composition and temperature dependent optical database of $Al_xGa_{1-x}As$ developed by G. Maracas[1]. We have used the virtual interface approximation to extract the growth rate and composition of of $Al_xGa_{1-x}As$ films grown at normal and elevated temperatures. At elevated temperatures, Ga possessed a sticking coefficient less than 1. Figure 1 is a plot of the percent Ga desorption measured by SE and desorption mass spectrometry. Below 900K Ga was observed to grow at a constant rate. At elevated temperatures the Ga growth rate decreased until at 940K no continued growth was observed. Under all conditions SE accurately predicted the observed growth rates.
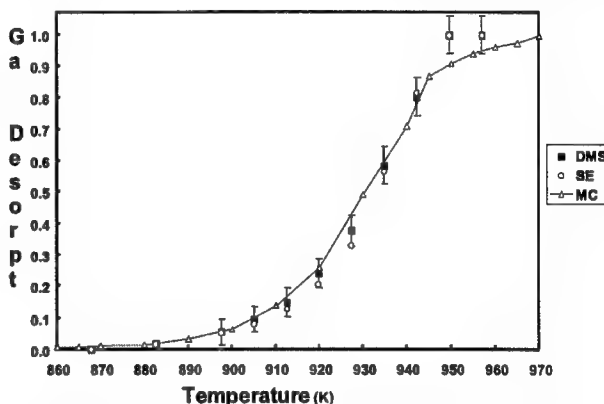
Figure 1. The percentage of Ga desorption as a function of growth temperature

Our control software was modified to use real-time SE data to target pre-determined growth rates for Al and Ga by adjusting the cell temperatures. As part of this effort a Guide Evolutionary Stimulated Annealing algorithm has been developed for real-time optimization of a growth model[2]. Figure 2 is a plot of an extracted Al composition using the GESA algorithm from an $Al_xGa_{1-x}As$ growth in which the target composition was changed from 0.25 to 0.35. After an initial settling, the composition tracked with a precision of better than 0.005 in the standard deviation. For our current applications, compositional

Figure 2. A pot of the extracted composition during a set point change from 0.25 to 0.35 was given to the control system. The associated Ga cell temperature is also given.

control of 1% was sufficient. This technique and the standard Marquardt-Levin (M-L) approach

gave similar precision during tracking. A small difference in the absolute number was observed which was traced to the smaller range of wavelength used in the GESA than the M-L approach.

It was also observed that the GESA algorithm was less likely to get stuck at a local minimum that the M-L method.

Using SE to accurately measure in-situ growth rates and compositions, a timing sequence for AlGaAs/GaAs could be made. A Be-doped quantum well infrared photodetectors structures was made with the SE precalibration. These QWIPS achieved the target absorption edge of ~9μ as measured by photoconductivity[3]. This indicated that in-situ pre-calibration using SE was an effective approach for growth control. The ability of in-situ pre-calibration to grow compositonally graded structures was also tested. We grew a parabolic and trapezoidal $Al_xGa_{1-x}As$ structure using the dependence of the composition and growth rate on the Al and Ga effusion cell temperatures. The effusion cell growth rate dependence was measured using the in-situ SE. Figure 3 shows the calculated temperature profile needed to

Figure 3. (Top) Temperature profile used to make a trapezoidal and parabolic structure. (Bottom) Composition, x_{Al} extracted in real-time.
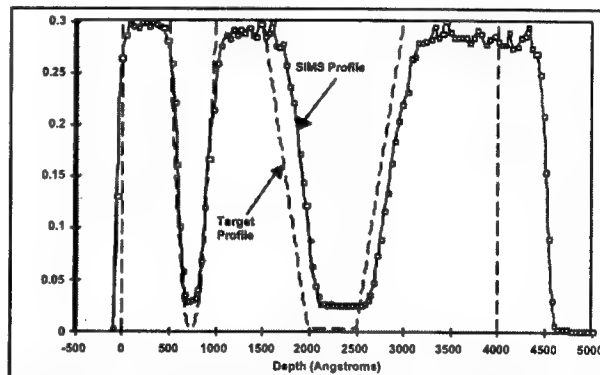
Fgure 4. The SIMS(o) depth analysis of the parabolic and trapezoidal structures plotted with the target profile (-). Note these curves are inverted from those in figure 3.

achieve the parabolic and trapezoidal structures. The associated SE data shows that the in-situ x composition approximately followed the expected profile. We currently believe the overall poor SE monitoring is due to constant composition of the film used in the virtual interface model. We are currently exploring this assumption. Figure 4 shows the SIMS analysis of these profiles. As can be seen the structures approximately fit the compositional profile for the parabolic structure. A lag in the cell response appears more evident in the latter trapezoidal profile. From this analysis it is not certain if pre-calibration is adequate for graded compositions and suggests that real-time feedback maybe required for grading.

[1] G. Maracas et al JVST B12 (1994) p1214.
[2] Z. Meng et al, *Computational Intelligence Procedures for Monitoring and Control of MBE Growth of Arbitrary Film Structures,* AIRTC 98 Conference Proceedings. October 5-8 (1998).
[3] Submitted to at ICMCTF 2000 in San Diego

Real-Time Control of Substrate Temperature Using Band Edge Thermometry

S. R. Johnson, M. Beaudoin, M. Boonzaayer, E. Grassi, and Y. H. Zhang
Center for Solid State Electronics Research, Department of Electrical Engineering,
Arizona State University, Tempe, AZ 85287-6206
Tel: 602-965-2565, Fax: 602-965-8118, E-mail: shane.johnson@asu.edu

In epitaxial growth, the sensitivity of material properties to growth temperature means that an accurate and reliable method for measuring substrate temperature is essential. Recently, optical methods have been developed that overcome some of the limitations of thermocouples and pyrometers [1-3]. Pyrometry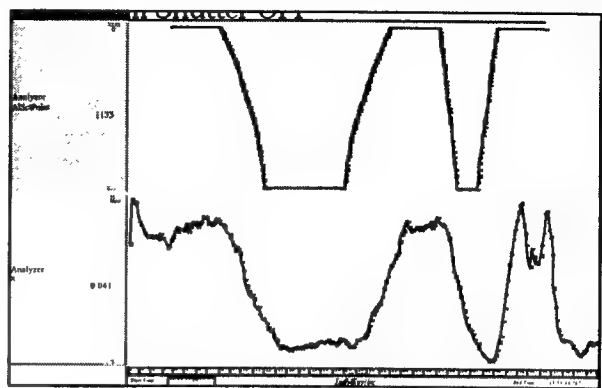 for example, does not work at low temperatures, is affected by surface roughness, window coating, and substrate emissivity changes during growth. Since both rotating and radiatively heated substrates are preferred during epitaxial growth, physical contact between the substrate and the temperature sensor is not practical. Therefore, thermocouples are radiatively coupled to the substrate and consequently have a large temperature offset compared to the substrate. Furthermore this offset depends on substrate and heater temperature, substrate back surface texture, doping level, and doping type, and on the changing absorptance and emittance of the epilayer during growth.
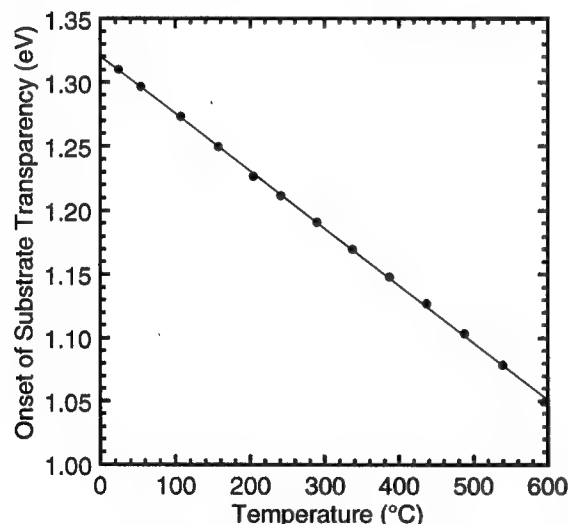
Fig. 1. The temperature dependence of the onset of transparency of a 350 µm thick InP:Fe substrate.

In these new optical methods, substrate temperature is inferred from the onset of transparency of the substrate its self. The band edge of III-V semiconductors cuts off exponentially and broadens and shifts to lower energies with temperature [4]. This band edge shift (or bandgap shrinkage) is linear in temperature above the Debye temperature (see Fig. 1). In practice, substrate temperature is inferred from the spectral position of various points in the diffuse reflectance spectrum [1] or transmission spectrum [2,3]. The onset of transparency of a 350 µm thick InP:Fe substrate is shown in Fig. 2. Here, the onset of transparency (or position of the spectrum) is defined as the intersection of the background signal with a linear extrapolation through the steepest part of the spectrum.
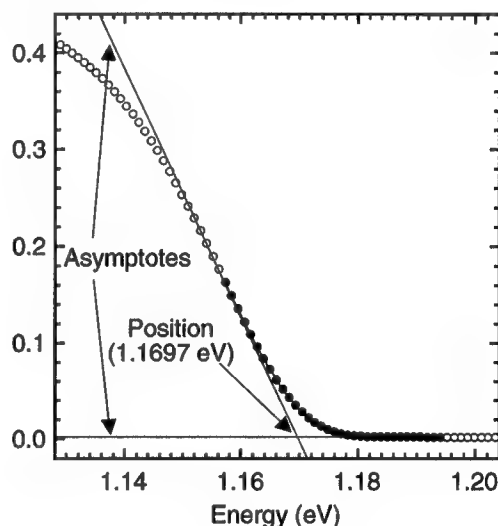
Fig. 2. The position of the spectrum and hence substrate temperature is given by the intersection of the asymptotes of the knee region of the spectrum. The knee region is shown by the solid dots.

The nested loop approach shown in Fig. 3 is a convenient way to add an accurate external temperature sensor to the conventional Eurotherm-thermocouple control loop found in molecular beam epitaxy systems. In this case, the outer control loop updates the Eurotherm (thermocouple) setpoint based on the difference between the user setpoint and the value measured by the external sensor, using a proportional-integral-derivative (PID) algorithm implemented in control software. This method has the advantage that the Eurotherm-thermocouple control system is left intact, so that, in the event the external sensor or control computer fails, the heater power will continue to be controlled.
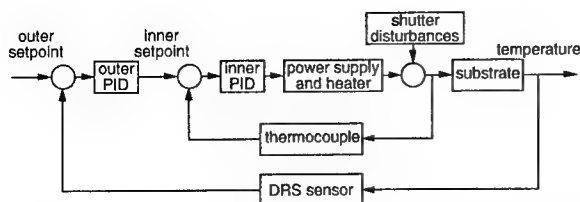
Fig. 3. Schematic of the nested proportional-integral-derivative (PID) control loop used to control substrate temperature.

The Eurotherm-thermocouple (or inner) loop primarily controls the heating element and is limited in its ability to detect and control true temperature of the substrate. This inability also means that the Eurotherm-thermocouple control loop only partially rejects external disturbances, such as the thermal-shutter transients that occur at the substrate when effusion cell shutters are toggled. In this control scheme, the outer loop periodically updates the thermocouple setpoint, causing the Eurotherm control loop to bring substrate temperature back in line with its target value.

During the growth of absorbing overlayers, radiatively heated substrates are known to heat up dramatically as the layer becomes thicker [5]. This occurs under either constant heater power or constant thermocouple temperature. Under these growth conditions, it is imperative that one has an alternative non-contact method of determining substrate temperature, such as, diffuse reflectance spectroscopy (DRS).

Thermocouple temperature, substrate (DRS) temperature, and heater voltage recorded during the growth of lattice-matched InGaAs on InP are shown in Fig. 4. The supervisory computer samples the DRS temperature every 30 s, if the DRS temperature has deviated more than $\pm$ 1 °C from the substrate setpoint of 435 °C, the outer PID loop updates the Eurotherm (inner) setpoint. Throughout most of the growth of the InGaAs layer, the substrate temperature is about 1 °C above its setpoint. Decreasing the update time would bring the substrate temperature closer to the setpoint during the first part of the growth. As can be seen in Fig. 4, each time the thermocouple setpoint is updated, there is a sharp drop in the heater voltage and the thermocouple temperature quickly moves to its new setpoint. The thermal response of the thermocouple-heater system is fast (4 s time constant) compared to the thermal response of the substrate (60 s time constant). This allows appropriate control action.

The thermocouple is insensitive to the substrate temperature increase caused by the

strong absorption of heater radiation in the overlayer. The small-bandgap epilayer absorbs a larger part of the heater radiation spectrum than the InP substrate, which is transparent to most of the blackbody spectrum at these temperatures. Therefore, as the InGaAs layer thickens, the transmission losses of heater radiation are reduced. In order to maintain constant substrate temperature, the control system continually reduces the heater power by decreasing the Eurotherm (thermocouple) setpoint over the course of the growth.
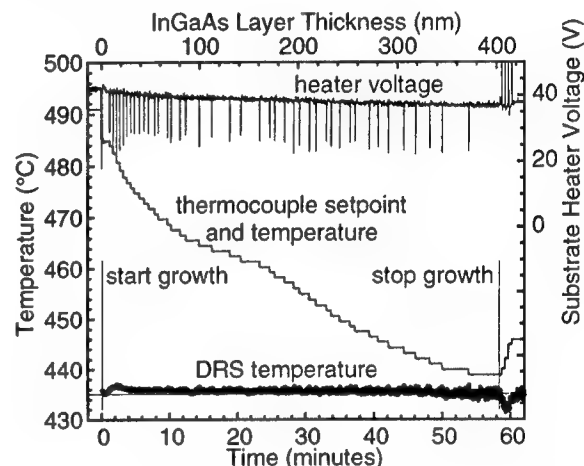

Fig. 4. Real-time control of substrate temperature during the growth of lattice-matched InGaAs on semi-insulating InP, using diffuse reflectance spectroscopy (DRS). The substrate setpoint is 435 °C.

The small oscillations in the substrate temperature at the start and stop points are caused by the abrupt changes in the thermal load on the substrate when the In and Ga cells are toggled. At the start of growth the thermocouple setpoint is reduced by 6 °C in an effort to correct for the thermal disturbance caused by additional radiant heat load of the In and Ga effusion cells. This is the simplest way of rejecting thermal disturbances. At the end of the growth, no shutter disturbance rejection is used and the substrate momentarily drops 4 °C below the setpoint.

[1] S. R. Johnson, T. Tiedje, J. Crystal Growth, **175/176**, 38 (1997).
[2] J. A. Roth, T. J. DeLyon, M. E. Adel, Mat. Res. Soc. Symp. Proc. **324**, 353 (1994).
[3] E. S. Hellman, J. S. Harris, J. Crystal Growth, **81**, 38 (1987).
[4] S. R. Johnson, T. Tiedje, J. Appl. Phys. **78**, 5609 (1995).
[5] B. V. Shanabrook, J. R. Waterman, J. L. Davis, R. J. Wagner, Appl. Phys. Lett., **61**, 2338 (1992).

Substrate Temperature Measurement and control by Emissivity Compensated Pyrometry during Metalorganic Vapor Phase Epitaxy of III-V Device Structures in Large Scale Rotating Disc Reactors

J.C. Ramer, B. Patel, V. Boguslavskiy, A. Patel, M. Schurman, A. Gurary
EMCORE Corporation, 394 Elizabeth Ave., Somerset, NJ 08873

The growth process for many III-V semiconductor devices is quite temperature sensitive. In fact, the temperature window for some of the more challenging device structures, such as InGaAsP/InP infrared laser diodes, and InGaP/GaAs heterojunction bipolar transistors, can be as narrow as 2-3 °C, depending upon how tight the final device specifications are. Clearly, measurement and control of the growth temperature in a MOVPE production environment is critical to maintaining high yields from the growth process.

We have solved this problem by using a pyrometric technique known as Emissivity Compensated Pyrometry (ECP) [1]. Simply stated, this in-situ measurement technique requires the combined functionality of a conventional pyrometer and a reflectometer. The reflectance of the substrate is measured at the same wavelength that the pyrometer measures the thermal radiance. By using the equation

$$\varepsilon = 1\text{-}R \qquad\qquad (1)$$

the spectral directional emissivity of the substrate surface can be calculated from the measured spectral directional reflectivity. This allows the measured thermal emission to be constantly corrected for the changing emissivity of the growth surface. In this way, the accurate temperature of the substrate can be measured at any time during growth.

The ECP sends measured emissivity and temperature values to a Windows NT based PC running a proprietary sorting and averaging algorithm. Emissivity and temperature values are sent to the computer every 25 ms. During growth, the wafer carrier is spinning at 800 RPM, meaning that measurements will be made both on the substrates, and on the wafer carrier surface. Since the reflectometer is calibrated to perform measurements on specular substrate surfaces, all measurements on the diffuse wafer carrier surface result in 100% emissivity measurements, so sorting and discarding the emissivity/temperature measurements made on the wafer carrier surface is quite straightforward. After removing measurements made of the wafer carrier surface, the system displays the temperature and emissivity of the substrates constantly throughout the growth run. The measurement is not synchronized with the rotation of the wafer carrier, so the measured temperature (and the emissivity) is an average temperature of all the substrates on the wafer carrier. The directional spectral emissivity measurement is calibrated by loading calibrated undoped Si substrates onto the wafer carrier, and setting the emissivity measurement to the known spectral directional emissivity of undoped Si at 905 nm (ε = 68%) [2]. All emissivity measurements made by the system are indexed to this reference point.

The growth experiments described in this work were performed on an EMCORE Discovery 180 production MOCVD reactor [3]. A 6x2" wafer configuration was used for most of the experiments, although much data was taken using 3x3", and 1x6" wafer configurations as well. It is important to note that much commercial laser diode production ($Al_xGa_{1-x}As$, $In_xGa_{1-x}As_{1-y}P_y$, and $In_xGa_{1-x}P$) is currently done on reactors of this size. The reactor is a vertical flow reactor, with 3 normal incidence viewports mounted on the top injection flange. The viewports are approximately 12 inches from the growth surface.

An example of the emissivity and temperature measurement of the growth surface during a deposition run is shown in the data in Figure 1. The structure grown is a simple InP/InGaAsP/InP doubleheterostructure. The quaternary material is lattice matched to InP ($\Delta a/a$ = -500 ppm) and the PL wavelength of the structure is approximately 1310 nm. Since the As:P ratio in the solid material is very sensitive to temperature (because the pyrolysis efficiencies of PH3 and AsH3 are very different at common growth temperatures), this kind of structure is an excellent epitaxial metric for in-situ temperature measurement.
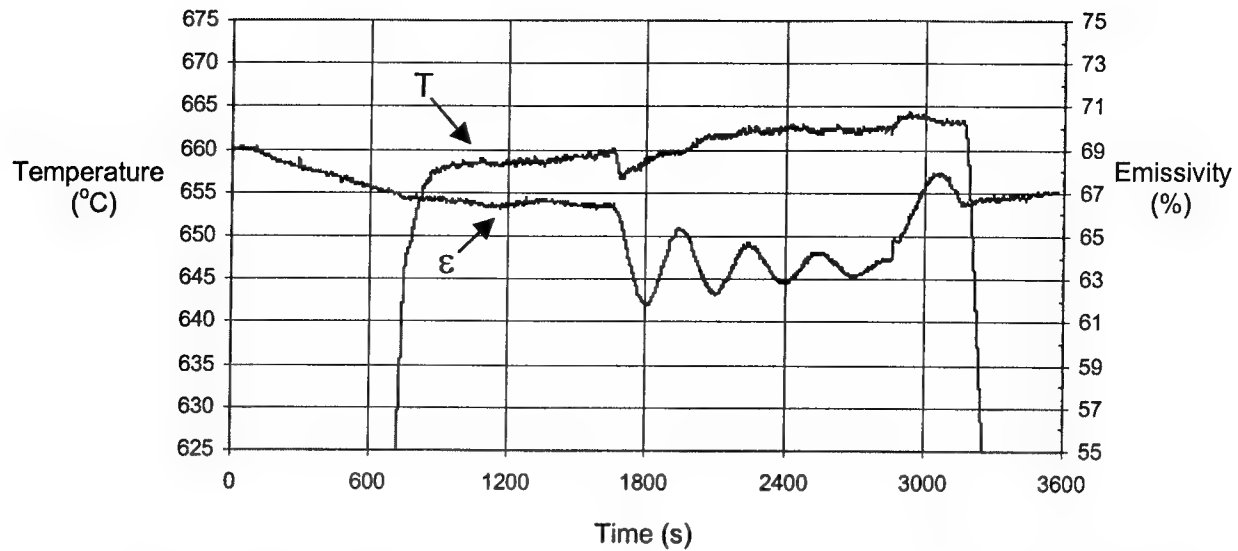
Figure 1: Substrate temperature and emissivity data for a InP/InGaAsP/InP lattice match calibration structure. The lower curve is the emissivity. Note that the entire growth takes place with fixed thermocouple setpoints.

In order to determine the precision of the ECP temperature measurement, two growth runs were done on different substrates using the same thermocouple setpoints. As seen in the data in Table I, a 30% increase in the doping level of the substrate, in this case Sulfur doped InP, results in a substrate temperature increase of 2.5 °C, which results in a ~7 nm PL wavelength shift. With the in-situ temperature measurement, the cause of the change in PL wavelength can be attributed to increased free carrier absorption in the substrate with the higher doping level.

substrate	doping level (cm^{-3})	substrate temperature (°C)	InGaAsP PL λ (nm)
InP:S	5.4e18	664.5	1338.3
InP:S	4.15e18	662.0	1345.0

Table I.: Sensitivity of substrate temperature to doping level in InP:S substrates. Identical process conditions were used for both deposition runs; the only difference is the substrate doping level. (Note: higher substrate temperature results in lower As:P ratio in the solid, which causes the lower PL wavelength.)

The precision and accuracy of this temperature measurement technique is sufficient to ensure that the surface temperature of the substrate can be held within a window of +/-1 °C for many months of continuous operation. Results from temperature sensitive epitaxial metrics such as Zn doped InGaAlP and compositionally sensitive InGaAsP structures show that the temperature of the substrate measured by ECP correlates with post growth characterization measurements of the temperature sensitive properties of these materials.

It is also worth mentioning that since the ECP system measures the normalized reflectance of the wafer surface during growth, the data generated also allows the calculation of the growth temperature optical constants (n and k) and the growth rate of thick layers. Using the virtual interface method of Breiland and Killeen [4] to fit the reflectance data, we estimate that the growth rate can be determined with an error of < 1%, for layers thicker than λ/n.

The ECP system has been applied to a wide range of reactor sizes, from 75 mm disc to 400 mm disc, with similar results. The same hardware and software configuration can be used on any reactor size, regardless of wafer size or arrangement on the wafer carrier, since there is no synchronization required with the disc rotation mechanism. This temperature measurement system will allow users of vertical rotating disc reactors to achieve much tighter control of temperature sensitive processes.

References:
1. I.P Herman, in *Optical Diagnostics for Thin Film Processing*, (Academic Press, 1995) p. 609-614.
2. P.J. *Timans, The Thermal Radiative Properties of Semiconductors, Advances in Rapid Thermal and Integrated Processing*, (Kluwer Academic Publishers, 1996), p. 35-101.
3. A.G. Thompson, Materials Letters 30, 255 (1997).
4. W.G. Breiland and K.P. Killeen, J. Appl. Phys. 78(11), 6726 (1995).

AUTHOR INDEX

Adams, S.	WB1.1	Mackrodt, P.	MB1.1
Amirtharaj, P.	MB4.2	Mahalingam, K.	WB1.1
Anderson, H.	MB3.3	Mantese, L.	TuB3.1
Armstrong, J.	MB4.2	Marinenko, R.	MB4.2
Aspnes, D.	TuB1.1	Maslar, J.	TuB2.2
Baker, J.	TuB1.2	McAndrew, J.	MB1.3
Barwood, G.	MB1.1	McNeil, B.	TuB3.2
Beaudoin, M.	WB1.2	Meyer, R.	TuB2.3
Benyon, R.	MB1.1	Oakley, D.	TuB2.2
Bertness, K.	MB4.2	Patel, A.	WB2.1
Boguslavskiy, V.	WB2.1	Patel, B.	WB2.1
Boonzaayer, M.	WB1.2	Paul, A.	MB4.2
Bowley, R.	TuB4.1	Pellegrino, J.	MB4.2
Breiland, W.	MB4.1	Perez, J.	TuB2.3
Canterbury, J.	TuB3.1	Rabinowitz, P.	MB1.2, MB2.1
Convey, D.	TuB1.2	Ramer, J.	WB2.1
Dorsey, D.	WB1.1	Ramus, T.	MB3.1
Downer, M.	TuB3.1	Raymond, C.	TuB4.1
Dudek, J.	MB1.2, MB2.1	Raynor, M.	MB3.1
Edwards, C.	MB1.1	Robins, L.	MB4.2
Ekerdt, J.	TuB3.1	Roth, S.	TuB2.1
Evans, K.	TuB2.1	Rubloff, G.	MB3.2
Eyink, K.	WB1.1	Schirmer, B.	MB1.1
Funke, H.	MB3.1	Schurman, M.	WB2.1
Germer, T.	TuB4.2	Selinidis, K.	TuB3.1
Gill, P.	MB1.1	Silver, J.	MB2.2
Grassi, E.	WB1.2	Smith, S.	TuB1.2
Green, D.	MB3.2	Stevens, M.	MB1.1
Gurary, A.	WB2.1	Strickland, S.	TuB2.3
Hayes, T.	TuB4.1	Taferner, W.	WB1.1
Hein, S.	MB3.1	Tompkins, H.	TuB1.2
Houlding, V.	MB3.1	Wang, C.	TuB2.2
Hovde, C.	MB2.2	Wilson, P.	TuB3.1
Inman, R.	MB1.3	Wo, Y.	MB1.2
Jiang, Y.	TuB3.1	Yan, W.-B.	MB1.2, MB2.1
Johnson, S.	WB1.2	Zhang, Y.-H.	WB1.2
Kirk, R.	MB3.1	Znamnensky, D.	MB1.3
Lehmann, K.	MB1.2, MB2.1		
Lim, D.	TuB3.1		
Littau, M.	TuB4.1		
Looney, J.	MB3.2		

2000 IEEE/LEOS
Summer Topical Meeting

26 - 27 July 2000

Electro-Optics in Space

Turnberry Isle Resort & Club
Aventura, FL

The papers in this book comprise the digest of the meeting mentioned on the cover and title page. They reflect the authors' opinions and are published as presented and without change in the interest of timely dissemination. Their inclusion in this publication does not necessarily constitute endorsement by the editors, the Institute of Electrical and Electronics Engineers, Inc.

Electro-Optics in Space

Co-Chairs:

Linda DeHainaut, *Air Force Research Laboratory*, Kirtland AFB, NM
James B. Breckinridge, *Jet Propulsion Laboratory*, Pasadena, CA
David Schwamb, *The Boeing Company*, Canoga Park, CA

Technical Program Committee:

L.N. Durvasula, *DARPA/TTO*, Arlington, VA
A. Duncan, *Lockheed Martin*, Sunnyvale, CA
D. Dyer, *Schafer Corporation*, Arlington, VA
J. Harvey, *CREOL/University of Central Florida*, FL
R. Jain, *University of New Mexico*, Albuquerque, NM
T. Kreifels, *Jackson & Tull*, Albuquerque, NM
J.M. Sasian, *University of Arizona*, Tucson, AZ
D. Williamson, *MIT Lincoln Laboratory*, Lexington, MA
N. Wallace, *TRW Space & Electronics Group*, Redondo Beach, CA

TABLE OF CONTENTS

Electro-Optics in Space

Wednesday, 26 July 2000

WD1:   Space Applications and Enabling Technologies
WD2:   Space-Based Communications
WD3:   Novel Imaging Approaches

<u>Wednesday Missing Papers</u>

WD2.2   "High Rate Space Laser Communications" R. Bondurant, *MIT Lincoln Laboratory, Lexington, MA, USA.*

Lasers and Space Optical Systems (LASSOS) Study: Application and Enabling Technologies

C. Giuliano, R. Berdine, R. Benedict, M. Hallada,
D. Johnston, and J. Piotrowski

Air Force Research Laboratory/Directed Energy,
Schafer Corporation,
United States Air Force, Retired

The Laser and Space Optical Systems (LASSOS) study gathered inputs from military users and technologists to identify over a hundred promising weapon and non-weapon applications for lasers and optical systems which make use of the space environment – either based in space or transiting space. Key enabling technologies for these applications, as well as roadmaps to develop them, as needed, were also identified. Thirty-six high interest concepts were selected during Phase I of the study and nine were examined in more detail in Phase II. Potential multi-mission implementations were investigated and potential acquisition strategies and demonstrations were suggested. A more detailed investigation of the multi-mission utility of relay mirrors was recommended. Study results were briefed to the Air Force Major Commands, from which requirements advocacy was sought. Expanded interactions between warfighters and technologists, as experienced during the study, were encouraged.

LASER SPACE COMMUNICATIONS

Ronald L. Phillips
Florida Space Institure
(407) 730-2601
FAX: (407) 658-5595
E-mail: fsiccas@mail.ucf.edu

Compared with conventional RF systems, there are several significant advantages offered by laser communication (lasercom) systems in space applications that are simple consequences of the short wavelengths (high frequencies) associated with optical waves. Among these advantages are (*i*) smaller antenna (telescope), (*ii*) smaller size and weight of the components, (*iii*) power concentration in a very narrow beam, and (*iv*) the potential increase in modulation bandwidth. The last advantage is particularly important because the amount of information transmitted by a communication system is directly related to the bandwidth of the modulated carrier, which is usually some fraction of the carrier frequency itself. Hence, increasing the carrier frequency has the potential to increase the information capacity of the system (higher data rates). Applications that could benefit from lasercom are those that have platforms with limited weight and space, require very high data links, and/or involve deep space return links.

Although lasercom systems offer certain advantages over RF systems as described above, there are some drawbacks that arise from the smaller wavelengths used in lasercom systems. For example, the high directivity of the transmitted beam makes acquisition and pointing more difficult. Also, optical component design requires its own technology separate from design techniques associated with RF systems. Thus, performance characteristics can be significantly different than those associated with RF systems. Optical turbulence resulting from small temperature variations in the atmosphere gives rise to power losses from spreading of the beam spot radius beyond that due to diffraction alone, and to temporal and spatial fluctuations of the laser beam known as *scintillation*. Small pointing errors can easily lead to unacceptable fade levels owing to a Gaussian roll-off in the mean irradiance profile combined with large off-axis scintillation.

FREE SPACE SATELLITE LASER COMMUNICATION

Adnan Cora-Hacer Atar

Karadeniz Technical University

Department of Electrical and Electronics Engineering

61080-Trabzon/TURKEY

e-mail: cora@ktu.edu.tr

In optical communication systems an electrical signal is converted to a modulated light wave, which then transmits the signal to a receiver. The light signal is converted back to an electrical signal at the receiver. Modulation of the wave is necessary in order to convey information. To transmit information with light we have to turn it on and off, or modulate it in some other way, to have it represent some sort of coded message that is recognizable at the receiver. This great potential of light waves for communication purposes has been recognized for a long time, but became practical only after the development of lasers [1].

On of its applications is satellite Laser Communications. Free spare optical communication between satellites networked together can make possible high speed communication between different places on the Earth. The advantages of an optical communication system instead of a microwave communication system in free space are 1) smaller size and weight, 2) less transmitter power, 3) large bandwidth, 4) higher immunity to interference. The main complexity of satellite optical communication is the pointing system satellites vibrate continually because of their subsystem operation and environmental sources. Due to vibrations to receiver receives less power. This effect limits the system bandwidth for given Bit Error Rate (BER).

Arnon, Rotman and Kopeika [2] derived an algorithm to maximize the communication system bandwidth using the transmitter telescope gain as a free variable based on the vibration statistics model and the system parameters. Their model makes it possible to adapt the bandwidth and transmitter gain to change of vibration amplitude.

BANDWIDTH MAXIMIZATION

The receiver is assumed to include an optical detector in direct detection mode with modulation format of On/Off Keying. In sush systems the BER for an optimal threshold receiver is given by

$$\text{BER} \approx \frac{1}{2}\int_0^\infty \left(\frac{1}{2}\left(\frac{\mu_1(\theta)-\mu_0(\theta)}{\sqrt{2}(\sigma_1(\theta)+(\sigma_0(\theta))} \right) \right) f(\theta)d\theta \quad (1)$$

where, $\mu_1(\theta)$ and $\sigma_1(\theta)$ are the received optical signal and the receiver noise standard deviation for receiver "1", respectively, and $\mu_0(\theta)$ and $\sigma_0(\theta)$ are the received optical signal and the receiver noise standard deviation for receiving "0", respectively .

TRANSMITTER AND RECEIVER

In this section the basic elements of the transmitter and the receiver defined. Figs. 1 and 2 describe a simple scheme of transmitter and receiver. The receiver (Fig. 1) model includes: telescope, optical band-pass filter, input insertion losses, optical amplifier, output insertion losses, optical band-pass filter, p-i-n photo-diode, electrical filter, and a decision rule circuit. The transmitter (Fig. 2) model includes: laser transmitter, optical phased-array telescope, control unit, and random attenuation (vibration effects) [3].
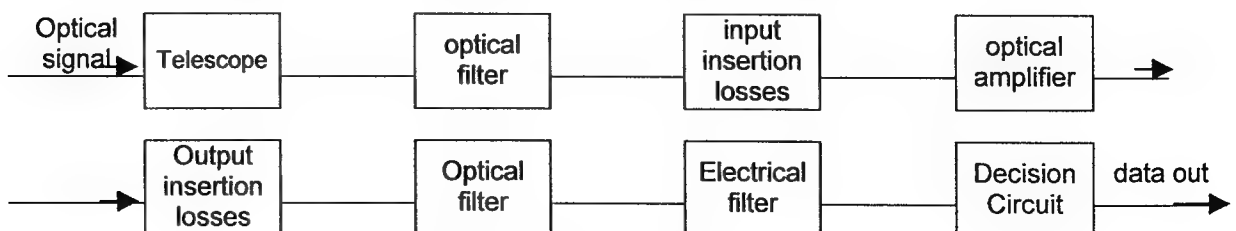
Fig. 1. Receiver scheme
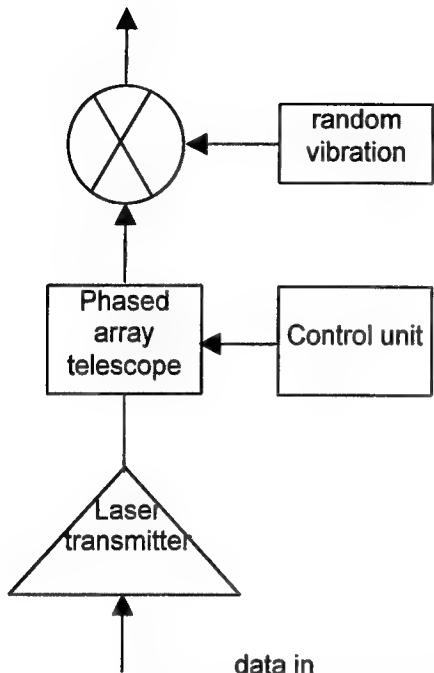
Fig. 2. Transmitter model

The optical power received by the receiver satellite is

$$P_R = K_1 G_T \qquad (2)$$

Where, G_T is the transmitter telescope gain and the pointing factor is

$$L = \exp(G_T \theta^2) \qquad (3)$$

Where θ is the radial pointing error angle. The receiver gain is

$$F_R = \left(\frac{\pi D_R}{\lambda}\right)^2$$

Where D_R is the receiver aperture diameter.

PRACTICAL EXAMPLE

The scenario considered here is communication between two LEO (low earth orbit) satellites. The satellites are placed at an orbit altitude of about 1400 km. The distance between satellites is assumed to be 4500 km. The important of the communication systems are the transmitter power is 1 W, the optical wavelength is 0,8 μm and the required BER is 10^{-9}. This analysis points out bandwidth maximization for satellite laser communication [4]. The implementation of this model is simple. From the results of the example it is easy to understand the importance of optimization for system bandwidth. This analysis also points out that even low values of vibration amplitudes decrease dramatically the possible system bandwidth.

References

1. R. K. Tyson, "Adaptive Optics and Ground to Space Laser Communications", Applied Optics. 35, 3640-3646 (1996).
2. E. V. Hosersten, Optical Communication Theory, Chap. 8, pp. 1805-1863.
3. S. Arnon, S. R. Rotman, and N. S. Kopeika, "Bandwidth Maximization for Satellite Laser Communication", IEEE Trans. Commun. 35, 675-682 (1999).
4. S. Arnon, "Vie of Satellite natural vibrations to Improve Performance of Free-Space Satellite Laser Communication", Applied Optics. 37, 5031-5036 (1998).

Photonics for Agile-Beam Wideband Antenna Systems*

L. M. Johnson, G. E. Betts, P. A. Schulz, P. W. Juodawlkis and W. G. Lyons

Massachusetts Institute of Technology, Lincoln Laboratory
244 Wood St.
Lexington, MA 02420-9108

For well over a decade, rf/photonic techniques have been under development for realizing wideband agile-beam rf antenna systems. Much of this work has centered on phased-array systems which, compared to mechanically scanned antennas, offer important performance features including multiple independent beams, rapid scanning, and wide instantaneous bandwidth. This talk will describe recent advances in rf/photonic architectures aimed at realizing wideband rf array-antenna systems. While hurdles remain, continuing advances in photonic device performance offer the prospect of rf/photonic antenna systems with significant performance advantages over all-rf approaches.

Photonics can positively impact the design of rf array antenna systems in several key ways. Large arrays require complex distribution networks, and optical fiber offers a clear advantage over rf coaxial cable or waveguide in terms of size, weight, and attenuation. In addition, true-time-delay (TTD) beamforming is required for squint-free wide-bandwidth array operation. A number of photonic bemforming techniques are under development (1-3) that exploit recent advances in photonic components for digital fiber-optic networks, including spatial switches, fiber Bragg gratings, tunable lasers, multiplexers and filters. Addressing the requirements of wideband analog signal processing and distribution remains an important challenge in adapting digital fiberoptic technology to rf antenna systems.

A generic rf/photonic receive antenna architecture is shown in Fig. 1. The rf signal from each element or subarray modulates an optical carrier wave. Time delays appropriate for the beampointing direction are applied to each subarray output, and the combined signal is converted back to rf in a photoreceiver. For TTD beamforming, hybrid approaches combining rf techniques for fine-scale TTD and photonic methods for coarse TTD show particular promise. For high-performance systems, EO conversion is typically accomplished using a CW laser and external electrooptic modulator. With components available today, analog modulation bandwidths of 10's of GHz are readily achieved. The dc power requirements of rf-to-photonic conversion is an important system consideration for space applications involving large arrays. Depending on system dynamic range needs, a single rf-to-photonic converter could consume in excess of 1 W with current technology. Improvements in modulator sensitivity (reducing V_π) and linearity, and in laser efficiency, offer the prospect of reducing dc power requirements by an order of magnitude.

Photonic TTD architectures can be realized utilizing a combination of (1) spatial switching between fiber elements, and (2) wavelength-addressable delay. Fiber-optic 1xm switches with low insertion loss and low crosstalk are now readily available. A photonic TTD design that combines spatial switching and wavelength addressable delay is shown in Fig. 2. The design exploits recent advances in optical wavelength multiplexing technology. A fixed wavelength is assigned to each input and the signals are combined through a wavelength multiplexer on a single fiber. A 1xm switch selects a fiber Bragg grating which applies the appropriate time delay to each wavelength component. Systems can be configured for two-dimensional beam steering. Photonic beamformers of this type offer a large size and weight savings over all-rf designs of comparable performance.

In summary, rf/photonic techniques which exploit the small size and weight of optical fiber, the wide bandwidths of optoelectronic components, and the unique capabilities offered by

wavelength multiplexing offer very significant opportunities for realizing high-performance array antenna systems.

References

1. M. Y. Frankel, P. J. Matthews, R. D. Esman and L. Goldberg, *Optical & Quantum Electronics*, **30**, 11-12, 1033-50 (1998).
2. H. Zmuda and E. N. Toughlian, *Photonic Aspects of Modern Radar*, Artech House (1994).
3. D. T. K. Tong and M. C. Wu, *IEEE Trans. Microwave Theory Tech.*, **46**, 1, 108-115 (1998).
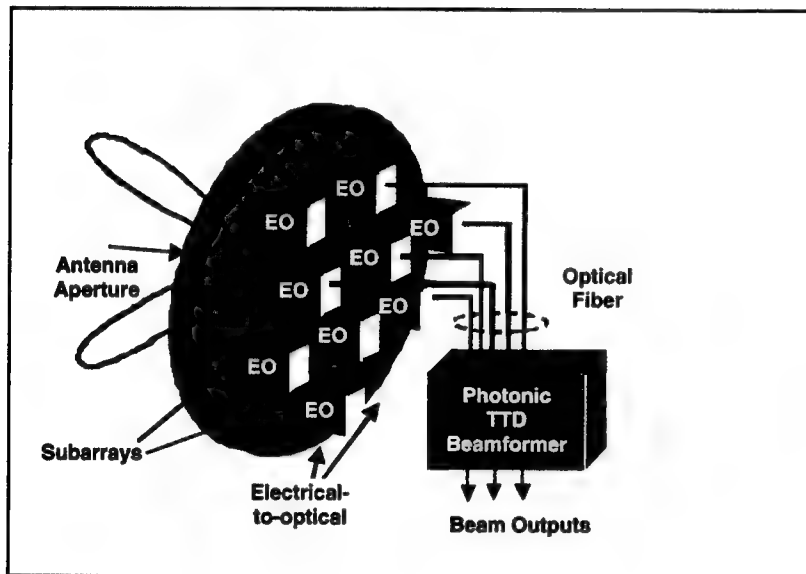
Fig. 1. Schematic view of an rf/photonic phased-array receive antenna. Subarray rf output signals modulate an optical carrier wave (EO converter) and the signals are sent via optical fiber to a photonic true-time-delay (TTD) beamforming network. The combined signal is converted back to rf to provide the beam output.
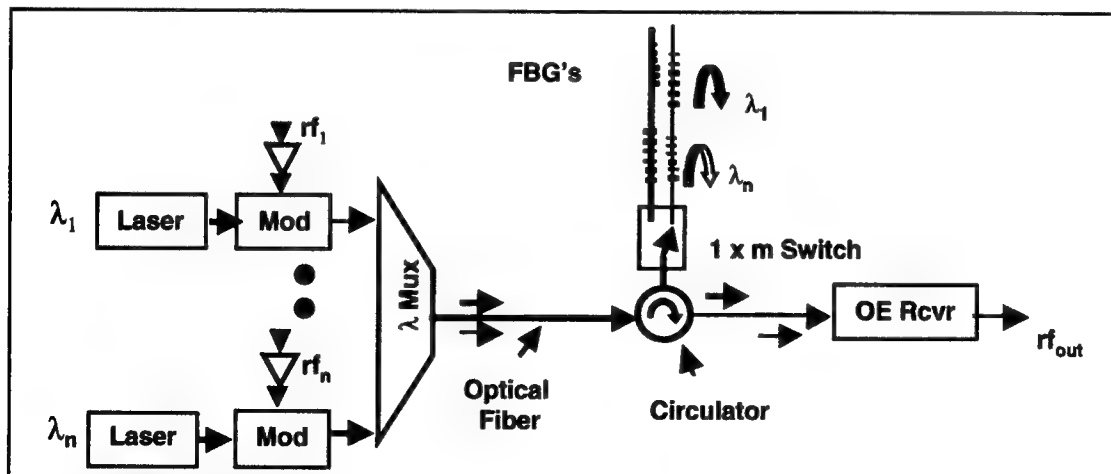
Fig. 2. Schematic diagram showing the basic functionality of a wavelength-multiplexed TTD beamformer. Each of n rf inputs is assigned an optical wavelength and the signals are combined in a wavelength multiplexer. A 1 x m spatial switch selects a fiber Bragg reflective gratings which applies the appropriate time delay to each subarray signal. The combined signal is then converted back to rf in the optoelectronic receiver.

A Concept for Very Large Telescopes Using Pupil Plane Correction Optics And Lower-Cost Spherical Primary Mirror Segments

Nelson Wallace
Electro-Optics, Lasers, and Research Center
Space & Technology Division
TRW Space & Defense, Redondo Beach, CA 90278

Abstract

For very large, space-erectable optical systems (NASA science missions, high energy laser weapons, etc.), the telescope's primary mirror (PM) would likely be an ensemble of mirror segments deployed as concentric rings of reflective mirror segments. Most optical design forms for high-performance telescopes employ a conic PM shape. The use of conic segments would require a different mirror shape for each ring of mirrors, and thus different fabrication and testing facilities for the mirrors in each ring, at significant cost and schedule. The prospect of assembling the primary mirror from small, low-cost identical spherical mirror segments is very attractive.

This paper discusses a concept for a telescope optical design form that would use one spherical shape for all of the PM segments, and correct the increased aberration with a segmented corrector downstream at a pupil. The PM segments would be individually despaced and tilted to optimize performance. Additionally, the aspheric coefficients on the segmented corrector surfaces would be different for each radial zone; this is the key feature of the approach, and allows a better correction than if a single aspheric shape were applied to the corrector surface. Preliminary design results for a 30 m Gregorian telescope show sixth-wave peak-to-valley residual optical path differences (OPD's) over a 0.6 arc-minute full field of view. The results show that the concept works well for small FOV systems, which may be sufficient given constraints on downstream instrument package sizes as a result of the optical invariant.

This high-risk, potentially high-payoff concept separates one very difficult problem into two (hopefully) less difficult ones. There remains the issue that, if the scheme were technically possible, the decrease in PM fabrication & testing cost from using spherical segments would have to more than offset the cost increase from the pupil corrector.

Electro-Optics in Space

Thursday, 27 July 2000

Thursday Missing Papers

ThD2.1   "SBL Optics Development", F. Hassell, TRW, *Redondo Beach, CA, USA.*

Thursday Withdrawn Papers

ThD4.2   "Issues in Space Qualification for Medium Power Fiber Optic Lasers", R. Rice, N.F. Ruggieri, *The Boeing Company, St. Louis, MO, USA.*

Liquid Crystal Devices as Holographic Recording Media for Aberration Compensation in Membrane-Mirror Based Telescope Systems

Ty Martinez and Mark Gruneisen,
United States Air Force Research Laboratory
Directed Energy Directorate, Kirtland AFB, New Mexico 87117
phone: (505) 846-9296, fax: (505) 853-6236, email: martinty@plk.af.mil

Kenneth MacDonald and Jeffery Baker
Boeing North American, PO Box 5670
Albuquerque NM 87185
phone: (505) 853-4362, email: kenneth.macdonald@plk.af.mil

ABSTRACT

Membrane mirrors are a lightweight alternative to conventional telescope primary mirrors. Membrane mirrors have large aberrations that exceed the correction capabilities of conventional adaptive optics. Liquid crystal hologram recording media can compensate membrane mirror aberrations.

INTRODUCTION

Telescopes are integral components of light gathering and beam projecting optical systems with diverse military and civilian applications. Orbiting space-based telescope systems offer many advantages including reduced effects from atmospheric turbulence. In order to achieve high-resolution optical performance from orbital distances however, the telescope apertures must be scaled to large diameters. For some applications, aperture sizes of tens of meters may be required. At these diameters, the size and weight of conventional primary mirrors are beyond the capacity of existing launch vehicles.

These limitations may be overcome with lightweight compact primary mirror architectures such as deployable membrane mirrors currently under development at the Air Force Research Laboratory (AFRL). In recent years, there have been significant improvements in the engineering of membrane optics. [1] Nonetheless, it is believed that such ultra lightweight, large aperture mirrors will have significant aberrations compared to conventional mirrors.

The large aberrations associated with the ultra lightweight primary mirrors create the need for an optical wavefront compensation technique that can remove 100's of microns of optical path difference (OPD). This exceeds the capabilities of conventional deformable-mirror adaptive optical systems, such as those developed and demonstrated by the AFRL Starfire Optical Range. [2] These deformable-mirror devices rely on actuators to deform a mirror surface and introduce an equal-but-opposite aberration to the aberrated wavefront. The achievable resolution and magnitude of displacement limit correctable OPD to only a few microns and consequently this technology is not adequate for the membrane mirror systems.

In recent years, compensation of severe dynamic aberrations in a membrane-mirror based telescope using real-time holographic phase subtraction has been demonstrated. [3] This technique used a liquid crystal optically addressed spatial light modulator (OASLM) to compensates for OPD errors on the order of 100 μm and was applied at rates up to 1 kHz, which is more than adequate to compensate time-dependent aberrations associated with the dynamic motion of the thin membrane. [4] Such a capability may dramatically reduce the primary mirror surface tolerances making feasible the implementation of ultra-lightweight deployable primary mirrors.

THEORETICAL LIMITS FOR THIN DIFFRACTION MEDIA

Historically, the principle shortcoming of the liquid crystal OASLM has been limited diffraction efficiency. As thin diffraction media, the maximum theoretical first-order diffraction efficiencies are 6% and 10% for analog and binary amplitude modulation and 34% and 40% for analog and binary phase modulation respectively. Commercially, OASLM devices have been primarily developed as amplitude modulators for incoherent-to-coherent converters and image projection applications. Consequently, only devices with diffraction efficiencies of a few percent were widely available. A commercially available nematic-based OASLM's can be operated as analog phase modulators with 30% diffraction efficiency. But the diffraction occurs for only one polarization and with relatively

slow relaxation time compared to ferroelectric based devices. [5] More recently, computer-generated blazed phase holograms have been demonstrated with 90% diffraction efficiency. [6]

BLAZED HOLOGRAPHIC CORRECTION OF ABERRATIONS IN A MEMBRANE-MIRROR TELESCOPE

A schematic of the compensated membrane mirror telescope experimental setup is shown in Figure 1. An object point source at infinity is simulated by illuminating a 20-μm pinhole with the 532 nm output of a frequency doubled Nd:YAG laser and collimating the transmitted light with a conventional f/6 parabolic mirror. The clear aperture of the collimated wavefront is restricted to 50 mm with a circular aperture. The object wavefront is then propagated to the low-optical-quality membrane mirror operating as a 50-mm diameter f/18 off-axis parabola. The membrane mirror is fabricated from 125-μm thick, aluminum-coated, upilex plastic mounted to a vacuum flange and held under partial vacuum.

The mirror surface is probed and an interferogram of the aberration is recorded on a video camera as shown in Fig. 1. The interferogram is then digitized and processed and the resulting blazed hologram used for the correction is applied on the EASLM, which is projected on the OASLM. The diffracted corrected order is then relayed to a camera located in an image plane for the object pinhole.
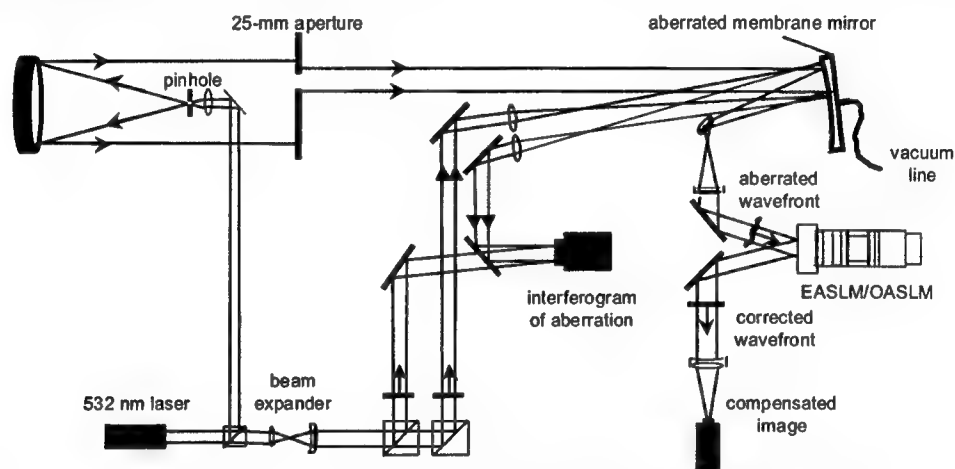
Figure 1. Experimental setup for demonstrating compensated membrane-mirror telescope with real-time blazed hologram.

CONCLUSIONS

Real-time holographic phase subtraction is demonstrated to be capable of removing significant aberrations from membrane-based primary mirrors. Historically, low diffraction efficiencies of real-time hologram recording media limited the performance of such compensated systems. Recent developments in liquid-crystal spatial light modulators have increased the diffraction efficiencies to approach the theoretical limits for simple thin phase holograms and blazed phase holograms.

ACKNOWLEDGEMENTS

REFERENCES

1. J. R. Rotge, D. K. Marker, R. A. Carreras, and D. C. Duneman, "Large, optically flat membrane mirors," in International Symposium on Optical Science, Engineering, and Instrumentation, K. Stefer, ed., Proc. SPIE, to be published (1999).
2. R. Q. Fugate, B. L. Ellerbroek, C. H. Higgins, M. P. Jelonek, W. J. Lange, A. C. Slavin, W. J. Wild, ""2 Generations of laser-guide-star adaptive-optics experiments at the Starfire Optical-Range," J. Opt. Soc. Am A-Optics Image **11**, 310 (1994).
3. M. Gruneisen, D. Wick, T. Martinez, J. Wilkes, "Correction of large dynamic aberration by Real-Time holography using Electro-Optical devices and Non-linear optical media," SPIE **3432**, 137 (1998).
4. M. T. Gruneisen, K. W. Peters and J. M. Wilkes, "Compensated Imaging by Real-Time Holography with Optically Addressed Spatial Light Modulators," in *Liquid Crystals*, Iam-Choon Khoo, Editor, Proceedings of SPIE **3143**, 171 (1997).
5. Hamamatsu technical data sheets for model X5641 PAL-SLM parallel aligned nematic liquid-crystal spatial light modulator and model X4601 FLC-SLM ferroelectric liquid-crystal spatial light modulator, Hamamatsu Corporation, 360 Foothill Rd., Bridgewater, NJ 08807 (1997).
6. H. Toyoda, Y. Kobayashi, N. Yoshida, Y. Igasaki, T. Hara, M. Ishikawa, and M. H. Wu, "High efficient electrically addressable spatial light modulator for reconfigurable optical connection," OSA, April 1999.

WAVEFRONT COMPENSATION USING LIQUID CRYSTAL SPATIAL LIGHT MODULATORS – SCALING ISSUES

Dennis Guthals, Dan Sox, Mike Joswick, and Paul J. Rodney
Lasers and Electro-Optical Systems, Boeing Space & Communications Group
6633 Canoga Ave. MC FA-04, P.O. Box 7922, Canoga Park, CA 91309-7922

1. INTRODUCTION

Large deployable space-based optical systems will likely require complex structure position controls in conjunction with an adaptive optic to maintain optical tolerances necessary for near diffraction-limited performance. A real-time holographic (RTH) compensation system can greatly reduce the requirements and complexity of the position control system and enable the use of novel or imperfect optical components for large mirror surfaces. Activities[1,2] in compensated imaging techniques have focused on methods such as holography to allow imaging with low quality optics.

The holographic method for correcting aberrations was first proposed by Gabor in 1949[3]. In the 60's Kogelnik and Pennington[4] and Upatnieks et al.[5] used holographic plates (static correction) to remove random aberrations and spherical aberration, respectively, for telescope systems. More recently, Munch et al.[6-8] have been using holographic plates to correct aberrated primaries in reflecting and refractive telescopes with broadband images[6,7] and most recently have demonstrated a diffraction limited system with a severely aberrated 0.5 m primary[8].

The spatial light modulator has allowed the realization of dynamic correction of aberrated primary mirrors. Recent activity has focused on using liquid crystal optically-addressed spatial-light-modulators (LC OASLMs) as the holographic medium of a dynamic correction element in holographic correction systems Both Vasil'ev et al.[2] and Gruneisen et al.[1] have used OASLMs and RTH to correct for primary mirror distrtions. The former demonstrated correction of a poor quality segmented primary mirror while the latter demonstrated correction of a membrane primary mirror.

Our group has been pursuing real-time holographic (RTH) image correction since 1990 to compensate for atmospheric turbulence[9] as well as turbulent boundary layer optical distortions[10]. The latter experiments concluded with successful dynamic image correction for field tests involving horizontal imaging at a range of one mile. In this paper we report on a dynamic correction system capable of 5 kHz operation using real-time holography to correct broadband (532 ± 40 nm) illuminated targets collected by an aberrated 0.75 m primary mirror. Scaling this technology to larger primary mirror diameters, higher optical efficiencies, and increased power handling capacity requires system level trades of temporal, spectral and spatial bandwidths, field of view, magnification and LC OASLM device development.

2. EXPERIMENTAL

A schematic diagram of the large optics compensator testbed is shown in Figure 1. The setup consists of a scene generator, a telescope receiver primary mirror, the telescope secondary with imaging optics, and a holographic compensator beacon leg. Both the scene generator and telescope receiver use identical 0.75 m f/4 parabolic aluminum surface Pyrex mirrors with measured figures around 0.5 λ peak to valley (P-V).
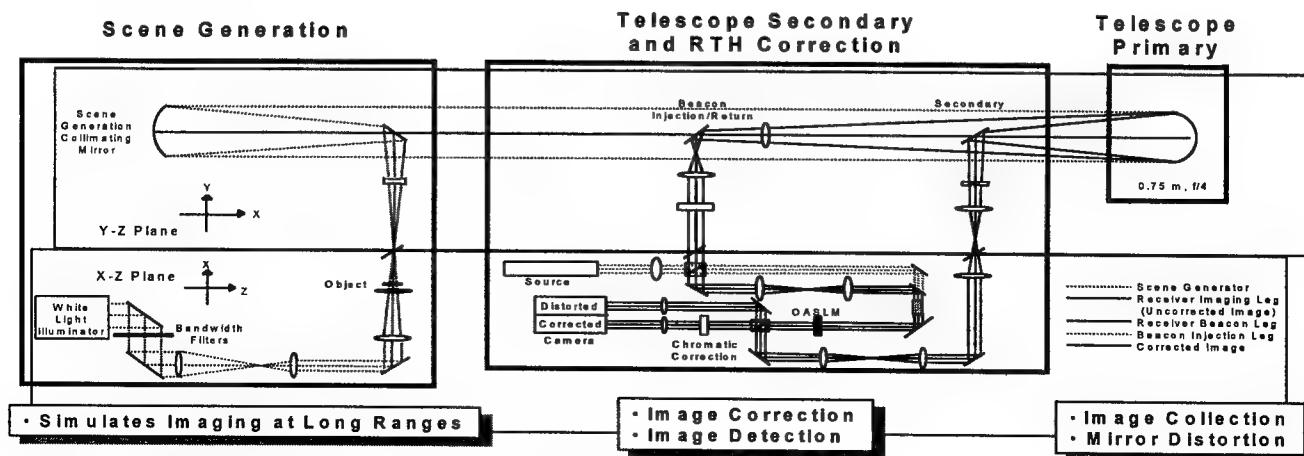
Figure 1. Schematic diagram of the Large Optics Compensation testbed.

3. TEST AND ANALYSIS

A series of tests was carried out to demonstrate broad spectral band compensation and explore the correctable phase/spectral bandwidth trade space. Initial setup and alignment tests used the 532 nm laser source for target illumination. These tests were followed by a complete series of monochromatic and polychromatic compensation tests with fixed mirror warps up to 22 λ. Figure 2 shows image correction of the Air Force Test Pattern for a 22λ misfigured primary. Dramatic correction is seen for the severely distorted primary. The expected degradation of image compensation with increasing spectral bandwidth is observed. Similar qualitative tests were carried out at mirror warps of 3, 7.5, and 12 λ.
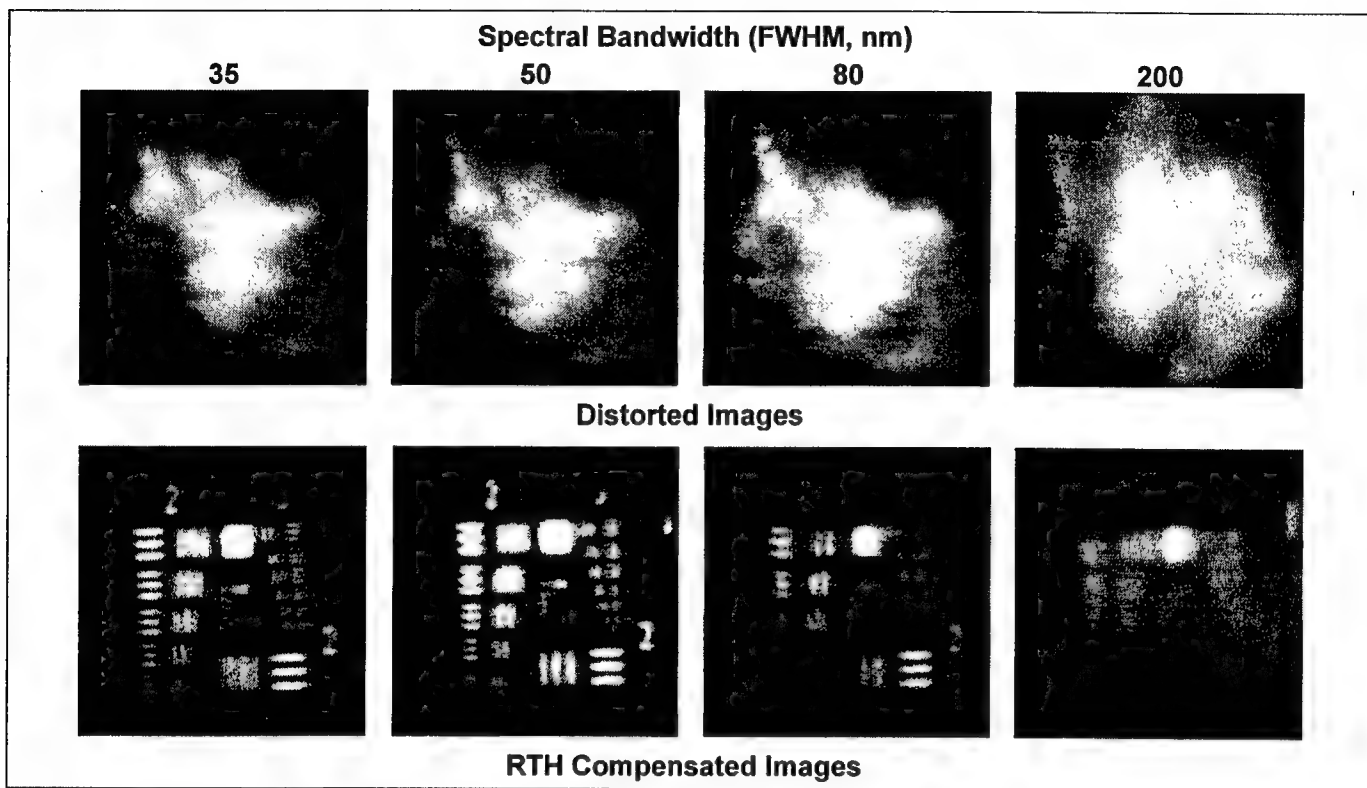
Figure 2. Distorted and corrected broad spectral band images with 22 λ of mirror warp.

4. CONCLUSION

We have demonstrated compensation of a severely warped meter-class telescope and explored the performance trade space. RTH compensation can permit the use of large imperfect mirrors of misphased mirror segments in aggressively lighweighted deployable optics. The technique can also compensate for dynamic aberrations introduced by vibrations and thermal loading. This can greatly reduce the weight and complexity of isolation and positioning systems for large deployable telescope systems. The optical efficiency of an OASLM-based holographic compensation system can approach 40% while providing the equivalent spatial resolution of deformable mirrors containing more than 10,000 actuators. We have also demonstrated increased optical efficiency by the generation of blazed gratings. Increased power handling and compensation of larger area primary mirrors requires development of larger area OASLMs.

5. REFERENCES

1. M. T. Gruneisen, K. W. Peters, and J. M Wilkes, "Compensated imaging by real-time holography with optically addressed liquid-crystal spatial light modulators, SPIE **3143**, 171-181 (1997) and references therein.
2. M. V. Vasil'ev, V. A. Berenberg, A. A. Leshchev, P. M. Semenov, V. Yu. Venediktov, "White light imaging using large numerical aperture telescope with dynamic holographic correction for primary mirror distortions," SPIE **3432**, 164-170 (1998) and references therein.
3. D. Gabor, "Microscopy by reconstructed wavefronts," Proc. R. Soc. London Ser. A **197**, 454 (1949).
4. H. Kogelnik and K. S. Pennington, "Holographic imaging through a random medium," J. Opt. Soc. Am. **58**, 273-274 (1968).
5. J. Upatnieks, A. VanderLugt, and E. Leith, "Correction of lens aberrations by means of holograms, Appl. Opt. **5**, 589-593 (1966).
6. J. Munch and R. Wuerker, "Holographic technique for correcting aberrations in a telescope," App. Opt. **28**, 1312-1317 (1989).
7. J. Munch, R. Wuerker, and L. Heflinger, "Wideband holographic correction of an aberrated telescope objective," Appl. Opt. **29**, 2440-2445 (1990).
8. G. Anderson, J. Munch, and P. Veitch, "Compact, holographic correction of aberrated telescopes," Appl. Opt. **36**, 1427-1432 (1997).
9. S. Ma, D. Guthals, P. Hu, and B. Campbell, "Atmospheric-turbulence compensation with self-referenced binary holographic interferometry," J. Opt. Soc. Am. A **11**, 428-433 (1994).
10. D. Guthals, "All optical imaging brassboard (AOIB)," Report # PL-TR--94-1104, Rockwell International (1994). NOTE: Distribution authorized to U.S. Gov't agencies only.

Noise and Distortion Characteristics of Cryogenic Vertical Cavity Lasers

Hanxing Shi, D. A. Cohen, D. Lofgreen, L. A. Coldren
Department of Electrical and Computer Engineering
University of California, Santa Barbara, CA 93106

High speed free-space optical interconnections, from focal plane arrays in a cryogenic environment to room temperature electronics, require the optical transmitter with favorable analog modulation properties over wide temperature range. Due to the small size, low-power consumption, and the possibility of integration, vertical cavity laser (VCL) is one of the best candidates for such applications [1,2]. In previous work, it has been demonstrated that the low-temperature optimized VCLs had higher output powers, higher quantum efficiencies, and larger modulation bandwidths at 77K [3]. In this paper, both the noise and distortion characteristics of the said VCLs are further investigated under both room temperature and cryogenic environment.

The measured lasers were the double intracavity, oxide-aperture, 5.4μm diameter VCLs with an operating wavelength of 940nm. The structure and the processing of the low-temperature optimized devices have been described previously in [2,3]. The 1×6 laser array collimated by a microlens was assembled into a cryostat to realize the cryogenic operation. The optical beams transmitted out from the cryostat were further converged by another lens and received by a silicon avalanche photodetector (APD). The measurement equipment was the HP 8566B electrical spectrum analyzer with 10Hz resolution.

Figure 1 shows the L-I-V curves of the VCL, which were measured outside the cryostat at 120 and 297K. The threshold of 0.15mA and differential efficiency of 0.5mW/mA were measured at 120K, while the values at 297K were respectively 0.4mA and 0.37mW/mA. The differential efficiency is much higher at lower temperature is because that, due to joule heating, the gain peak and the resonance mode are improving their mutual alignment as the device is biased.

Relative noise intensity (RIN) is the most important parameter to embody the noise properties of lasers. In order to measure it, a 40dB electrical amplifier was placed behind the APD to elevate the source noise above the noise floor of the whole link. Figure 2 shows the relative noise measured at 297K against various bias levels. At bias level of 1.5mA corresponding to the 0.5mW output power, the relative noise level is lower than −130dB/Hz, which is much lower than the practical requirement of the high-speed data communications.

Even though, it's found that the noise still dominatingly attributes to the shot noise of the APD, rather than the source RIN. To verify this, an optical attenuator was introduced to change the optical power detected by APD. The photodiode shot noise is directly proportional to the received optical power, while the source RIN is proportional to the square of the optical power. The relationship between noise level and the attenuation, which is shown as figure 3, confirms that the measurement link is limited by the shot noise at high bias current. Only under the bias level just above the threshold does the logarithmic slope approach two, which is because that the RIN of the laser is inversely proportional to the cubic of the relative bias level.
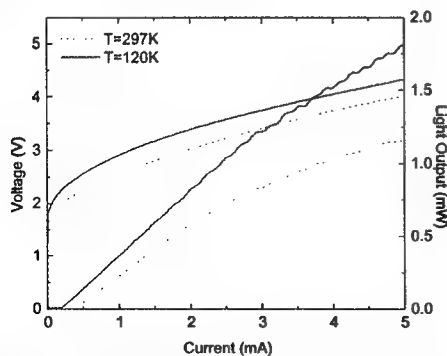
Fig.1 *L-I-V characteristics for 940nm VCL under both room and cryogenic temperatures.*
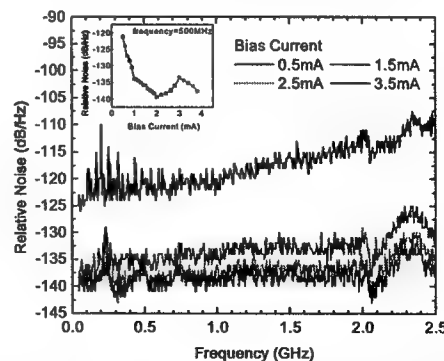
Fig.2 *Relative noise of the measuring link Inset is the relative noise versus bias current at 500MHz.*

19
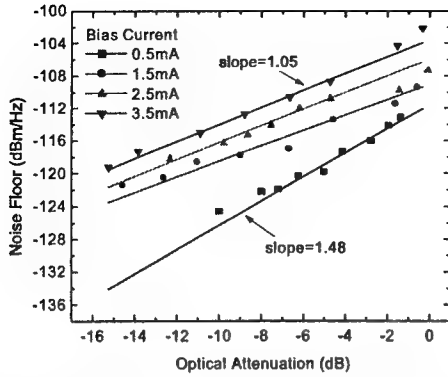
Fig.3 *Detected relative noise values while adjusting the optical attenuator between VCL and APD.*
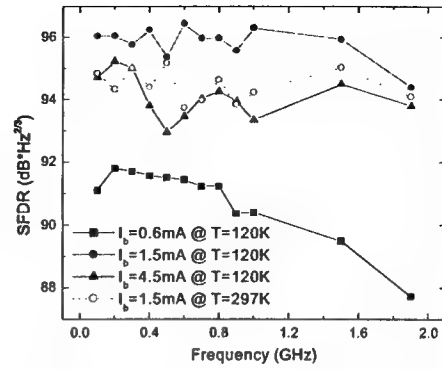
Fig.4 *SFDR value of VCL versus modulation frequency with different bias currents.*

Further comparing the relative noise levels at different biases shown as the inset of the fig.2, there is an evident rise around 3mA bias. The reason is that the linear polarization mode below 2mA won't be stable any more at higher bias current. The random mode hopping produces the additional polarization mode noise on the whole transmission link even without any polarization-sensitive component.

The spur free dynamic range (SFDR) of the VCL was measured with the conventional two-tone modulation [4]. The frequency spacing between the two equal-magnitude modulation signals was 1MHz. The SFDR value is defined as the input signal power ratio of the point where the fundamental crosses the noise floor to the point where the third-order distortion signal crosses the noise floor. Due to the above-mentioned limitation of the shot noise, the upper limit of the noise floor is assumed to be -150dBm/Hz below. Therefore, the practical dynamic range will be even higher than the calculated SFDR values here.

Figure 4 shows the dynamic range of the VCL against frequency and bias current under both room and cryogenic temperatures. Comparing the curves under different bias levels, it's evident that the optimal bias state corresponding to the highest dynamic range is around 1.5mA. The highest SFDR value, 96dB $Hz^{2/3}$, is much higher than the requirement for the personal communication systems which is in the range of 72-83dB $Hz^{2/3}$. Furthermore, the dynamic range at 120K is about 2dB higher than the case under the room temperature. It means that the low-temperature optimized VCL does have the better linearity under the cryogenic environment.

In conclusion, both the noise and distortion properties of the low power VCL have been studies under both room and cryogenic temperatures. The noise of the measurement link with high bias level is dominated by the photodiode shot noise. The upper limit on the RIN of the VCL with 0.5mW output power is -130dB/Hz. At high bias levels, the polarization mode hopping will induce additional noise, even without any strongly polarization-selective components in the link. The SFDR level of 90-100dB $Hz^{2/3}$ is measured. The best linearity is produced under 1.5mA bias current. Especially the higher dynamic range can be realized under lower temperature, which authenticates the validity of the low-temperature optimized VCLs.

References

[1] E. Goobar, M. G. Peters, G. Fish and L. A. Coldren, "High efficient vertical-cavity surface-emitting Lasers optimized for low-temperature operation", *IEEE Photon. Technol. Lett.*, **7**(8), pp. 851-853, 1995.
[2] Y. A. Akulova, J. Ko, D. Lauderback, B. J. Thibeault, and L. A. Coldren, "High-speed modulation of low-temperature optimized vertical cavity lasers over 77-300 K temperature range," *Electron. Letts.*, **34** (8), pp. 774-775, 1998.
[3] Y.A. Akulova, B. J. Thibeault, J. Ko, and L. A. Coldren, "Low-temperature optimized vertical-cavity lasers with submilliampere threshold currents over the 77-370 K temperature range," *IEEE Photonics Technol. Lett.*, **9** (3), pp. 277-279, 1997.
[4] T. Olson, "An RF and microwave fiber-optic design guide", *Micro. Journal*, **39** (8), pp. 106-116, 1996.

Detector Array Considerations for Laser Remote Sensing

By

Pri Mamidipudi and Dennis Killinger
Department of Physics
University of South Florida
Tampa, FL 33620

We have developed a 1.5 micron multi-detector heterodyne Doppler lidar type system in the laboratory to study the enhancement in expected S/N through use of a multi-element and balanced heterodyne detector array.   Preliminary experiments have been conducted and indicate that the coherent summation of two separate balanced heterodyne detector signals seems to provide enhanced detection of the Doppler shifted signal.   Initial studies regarding the expected Doppler shift, geometrical vibration effects, and other system noise sources are being studied.   We are in the process of comparing these new results with those obtained previously by us at 1 micron using an atmospheric Heterodyne multi-detector Lidar system.

Our 1.5 micron Doppler lidar (laboratory) system is as follows: A 30 mW 1.5 micron, single-frequency diode laser is used as the main excitation source.   The beam is split into a L.O. channel and a main projected beam followed by a 27MHz shifted Acousto-Optic frequency shifter.   The main portion is sent to a rotating target, and the reflected backscatter collected by 2 spatially separated (V groove blocks) fiber-optic , single frequency, polarization preserving fibers.   At present, the two collection fibers are separated by 100 microns; as such, this is the effective separation of the two coherent detectors. The two collected signals are branched into a I & Q channels for balanced heterodyne detection.   The fours channels are detected and the electrical signals analyzed by spectrum analyzers, 4 channel oscilloscopes, and computer interfaced.

We are currently studying the change in the Doppler center frequency, spread of the Doppler shifted signal, influence on the geometrical and velocity aspects of the target, ·and linewidth stability of the diode laser.

Developments in Remote Sensing Instrument Optical Designs

Michael P. Chrisp

Ball Aerospace and Technologies Corporation,
1600 Commerce St., Boulder CO 80301

1. Introduction

Remote sensing from space utilizing imaging spectrometry is placing greater demands on the design of these instruments. The requirements for quality and purity of the spectral data increases with each generation of imaging spectrometers and drives the development of improved designs. These designs provide control of the spectral stray light, the non-linearity of the spectral dispersion, the spectrometer size, and spectral transmittance.

This presentation covers the application of imaging spectrometer designs based on convex gratings, and designs utilizing apochromatic lens systems. Convex grating designs are compact with good spectral stray light control. The apochromatic lens designs can provide good performance over large wavelength ranges.

2. Imaging Spectrometers utilizing Convex Grating Designs

Imaging spectrometers based on the Offner type convex grating design provide extremely good spectral and spatial resolution. They consist of two concave mirrors and a convex grating arranged in a similar arrangement to the Offner reflective relay. The power of these optical elements is balanced to ensure a flat field. At reasonable f-numbers, spherical surfaces can be used, for lower f-number designs aspheric surfaces help control the higher order aberrations. These spectrometer designs have very low spectral slit curvature and low spatial distortion over the spectral range. The grating provides good linearity of the spectral dispersion across the focal plane. Because these designs are all-reflective system, they are less sensitive to the thermal and radiative environments compared to refractive designs.

Convex grating spectrometers have extremely low stray light for a single stage spectrometer system. There are only three reflecting optical elements that can scatter, and a high quality holographic grating in the spectrometer provides good spectral stray light control. The principal difficulty with these designs is the low diffraction efficiency of holographic gratings (which have sinusoidal profiles). For greater diffraction efficiency, electron beam written gratings are necessary, and these are currently produced by the Jet Propulsion Laboratory.
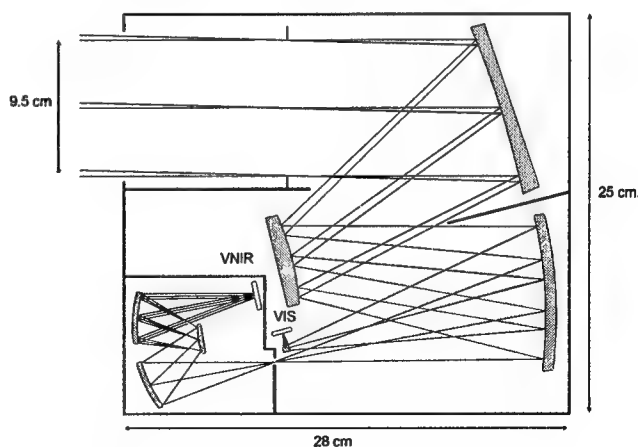
Figure 1 Convex Grating Pushbroom Imaging Spectrometer (M. Chrisp Patent No. 5,880,834)

Shown in figure 1 is an imaging spectrometer based on a convex grating design. This design has a three mirror anastigmatic telescope followed by a convex grating imaging spectrometer. The exit pupil position from the telescope, although not telecentric, is a good match for the convex grating spectrometer. This pushbroom imaging spectrometer is designed for space remote sensing and has good spatial and spectral performance.

3. Imaging Spectrometers utilizing Apochromatic Lens Systems

Imaging spectrometers with apochromatic camera and collimator lenses provide good spectral and spatial performance over extended wavelength ranges. They are useful for the visible and infrared regions, but are not applicable to the ultraviolet region. The multiple lens surfaces create higher spectral stray light than reflective spectrometer systems, primarily due to the multiple ghost images.

Shown in Figure 2 is a design of a prism spectrometer covering a large wavelength range over the visible and near infrared. The apochromatic lenses enable this wavelength range to remain in focus over the detector array. The prism has the advantage, over a grating system, of high transmittance over this large wavelength range.

Prism designs, like this, are limited in their spectral resolution, and also the non-linearity of their spectral dispersion. It is possible to use multiple prisms to linearize the spectral dispersion, but this decreases the spectral resolution further. However, prism systems avoid the grating systems' problem of order overlap for multiple-octave wavelength ranges.
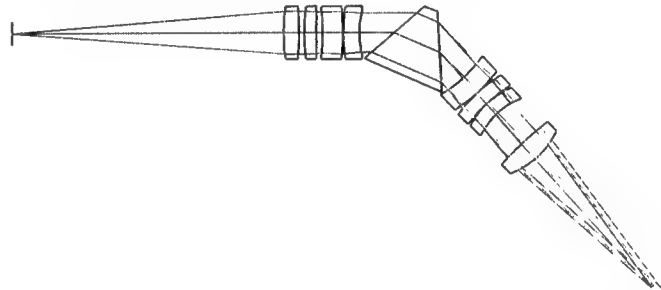
Figure 2 Imaging Spectrometer utilizing Apochromatic Lenses

For higher spectral dispersion, grating systems with apochromatic lenses provide good spectral performance. They can use readily available high diffraction efficiency plane gratings (unlike the convex grating designs); however, correcting the spectral line curvature in these designs is very difficult.

4. Conclusion

The choice of an imaging spectrometer design for a given application depends upon the dominant requirements for spectral retrieval algorithms. These algorithms set the tolerances on the linearity of the spectral dispersion, and the signal-to-noise ratios required. They also determine if the detector array can be resampled for spectral correction. The latest convex grating spectrometer designs provide good spectral performance in a compact instrument, and the latest apochromatic lens spectrometer designs provide high transmittance over large wavelength ranges.

Design and Operation of the Hopkins Ultraviolet Telescope

By

Samuel T. Durrance

Florida Space Institute, University of Central Florida

The Hopkins Ultraviolet Telescope (HUT) was flown aboard the Space Shuttle *Columbia* for 9 days in December 1990 and the Space Shuttle *Endeavour* for 17 days in March 1995. Specrtophotometric observations of numerous astronomical sources were made throughout the far ultraviolet (912-1850 Å) at a resolution of ~3 Å, and for some sources, in the extreme ultraviolet (415 – 912 Å) at a resolution of ~1.5 Å. In this paper we describe the HUT instrument and its performance in orbit.

The optical system consists of a 90 cm diameter $f/2$ primary mirror and a prime-focus, Rowland circle spectrograph. These elements are held in position by a metering structure of low-expansion Invar. The entire assembly is housed within an aluminum environmental control canister, which protects against contamination on the ground and provides a thermally-controlled, optically-shielded environment during observations. The parabolic primary mirror is fabricated of Zerodur and figured to provide 1 image quality at the focal plane. It was coated with iridium for Astro-1, which provides ~20% reflectivity and is stable in the low-Earth orbital environment. It was coated with SiC for Astro-2, which provides ~ 40% reflectivity but may degrade in the low-Earth orbital environment. Three motorized mechanisms in the Invar mirror-mounting structure provide the capability to focus and align the instrument during the mission.

The prime focus spectrograph is housed in an evacuated stainless steel enclosure, whose vacuum is maintained at ~10^{-6} torr by redundant Vac-Ion pumps. The spectrograph contains a 20 cm diameter $f/2$ spherical concave grating, holographically generated (600 lines mm^{-1}) and overcoated with osmium. The depth of the sinusoidal groove profile is chosen to provide optimal first-order efficiency at 1000 Å. Light passing through the spectrograph entrance aperture is diffracted and focused onto a photon-counting CsI coated microchannel-plate intensifier at a dispersion of 41 Å mm^{-1}. The intensifier employs a chevron pair microchannel plates (MCPs) with 10 m di ameter pores and 25 mm active area, operated at a gain of 2 x 10^{6}. Charge pulses from the MCPs impinge on a P20 phosphor, whose visible light output is coupled via fiber optics to a one-dimensional 1024 element self-scanned photodiode array (Reticon) clocked at 1 scan ms^{-1}. A typical charge pulse covers ~ 8 photodiodes (200 m) at threshold. Each pulse is centroided by an onboard computer, yielding a pixel size of 12.5 m (half the diode width or 0.51 Å in first order), and is accumulated in a 2048 element spectral array. The detector resolution is ~1 Å, but the aberrations of the $f/2$ optical system limit the effective resolution for a point source to about 3 Å in first order. The plate scale at the detector is 2.8 Å^{-1}, so when the pointing is stable (±1) the resolution is not significantly degraded by image motion.

An eight-position rotating mechanism at the spectrograph entrance provides a choice among six aperture sizes and/or filters for observations, as well as two positions for ground operations (a vacuum seal position and a large aperture for calibration). Point source observations are generally made through one of two circular apertures of 18 and 30 diameters. Extended source observations are generally made through one of two

long-slit apertures with dimensions of 9.4″ x 116″ and 17″ x 116″, providing resolution of 3.3 and 6 Å, respectively.

The apertures were etched into a mirrored surface that reflects visible light from the surrounding star field through a re-imaging lens system and filter wheel onto the focal plane of a silicon intensified target (SIT) vidicon camera. The camera views a 9′ x 12′ field surrounding the spectrograph aperture. Digitized video images are analyzed by the onboard processor and compared with pre-defined target and guide star positions. Final target identification is made onboard by an astronaut, who completes the acquisition by adjusting the Instrument Pointing System. Adjustments to the camera gain and integration time, as well as selection of an appropriate neutral density filter wheel position, permit acquisition of targets with visual magnitudes ranging from -4 to +17.

HUT incorporates two custom-built microprocessors. The spectrometer processor (SP) handles the high-rate data from the Reticon, applying commandable pulsewidth and amplitude limits to the digitized Reticon output for noise rejection, calculating centroids, and creating telemetry messages in several possible formats. A high-time-resolution mode provides a time-tagged list of each individual photon event, with an accuracy of ± 1 ms. This mode can be employed for sources whose total count rates do not exceed ~ 600 counts s^{-1}. For higher rate sources, histogram mode is employed, in which a cumulative 2048 element histogram is output to the telemetry every 2 s. This cumulative histogram is also downlinked every 60 seconds in high-time-resolution mode. Thus when data dropouts occur, only the photon arrival time information is lost, and the spectral data are preserved. The dedicated experiment processor (DEP) performs all the functions of command and control of the HUT instrument, and also digitizes, stores and analyzes the video images from the target acquisition camera.

The HUT detector is limited by phosphor persistence, pulse size and scan rate to total count rates $\lesssim 5000$ counts s^{-1}. To observe targets with higher count rates the HUT telescope aperture may be reduced from the nominal full aperture size of 5120 cm^2. A 50% reduction is accomplished by closing one of two semi-circular shutter doors. Further reduction to 1% (50 cm^2) and 0.02% (1 cm^2) of full aperture can be made by closing both shutter doors and opening either of two small apertures provided for this purpose.

The stability of the instrument throughput was monitored for Astro-2 by making multiple observations of the DA white dwarf GD 394 (at 64, 92, 138, 211, and 341 hours MET), in addition to the three observations of HZ 43. The sensitivity was found to decline gradually over the course of the mission in a wavelength-dependent fashion. The total decline was relatively small at long wavelengths (5% at 1800 Å), and rose steadily towards shorter wavelengths (27% at 912 Å). The rate of decline was greatest early in the mission, with roughly half of the total decline occurring prior to 100 hours MET, and 75% of the total decline occurring by 138 hours MET.

Neither the wavelength dependence nor the time dependence of this degradation matches that of the detector exposure: the total flux per unit area on the detector has a broad maximum over 1100-1350 Å and drops rapidly towards either end of the detector, and it increases with time during the mission. Both, however, are consistent with possible degradation of the primary mirror. Two possible mechanisms for this are condensation of contaminants onto the mirror, and oxidation of the SiC coating by energetic atomic oxygen. One of the witness mirrors removed from the telescope shortly after the flight shows similar degradation, and is being investigated further.

The Goddard Space Flight Center Laser and Electro-Optics Branch

By

William S. Heaps

The Laser and Electro-Optics Branch at Goddard Space flight Center was established about three years ago to provide a focused center of engineering support and technology development in these disciplines with an emphasis on development of spaced based instruments. The Branch has approximately 15 engineers and technicians with backgrounds in physics, optics, and electrical engineering. Members of the Branch are currently supporting a number of space based lidar efforts as well as several technology efforts aimed at enabling future missions.

The largest effort within the Branch is support of the Ice, Cloud, and land Elevation Satellite (ICESAT) carrying the Geoscience Laser Altimeter System (GLAS) instrument. The ICESAT/GLAS primary science objectives are:

> To determine the mass balance of the polar ice sheets and their
> contributions to global sea level change
> To obtain essential data for prediction of future changes in ice
> volume and sea-level.

The secondary science objectives are:

> To measure cloud heights and the vertical structure of clouds
> and aerosols in the atmosphere
> To map the topography of land surfaces
> To measure roughness, reflectivity, vegetation heights,
> snow-cover, and sea-ice surface characteristics.

Our efforts have concentrated on the GLAS receiver component development, the Laser Reference Sensor for the Stellar Reference System, the GLAS fiber optics subsystems, and the prelaunch calibration facilities. We will report on our efforts in the development of the space qualified interference filter [Allan], etalon filter, photon counting detectors, etalon/laser tracking system, and instrument fiber optics, as well as specification and selection of the star tracker and development of the calibration test bed.

We are also engaged in development work on lidar sounders for chemical species. We are developing new lidar technology to enable a new class of miniature lidar instruments that are compatible with small Discovery-class orbiters now in the NASA planetary program. The purpose of the lidar is to continuously profile the water vapor and dust in the Mars atmosphere from orbit in order to quantify its dynamics, their relationship in the diurnal cycles, and to infer water vapor exchange with the Mars surface. To remotely measure the water-vapor height profiles, we will use the differential absorption lidar (DIAL) technique. We are also developing a laser sensor for measuring the total column content of CO_2 in the atmosphere of the earth. CO_2 is the principal greenhouse gas and has increased by roughly 80 ppm in the last century and a half.

We will report our efforts in the development of the laser transmitter and photon counting detector components for a Mars Orbiting DIAL system and for the CO_2 sounder.

The Branch is also involved in a number of smaller technological efforts aimed at furthering our capability to make laser based measurements from space. One of these is an effort in FM spectroscopy for remote sensing of chemical constituents. The standard approach for constituent measurement has been Differential Absorption Lidar. Here two wavelengths of light are used to probe on and off the absorption line of the species of interest. The concentration of the species of interest is determined from the small difference in the returns at the two wavelengths. Remote FM spectroscopy promises to increase the sensitivity by 2 or 3 orders of magnitude. A laser is modulated and the resulting sidebands used to probe the absorption line. Heterodyne techniques can then be used to sensitively detect the return. Our group is conducting experiments on using this technique in a remote sensing, range resolved mode to get constituent profiles vs. distance from airplane and space based platforms.

Another small effort is underway to develop a device called a recirculating optical frequency shifter. This project was conceived as a way to calibrate, on the ground, a wind-speed-measuring Doppler lidar instrument intended for use from orbit. The Doppler shift in the return light due to orbital velocity is at least an order of magnitude greater than what can be achieved by a single pass through an acousto-optic frequency shifter. In this experiment, a light pulse is circulated several times through a fiber-optic loop that contains an acousto-optic frequency shifter and optical amplifier. A large frequency shift is built up before the pulse is switched out of the loop.

Finally a number of other still smaller efforts are underway to improve the efficiency of transmission through a Fabry-Perot interferometer and to reduce the effects of signal induced noise in photomultiplier tubes. These will be discussed if progress and time permits.

References:

"Narrow Pass-Band Optical filters for Space-Borne Remote Sensing Applications". G. R. Allan, M. A. Krainak and M. A. Stephen. Paper RWC9. OSA Topical Meeting on the Remote Sensing of the Atmosphere. June 1999.

Nonlinear Optical Properties and Morphologies of VOPc Thin Film Prepared on Polyimide Film

H.Nakano*, J. Ito*, H. Furuhashi*, A. Maeda*, T. Yoshikawa*, Y. Uchida*,
K.Kojima*, A. Ohashi*, ○S. Ochiai* and T. Mizutani**

*Dept. of Electrical Eng., Aichi Inst. Tech., Toyota 470-0392, JAPAN
**Dept. of Electrical Eng., Nagoya Univ., Nagoya 464-8603, JAPAN
Tel: +81-565-48-8121, Fax: +81-565-48-0010, e-mail: ochiai@ee.aitech.ac.jp
○Corresponding Author: Shizuyasu Ochiai

If the third harmonic phase matching condition of a nonlinear optical material is satisfied, the efficiency of third harmonic wave is improved, and the TH strength increases in proportion to the square of the film thickness. Therefore, the phase matching condition was examined from the relation of the TH strength vs. the film thickness. Symbols used are Ts: substrate temperature, t: evaporating time and d: film thickness. Figure 1 shows the UV/VIS spectra of samples 1, 2 and 3. They show a shoulder around 680nm, an absorption peak at 740nm and a shoulder around 820nm in the Q band region. It suggests that these films have Phase I and II. In UV/VIS spectra of samples 1 and 3, the absorbances at 680nm and 740nm increase with the film thickness. It suggests that sample 3 is dominantly formed with the Phase I. Figure 2 shows the incidental angle dependence of TH strength for samples 1, 2 and 3 irradiated with P polarized laser beam. The TH strength saturates with the film thickness. It suggests that the TH strength strongly depends upon the morphology of VOPc thin film prepared on polyimide (PI) film. Figure 3 shows the UV/VIS spectra of samples 4, 5 and 6. Three samples have an absorption peak at 840nm in the Q band region. It suggests the transition from Phase I to Phase III in samples 4, 5 and 6. Figure 4 shows the incident angle dependence of TH strength for samples 4, 5 and 6 irradiated with P polarized laser beam. The TH strength increases with the film thickness.

It means that the packing density of the Phase III is higher than that of Phase I. Figure 5 shows the TH strength vs. film thickness characteristics. Although a VOPc thin film dominated with Phase III satisfies a Phase matching condition, a VOPc thin film of Phase I does not.
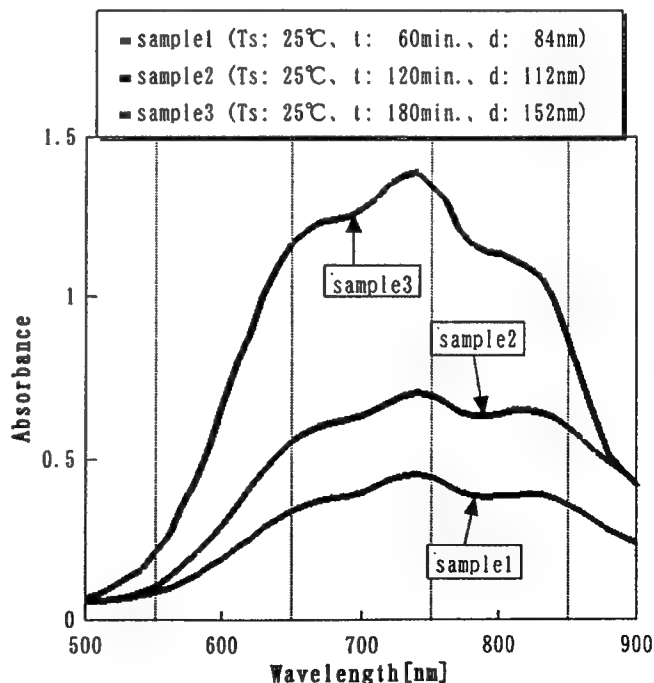
Figure1 UV/VIS spectra of samples 1, 2 and 3.

□ sample1(Ts: 25℃、t: 60min.、d: 84nm)
◇ sample2(Ts: 25℃、t: 120min.、d: 112nm)
▲ sample3(Ts: 25℃、t: 180min.、d: 152nm)

P-polarized light

■ sample4 (Ts: 150℃、t: 60min.、d: 71nm)
■ sample5 (Ts: 150℃、t: 120min.、d: 108nm)
■ sample6 (Ts: 150℃、t: 180min.、d: 130nm)

sample6
sample5
sample4
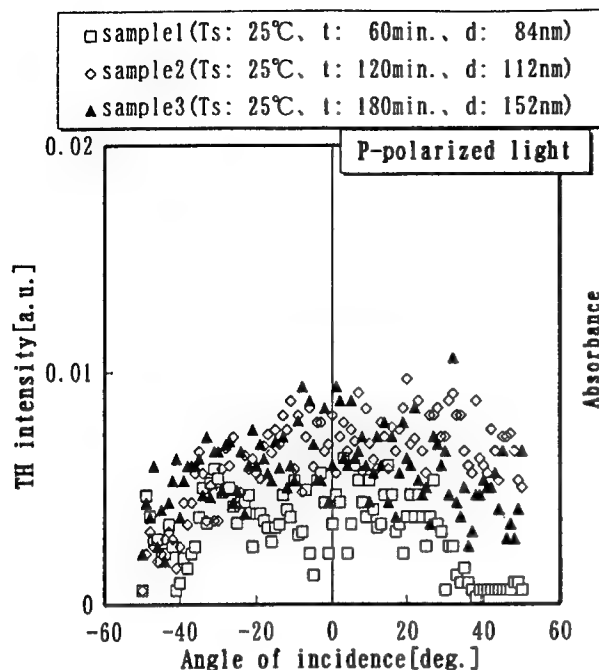
Figure 2 Incidental angle dependence of TH strength for Samples 1, 2 and 3 irradiated with P polarized laser beam.
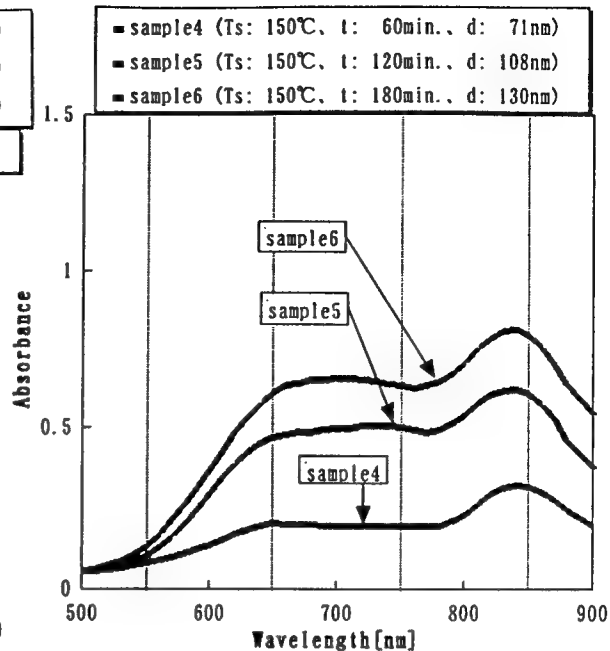
Figure.3 UV/VIS spectra of samples 4, 5 and 6.

■ sample4(Ts: 150℃、t: 60min.、d: 71nm)
○ sample5(Ts: 150℃、t: 120min.、d: 108nm)
▲ sample6(Ts: 150℃、t: 180min.、d: 130nm)

P-polarized light

P-polarized light

◇ Ts:25℃
■ Ts:150℃
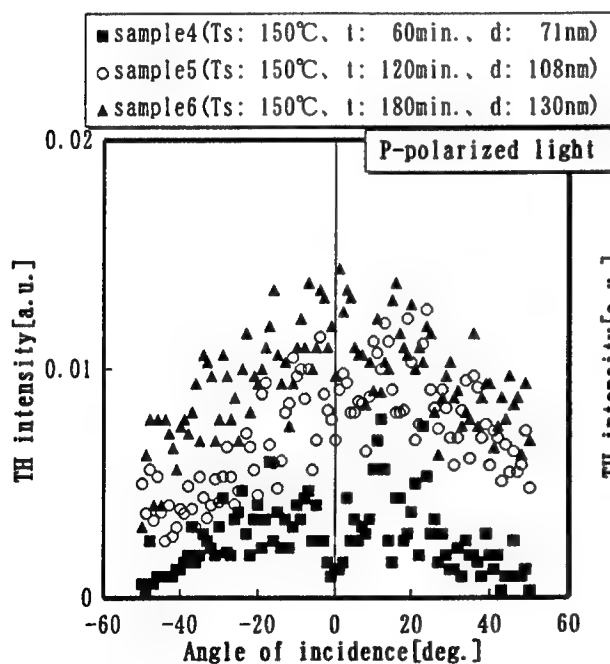
Figure 4 Incidental angle dependence of TH strength for Samples 4, 5 and 6 irradiated with P polarized laser beam.
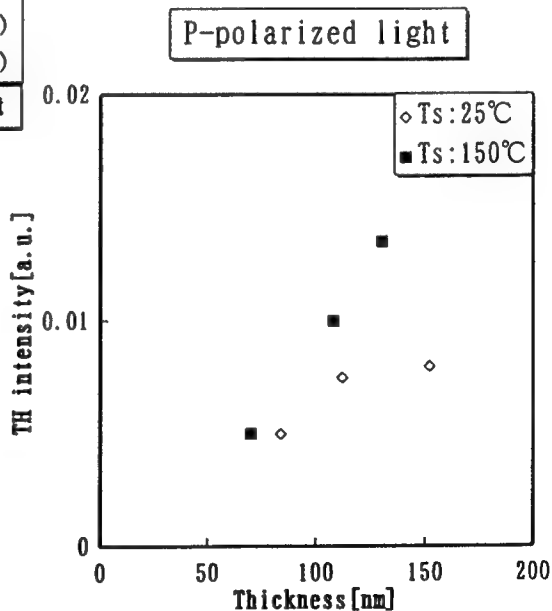
Figure 5 TH intensity vs. film thickness.

AUTHOR INDEX

Atar, H.	WD2.3	Killinger, D.	ThD3.1
Baker, J.	ThD1.1	Kojima, K.	ThD5.1
Benedict, R.	WD1.1	Lofgreen, D.	ThD2.2
Berdine, R.	WD1.1	Lyons, W.	WD2.4
Betts, G.	WD2.4	MacDonald, K.	ThD1.1
Bondurant, R.	WD2.2	Maeda, A.	ThD5.1
Chrisp, M.	ThD3.2	Mamidipudi, P.	ThD3.1
Cohen, D.	ThD2.2	Martinez, T.	ThD1.1
Coldren, L.	ThD2.2	Mizutani, T.	ThD5.1
Cora, A.	WD2.3	Nakano, H.	ThD5.1
Durrance, S.	ThD4.1	Ochiai, S.	ThD5.1
Furuhashi, H.	ThD5.1	Ohashi, A.	ThD5.1
Giuliano, C.	WD1.1	Phillips, R.	WD2.1
Gruneisen, M.	ThD1.1	Piotrowski, J.	WD1.1
Guthals, D.	ThD1.2	Rice, R.	ThD4.2
Hallada, M.	WD1.1	Rodney, P.	ThD1.2
Hassell, F.	ThD2.1	Ruggieri, N.	ThD4.2
Heaps, B.	ThD4.3	Schulz, P.	WD2.4
Ito, J.	ThD5.1	Shi, H.	ThD2.2
Johnson, L.	WD2.4	Sox, D.	ThD1.2
Johnston, D.	WD1.1	Uchida, Y.	ThD5.1
Joswick, M.	ThD1.2	Wallace, N.	WD3.1
Juodawlkis, P.	WD2.4	Yoshikawa, T.	ThD5.1

2000 IEEE/LEOS
Summer Topical Meeting

26 - 28 July 2000

Broadband Optical Networks

Turnberry Isle Resort & Club
Aventura, FL

Broadband Optical Networks

Co-Chairs:

Nick Frigo, *AT&T Labs - Research,* Red Bank, NJ
Gee-Kung Chang, *Telcordia Technologies*, Red Bank, NJ

Technical Program Committee:

K. Lu, *Telcordia Technologies*, Morristown, NJ
A. Saleh, *Corvis, Inc.*, Columbia, MD
M. O'Mahoney, *University of Essex*, Colchester, UK
W. Way, *National Chiao Tung University*, Hsinchu, Taiwan

TABLE OF CONTENTS

Broadband Optical Networks

Wednesday, 26 July 2000

WC1:   Optical Networking I

Economic and Architectural Benefits of Hierarchical Backbone Networks

Jane M. Simmons

Corvis Corporation, 7015 Albert Einstein Drive, Columbia, MD 21046-9400

jsimmons@corvis.com

The explosive growth in data traffic will necessitate that service providers deploy networks with hierarchical logical structures. In a hierarchical network, each layer is designed to hide the details of its layer from those above, thus enabling cost effective and scalable network growth. At each layer, the appropriate traffic granularity, switching and grooming technology, and both physical and logical topologies must be selected. Significant cost benefits can be realized in both capital and operational expenditures. Multi-tiered architectures can: take advantage of cost-effective banded switching technologies as described in [1]; enable a large amount of optical bypass, which reduces the amount of required electronic termination equipment; and reduce the number of elements that need to be managed, thereby simplifying network operation. Also, with respect to restoration, a hierarchical scheme provides efficient use of restoration capacity, reduces the amount of electronic access equipment that needs to be deployed for the capacity to be effectively shared, and simplifies the restoration decision process [1].

A good example of a hierarchical architecture is that of the two-tiered scheme shown in Figure 1. In this architecture, the upper layer is comprised of localized collector rings, operating at granularities of DS-3 or OC-3, whereas the lower layer consists of a nationwide 'express mesh' operating at granularities of OC-48, OC-192, and higher. Each collector ring is typically populated with SONET Add/Drop Multiplexers (ADMs), with all nodes in the ring being logically connected (although not necessarily on all wavelengths). The functions of the collector ring are two-fold: route traffic within the ring, and collect inter-ring traffic and deliver it to the large mesh nodes located on that ring. The ring topology is suitable for this layer due to the limited geographic extent of the collector rings and the simple protection properties of rings. Furthermore, many carriers already have made huge investments in SONET-ring-based networks. The capacity of these rings is currently being exhausted by the tremendous growth in traffic, exacerbated by the inefficiencies of inter-ring routing. These legacy rings can be more effectively utilized with their role restricted to serving as the collector network – SONET ADMs are well suited for adding, dropping, and grooming traffic, and current capacity demands will be lessened by migrating the inter-ring traffic to an express mesh. Alternatively, a mesh architecture with grooming cross-connects can be used for the collector network.

As opposed to the fine granularity, limited extent nature of the collector network, the lower-layer express mesh of Figure 1 must carry large amounts of traffic for long distances. These requirements are best met with emerging ultra-long reach, high-capacity transport systems and all-optical switches. Since the collector rings perform the function of aggregation, the express mesh can carry traffic at coarser granularities – OC48 and above. Not all network nodes are included in the logical mesh; only those nodes that generate traffic at levels comparable to the granularity of this level, or those that are strategically located, should be included. Thus, depending on traffic patterns in the network, the express mesh will completely bypass a major portion of the nodes. To take full advantage of this architecture, ultra-long reach transport must be deployed such that traffic can be routed between (and through) lower-layer nodes without any intermediary regeneration. The combination of a sparsely populated express mesh (roughly 20 nodes nationwide) with ultra-long reach transport eliminates a significant portion of electronic termination in the network [2].

In addition to limiting the nodes that are included in the lower layer, it is also important to create a 'streamlined' physical topology. Thus, fiber links that do not pass by major nodes may not be included in this layer. First, not populating a fiber route eliminates the capital and operational costs of deploying amplifiers on that route. Second, streamlining the underlying topology results in larger bundles of traffic that can be routed at lower cost; i.e., restricting the diversity of routes produces more efficiently packed traffic pipes. While removing fiber routes results in greater traffic on the remaining routes, next-

generation high-capacity transport systems can accommodate such high bandwidth demands. In addition, while fewer fiber paths may result in somewhat longer end-to-end paths for some connections, this very likely does not lead to more regeneration if ultra-long reach systems are deployed. Of course, restoration options must also be considered when laying out the physical topology.

A mesh topology is most appropriate for the lower level since, through the use of switches, it creates virtual topologies that can be optimized for the routing of working traffic and the sharing of protection bandwidth. One of the most significant benefits of a hierarchical architecture, in terms of cost and scalability, is that it enables the deployment of a hierarchical switch architecture, as shown in Figure 2. The streamlined architecture of an express mesh creates large bundles of traffic that can be switched as a single unit. For example, increasing the switching granularity by a factor of B decreases the switch fabric size by a factor of somewhere between $B\log B$ and B^2, depending on the switch technology. This directly translates to a saving in switch cost, switch size, number of physical interfaces, power, and switch states that must be managed. In Figure 2, we assume there are two levels of switches, operating at granularities of G_1 and G_2, where G_1 is coarser than G_2. With efficient packing algorithms, only a small portion of the traffic needs to be switched at the finer granularity; the remainder is more cost effectively switched at the coarser level. While the switches can operate in the optical or electrical domain, to best take advantage of an express mesh, optical switches should be used for the coarse granularity traffic. This enables large bundles of traffic to express through the node without any electronic termination.

Thus far, we have discussed a two-tiered approach to network design. Ultimately, what will drive the number of layers and the granularity of each layer is cost and technology. Assume that the cross-sectional traffic on any link in a particular layer of the network is T, and assume that the finest level of granularity required at that layer is G. Then the number of elements per link that are potentially switched are T/G. At a node of degree-N, this translates to a switch size of approximately $(NT/G) \times (NT/G)$. Due to limits of technology and physical space, the switch size may be limited, resulting in multiple tiers, where, for the ith tier, T_i and G_i are chosen such that NT_i/G_i remains tractable. This will enable networks to continue to grow gracefully.

We have presented a qualitative argument for the economic and architectural benefits of deploying hierarchical networks, and outlined how these benefits can be best realized with new generation transport and switching systems.
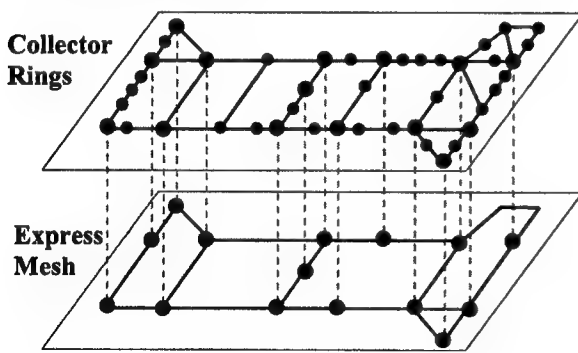
Figure 1. An example of a two-level hierarchy, where a group of collector rings aggregates and grooms fine granularity traffic, and delivers traffic to a streamlined, coarse granularity express mesh.
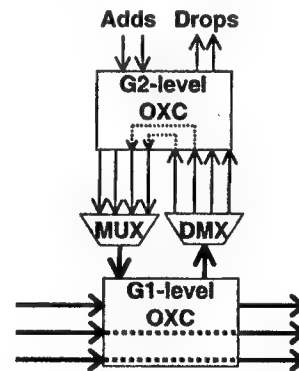
Figure 2. A hierarchical architecture can take advantage of hierarchical switching. At the lower level, an OXC switches traffic at a coarse granularity (G1). Only a small percentage of the traffic needs to be switched at the finer granularity (G2).

References:
[1] Simmons, J.M., "Hierarchical Restoration in a Backbone Network," *OFC'99*, Feb. 21-26, 1999, San Diego, CA.
[2] Saleh, A.A.M., "Transparent Optical Networking in Backbone Networks," *OFC'00*, Mar. 7-10, 2000, Baltimore, MD.

Digital Wrappers for IP over WDM systems

Paul Bonenfant* and Antonio Rodriguez Moral
Lucent Technologies
pbonenfant@lucent.com, arodmor@lucent.com

*101 Crawfords Corner Road, Room 3C-515
Holmdel, NJ 07733
Tel: +1 732 949 8760
Fax: +1 732 949 1124

Summary

There is considerable interest within the rapidly converging telecommunications and data communications networking environments around a simplification of the data/transport network known as "IP over WDM." The ubiquity and critical role of core IP routers, and the emergence of Label Switching Routers (LSRs) based on Multi-Protocol Label Switching (MPLS) technology, when combined with Optical Transport Networks (OTNs) has also raised the issue of optimized network architectures for the Optical Internet.

In marketing terms, the notion of "IP over WDM" makes for remarkable hype: take the most widely talked about data networking protocol—IP—and combine it with the ultimate in bandwidth provisioning—WDM—to realize the ultimate "blend" of hot technologies. What is meant by "IP over WDM," however, is less than clear. The intention of this paper is to demystify the notion of "IP over WDM," and in doing so, to indicate what features may be required in future "collapsed" data/transport networks.

In reality, "IP over WDM" invariably implies one of a multiplicity of mappings of IP onto fiber (or wavelengths), as illustrated in Figure 1. To state that any *one* particular mapping represents "IP over WDM" is extremely disingenuous, and ignores the fact that every data network is unique in a marketplace governed by differentiation.
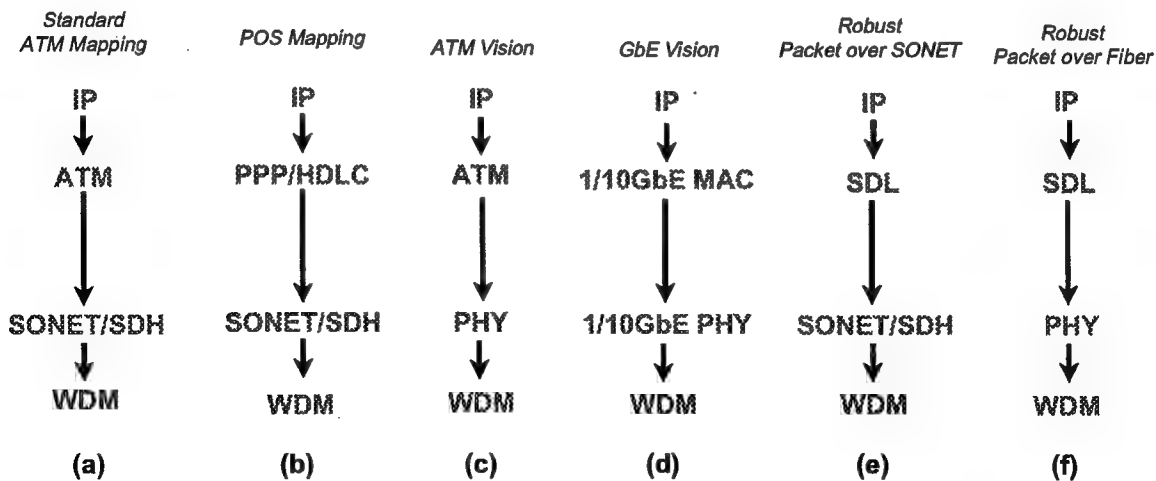
Figure 1. Variations on a Theme: What is "IP over WDM"?

Commensurate with the emergence of "IP over WDM" protocol mappings is the demand for transport networking at unprecedented levels of granularity—on the order of Gigabits to tens of Gigabits per second—and the evolution from time-division multiplexing (TDM) to Optical Transport Networking via WDM. We discuss the move from TDM to Optical Channel networking as a natural step in the evolution of the transport network, which will be predicated upon the support of operations, administration, and maintenance functions at the Optical Channel layer.

Current deployments of IP networks presuppose that delivery will be on a "best effort" basis. However, many network operators want to provide new services that require traffic management of IP flows. One of the most significant of these is virtual private networking, where one customer's traffic is separated from another in a single IP network with well-defined quality of service and security. While this is not possible with today's "best effort" IP network, it can be achieved by means of a protocol that allows IP packets to be partitioned into traffic flows that can be manipulated in their own right. Examples of such protocols include ATM, and MPLS. The partitioned flows must then be encapsulated to be carried over WDM. From the perspective of IP, it is of no consequence if IP is partitioned or not, only that it is encapsulated.

The management of optical networks will also undergo a profound evolution. The emergence of digital wrapper technology will enable optical networks to provide similar management features to those existing today in Synchronous Optical Network (SONET) and Synchronous Digital Hierarchy (SDH) networks, while at the same time opening the optical layer to a wide variety of client signals. This will allow service providers to accommodate different protocol stacks and network architectures for their next-generation IP backbones. This feature, known as service transparency, together with the required technologies and protocols for optical switching, protection and restoration, are critical in a marketplace that will be governed by service differentiation and rapid service provisioning. We present a perspective on the impact of technologies such as digital wrappers, optical switching and optical layer protection and restoration, on the services and capabilities of next-generation optical transport networks and optical internetworks.

Another issue under intense research and debate is the design of the control plane of next-generation OTNs and optical internetworks. The concept of Multi-Protocol Lambda Switching introduced in the Internet Engineering Task Force (IETF) has emerged as a potential solution, but it has also added a degree of confusion to the problem. We introduce some of the concepts and protocols that are under consideration in the IETF and other fora, including the Optical Internetworking Forum (OIF), the Optical Domain Service Interconnect (ODSI) initiative, and the Amercian National Standards Institute Committee T1 – Telecommunications (ANSI T1) and International Telecommunications Union (ITU) standards bodies. The goal of these initiatives is to enable rich services such as rapid optical channel provisioning, protection and restoration, optical layer network topology auto-discovery, and optical bandwidth management services.

Finally, we propose that true optical internetworks will not result from a blind simplification of the protocol stack, but rather from a well-engineered combination of network architectures, protocol stacks, service transparency, and enhanced optical layer management. Enabled by the use of digital wrappers in the OTN, together with an innovative control plane that reuses and adapts many existing protocols from the IP world, the Optical Internet will provide feature-rich services that have yet to be implemented in legacy data networks and traditional WDM-based optical transport networks.

IP over WDM Traffic Engineering

John Y. Wei, Changdong Liu, and Kevin H. Liu

Telcordia Technologies Inc, 331 Newman Springs Road, Red Bank, NJ 07701-5699

Email: {wei, cdliu, liuke}@research.telcordia.com

Traffic engineering in IP/WDM networks can be pursued in two fashions: overlay and integrated as shown in the figure below. With *overlay traffic engineering*, operations in one layer can be independent from those in the other layer. Traffic engineering solutions developed for either IP networks or WDM networks can be directly applied to each layer, respectively. At the present stage, an anticipated first step towards IP over WDM is to hook up IP router interfaces to OADM (optical add/drop multiplexer) client add/drop ports. This forms an overlay network in which WDM serves as the server layer and IP behaves like the client layer. This overlay client-server network is a natural match to the notion of overlay traffic engineering. With *integrated traffic engineering*, optimization with respect to selected objectives is pursued coordinately across both the IP and WDM layers. It is made possible by mechanisms such as Multi-Protocol Lambda Switching [1] that allows a unified control plane across both layers. With the emergence of more sophisticated hardware that integrates functionality of both IP and WDM at each network element (NE), integrated traffic engineering can be performed more naturally and efficiently.
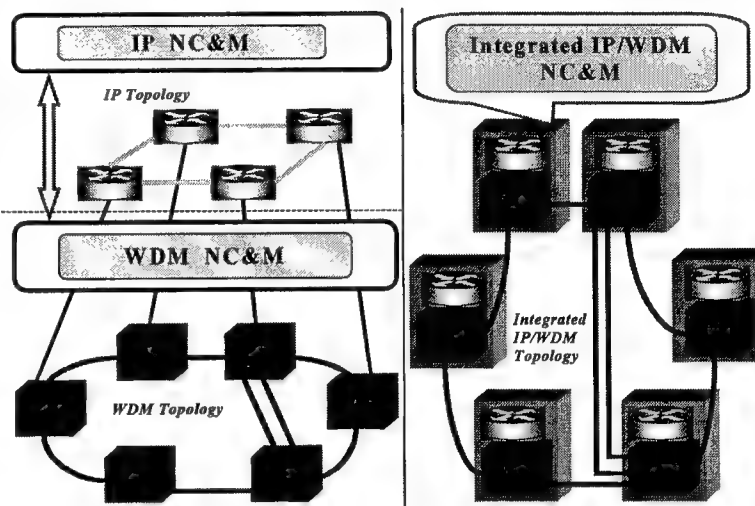
IP/WDM Traffic Engineering Paradigms: With overlay traffic engineering, operations in one layer are pursued independent from those in the other layer. Traffic engineering solutions developed for either IP networks or WDM networks are applied directly to their respective layer, with little or no inter-layer coordination. In IP/WDM networks, traffic engineering in the IP layer can theoretically be effected via IP routing algorithms that can adapt the IP packet routes, and perform load balancing. Likewise, traffic engineering in the WDM layer can be effected through light path reconfiguration that adapts the IP network's virtual topology to the evolving traffic pattern. In the case of switched WDM, the WDM layer can also adjust the number of wavelengths allocated to each virtual link, thereby affecting the bandwidth and contention statistics of the virtual link. In practice, because traditional IP routing algorithms are all oblivious to traffic loading, traffic engineering in today's IP networks often relies entirely on link layer adjustments. For example, an IP over ATM network typically maintain a full IP mesh connectivity, and rely entirely on the ATM layer to adjust the bandwidths provisioned for the ATM virtual circuits that support the IP links. These ATM layer actions are completely transparent to the IP layer routing algorithm. Overlay traffic engineering is most likely adopted in near-term deployment of overlay IP/WDM networks.

With the emergence of MPLS-based IP routers, and MPλS-based WDM OXCs, it is now possible to define an integrated control plane for both layers, which makes it easier to pursue a more integrated approach. With integrated traffic engineering, optimization with respect to selected objectives is pursued coordinately across both the IP and the WDM layers. All of the IP and WDM traffic engineering mechanisms described above still exist, and can now be considered together. Time scale and traffic granularity considerations will determine which specific mechanisms from the different layers are most suitable for different traffic conditions. With more sophisticated hardware that integrates functionality of both IP and WDM at each network element (NE), integrated traffic engineering can be performed even more naturally and efficiently. Emerging technologies such as Optical Label Switching (OLS) [2] will further enrich the set of available traffic engineering choices.

Traffic Engineering Functional Components: Regardless of which traffic engineering approach is adopted, an IP/WDM traffic engineering solution will always consist of a number of basic functional components. We enumerate the most important components below:

Traffic monitoring, analysis and aggregation is responsible for collecting traffic statistics from the network elements, e.g. IP routers and OXC. Then the statistics are analyzed and/or aggregated to prepare for the traffic engineering and network reconfiguration related decision-making.

Bandwidth demand projection projects the bandwidth requirements in the near future based on past and present measurements and the characteristics of the traffic arrival processes. The bandwidth projections are used for subsequent bandwidth allocation.

Reconfiguration trigger consists of a set of policies that decide when a network level reconfiguration is performed. This is based on traffic measurements, bandwidth predictions, and on operational issues, e.g., to suppress influence of transitional factors and reserve adequate time for network to converge.

Topology design provides a network topology based on the traffic measurements and predictions. Conceptually this can be considered as optimizing a graph (i.e. IP routers connected by light paths in the WDM layer) for specific objectives (e.g. maximizing throughput), subject to certain constraints (e.g. nodal degree, interface capacity), for a given load matrix (i.e. traffic load applied to the network.) This is in general a NP-hard problem. Since reconfiguration is regularly triggered by continually changing traffic patterns, an optimized solution may not be stable. It may be more practical to develop heuristics that emphasize more on factors like fast convergence, and less impacts on ongoing traffic, than on optimality.

Topology migration consists of algorithms to coordinate the network migration from an old topology to a new topology. As WDM reconfiguration deals with large-capacity channels, changing allocation of channel resources in this coarse granularity has significant effects on a large number of end user flows. Traffic flows have to adapt to the light path changes at and after each migration step. These effects can potentially spread over the routing pattern of the network, which in turn may affect more user flows.

Simulation Results: To gauge the benefits possible in IP/WDM traffic engineering, we performed extensive simulation studies. The topology used in the simulation is derived from a major carrier's IP backbone covering the United States. The simulation's offered traffic loads captured typical Internet traffic characteristics, such as sudden surge between some node pairs, spatially unbalanced loading and regional congestions. The different loads emulate short-term hot-spot problems, and long term unbalanced resource usage due to poor planning. Simulation results show that network performance is improved in many ways: overall IP traffic throughput is increased when the traffic pattern is skewed; the congestion-free region is expanded by the same scale (top right figure,) network resiliency is also enhanced. The simulation also shows that network wide average packet end-to-end latency improved in all load regions (middle left figure.) These delay improvements are the results of more efficient network resource allocation, which migrates loads on congested links to less utilized ones (right bottom figure.)
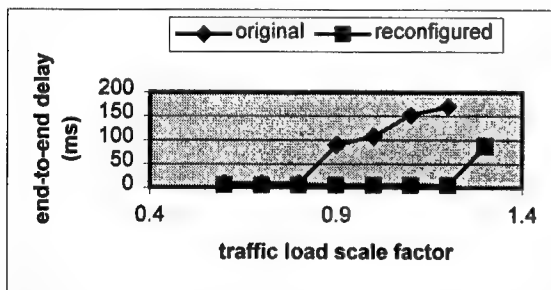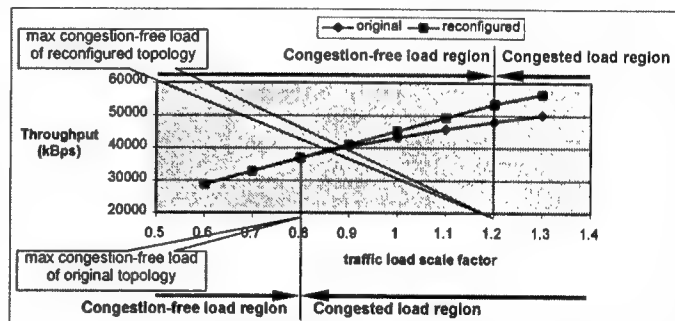
References

[1] D. Awduche, *et al.*, "Multi-Protocol Lambda Switching: Combining MPLS Traffic Engineering Control with Optical Cross-connects", *IETF Internet Draft*.

[2] G. K. Chang, *et al*, "A Proof-of-Concept, Ultra-low Latency Optical Label Switching Testbed Demonstration for Next Generation Internet Networks," *OFC'2000*, Vol. 2, Section WD5, pp. 56-58, Baltimore, Maryland, March 2000.
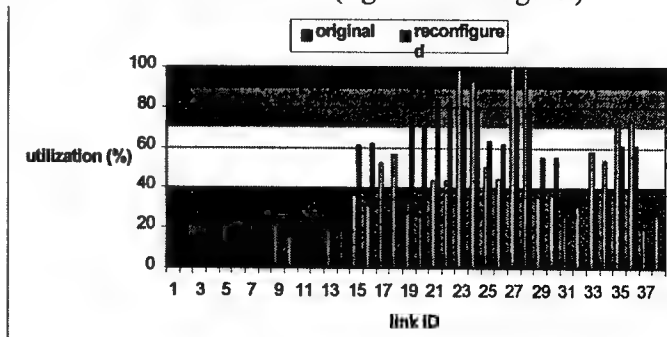
Transport of Gigabit Ethernet directly over WDM for 1062 km in the MONET Washington DC network

W. Xin (1), G. K. Chang (2), T. T. Gibbons (3)

(1) Oplink Communications, 3475 North First Street, San Jose, CA 95134, (michaelx@oplink.com)
(2) Telcordia Technologies, 331 Newman Springs Road, 3Z285, Red Bank, NJ 07701, (gchang@telcordia.com)
(3) USC/ISI, 4350 North Fairfax Drive, Suite 620, Arlington, VA 22293, (tgibbons@isi.edu)

1. Introduction

DWDM point-to-point transport systems have been widely deployed in the backbone networks. Recently research and development have been focusing on developing the reconfigurable optical networking systems and technologies that would possess network intelligence to directly accommodate IP, ATM as well as traditional voice traffic. In this paper we report the successful transport of Gigabit Ethernet for 1062 km over the multi-vendor, reconfigurable, MONET Washington DC network.
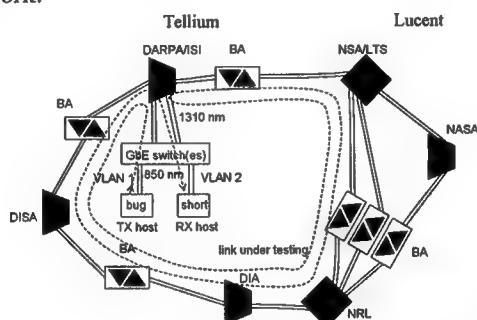
Fig. 1. MONET Washington DC network.

2. Network Architecture

The MONET Washington DC Network consists of two two-fiber rings as shown in figure 1. The east ring is provided and maintained by Lucent Technologies. This ring consists of two wavelength selective cross-connects (WSXCs) in the Laboratory for Telecommunication Sciences at National Security Agency (NSA/LTS) and the Navel Research Laboratory (NRL), one wavelength add/drop multiplexer (WADM) at National Aeronautics and Space Administration (NASA), and two wavelength amplifiers (WAMPs) in the Bell Atlantic central office. The west ring is provided by Tellium and managed by Telcordia Technologies. This ring consists of three WADMs at the Defense Advanced Research Projects Agency/Information Systems Institute (DARPA/ISI), Defense Information Systems Agency (DISA), and Defense Intelligence Agency (DIA) as well as four WAMPs in the Bell Atlantic central offices. Bell Atlantic provides the in-ground fiber infrastructure for the network. The whole network is controlled and managed by Telcordia Technologies' CORBA based network control and management (NC&M) system which runs on the ATM network at OC-3c rate over the 1510 nm optical supervisory channel.

The switching fabric of Lucent network elements is based on lithium niobate technology. It is therefore transparent. The Tellium WADM is based on wavelength transponders and transceivers of OEO conversion and electrical switching fabric. Thus the west ring is opaque and has the wavelength interchange capability.

3. Gigabit Ethernet

The Tellium west ring has 4 modes of transmission: OC-3, OC-12, OC-48, and OSIG (optical signal). The OSIG mode is to transmit non-SONET rate signals up to 2.5 Gbps without timing recovery during the OEO conversion.

We have conducted an experiment to test the long distance transmission of Gigabit Ethernet (GbE) using the OSIG mode. The equipment used in the experiment were: two Pentium II workstations as test hosts running FreeBSD 3.2 with Netgear GA620 GbE Cards with 850 nm SX ports; these two hosts were connected to an Extreme Networks Summit 1 GbE switch. The switch was configured into two virtual LAN (VLAN), with the test hosts each residing on a separate VLAN. This configuration prevented the switch fabric from bridging packets between the two hosts directly. Instead, packets were forced over the switch LX GbE ports (1310 nm). The link from the host named 'bug' to the host named 'short' was under testing. The received optical power was attenuated. The experiment was to measure the packet loss rate or frame loss rate versus the received power.

The first step was to measure a back-to-back baseline and a network baseline. The network baseline was obtained by configuring the WADM that the GbE packets traveled through the WADM switch fabric only. We then

sent the GbE signals out of the node over the fibers towards DISA, DIA and all the way around the ring back to DARPA/ISI and looped back at each site with distance of 100 km, 238 km and 412 km, respectively.
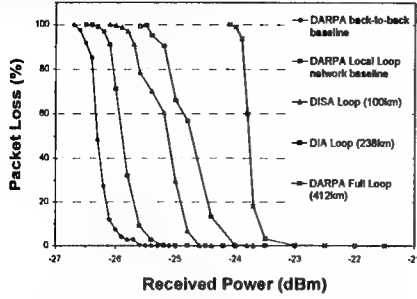
Fig. 2. UDP packet loss rate vs. received power.
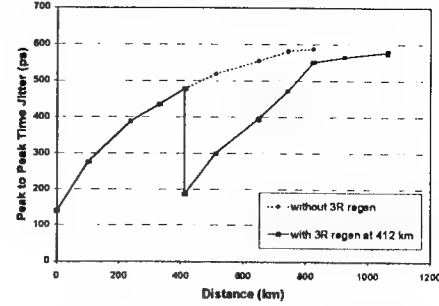
Fig. 3. Time jitter vs. transmission distance.

Multi-generator (MGEN) and Test TCP (TTCP) were used to generate frames filled with UDP packets for the test. The UDP packets were 1400 byte in size and each packet filled in one frame. The frames transmitted and received were monitored and the frame loss rates or the packet loss rates were calculated.

The experimental results are shown in figure 2. The power penalty for the network baseline over the back-to-back baseline is about 0.5 dB at 10% packet loss rate. The power penalties for 100 km, 238 km and 412 km transmissions are 1.2, 2 and 2.5 dB. The maximum received power for the Summit 1 switch is -3 dBm. The received power for 412 km transmission at less than 1% packet loss rate is -22 dBm. This gives a system margin of 20 dB, which indicates the possibility of transmission for more than 1000 km over the wide area optical network.
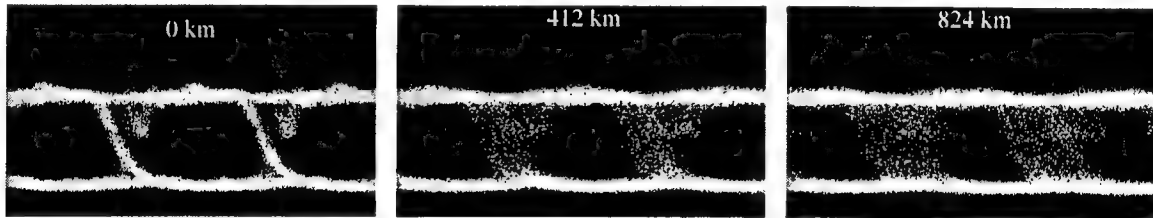
Fig. 4. Eye diagrams at 0, 412 and 824 km.

Testing one switch with two VLANs might not show any time synchronization problems. We used two switches to investigate the timing issue. We did not observe any significant performance differences.

In order to achieve long distance transmission, we connected 'short' to 'bug' directly through the switching fabric. And we used λ_3, λ_4 and λ_8 for the link from 'bug' to ' short' to have a total of 1236 km transmission distance.

We suspected that the limiting factor for the long distance transmission of the GbE was the time jitter accumulation. Thus we measured the peak-to-peak time jitter from the eye diagrams. Figure 3 shows the time jitter versus the transmission distance with and without 3R regeneration. The dashed curve is without any 3R regeneration and the maximum distance is 824 km where the jitter is 588 ps, almost reaching the GbE standard of total jitter budget 599 ps [1]. Figure 4 shows the eye diagrams at 0, 412 and 824 km. The corresponding eyes experienced 2, 18 and 36 2R regeneration. The measurement was made at normal operation condition with -10 dBm received power.

In order to increase the transmission distance, we built a 3R regenerator to overcome the time jitter accumulation. We put the regenerator at 412 km. The time jitter has been improved from 478 ps to 188 ps, almost the same as that of the 0 km eye which is 141 ps. We increased the transmission distance to reach a maximum of 1062 km where jitter reaches 579 ps. Again, beyond this distance the link was down. The jitter vs. distance is shown as the solid curve in Fig. 3. We also put the 3R regenerator at 650 km and 824 km. In both cases, we could not reach 1062 km distance. It seems that when time jitter reaches 400 ps, which is half of the bit period, it requires 3R regeneration; additionally when the time jitter reaches 599 ps, no data can be transmitted.

4. Conclusions

For the first time, to our knowledge, we have transported Gigabit Ethernet packets directly over WDM for 1062 km in the successfully deployed MONET Washington DC network. The experiment indicates that the Gigabit Ethernet can be used for WAN or backbone transmission bypassing the ATM and SONET intermediate protocol layers. It also indicates that the physical layer of the Fibre Channel, which is adopted by the Gigabit Ethernet, can be used as a long-haul transmission protocol.

[1] IEEE Standard 802.3, 1998 Edition.

Broadband Optical Networks

Thursday, 27 July 2000

CPLE: Plenary Session
ThC1: Network Performance and Management
ThC2: Broadband Access Technologies

Thursday Missing Paper

CPLE1   "Broadband Access for Future Information Networks" R. Lucky,
Telcordia Technologies, Red Bank, NJ, USA.

Performance Issues in WDM Networks

Guido Maier

Optical Networks Laboratory, CoreCom

Via Ampere 30, 20131 Milan, Italy
maier@corecom.it

Innovation of optical technologies for telecommunications has acquired an extremely rapid pace in the last year. As the recent OSA Optical-Fiber-Communications 2000 Conference exhibit very well testify, all the main components necessary for switching and transmission of WDM lightpaths are now available as commercial products on the market. WDM transmission-system capacity has grown towards hundreds of WDM channels, each one modulated at 10 Gbit/s or more, over very long transmission spans; opto-electronic regenerators and wavelength converters operate in the 10 Gbit/s range; Optical Add-Drop Multiplexers (OADMs) are already quite common devices, while several Optical Cross-Connect (OXC) products have been recently presented or announced. This technological evolution makes the full development of WDM networking a reality: new complex meshed topologies can be developed at the side of more traditional and simpler schemes such as WDM rings; wavelength conversion can be used to add flexibility, while lightpath control algorithms can be upgraded to improve the efficiency of connection provisioning.

In this ever-changing scenario also the relationship between the entities that generate telecommunication traffic and the entities that control the provisioning of transport resources is evolving. In the recent past the large-capacity transport networks were typically operated by single nation-wide telephone companies that used them mainly to transport the traffic generated by their own subscribers. Today, instead, a new model is becoming more and more frequent in which an optical transport network operator provides capacity on-demand in terms of optical connections (lightpaths) to independent customers such as Internet service providers or the telephone companies themselves. Thanks to the transparency of the optical network, once a customer has leased a lightpath he is able to manage it at his will and according to the need of the services he is providing to its own subscribers, for example adopting the most suitable electronic transport technology with the option of choosing among SDH, raw IP packets, raw ATM cells, raw HDTV data and so on. This makes the WDM layer a common platform for heterogeneous customers and service providers.

The evolution we depicted implies also that the approach to WDM network analysis and design may change. In the past decade a large number of studies have been carried out aimed at the cost optimization of a WDM network given the forecast average traffic-demand, evaluated in advance on the basis of the previous utilization history. This approach, that we shall call static-traffic WDM design, is no longer easily applicable for a network operator of the new type that not only ignores how many customers it will have in a given time in future, but also what kind of service they will provide to their subscribers. How is it possible to predict the values of a static traffic-matrix in these conditions? Incidentally it must be considered that some of the services that the optical transparency may allow to support may well be entirely new, without a case-history on which to base statistical predictions.

A more effective approach to WDM network planning may be based on the dynamic traffic, where by this term we mean that requests for lightpaths can arrive to the network at any random time instants, when other connections are already active. If the new request can be accommodated without disrupting the existing connections, a lightpath is created and it is maintained active for the whole duration of the connection specified by the customer that asked for the resources. The performance of the network in this scenario can be well measured by the blocking probability of the network, i.e. the probability that a new potential customer can not be satisfied due to shortage of transmission resources.

Optimal design criteria in these conditions have been up to now quite seldom investigated and are not as known as in the static-traffic case. Useful elements to optimize complex systems always come from the analysis

of their behavior in various conditions. Therefore in the present contribution we would like to summarize the studies we have carried out concerning the behavior of both ring and mesh WDM networks under dynamic traffic.

The analyses we performed are all based on a model of the network which allows to run a set of simulations in which the events of lightpath-setup and lightpath-tear-down request are generated by the nodes according to suitably defined random processes. A lightpath setup implies solving a problem of Routing and Wavelength Assignment (RWA) for the new connection, according to a certain set of RWA algorithms. The blocking probability is then evaluated by gathering the statistical data from the simulation run in steady-state conditions. Another measure of the network performance can be provided by comparing the blocking probability of connections between adjacent nodes and between very distant nodes. This measure is called fairness: a network providing a good quality service should be equally fair to all the potential customers regardless of the distance of their terminal nodes.

In particular we intended to understand the effects of certain network-design approaches and system parameters on the blocking probability. We have considered the cases that we are going to very briefly summarize in the following.

> *WDM ring networks.* Wavelength conversion capacity increases the flexibility of a WDM network and its capacity to accommodate new connections. However converters are expensive devices: we considered therefore the solution of placing converters only in some nodes of a ring WDM network. Both the unidirectional and bidirectional rings were tested and converters were uniformly distributed among the nodes or placed in adjacent nodes [1], [2].
>
> The analyses were carried out employing different types of connection-request generators to simulate situations in which the traffic is smooth, regular (Poissonian) or peaked. This was done in order to take into account a wide range of traffic types, since there is no precise idea yet of how to statistically characterize the lightpath traffic.
>
> Our analysis showed that, provided wavelength converters are evenly distributed, only a few of them are sufficient to lower the blocking probability almost to the same level reached when wavelength converters are placed in all the nodes. We also showed that wavelength conversion capability is much more important to obtain a fair network than to improve blocking, especially in the unidirectional ring. Finally, the blocking probability rises with peaked traffic, but in this conditions the network is more fair.
>
> *WDM mesh networks.* The topology of a mesh network has a direct impact on its blocking properties. The analysis we carried out on the WDM mesh networks [3] was therefore mainly aimed at the understanding of the relation between blocking and fairness and some topological parameters, such as nodal degree and the average minimum distance between the nodes. Moreover we compared the performance attainable by different routing and wavelength assignment algorithms. All the simulations were repeated twice to compare the cases with full and absent wavelength conversion capability.
>
> The results obtained show that not only the blocking probability decreases by increasing the node degree, as expected, but also decreasing the average minimum distance between the nodes. Moreover we could verify that the best performing wavelength assignment and routing algorithms are, respectively, First-Fit and Least Loaded Routing. Finally we verify that the wavelength conversion capability is always useful to improve the fairness of the network, especially in those networks having a low connectivity degree: this is the generalization of the results we have obtained concerning rings to any topology.

In conclusion we have discussed some issues concerning WDM network performance with a dynamic offered traffic by showing the results obtained by discrete-event simulation. Our work is essentially an analysis aimed at finding out which can be the most important parameters that must be taken into account in designing WDM networks in a dynamic environment. We believe that, thank to the optical technology improvement, the dynamic-traffic scenario will become more and more important in the future.

REFERENCES

[1] G. Maier, M. Martinelli, A. Pattavina, and M. Scappini. Performance of WDM rings with partial and sparse wavelength conversion under general dynamic traffic. *European Transaction on Telecommunications*, 11(1), Jan.-Feb. 2000.

[2] G. Maier, M. Martinelli, A. Pattavina, and M. Scappini. Performance of WDM rings with wavelength conversion under non-Poisson traffic. In *Proceedings, IEEE International Conference on Communications*, page s51.4, June 1999.

[3] G. Maier, M. Martinelli, A. Pattavina, and M. Pierpaoli. Performance analysis of wavelength division multiplexing mesh networks. In A. Bononi, editor, *Optical Networking*, pages 52–63. Kluwer, September 1999.

Management Optical Networks:
View of the EURESCOM Project P918

Antonio Manzalini
CSELT Via Reiss Romoli, 274, 10148 Turin ITALY
Andreas Gladisch
Deutsche Telekom AG; T-Nova , Goslarer Ufer 35, D-10589 Berlin, Germany
Georg Lehr
Deutsche Telekom AG; T-Nova , T-Nova , Am Kavalleriesand 3, 64307 Darmstadt, Germany

Summary

The actual program of EURESCOM – a common research and Development Organisation of European Operators - includes the P918 project "Integration of IP over Optical Networks: networking and management". One of the main goals of the P918 project is to define the functional architecture for a client-independent Optical Transport Network (OTN) carrying different clients including also an optimised IP-based network. In particular, aspects of management of an OTN are investigated to reach a recommended view for Network Operators.

In general P918 is applying a transport network modelling recommended by ITU (Rec.805), which means that network scenarios, functional architecture and management requirements will be the basis for the specification of atomic functions and management information models.
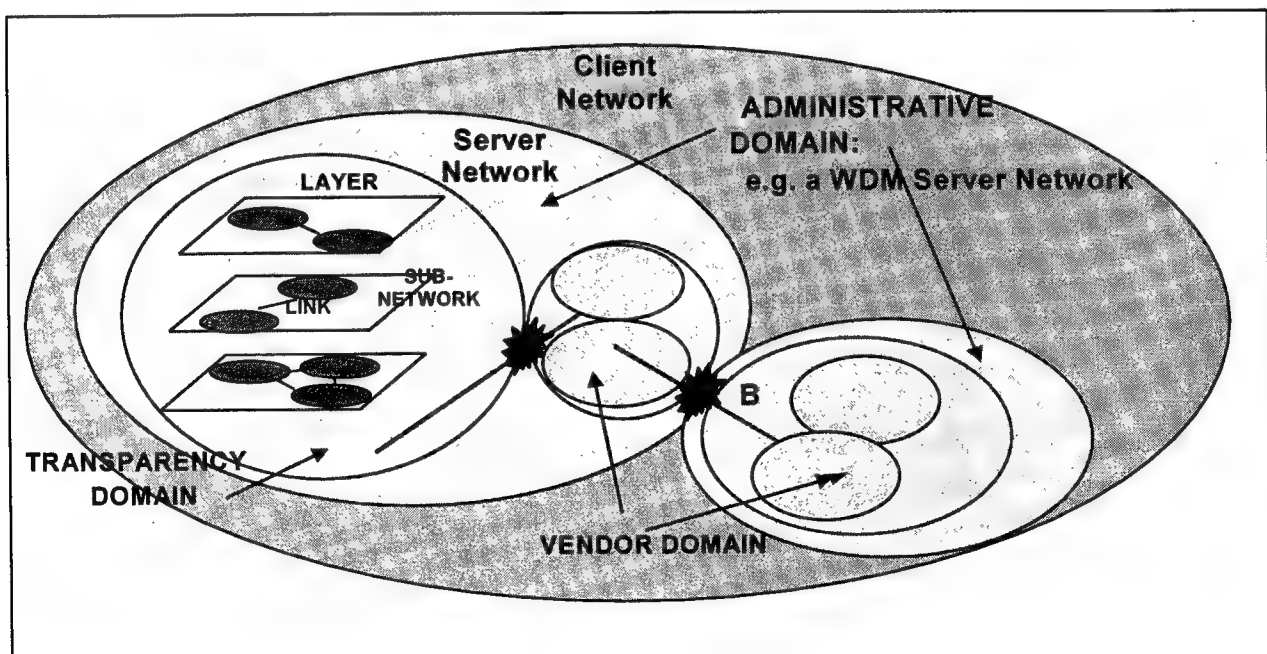
Fig. 1 General Description of Domains

The presentation will highlight some relevant results coming from of P918, including a discussion on the way to define the OTN functional requirements, in line with the reality of implementation of optical networks. An issue that has to be addressed, for example, is the

limited optical transmission length of un-regenerated (3R) optical channels. In order to account for this effect, the concept of the transparency domain has been introduced.

Based on this overview and based on distinction between protocol transparency and transmission transparency basic OTN scenarios will be discussed, which consider transparent transmission domains, operator domains and vendor domains. (Fig.1)

The concept of the different domains allows to match the requirements of standardised management of optical networks with the fairly early idea of optical transmission transparency.

The basic management requirements of managing the different domains and the end-to-end optical channel will be introduced and possible implementations of related OAM functions will be compared, while the realisation of the end-to-end view is based on a digital frame format. Two solutions of integration of the digital frame and of the 3R regeneration into the functional architecture based on the recommendation ITU-T G.872 will be discussed.

Finally, requirements on protection and restoration will be discussed assuming the viewpoint that an integration between layer networks is required to optimise network survivability costs.

Confidence Limits for Network Performance in the Presence of Homodyne Optical Crosstalk

Khurram Durrani, Melanie J. Holmes

King's College London, Department Of Electronic Engineering, The Strand, London WC2R 2LS, U.K.
Tel. +44 (0)207 848-1849, Fax. +44 (0)207 848-2932
E-mails: khurram.durrani@kcl.ac.uk, melanie.j.holmes@kcl.ac.uk

1. Introduction: Simulation of network impairments in wavelength-routed networks can be extremely time-consuming due to the intensive computation required to calculate wavelength assignment. In a real network there may be many possible solutions for the wavelength assignment for the same input parameters: in practice the actual assignment will depend on the previous state of the network. For a fair assessment of network impairments, and hence a reliable calculation of component requirements, the variation in the performance should be calculated, as well as the expected performance. In order to address these three problems we have developed a semi-analytic method using probability theory to simulate the flow of signals through the network, and to calculate confidence limits for the bit error rate (BER). Previous results have been reported in [1]. In this paper we describe the basics of our network model, and use it to calculate confidence limits for the BER due to the accumulation of homodyne beat noise.

2. Network Probability Model: Given traffic data, a routing algorithm is used to calculate the required number of wavelength channels per link. Our analysis then assumes the wavelength assignment to be randomly distributed across the fibres in each link. Assuming no wavelength conversion to overcome wavelength blocking requires a link utilization (L_U) of less than 100%: hence a link utilization parameter is included as a measure of the 'efficiency' of the wavelength assignment algorithm. These assumptions allow us to derive analytical expressions for the PDFs (probability distribution functions) of the number of crosstalk interferers collected in the space-switch, demultiplexer and multiplexer stages of a wavelength-routing node. Homodyne crosstalk can be categorized according to whether the crosstalk terms are time-delayed replicas of a received signal (same laser), or from different lasers at the same nominal wavelength (different laser) [2,3]. Hence in our model we calculate a joint PDF for the accumulation of each class of interferer onto each output link in the network. Convolution of the joint PDFs of the appropriate links traversed by a signal determines the PDF of the total crosstalk accumulation over an end-end path. This methodology takes into account all possible wavelength assignments for a fixed set of input parameters, and runs very quickly on a PC. We have used the model to investigate the effects on the crosstalk accumulation PDF (over a worst-case path) as a function of link utilization, no. of wavelength channels per fibre, nodal connectivity and choice of routing algorithm [1].

3. Calculation of Confidence Limits for Acceptable Network Performance: Recently [4] we presented results on homodyne beat noise effects showing that the effect of laser wavelength referencing error and drift is to reduce the total beat noise power from a fraction $2.N.10^{\varepsilon/10}$ of the incident power to $SF.N.10^{\varepsilon/10}$, where SF is a scaling factor, varying between 0 and 2, ε is the component crosstalk, and N is the number of interfering crosstalk terms, assumed to originate from different laser sources. For a typical laser misalignment of 0.1 nm, the scaling factor has values of 0.1 and 0.4 at bit-rates of 2.5 Gbs^{-1} and 10 Gbs^{-1}, respectively. In the presence of a further M crosstalk interferers originating from the same laser as the signal, the total beat noise power becomes a fraction $SF.N.10^{\varepsilon/10} + 2M.10^{\varepsilon/10}$. In our simulations we have found that different laser crosstalk from the space switch is dominant. Hence, for reasons of brevity, in this paper we present a simplified model for the confidence limits, assuming component crosstalk levels to be equal for the combined demux-mux characteristic and the space switch, and treat all interferers to be from different lasers.

At high power penalties the bit error rate (BER) can be approximated by considering only the tail under the PDF of a received one bit at the receiver system. For the purposes of this simplified calculation the joint PDF for different and same laser crosstalk accumulation is converted to a 1-D PDF, denoted $P_N(N)$. The BER then depends on N, the total number of crosstalk interferers accumulated from the network model, and X, the number of channels out of this N, in which a '1' bit is arriving at the receiver at the decision time:

$$BER \approx \frac{1}{2} Q\left(\frac{(1+\beta)(1+(2X-0.5N)10^{\varepsilon/10})}{2\sqrt{2\sigma^2 + (1+\beta)^2 2X(SF/2)10^{\varepsilon/10}}} \right) \quad (1)$$

where Q is the Q-function integral, β is the adjustment in the power signal required to overcome crosstalk interference, and σ^2 is the receiver noise in the absence of crosstalk. Our network model produces a discrete PDF for the statistics of N. The statistical properties of the BER depend upon the statistical properties of the terms $2X - 0.5N$ and $2X$, which we call m and v respectively: m and v denote the relative change in mean and variance in the Q-function argument, for a 1 bit received. Calculating the joint PDF $P(m,v)$ for these two random variables, determines the likelihood of m and v attaining a given value:

$$P(m,v) = \left(\frac{1}{2}\right)^{2(v-m)} \frac{(2(v-m))!}{(3v/2-2m)!.(v/2)!} P_N(2(v-m)) \quad (2)$$

where P_N is the 1-D crosstalk accumulation PDF.

Figure 1: Probability of acceptable system performance vs power penalty
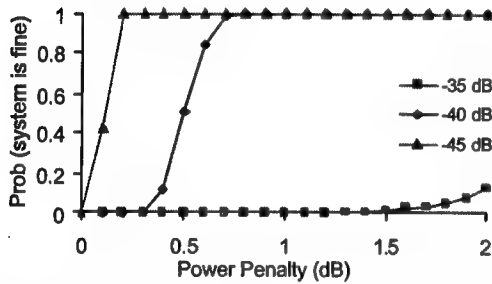
For given values of m and v, the power penalty may be calculated from eqn. (1). In fact, for a given power penalty, $P = 10\log(1+\beta)$, eqn. (1) defines a contour in the (m,v) plane. For all values of m and v on the appropriate side of this contour, the BER will be less than or equal to the required value. Hence, by summing the PDF of m and v for all points on the appropriate side of the contour, we may calculate the probability that the system BER is maintained or bettered. This calculation takes into account all possible network configurations. Figure 1, shows the results of such a calculation assuming a target BER of 10^{-12}, a noise power scaling factor of 0.4 (corresponding to a 10Gbs^{-1} data rate and an RMS laser wavelength misalignment of 0.1nm) and as a function of the component crosstalk. The results indicate that for component crosstalk of -40dB, the probability that the system will perform acceptably exceeds 99 % for a power penalty of only 0.7 dB. The results also indicate that a small change of 0.2dB in the power penalty is sufficient to bring the confidence limit down to 50 %. The results also show the confidence limits to be very sensitive to the crosstalk level.

4. Conclusion: We have described novel probabilistic methods to analyze the accumulation of impairments in wavelength-routed networks. We have used the model to calculate confidence limits for acceptable bit error rate performance in the presence of crosstalk from routing elements such as optical switches. Our calculation takes into account all possible network configurations and laser wavelength misalignment due to drift and referencing error.

5. References:

1. K. Durrani and M. J. Holmes, "Optical crosstalk accumulation in WDM networks," IEE Colloquium on Multiwavelength Optical Networks, London, 7/1-7/6 (1998).
2. L. Moura, N. Karafloas, P. Lane, A. Hill and J. O'Reilly, "Modelling of Interferometric Crosstalk in Optical Networks," Proc. IEEE Global Telecommunications Conf., London, 333-337 (1996).
3. M. J. O'Mahony, D. Simeonidou, A. Yu and J. Zhou, "The Design of a European Network," IEEE J. Lightwave Technol. **13**, 817-828 (1995).
4. K. Durrani and M. J. Holmes, "Relaxed space switch crosstalk requirements: crosstalk analysis in the presence of laser wavelength referencing error and drift," Proc. OSA Optical Fiber Communications Conf., Maryland U.S.A., (2000).

"Computer Simulation of a Metro WDM Ring Network"

N. Antoniades, K. Ennser and V. L. da Silva
Photonics Research and Test Center
Corning Incorporated, 2200 Cottontail Lane, Somerset, NJ 08873
Tel: (732) 748-3719, fax: (732) 748-3760, Antoniadna@corning.com

M. Yadlowsky
Science and Technology Division
Corning Incorporated, SP-AR-01-2, Corning, NY, 14831
Tel: (607) 974-3435, fax: (607) 974-9472

I. Network simulation case study

This paper investigates optical transmission impairments in a metropolitan WDM ring network using simulation. We find that these networks can lead to paths long enough where non-linear effects can become noticeable and should be properly engineered to balance the effects of both receiver electrical noise as well as fiber nonlinearities. This becomes increasingly important for the design of WDM networks in the emerging metro market.

Fig. 1 presents the architecture of our metro network simulation case study which consists of optical network elements arranged into two interconnected, self-healing rings. Each ring consists of six bi-directional parallel Wavelength Add/Drop Multiplexers (WADMs) [1] connected with duplex standard fiber links. Two 2 x 2 Wavelength Selective Cross-connects (WSXCs) are used to provide dynamic wavelength routing between the two rings. All fiber links are assumed equal in length (20 km) with a 0.4 dB/km total attenuation (includes installation splices, fiber attenuation and connectors)..
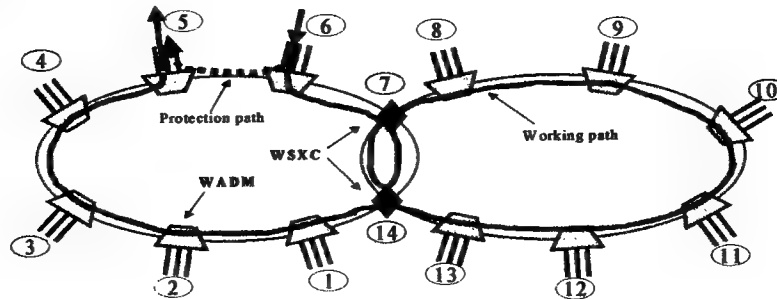
Fig. 1: Metro WDM interconnected ring simulation case study with examined worst-case optical path.

Thirty-two channels spaced at 100 GHz (1536.6-1561.4 nm) are used in the network. All amplifiers within the WADMs and WSXCs are identical with an effective noise figure of 7.8 dB that takes into account WADM interstage losses. The gain ripple for each amplifier has a sinusoidal shape with a 1 dB peak-to-peak value. The above network is decomposed into worst-case paths and the one that represents the absolute worst-case for most of the network impairments (non-linear effects, ASE noise and crosstalk) is chosen in Fig. 1 (path 6-7-14-7-8-9-10-11-12-13-14-1-2-3-4-5). This long path was intentionally routed through both WSXCs for crosstalk enhancement. Simulation results show that optimum system performance is obtained for an average input power per span of 1 dBm/channel. For channel powers less than that, the performance is affected by electrical noise at the receiver, whereas for launched powers above 1dBm non-linear effects (mainly XPM) become important. All simulation parameters are shown in Table I.

II. Results-Discussion

Figure 2 presents results based on the Q-factor for the above worst-case path obtained using our link simulation tool and assuming externally modulated transmitters with zero chirp. In Fig. 2 (a) we observe that around the strongest channels (# 4-14) the shape of the curve is flat because the channel performance is affected mostly by XPM. The weakest channel (i.e. channel #25) is affected by receiver electrical noise since its power has been reduced due to the accumulated amplifier ripple. All thirty-two channels have performance better than the target BER of 10^{-12} (Q >=8.47 dB) however their performance

varies by about 3.5 dB. Included are Q-penalties due to crosstalk contributions, waveform distortion due to filter concatenation and other transmitter/receiver imperfections (1dBQ for each of these impairments) resulting in a system margin of 0.5 dB for the weakest channel, barely above the required 8.47 dB (Fig. 2 (a).).

Table 1: Network simulation parameters

Bit rate (Gbps)	2.5
Signal wavelengths (nm)	1536.609 - 1561.419
Channel spacing (GHz)	100
T_x launched power/ch (dBm)	0
T_x extinction ratio (dB)	13
Span launched power/ch (dBm)	1
Fiber total loss (dB)	8
EDFA Noise Figure (1550 nm) (dB)	7.8
R_x Electronic Bandwidth (GHz)	1.625
R_x DMUX Bandwidth (GHz)	62.5
R_x Filter Model	3rd order Butterworth
R_x Type	APD
Indiv. MUX/DMUX Ins. Loss (dB)	4.5

(a)   (b)   (c)
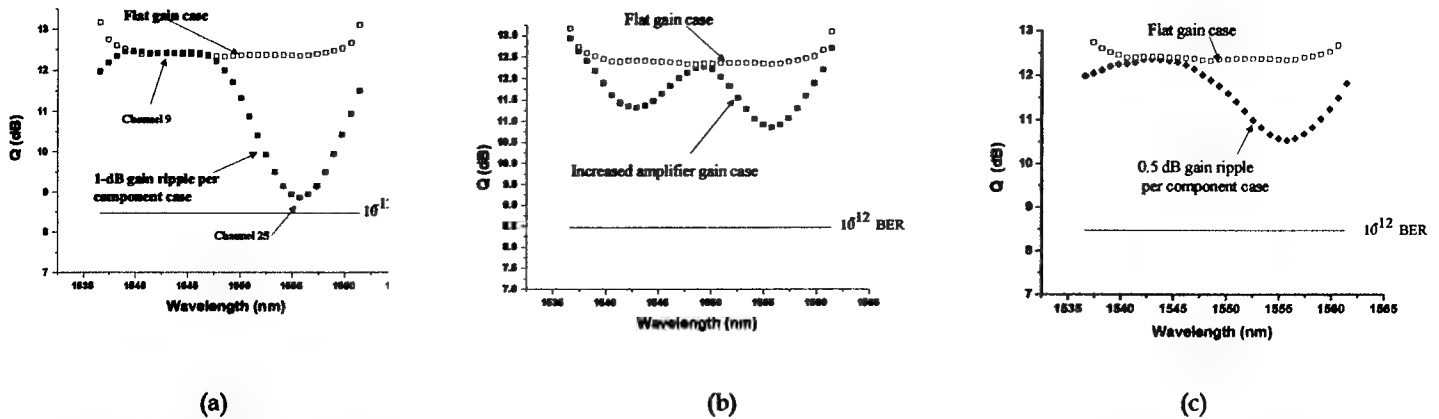
Fig. 2: Q-factor (dB) for worst-case path of Fig. 1; (a) assuming 1 dB sinusoidal gain ripple per amplifier; (b) same as (a) but increasing the amplifier gain by 0.5 dB ; (c) same as (a) but reducing the ripple of each component to 0.5 dB. Solid squares: sinusoidal shape amplifier gain ripple; Open squares: flat amplifier gain.

To improve the performance of the network we can increase the gain of each amplifier so that the weakest channels are not affected by electrical noise at the receiver, or improve the ripple characteristics of the amplifiers. The former approach is effective as shown in Fig. 2(b) where we get a 2 dB improvement, but presents the challenge that increased amplifier gain will introduce more penalties from non-linear effects (mostly XPM) on the strong channels, and the optimum point will be difficult to find. Reducing the ripple characteristics of the amplifiers is also an effective approach for improving network performance. Fig. 2 (c) shows the more drastic effect of reducing the amplifier gain ripple to 0.5 dB resulting in performance improvement of 1.8 dB.

In the above case study, crosstalk level requirements can also be set for each elementary component. This study focused on common-channel crosstalk which is generated at the WSXCs. The path of Fig. 1 will accumulate four first-order crosstalk terms corresponding to the number of times the signal goes through a WSXC as well as a number of higher-order terms which for this study are neglected. Using a model similar to the one presented in [2], details of which will be presented at the conference, the Q-penalty due to crosstalk can be evaluated for different individual crosstalk levels ε of the WSXCs.

The above work provides useful design information regarding trade-offs among different transmission impairments in the network. It was shown that for worst-case paths in a metro optical network, amplifier ripple can introduce significant power divergence among channels. In such case, non-linear fiber transmission impairments may become significant for the strongest channels whereas electrical noise at the receiver will affect the weakest channels. Balancing the above effects by properly engineering these paths in the network will be very important for obtaining the best possible network performance.

References

[1] N. Antoniades et. al., Phot. Technol. Letters, vol. 9, n. 9, September 1997.

[2] K.-P. Ho, IEEE/OSA J. Lightwave Technol., vol. 17, n.2, pp.149-154, February 1999.

BEYOND MOORE'S LAW

Xiaolin Lu

AT&T Broadband

Abstract

The computer industry has been proudly riding on the exponential curve based on Moore's law for decades. What Moore did not expect, and perhaps nobody has ever dreamt of, is that the photonic technology, especially its application in cable industry, has similar if not more profound impacts on the communication infrastructure and service delivery mechanism.

This presentation will discuss the evolution of cable infrastructure from the point of view of a Photonic Moor's Law that is based on the continuous technology innovation in lightwave, RF, and digital processing. We will describe the new exponential curve that represents this evolution, starting from conventional Fiber-to-the-Serving-Area with fiber node segmentation, through DWDM-based Secondary Ring architecture, to the LightWire^{TM} network with fully-passive coax plant, and to the CoraLight^{TM} architecture based on digital and distributed processing platform with DWDM deployment to the last thousands feet.

Performance of Broadband DWDM Networks

by Sudhesh Mysore, Ricardo Villa and Gregory Beveridge
MediaOne Labs, Westminster, CO

Broadband companies have started deploying DWDM networks for the transport of narrowcast (NC) services such as telephony, high-speed-data and video-on-demand. In this paper we compare the performance of four different broadband DWDM architectures. All four architectures describe a broadband DWDM overlay system between the HE and the hub for the transport of NC services. Separate fibers are required for the DWDM overlay and for the broadcast (BC) transport since otherwise the SRS-induced crosstalk would destroy the signal quality of the predominantly analog BC video channels. At the hub, each of the demultiplexed wavelengths carrying the NC signal is routed to a specific node. The differences in the architectures lie in the way the BC and NC signals are combined prior to distribution over the coax plant. The four architectures are shown in Figures 1 to 4.

Figure 1 shows a simple single-node-receiver (SNR) design. In order to meet a signal quality of at least 50 dB carrier-to-noise ratio (CNR) at the node receiver, the BC path (50 – 550 MHz) employs an externally-modulated 1550 nm laser from the HE to the node. The NC lasers at the HE are directly-modulated, 1550 nm ITU-compliant lasers carrying NC services above 550 MHz. The demultiplexed NC signal is optically combined (using a simple 1x2 coupler) with the BC signal at the hub and transported to the optical node over a single fiber. A single receiver at the node detects both the BC and NC optical signals. The addition of the NC optical signal to the BC signal at the node receiver will degrade the CNR performance of the BC path (and vice versa). Combining both the BC and NC optical paths together at a single receiver results in excess shot noise and relative intensity noise (RIN). The degradation of the BC signals increases as the average optical power of the NC signal is increased. Even more severe consequences are composite second-order (CSO) and composite triple beat (CTB) distortion products generated in the NC path that result from laser chirp of directly modulated ITU lasers interacting with high fiber dispersion at 1550 nm. If the bandwidth of the NC signals exceeds 50 MHz then the CSO distortion products of the NC signal will degrade the lower-frequency analog channels in the BC band.

Figure 2 shows a dual-node-receiver (DNR) design in which the BC and NC optical signals travel over separate fibers and are detected by separate node receivers. They are then combined together in a forward combining filter that acts as a low-pass filter for the BC signals and a high-pass filter for the NC signals. Thus, noise and distortion products present at the output of the NC receiver are filtered out and do not affect the performance of the BC signals, and vice-versa. In addition, the performance of each path can be individually optimized without affecting the other. This is the optimum architecture but requires a second receiver and fiber as well as a forward combining filter at each node.

Figure 3 shows a dual-hub-receiver (DHR) design, a variation of the DNR design in which the BC and NC receivers and the forward combining filter are all located at the hub. An overlay 1310 nm DFB laser is then used to transport combined BC/NC signals from the hub to the node.

Figure 4 shows a hybrid-distributed-receiver (HDR) design, an interesting variation that MediaOne has deployed in one of its systems. In this design, the NC signal is detected at the hub, high-pass filtered (to filter out noise and distortion products that would otherwise fall on top of the BC signal) and transported to the node over an overlay 1310 nm link. A coarse WDM coupler is used to combine the 1550 nm BC and 1310 nm NC signals onto the same fiber. At the node, the combined signals are detected using a single receiver. This architecture is therefore a hybrid of the single and dual-receiver designs.

The overall performance of each of the above DWDM designs were modeled. The modeling took into account the major impairments in the system including shot noise, thermal noise, laser intensity noise, chirp-induced CSO and CTB and EDFA noise. The modeling assumed a HE-to-hub distance of 100 km and a hub-to-node distance of 10 km. This closely approximates the twenty-optical-channel DNR-DWDM experimental system in MediaOne Labs. The BC bandwidth is assumed to be from 50 – 550 MHz (78 analog video channels) and the NC band is above 550 MHz. We have also assumed that the RF power of each NC channel is –5 dBc (referenced to broadcast video carrier level) and that the optical modulation index of the channels have been optimized so as to avoid laser clipping. The purpose of the modeling was to predict the maximum NC bandwidth capability of each DWDM design.

As expected, the DNR design provided the best performance, supporting a full 310 MHz complement of NC 256-QAM channels from 550 MHz to 860 MHz. The DHR design also provides for a 310 MHz NC payload except that the effective SNR values are reduced because of the presence of the 1310 nm link. In a SNR design, the NC bandwidth is limited to 50 MHz due to the effects of chirp-induced distortion products previously mentioned.

The performance of the HDR design lies between that of the SNR and DNR designs. The presence of the high-pass filter after the NC receiver in the hub means that chirp-induced CSO in the NC path is filtered out prior to being combined with the BC signal. Both theoretical results and experimental evidence indicates that this hybrid architecture gives adequate performance (defined as a BC CNR of 50 dB and a NC SNR of 38 dB) as the number of NC 256-QAM channels are increased to 25 (150 MHz). This is more than sufficient narrowcast bandwidth for the next several years. Considering that a NC bandwidth of 150 MHz is equivalent to a data rate of 975 Mb/s (using 256-QAM) this is equivalent to providing each home (in a 250-home node size) with a dedicated bandwidth of 3.9 Mb/s. Assuming a more

realistic take rate of 50 % and a usage factor of ten, the typical data rate provided to each active subscriber is greater than this by a factor of 20, or 78 Mb/s. This is well above what can be provided by competing DSL or even VDSL providers.

In conclusion, experimental results illustrate the markedly superior technical performance of the dual-receiver DWDM designs in accordance with our modeling predictions. A simple single-receiver implementation is adequate for rapid initial deployment of a DWDM system with NC bandwidth requirements of less than 50 MHz. As narrowcast bandwidth requirements exceed 50 MHz, a narrowcast receiver and high-pass filter can be added in the hub to convert the system into a HDR design. This design can support a narrowcast bandwidth up to 150 MHz (twenty five 256-QAM channels) which provides more than sufficient bandwidth for the foreseeable future. If narrowcast bandwidth exceeding 150 MHz is required someday, then the system can be upgraded to one of the two flavors of dual-receiver designs. In the upstream direction, either a 10-bit digital reverse or a 4-channel block conversion scheme in conjunction with DWDM results in the most cost-effective return path solution. Experimental results on both return-path techniques are presented.
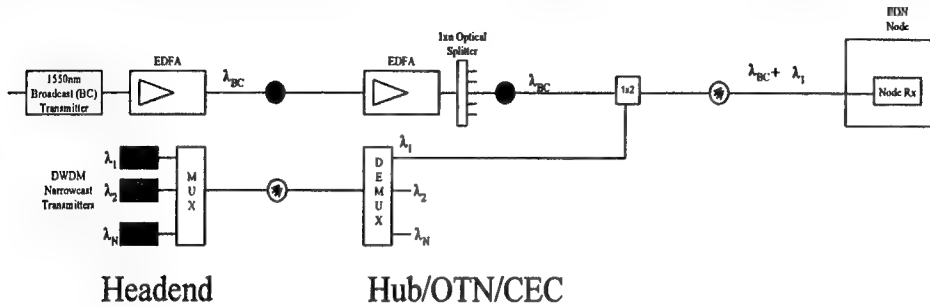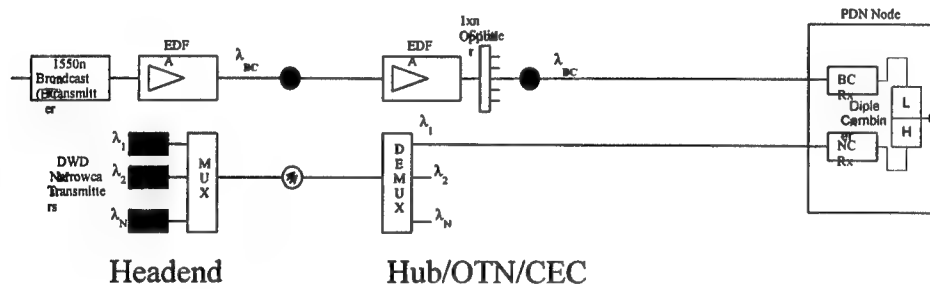

Figure 1 – Single-node-receiver (SNR) design.

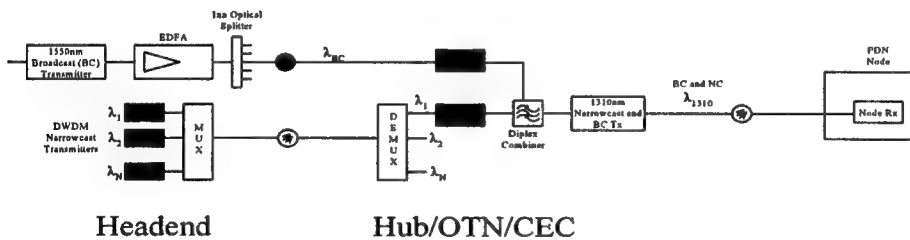
Figure 2 – Dual-node-receiver (DNR) design.

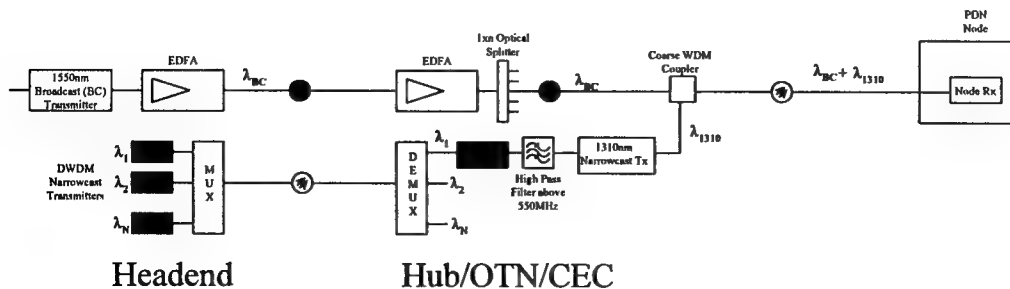**Figure 3** – Dual-hub-receiver (DHR) design.

Figure 4 – Hybrid-distributed-receiver (HDR)design.

Evaluation of SuperPON demonstrator

C. Bouchat, C. Martin, E. Ringoot, M. Tassent, I. Van de Voorde.
B. Stubbe, P. Vaes, X.Z. Qiu, J. Vandewege.

Abstract— The paper presents evaluation results of the SuperPON demonstrator. It shows the feasibility of a Passive Optical Network with increased bitrate (2.5 Gbit/s downstream and 311 Mbit/s upstream), extended range (100 km) and enlarged splitting factor (2048).

Fig. 1. SuperPON setup for the evaluation.

I. INTRODUCTION

The end-to-end performance of the SuperPON (Super Passive Optical Network) demonstrator has been evaluated. The SuperPON system is an optical ATM access network, which can support a large number (2048) of ONUs (Optical Network Units) and cover a long distance (100 km). To overcome the large losses, optical amplifiers are introduced. EDFAs (Erbium-Doped Fiber Amplifier) are used for 2.5 Gbit/s downstream TDM (Time Division Multiplexing) transmission at 1550 nm towards the subscribers and SOAs (Semiconductor Optical Amplifiers) for 311 Mbit/s upstream TDMA (Time Division Multiple Access) transmission at 1310 nm towards the Access Node. While a first lab model was restricted to the evaluation of the optical transmission part of SuperPON [1], the present demonstrator [2] was realised with a dedicated chipset for the SuperPON transport system [3]. The performance of the optical layer was further improved by a newly designed BMRx (Burst Mode Receiver) [4] and the use of reflective SOAs [5].

An earlier paper already described standalone tests on the uplink consisting of the BMRx and a cascade of SOAs [4]. The present paper reports on the integration of the transport system enabling ASICs in the system and the end-to-end performance in downstream and upstream direction between the service interfaces at the Line Termination (LT) and ONU.

II. SUPERPON SETUP

The evaluation setup is shown in figure 1. Two ONUs situated in two different branches are used to evaluate the performance of the system.

The downstream communication consists of a continuous bitstream with constant power level that is

C. Bouchat, C. Martin, E. Ringoot, M. Tassent and I. Van de Voorde are with Alcatel Corporate Research Center, F. Wellesplein 1, B-2018 Antwerpen, Belgium.

B. Stubbe, P. Vaes, X.Z. Qiu and J. Vandewege are with University of Gent IMEC/INTEC, Sint-Pietersnieuwstraat 41, 9000 Gent, Belgium.
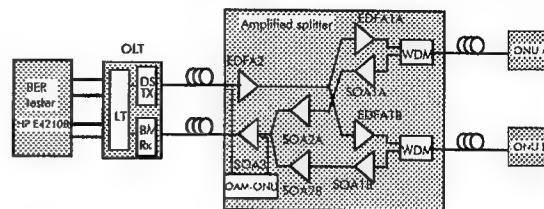
broadcast to all ONUs. After the feeder section, the signal arrives at the Amplified Splitter, where a first splitting is achieved, together with optical amplification. The signal then passes via the drop section, where a second splitting stage is situated, and finally arrives at the ONU.

The upstream communication consists of a sequence of data cells coming from different ONUs and, hence, exhibits bursty variations of the power level. The two first stages of SOAs (SOA1 and SOA2) are switched on/off on a cell by cell basis in order to reduce noise accumulation from amplifiers in parallel branches, while the SOA common for the different branches (SOA3) operates in continuous-wave mode. A SOA has a fast response so that the signal is not corrupted by slow settling of the gain due to abrupt changes of the input power. The use of reflective SOAs [5] in the first two stages decreases the polarization dependency of the gain, which is only 2.5 dB for 4 SOAs in cascade.

For the reception of the upstream, an improved BMRx with an offset compensation, a gain control on a burst by burst basis and a duty cycle compensation has been designed [4].

A dedicated chipset has been developed that provides the necessary operations for the SuperPON transport system. The functionality is very similar to a standardised APON system [6], but in the present case supports the long round trip delay (corresponding to 100 km), the identification of 2048 ONUs, and increased bitrates (2448/311 Mbit/s).

The SuperPON Transport System Protocol initialises the system and provides the operation and maintenance during normal operation. It puts the different thresholds and gains of the BMRx and the SOAs, depending on the power level of the upstream cells sent

by the respective ONU. The STSP synchronises each ONU to ensure a proper operation of the TDMA and allocates the bandwidth per connection. It handles the pulse width correction at the LT and the power leveling of the ONUs.

In order to evaluate the system, a BER tester HP E42108 was connected to the LT. It generates an ATM cell stream with PRBS-23 data pattern for each ONU. This traffic is sent to the LT via STM1 interfaces of 155 Mbit/s and is multiplexed by the LT into the 2.5 Gbit/s downstream of SuperPON. In order to evaluate the complete path (downstream-upstream), the data traffic is loopbacked in the ONUs and is received at the LT side, which sends it back to the BER tester for verification.

In order to measure the allowed optical budget and dynamic range in the drop section, power meters and tunable optical attenuators have been inserted in the various sections of the system.

III. PERFORMANCE

Figure 2 shows the BER in function of the average input power at the BMRx (in dBm) for one ONU. A BER smaller than 10^{-9} is obtained for an average input power at the BMRx varying from -19 dBm to -32 dBm (in order to study the behaviour of the BMRx, all the SOAs are removed from the setup).
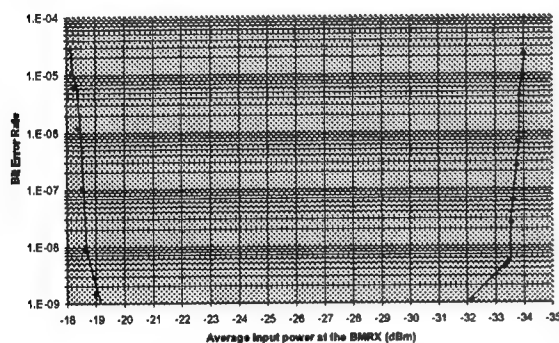
Fig. 2. BER for one ONU.

Figure 3 shows the region with a BER smaller than 10^{-9} for the average input power at the BMRx coming from the two ONUs. The graph is symmetric with regard to the diagonals, showing that the two branches are equivalent. The region looks like a truncated square, in which the truncated regions are situated at extreme differences of average input power from the two ONUs.

IV. DISCUSSION AND CONCLUSION

This paper reports results of the end-to-end performance of a SuperPON demonstrator with trans-
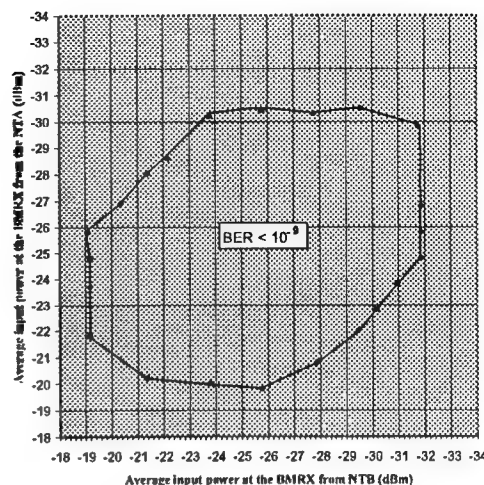
Fig. 3. BER for two ONUs.

port system enabling ASICs. The measured dynamic range of 13 dB at the BMRx is sufficient in such a system where optical losses and amplifier gains may become very large. It is because the excess of variations in the optical budget is compressed on one hand by the gain saturation of the SOAs and on the other hand by the control of the gain on a cell by cell basis [4]. The losses in the drop section allow to support a split of 64 and a drop length of 10 km. In combination with a split of 32 in the amplified splitter and a feeder of 90 km, a total of 2048 ONUs can be serviced at a range of up to 100 km. The prototype system is installed in a technical field trial and integrated with an optical core network in the frame of ACTS PELICAN during the first half of this year.

ACKNOWLEDGMENT

REFERENCES

[1] X.Z. Qiu, *Final results of the PLANET Lab Demonstrator*, LEOS Benelux 98, Gent, Belgium, pp. 49-52.

[2] C. Bouchat, *Realisation of SuperPON Demonstrator*, LEOS Benelux 99, Mons, Belgium, pp. 21-24.

[3] I. Van de Voorde, *The Super PON Demonstrator: A Versatile Platform to Evaluate Possible Upgrades of the G.983 APON*, ISSLS 2000, Stockholm, Sweden.

[4] J. Vandewege, *Uplink performance evaluation of super optical access networks*, ECOC 99, Nice, France, pp. 138-139.

[5] L.F. Tiemeijer, *High gain 1310 nm reflective SOA with low gain uncertainty*, PTL, Vol. 9, no. 1, January 97.

[6] ITU G.983.1, *Broadband Optical Access Systems Based On Passive Optical Networks (PON)*.

Receiver Performance of Broadband Data Delivery on
WDM Systems Using Spectrally Sliced Spontaneous Emission Sources

Cedric F. Lam, Mark D. Feuer, and Nicholas J. Frigo
AT&T Labs – Research, 100 Schulz Dr., Red Bank, NJ 07701, USA
E-mail: cflam@research.att.com

Spectral slicing of spontaneous emission sources has been proposed to deliver broadcast services on WDM passive optical networks [1]. Recent advances in ultra-high power LEDs makes spectral slicing a more promising solution for fiber to the home (FTTH) broadband access systems. However, the output from a spontaneous emission source contains spontaneous-spontaneous emission beat noise [2], also called "excess intensity noise". The signal to spontaneous-spontaneous emission beat noise ratio is proportional to the ratio of the optical bandwidth of the optical source to the electrical detection bandwidth [3]. With the new requirements of delivering high speed broadband data in access networks and the introduction of closer and narrower bandwidth optical wavelength channels, the effects of spontaneous-spontaneous emission beat noise becomes more pronounced in spectrally sliced WDM systems. In this paper, we experimentally study the performance of broadband data delivery on WDM systems using spectrally sliced spontaneous emission sources.

Fig. 1 shows the experimental setup. An ultra-high power LED is directly modulated with a broadband 2^7-1 PRBS sequence. The output from the LED is transmitted through a spool of 5km All-Wave™ fiber and spectrally sliced using a commercial thin film wavelength add/drop multiplexer with 0.55nm 3-dB optical bandwidth before being detected with a photodetector. Both PIN and APD detectors are used in the experiment.

We measured the bit error rate (BER) versus received optical power at 622Mbps (OC-12 speed) and 1.25Gbps (Gigabit Ethernet speed). The results are

Fig. 1   Experimental setup

plotted as dots in Fig. 2 and Fig. 3. In spite of the fact that a 0.55nm wide optical signal was detected, there was hardly any dispersion penalty due to the 5km fiber link.

The BER is determined by the signal to noise ratio. For the PIN receiver, the noise variation is given by:

$$\sigma_{PIN}^2 = \frac{4kTB_e}{R} + 2qIB_e + (1+p)\frac{B_e}{B_o}I^2 \qquad (1)$$

The three terms represent thermal noise, shot noise and spontaneous-spontaneous emission beat noise. In (1) R is the receiver load resistance, I the photocurrent, B_e and B_o the receiver electrical bandwidth and optical bandwidth of the spectrum slice. The factor p ($0 < p < 1$) in (1) represents the degree of polarization of the received optical signal. For a completely unpolarized signal, $p = 0$ and for a pure polarized signal, $p = 1$. The optical signal at the receiver end was measured to be 70% to 80% polarized in our experiment, which was expected from an edge emitting LED device. The dark current is neglected.

For APD receivers, the shot noise and spontaneous-spontaneous emission beat noise are enhanced so that

$$\sigma_{APD}^2 = \frac{4kTB_e}{R} + 2NF_{APD}\langle M\rangle qIB_e + NF_{APD}(1+p)\frac{B_e}{B_o}I^2 \qquad (2)$$

where M is the avalanche multiplication factor of the APD detector and $NF_{APD}=\langle M^2\rangle/\langle M\rangle^2$ is the APD noise factor [4]. Therefore, although the detected photocurrent has been amplified by a factor of $\langle M\rangle$, the optical noise is also enhanced. The continuous lines in Fig. 2 and Fig. 3 are the computed BER assuming Gaussian statistics for the total noise at 622Mbps and 1.25Gbps respectively, using (1) and (2). The dashed lines in Fig. 2 and Fig. 3 are the calculated BER using the same parameters but with the spontaneous-spontaneous emission beat noise turned off. This corresponds to the situation when a laser diode having low RIN noise or when an unsliced spontaneous emission source with very broad bandwidth is used.
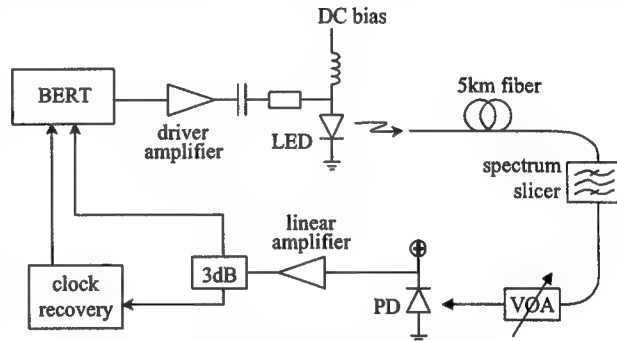
As seen from the dashed lines in Fig. 2 and Fig. 3, in the absence of spontaneous-spontaneous emission beat noise, APD receivers have an advantage over PIN receivers, due to avalanche multiplication gain. When the optical noise is considered, this is still the case at low optical power, i.e. when I is small in (1) and (2). As received optical power increases, both the PIN and APD receiver performance relative to the thermal noise only case degrades, with the APD degrading more rapidly due to the multiplicative terms in (2) which increases the importance of the shot noise and spontaneous-spontaneous emission beat noise. Considerations of (1) and (2) indicates a floor at $SNR=\eta B_o/B_e(1+p)$, where $\eta=1$ for PIN and $\eta=NF_{APD}>1$ for APDs. Thus, we can see from Fig. 3 that the APD BER quickly reaches an error floor. At 622Mbps, the APD receiver achieved a 10^{-9} BER at –34dBm sensitivity. However, for 1.25Gbps data rate, the APD receiver BER flattened at about –26dBm received power with a BER slightly larger than 10^{-9}. On the other hand, the PIN receiver achieved 10^{-9} BER at both 622Mbps and 1.25Gbps with -24.5dBm and –21.5dBm received optical power, before reaching the error floor in our experiment.
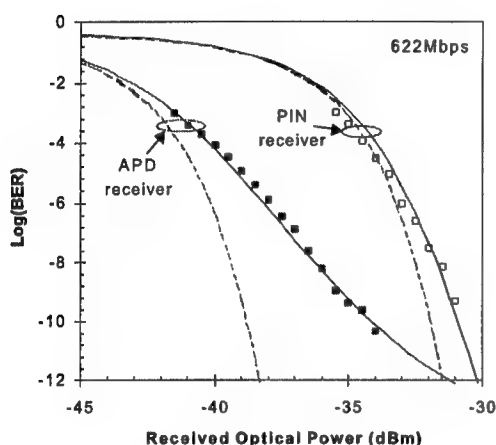
Fig. 2 BER vs. received optical power for PIN and APD detectors at 622Mbps
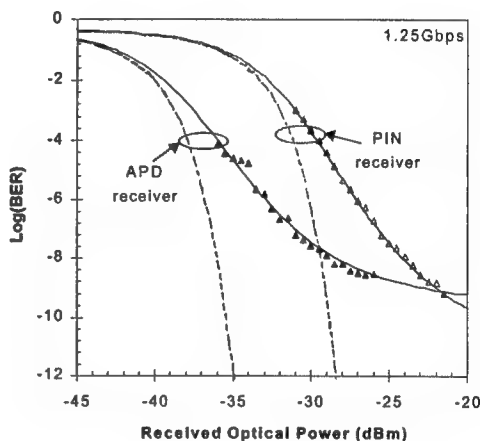
Fig. 3 BER vs. received optical power for PIN and APD detectors at 1.25Gbps

From a systems viewpoint, the BER crossover point between APD and PIN receivers in a high data rate spectrally sliced DWDM link depends on the gain and noise figure of the APD receiver, and the relative ratio of the electrical bandwidth and optical channel bandwidth. When the optical channels are narrow, as in closely spaced (e.g. 50GHz or 25GHz spacing) systems, it is possible that APDs will not offer any advantage. Fig. 2 and Fig. 3 also showed that the relative performance of APD and PIN receivers depends on the power budget and affordable maximum bit error rate. If forward error correction (FEC) is used to enable the system to operate with a small power budget, one may still prefer APD receivers and let FEC to take care of the error floor.

In conclusion, we compared the performance of PIN and APD detectors for broadband data delivery using spectrally sliced spontaneous emission sources. Under spontaneous-spontaneous emission beat noise limitation, APD receivers may lose its advantage more quickly as a result of the optical signal to noise degradation, which arises from the stochastic avalanche multiplication effect.

References:
[1]   P.P. Iannone, et. al, *IEEE Photonic Techno. Lett.*, Vol. 10, No. 9, Sep. 1998, pp 1328-1330.
[2]   H. Hodara, *Proceedings of the IEEE*, July 1965 pp.696-704.
[3]   G.J. Pendock and D.D. Sampson, JLT, 14(10), Oct. 1996, pp2141-2148.
[4]   S.M. Sze, *Physics of Semiconductor Devices*, John Wiley, 1981

Performance of Radio-Over-Fibre Broadband Access in the Presence of Interferometric Noise.

J.E. Mitchell, P.M. Lane, J.J. O'Reilly.
Department of Electronic and Electrical Engineering, University College London,
Torrington Place, London, WC1E 7JE, ENGLAND.

Abstract : We present a discussion of the impact of interferometric noise in radio-over-fibre delivery networks, and provide rigorous bit error rate results for the transmission of quadrature amplitude modulation (QAM).

Introduction : The prospect of broadband wireless access systems provides a number of service opportunities, for instance, wireless local area networks (WLANs) or fixed wireless access systems. Added to this, the cost and reach advantages of optical delivery of the radio signals it is fairly obvious that this technology will have a huge impact on the access network. To provide the required high bandwidth and frequency reuse, it is envisaged that such systems will operate well into the millimetre-wave (mm-wave) spectrum, so that even optical transport of these signals is not without problems due to the high frequencies that are involved. To over come the main restricting factor, dispersion, single sideband (SSB) techniques have been adopted, which effectively eliminates the dispersion-induced carrier power fluctuations, allowing operation over tens of kilometres [1].

A number of methods have been investigated to generate the optical SSB signal carrier, however we focus on the method of [2] which uses carrier suppression to create the two carriers required for self-heterodyne mm-wave transmission. We consider the impact of interferometric noise (IN) in such delivery networks. IN is formed when the desired signal is received with other lightwave components at nominally the same wavelength. The components may emanate from distinct laser sources or may be replicas of the desired signal delayed by greater than the coherence time of the source laser. These crosstalk signals may be formed due to reflections at fibre splices, or by leakage in filtering or routing elements. Previous studies have considered this phenomenon for transmission of binary OOK data on radio-over-fibre systems [3]. However, here we extend this analysis to quadrature amplitude modulated (QAM) data, which is a more usual modulation scheme for access links.

Radio-over-Fiber Transmission : The method of [2] creates two coherent optical spectral lines separated
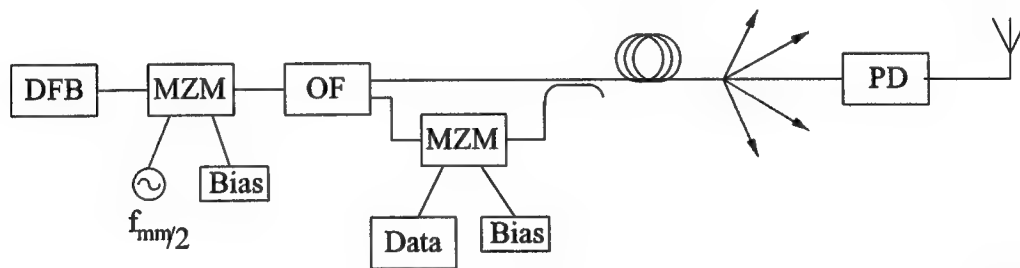
Figure 1: Schematic of mm-wave transmission. DFB = DFB Laser Diode Source, MZM = Mach-Zehnder Modulator, OF = Optical Filter PD = Photo-diode

by the desired millimetre wave frequency using a single laser source and a Mach-Zehnder modulator driven with half the required mm-wave frequency. Due to the co-sinusiodal nature of the Mach-Zehnder response, when biased at the point of minimum transmission ($V_{bias} = V_\pi$) all even terms, including the carrier will be suppressed, with first sidebands being dominant. It is then possible to modulate data onto one of the sidebands for transmission to the base station as shown in figure 1

Theoretical Analysis : We define the signal space of a M-ary QAM system to be:

$$m(t) = \sum_{k=-\infty}^{\infty} a(t) \, \text{rect}\left(\frac{t - kT}{T}\right) \cos(2\pi f_c t) + \sum_{l=-\infty}^{\infty} b(t) \, \text{rect}\left(\frac{t - lT}{T}\right) \sin(2\pi f_c t) \tag{1}$$

where f_c is the carrier frequency, T the signalling interval, and $\text{rect}(\cdot)$ is the rectangular window function. We consider that the signal is made up of two independent and identically distributed data streams $a(t), b(t) \in \{\pm\gamma, \pm 3\gamma, \cdots, \pm(2N-1)\gamma\}$ for M-ary QAM, where $M = (2N)^2$

Therefore, using the system presented in figure 1, for uncorrupted transmission the signal at the photo-diode can be described by:

$$E_t(t) = \sqrt{P_o}\left[e^{j[(\omega_o - 2\pi f_{mm}/2)t + \phi_o(t)]} + m(t)e^{j[(\omega_o + 2\pi f_{mm}/2)t + \phi_o(t)]}\right] \tag{2}$$

where ω_o and $\phi_o(t)$ are the optical frequency and phase respectively. The inclusion of interfering terms will, upon detection, create noise terms that will affect both the amplitude and phase of the QAM signal. The noise terms have been rigorously modelled to produce a moment generating function (MGF) for the i channel:

$$\Psi(s) = I_0\left(sP_r\sqrt{\epsilon}a(t)\right) + I_0\left(sP_r\sqrt{\epsilon}\sqrt{a_i^2(t) + b_i^2(t)}\right) \tag{3}$$

where ϵ is the relative strength of the interfering terms designated with the subscript i. Using the modified Chernoff bound [4] we calculate the bit error rate for QAM transmission with various signal amplitudes γ.

Results and Discussion : In figure 2 we demonstrate that QAM transmission offers an improvement in BER over a standard binary channel, for a normalised received amplitude signal, (decision threshold 0.5). This is predominately due to the use of gray coding for QAM transmission, which places certain symbol combinations further from the decision threshold than would normally be the case. We see however that QAM transmission is subject to higher degradation due to interferometric noise than would be the case in standard binary ASK transmission. This conclusion is logical, as interference effects not only the amplitude, but also the phase of the received signal, which is a major factor in the performance of coherently demodulated signals.
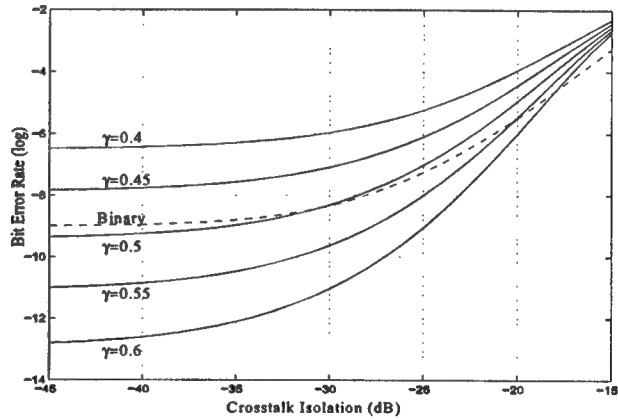
Figure 2: Bit Error Rate evaluation for QAM

References :
1. R.A. Griffin, P.M. Lane and J.J. O'Reilly. International Topical Meeting on Microwave Photonics, 1998.
2. J.J. O'Reilly P.M. Lane, R. Hiedemann, and R. Hofstetter, IEE Electronic Letters, 1992, vol. 28, pp. 2309–2311.
3. L. Moura, M. Darby, P.M. Lane and J.J. O'Reilly, IEEE Transactions on Microwave Theory and Techniques, 1997, vol. 45, pp. 1398–1402.
4. V.K. Prabhu, IEEE Transactions on Information Theory, 1982, vol. IT-28, pp. 95–100.

Broadband Optical Networks

Friday, 28 July 2000

Friday Missing Papers

FC3.1   "10 Gb Ethernet - Why and How it will Change Optical Networking"
M. Nuss, *Bell Laboratories, Lucent Technologies, Red Bank, NJ, USA.*

FC3.3   "Broadband Access over HFC Networks" C. Lin, *Jedai Broadband
Networks, Holmdel, NJ, USA.*

Managed Reach Optical Networks

R. E. Wagner

Corning Incorporated, Corning, NY, USA

Introduction

Over the past several years, there has been an industry-wide push to examine the combination of WDM and optical switching technologies to provide a configurable optical layer for national scale and metropolitan transport applications. Early on, the vision of this optical layer was one in which signals were transported transparently through a national scale network without regeneration along the way [1,2]. After preliminary experimental work, it became clear that the transparent reach distances over which WDM signals could be transported in such configurable optical networks was limited by physical constraints to about 2000 km [3], which is shorter than necessary on most continents. Recognition of this led to two alternate proposals. One became known as the "Opaque" network solution because it used regeneration on every channel at every configurable point in the network [4]. This solves the problem of limited reach, but introduces many more regenerators into the network, which are one of the more costly components of the equipment. The other approach became known as "Islands of Transparency" because smaller transparent sub-networks were defined that were connected via regeneration sites to form a national scale network [5]. This approach solves the problem of expensive regenerators, and allows the sub-network size to be tailored to the reach length that can be achieved. But even then, a reach length of 2000 km is not enough to handle the WDM ring sizes that would be needed in the West and Southwest regions of the United States.

A fresh look at this problem indicates another potential network solution. In this case, each wavelength path in the network is routed in the network in such a way that regenerators are placed at known sites and at distances that are consistent with the reach length of the technology. This approach minimizes the number of regenerators, but requires that the route length of each link of the network be recorded and communicated to adjoining network management systems each time a new wavelength path is established.

These network solutions are coming in response to rapidly growing demands for voice, transaction data, and internet traffic, which shape the new WDM network topologies and approaches. For example, the characteristics of internet traffic set the reach length needed for internet backbone applications, and the cost savings of a managed reach approach are linked to these traffic characteristics and to the technically achievable reach length. The United States long-distance network is used as an example to illustrate these points. It indicates that for internet traffic, a managed reach network with achievable reach lengths of 2500 km or so can virtually eliminate redundant regenerators and significantly reduce equipment costs, as compared to other approaches.

Traffic Demand Growth and the Value of Extended Reach Length

A comprehensive traffic demand and growth study has been performed for a USA network consisting of 46 major cities connected by 63 fiber links [6]. The network topology is similar to those used by current USA long-distance carriers. In this study, revenue-bearing traffic demands between city pairs are computed for voice, transaction data, and internet applications separately, and the growth of each of these three components of the traffic estimated from available trends. These traffic demands are used to determine the required capacity, taking into account peak-to-average ratios, framing overheads, and TDM channel loading inefficiencies. Each demand pair is routed in the network using the shortest distance available, and network statistics are recorded describing the number of channels per link, the number and location of regenerator sites, the number of channels dropped at each city, and the total number of channels entering a city. These are used to understand the required reach length and the network economics. The aggregate network traffic demands and growth rates for this study echo the well-known point that internet traffic, if it continues to grow at its present rate of about 150% per year, will dominate the network in a few years

One important observation from the traffic studies is that the average connection distance for internet traffic is significantly longer than that for voice traffic. A span distances of 600 km, as is ordinarily used today, satisfies more than 60% of the connections for voice traffic. But for internet traffic, which is not distance dependent as is voice traffic, a reach length of about 3000 km is sufficient to satisfy 60% of the connections. If the reach length is shorter than this, then unnecessary regeneration is needed on many internet backbone connections.

To illustrate this point, the study calculates the fraction of traffic that can pass transparently through each city, as a function of the reach length achievable by the technology, as shown in Figure 1. The pass-through traffic does not need regeneration, so this fraction represents the fraction of regenerators that can be eliminated from the network at each reach length. It is clear from this illustration that longer reach is needed for efficient routing of internet traffic and that available technologies that achieve about 2500 km reach length can help to eliminate expensive regenerators from the network.

To quantify this concept, a cost study was performed for the USA network described above, considering four different scenarios. The first scenario assumes that the configurable WDM layer is achieved by "Opaque" crossconnects that consist of transcievers surrounding an electronic switch fabric. The other three scenarios assume that the managed reach approach is employed, where configurability is achieved with optical switch fabrics, allowing only those channels needing regeneration to be handled by transcievers and electronic switch fabrics. These four scenarios, illustrated in Figure 2, show that a modest investment in optical fabrics for configurability, coupled with technologies that achieve a reach length of 2500 km or more, can result in a significant overall reduction in network infrastructure costs.
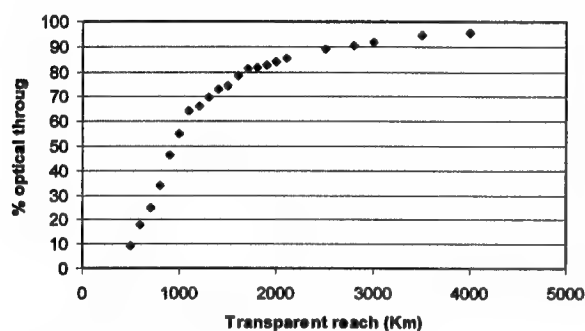
Figure 1: Fraction of pass-through traffic.
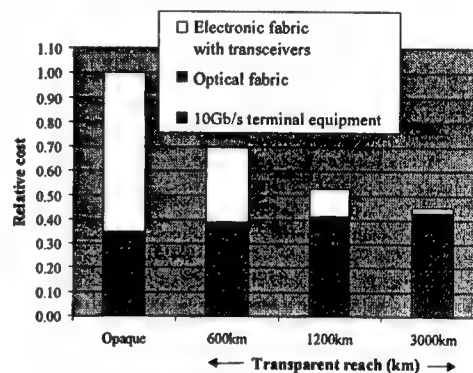
Figure 2. Value of transparent reach.

Of course long reach technologies require introduction of a combination of new transmission approaches, such as optimized fibers, Raman amplification, near-perfect dispersion compensation, RZ modulation formats, and Forward Error Correction coding techniques. But these are well within the scope of today's capabilities at rates up to 10 Gb/s [7]. Additional challenges include providing technological solutions for optical performance monitoring and optical network management of such managed reach networks.

Summary

Traffic growth for internet applications will likely dominate long-distance networks in the foreseeable future, which presents opportunities for new optical layer approaches that are tailored to internet traffic characteristics. One important difference between the traffic patterns generated by internet applications is that the internet connections on average are significantly longer than the conventional voice connections, which allows for network cost savings by combining long reach transport with optical switching technologies to route and manage those connections. Fortunately there is an industry-wide effort to create the required technology for such a managed reach optical layer. The value of the optical layer will be more effectively achieved as reach lengths increase to match internet traffic needs.

Acknowledgment and References

1. A. A. M. Saleh, OFC'95, San Diego, CA, p. 241, February 26-March 3, 1995.
2. R. E. Wagner, R. C. Alferness, A. A. M. Saleh, and M. S. Goodman, J. of Lightwave Technol. 14, p. 1349, 1996.
3. R. S. Vodhanel, et al., OFC'97, Postdeadline Paper PD27, Dallas, TX, February 16-21, 1997.
4. K. Bala, R. R. Cordell, E. L. Goldstein, IEEE/LEOS Summer Topical Meeting on Global Information Infrastructure, Keystone, CO, August, 1995.
5. A. A. M. Saleh, IEEE/LEOS Summer Topical Meeting on Broadband Optical Networks and Technologies, p. 36, Monterey, CA, July 20-24, 1998.
6. Anurag Dwivedi and R. E. Wagner, OFC2000, Paper TuK1, Baltimore, MD, March 7-10, 2000.
7. K. S. Jepsen, et al., OFC2000, Postdeadline Paper PD35, Baltimore, MD, March 7-10, 2000.

Circuit and packet switching in high capacity optical networks

D. Chiaroni, N. Le Sauze, E. Dotaro, A. Jourdan

Alcatel CIT / Alcatel CRC, URP, Route de Nozay, 91461 Marcoussis Cedex, France
Tel: 33 1 69 63 18 67, Fax: 33 1 69 63 18 65, email: **Dominique.Chiaroni@alcatel.fr**

1. Introduction

The introduction of Internet, firstly driven by an enterprise traffic increasing dramatically the volume of informations transported, and followed by an offensive introduction of new applications at the subscriber side, pushes telecom company to think differently. To propose short term solution, the ATM community has proposed to superpose layers such as IP/ATM/SONET/WDM whereas the IP community tries to offer a Quality of Service through the introduction of Int-Serv and Diff-Serv techniques /1-2/. For the optical community, the integration of an electronic IP router with an optical cross-connect (OXCs) to provide the required flexibility offered by the IP network together with an optimised transport capacity offered by the OXCs has been proposed.

In this paper we propose a new IP&ATM/Optical packets/WDM layer. Studied in the frame of a French Research program called ROM, circuit and packet switching techniques are mixed on a single optical platform with adequate interfaces to support a high quality of service. In particular, the introduction of the optical technology required to offer the capacity of transmission pushes naturally equipment constructors to envisage a new framing at the transmission side.

2. Optical circuit and packet switching

To cope with the traffic volume increase, the first efforts were focused on optical cross-connects to provide a robust and secure technique to switch wavelengths. However, with the traffic profile evolution, the solution is probably in the introduction of optical packet switching techniques /3-4/ in the metro and in the backbone. Then, circuit switching will be always mandatory, to establish connections aiming to interconnect fibers through a network topology in presence of a stable traffic matrix or to provide leased links. Thus, the future optical network will undoubtedly mix circuit switching and packet switching techniques in MANs and WANs.

3. IP and/or ATM /Optical packets/WDM for the backbone

At the backbone level, the proposed solution is based on an optical platform capable to interconnect client layers through electro-optic edges.

Two scenarios could be envisaged. The first one is based on a burst switching mode. The optical packet, created in the edges, has a variable duration (to be adapted to the IP) with a minimum dimension : the time slot. The advantage of this approach is to have only one header for one or a group of time slots opening the way to large switch capacities. The second approach could consist to adopt long packets (several μs lengths) taking benefit of the high level of aggregation of the traffic profile. In both cases, the header can be transported on the same wavelength than the payload or simply carried on an other wavelength.

At the core node level, the massive presence of the WDM dimension and the low number of neighbors surrounding a core node opens the way to fast optical cross-connects. The contention resolution is achieved thanks to the statistical distribution of colored packets. However, in the edge node, an optical switch is mandatory to solve the contention in real time before acceding to the electronic interfaces bridging the client layers. Figure 2 describes the core node structure envisaged with a potential throughput of 10 Tbit/s and a Packet Loss Rate (PLR) better than 10^{-6} for a 0.7 load, whereas figure 3 shows the structure of the interface required. The structure of the switch : a fast cross-connect, facilitates the circuit switching since it is easy to activate through a wavelengths partitioning.

4. IP and/or ATM/Optical packets/WDM for the metro

The metro is probably the more critical case since the traffic profile is sporadic, close to a self-similar traffic profile for the data, and close to a Poisson traffic profile for the voice & video. In addition, the WDM dimension being not fully exploited for cost reasons, a network must operate with a low number of available wavelengths at least at the beginning. For these reasons, a switching architecture must tolerate 4 wavelengths per port, and small packets (< 1μs) to don't impact the packet transport efficiency while maintaining constant the logical performance. This imposes the adoption of low capacity optical packet switching matrices (below 320 Gbit/s : demonstrated feasible in SOA-based Broadcast-and-Select packet switching architectures) with a high level of flexibility to adapt the

capacity to the demand evolution while keeping the logical performance at a constant value. Figure 4 illustrates a possible introduction scenario in the network: meshed topologies at a regional level and ring topologies for the urban part. Figure 5 describes a possible architecture for the metro. It has been designed to be fully flexible in term of bit rate evolution by introducing optical buffers and providing bit rate adaptation in the 3R regenerators. It is basically composed of a number of parallel planes, interconnected with a transverse plane aiming to reshape the traffic profile in order to have an additional flexibility on the load evolution. Circuit switching can be activated in one parallel plane through a wavelength partition reservation. Typically, the architecture can offer a capacity form 40 Gbit/s to 1.28 Tbit/s by adding planes or by increasing the input bit rate from 2.5 to 10 Gbit/s and a PLR better than 10^{-10} for a 0.6 load.
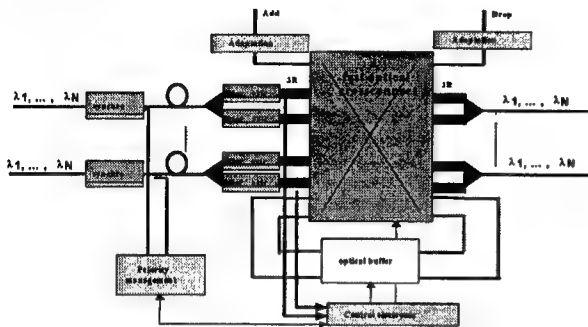
Figure 2 : Structure of the core node
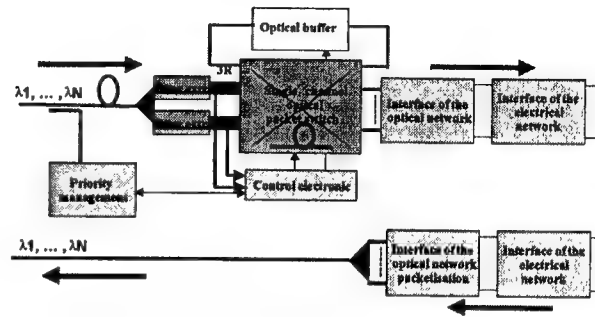
Figure 3 : Structure of the edge node
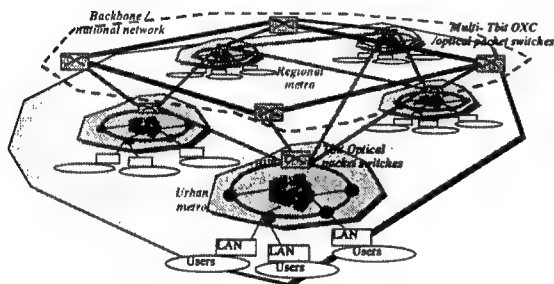
Figure 4 : Introduction scenario in the metro
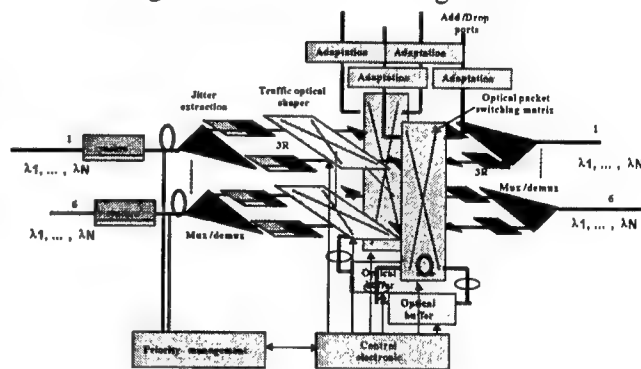
Figure 5 : Structure of the core node for the metro

6. Transmission requirements

In both introduction scenarios, the transmission represents an important issue. Since optics suffer from a lack of digital memory, for cost reasons, the synchronization at the bit level is not recommended inside the optical network, whereas a synchronization at the time slot/packet level is still mandatory to optimize the logical performance or to simplify the electronic circuitry dedicated to the control of the node. It is then vital to envisage an asynchronous packet transport with a new framing (FEC for the backbone) adapted to the optical technology.

7. Conclusions

In this paper we have described how optical techniques could be used to offer at the same time capacity of transport required and flexibility to envisage a progressive but rapid evolution of the node throughputs. The paper describes two kinds of optical nodes enabling circuit and packet switching connections. Two introduction scenarios have been proposed : one for the backbone and a second for the metro. A strong need for a new framing in the point-to-point-transmission layer is highlighted. This paper clearly indicates that optical techniques have a great potential in the network., not only for the point-to-point transmission but also in the nodes to simplify the protocol and to converge progressively towards ATM&IP/Optical packets/WDM while being compatible with QoS requirements.

References :

/1/   R. Brained et al., "Integrated Services in the Internet Architecture", IETF RFC 1633, July 1994
/2/   S.Blake et al., "An architecture for differentiated services", IETF RFC 2475, Dec. 1998
/3/   Y. Maeno et al. , ECOC'99, pages 118-119, vol.1
/4/   N. Le Sauze et al., ECOC'99, p14-15, vol.1.

Integrated Slim Layer for IP over WDM

Jing Wu, and H.T. Mouftah
Department of Electrical and Computer Engineering
Queen's University, Kingston, Ontario, Canada K7L 3N6
Tel: (613) 533-2934, Fax: (613) 533-6615, Email: {jingwu, mouftah} @ eleceng.ee.queensu.ca

Introduction

The fast growing of Internet pushes the evolution of optical transport networks. Wavelength Division Multiplexing (WDM) offers a new dimension of the transportation of IP traffic. By using WDM, the transport capacity of optical fibers and systems expands greatly. It is more important that WDM provides some new features, i.e. the wavelength routing, and some new protection and restoration features. In order to fully utilize these capabilities, we have to develop new architectures to import IP traffic into WDM highways while providing Quality of Service management in a cost efficient way.

The interaction of the IP layer and the optical layer is of much concern. Recently several new proposals in IETF were introduced for IP over WDM [AR, CH, BA, KN, RS, WF, FS]. Multi-Protocol Lambda Switching (MPLS), cooperating with OSPF with optical routing extensions, is very promising to become the intermediate layer between IP and WDM.

This paper focuses on the architectures for the efficient transport of IP traffic on WDM networks and proposes a functionally separate intermediate layer between the IP network layer and the WDM optical transport layer. First, we summarize the roles of IP routers in the WDM optical switched networks. Then we describe the definition of the proposed integrated slim layer for IP over WDM.

IP routers in the WDM optical switched networks

There are three approaches of interaction between the IP layer and the optical layer [GH]. The first one is the traditional overlay approach, where the IP routers, together with the links, form a virtual topology. In the second, IP routers have the intelligence of resource management of both IP network layer resources, e.g. electronic buffers, and the WDM optical layer resources, e.g. optical cross-connects, converters, etc. In the third, IP routers are totally black boxes where only optical interfaces can be seen from outside and all the resource management becomes the build-in function of the IP routers.

It is argued that the second approach outcomes the other two in the aspects of better leverage the strength of IP and WDM. In this case, the IP routers play the role of both traffic bearing and resource management. Actually here the IP routers are the functional combination of the traditional packet store and forward engine and the network management agent.

Integrated slim layer for IP over WDM

It is necessary to make the intermediate layer between the IP layer and the WDM layer as simple as possible, therefore the trend is to integrate the functions of several traditional layers between the IP layer and the WDM layer instead of using several overlay layers for different functions. It will be beneficial that IP router is responsible for all non-local management functions, including the management of optical resources, configuration and capacity management, addressing, routing, traffic engineering, topology discovery, exception handling and restoration [CH]. The proposal of the integrated slim layer is to encapsulate some implementation details and provide a uniform interface to the IP network layer. It will localize some functions which are closely dependent on the implementation. Therefore it is important for the generalization of non-local management functions of the IP router.

The functions of the integrated slim layer must include but not limit to the following.

1. Framing. IP packets have to use a suitable frame structure to be transmitted in the WDM channels. Both the source node and the destination node rely on this function of the integrated slim layer to simplify the operation of IP layer.

2. Performance monitoring. Local performance monitoring (*not* end-to-end performance monitoring), which may highly depend on the implementation, is another important function of the integrated slim layer. Since the integrated slim layer is likely to act as the driver module of specified optical connections, it will have more detailed information about the structure and the components in the optical cross-connection. This makes it possible to monitor the status of the lower layer WDM system. It is also the responsibility of the integrated slim layer to translate the physical element parameters to the required format of status reports or alarms which is understandable by the IP layer. The operation of performance monitoring may be done periodically or on demand upon receiving the command from the IP layer.
3. Lightpath maintenance. When and which a lightpath should be set up or torn down is the decision of the IP layer, while the action of setting up or tearing down a lightpath is executed by the integrated slim layer. This particular function of the integrated slim layer is also referred to as a mediation device function, i.e. a vendor specified controller function [CH].
4. Localized protection switching. It will be potentially advantageous to implement protection and restoration at different levels, for example, the service restoration in TCP layer, the transport path protection in IP layer. The integrated slim layer may do some fast localized protection switching without consulting the IP layer. In order to maintain the consistence of the protection and restoration operations at different layers, the integrated slim layer will temporarily lock the protection switching command issued by the IP layer. The timing of localized protection switching of the integrated slim layer must be strictly defined. If within the time bound the protection switching is not finished, the integrated slim layer must give up immediately in order to leave the protection function to the IP layer. Localized protection switching may include the switching from a fault component to a local abundant component.

Conclusion

In order to make the IP layer independent of the specified implement of the optical cross-connects, we propose to use an integrated slim layer to encapsulate the implementation details. It integrates the functions of framing, performance monitoring, lightpath maintenance, and localized protection switching. These functions traditionally belong to different layers. The integrated slim layer can be implemented as the driver module of the optical transport system.

References

[GH] A. Greenberg, G. Hjalmtysson, and J. Yates, "Smart Routers – Simple Optics: A Network Architecture for IP over WDM", OFC'2000, ThU3

[AR] D.O. Awduche, Y. Rekhter, J. Drake, etc. "Multi-Protocol Lambda Switching: Combining MPLS Traffic Engineering Control with Optical Crossconnects", IETF draft: draft-awduche-mpls-te-optical-01.txt

[CH] S. Chaudhuri, G. Hjalmtysson, and J. Yates, "Control of Lightpaths in an Optical Network", IETF draft: draft-chaudhuri-ip-olxc-control-00.txt

[BA] D. Basak, D.O. Awduche, J. Drake, etc. "Multi-Protocol Lambda Switching: Issues in Combining MPLS Traffic Engineering Control with Optical Cross-connections", IETF draft: draft-basak-mpls-oxc-issues-01.txt

[KN] M. Krishnaswamy, G. Newsome, J. Gajewski, etc. "MPLS Control Plane for Switched Optical Networks", IETF draft: draft-krishnaswamy-mpls-son-00.txt

[RS] B. Rajagopalan, D. Saha, B. Tang, etc. "Signaling Framework for Automated Provisioning and Restoration of Paths in Optical Mesh Networks", IETF draft: draft-rstb-optical-signaling-framework-00.txt

[WF] G. Wang, D. Fedyk, V. Sharma, etc. "Extensions to OSPF/IS-IS for Optical Routing", IETF draft: draft-wang-ospf-isis-lambda-te-routing-00.txt

[FS] Y. Fan, P.A. Smith, V. Sharma, etc. "Extensions to CR-LDP and RSVP-TE for Optical Path Set-up", IETF draft: draft-fan-mpls-lambda-signaling-00.txt

[CC] Franco Callegati, Maurizio Casoni, Carla Raffaelli, and Bruno Bostica, "Packet Optical Networks for High Speed TCP/IP Backbones," IEEE Communication Magazine, Jan 1999, pp.124-129.

Robust Routing for Local Area Optical Access Networks

Muriel Médard, LIDS, Massachusetts Institute of Technology

Room 35-212, 77 Massachusetts Avenue, Cambridge, MA 02139, *medard@mit.edu*

Steven S. Lumetta, CSRL, University of Illinois at Urbana-Champaign

1308 West Main St., Urbana, IL 61801, *lumetta@uiuc.edu*

One approach to providing the benefits of the high data rates afforded by optics is to attempt to implement traditional electronic and electro-optic approaches using optical technologies. In electronics, operations such as buffering, adding packets and dropping packets, or merging packet streams, are done with ease. In optics, however, buffering is onerous. Operations such as retrieving a packet from a traffic stream affect the whole stream. The routing approach we propose seeks to make use of the strengths of optics and avoids operations that are cumbersome or expensive in optics. Our goal is to provide robust and reliable approaches to access at optical data rates. Our design rationale is the following:

Avoid buffering. Buffering in the network, with the attendant issues of cost and possibility of overflow, is to be avoided. Therefore, we avoid traffic merging. Traffic splitting, on the other hand, does not require buffering.

Do not use a switch unless necessary. While traffic to remote locations should be handled by such switches, local traffic need not be handled by these switches. It is desirable to isolate local traffic from the vagaries of congestion associated with external traffic. Finally, switches are expensive and extensibility is often difficult. Thus, allowing traffic that does not need to be routed through switches to bypass switches avoids unnecessary costs and disruptions caused by switch upgrades.

Use the optical layer to provide recovery. Our routing is well suited to packet-switched traffic, but does not rely on a specific protocol such as IP or ATM. Instead, our access scheme operates below such protocols. Recovery is performed at the optical layer, in a manner which is robust, simple and rapid enough that recovery at higher layers does not need to be triggered.

We consider routings that allow automatic recovery from link failures. An undirected graph $G = (N, E)$ is a set of nodes N and edges E. With each edge $[x, y]$ of an undirected graph, we associate two directed arcs (x, y) and (y, x). Each arc corresponds to one of the fibers forming the link. We assume that if an edge $[x, y]$ fails, then arcs (x, y) and (y, x) fail. Assume that the graph G is two edge-connected, *i.e.*, removal of an edge leaves the graph connected, which is necessary to make recovery from link failures feasible.

We describe a routing such that recovery is possible even in the event of any link failure. Our routing consists of two parts: a "collection" portion and a "distribution" portion. The collection portion allows all nodes to place their traffic on the access wavelength(s) and the distribution portion ensures that packets can reach all nodes. The architecture we consider is the following: nodes place traffic on a shared optical medium (we consider a single wavelength onto which traffic is written and a single wavelength off of which traffic is read). Traffic that needs to be sent to or received from outside the local area can go through a switch, which acts as any other node, placing traffic onto the collection wavelength and retrieving traffic off the collection wavelength. Local traffic need not be handled by the switch.

The collection portion of the routing is constructed as follows. We select a root node and build a depth-first search (DFS) numbering beginning at the root node. The routing is a walk that traverses nodes as they are considered by the DFS numbering algorithm. A collection routing traverses every node at least once. Moreover, it traverses each edge at most twice. If an edge is traversed twice, it is in opposite directions at each time. Thus, each arc is traversed at most once and so a single wavelength, in both directions, is sufficient to establish the collection portion of the routing. The solid lines in Figure 1 show a DFS construction on a sample network.
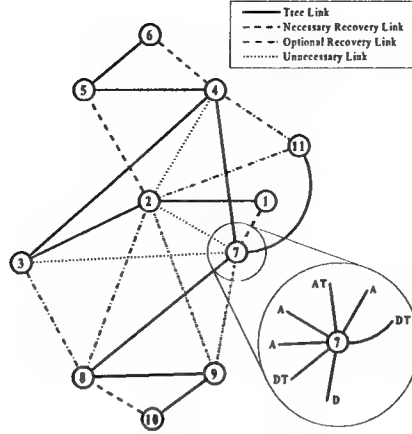
Figure 1: Example DFS tree and labeling. The graph shown is the NJ LATA network. An expanded version of node 7 is labeled with ancestor (A), descendant (D), and tree (T) markings. Link styles indicate their use in the access collection recovery protocol.

The distribution portion of the routing is a directed spanning tree rooted at the last node traversed by the collection routing. Call this tree the primary tree. Robustness is afforded in the distribution section by constructing a secondary tree, which shares the root but no arcs with the primary tree, and such that removal of any edge (and its two associated arcs) leaves the root connected to every node on at least one of the trees. Such trees were first introduced in [1, 4], using s-t numberings ([2]), and a more general method of constructing them was given in [3]. A single wavelength, used in both directions, is sufficient to construct the primary and secondary trees. The roots of the primary and secondary tree must therefore be able to perform wavelength conversion, by placing the traffic from the collection routing onto the distribution trees. We only require two nodes to perform wavelength conversion.

Our algorithm performs recovery separately both in the collection and the distribution portions of the routing, even though they co-exist over a common physical infrastructure. The crux of our algorithm lies in our method of performing link recovery in the collection portion of the routing. Suppose that link $[i, j]$ fails. If link $[i, j]$ is not included in the DFS tree, then its failure leaves the collection routing unaffected. We therefore need only consider the case where link $[i, j]$ is included in the DFS tree. Assume wlog that the node i is the ancestor of j. Failure of $[i, j]$ entails disconnection of all the descendants of i. From the DFS construction and the fact that that we have a two-edge-connected graph, some descendant of j must have an edge connecting it to some ancestor of i. We have developed a distributed algorithm that uniquely selects one such link and uses it to reconnect j and its descendants to the upper partition of the collection route. For the distribution portion, each node downstream of a link failure in the primary tree switches to receiving on the secondary tree.

We have extended this approach to node failures and have developed an algorithm for implementing this routing and the associated recovery.

References

[1] A. Itai, M. Rodeh, "The Multi-Tree Approach to Reliability in Distributed Networks," *Information and Computation*, Vol. 79, 1988, pp. 43–59.

[2] A. Lempel, S. Even, I. Cederbaum, "An Algorithm for Planarity Testing of Graphs," in *Theory of Graphs*, International Symposium, July 1966, pp. 215–232.

[3] M. Médard, S. G. Finn, R. A. Barry, R. G. Gallager, "Redundant Trees for Preplanned Recovery in Arbitrary Vertex-Redundant or Edge-Redundant Graphs," in *IEEE/ACM Transactions on Networking*, 1999.

[4] A. Zehavi, A. Itai, "Three Tree-Paths," *Journal of Graph Theory*, vol. 13, no. 2, 1989, pp. 175–188.

Planar Waveguide Technology

Katsunari Okamoto

NTT Photonics Laboratories
162 Tokai, Naka-gun, Ibaraki, 319-1193, Japan
E-Mail : okamoto@iba.iecl.ntt.co.jp

1. Introduction

Wavelength filters with large channel numbers and narrow channel spacings are quite important in dense WDM systems. Other important application of the filter is a spectrum slicing of supercontinuum light to make multiwavelength source for WDM. This paper reviews the current performances and future prospects of arrayed-waveguide grating (AWG) filters.

2. Large Channel with Narrow Spacing AWGs

Crosstalks in AWGs are attributed to the phase and amplitude fluctuations in the total electric field profile at the output side array-slab interface since the focused beam profile is the spatial Fourier transform of the electric field in the array waveguides [1]. Phase fluctuations are caused by the nonuniformity of refractive indices and core geometries in the array waveguide region. By the improvement of the waveguide fabrication technologies, the crosstalks of less than -33 dB have been achieved in 256ch-25GHz spacing AWG as shown in Fig. 1. Geometry and index difference of the core are $4.5\,\mu m \times 4.5\,\mu m$ and 1.5 %, which enables the minimum bending radius to be 2 mm. This AWG was fabricated on single wafer of 4-inch Si.

The maximum available wafer size of PLC is limited by the fabrication apparatus such as electric furnace and mask aligner etc. Therefore, it is not so easy to fabricate AWG with larger channel numbers. One possible way to increase the total number of channels is to use two kinds of AWGs, which are cascaded in series. We made 320ch-10GHz spacing AWG by cascading a 32 ch-100GHz spacing flat AWG as a primary filter and a 16ch-10GHz spacing AWG (10 channels are used) as a secondary filter [2]. Fig. 2 shows the configuration of a cascaded multiplexer to realize 320-channel AWG with 10 GHz spacing. Fig. 3 shows the demultiplexing properties for the entire 320 channels. Crosstalk to the neighboring channels is about -20 dB. The transmission losses range from 14 to 21 dB. Loss variation can be reduced by employing a primary AWG whose pass bands overlap at lower loss value. Though crosstalk and insertion loss characteristics are not satisfactory, these performances will be improved by the improvement of transmission characteristics of each stage of AWGs.

3. Summary

Large channel AWGs that are realized on single wafer and with the cascaded configuration are reviewed. Functional PLCs such as frequency spectrum synthesizer [3] and coherent optical transversal filter [4] will also be presented in the conference.

References
[1] K. Okamoto, Academic Press, chapter 9 (2000).
[2] K. Takada et al., Electron. Lett., vol. 35, p.824 (1999).
[3] K. Okamoto et al., Electron. Lett., vol. 35, p.733 (1999).
[4] K. Okamoto et al., Electron. Lett., vol. 35, p.1331 (1999).
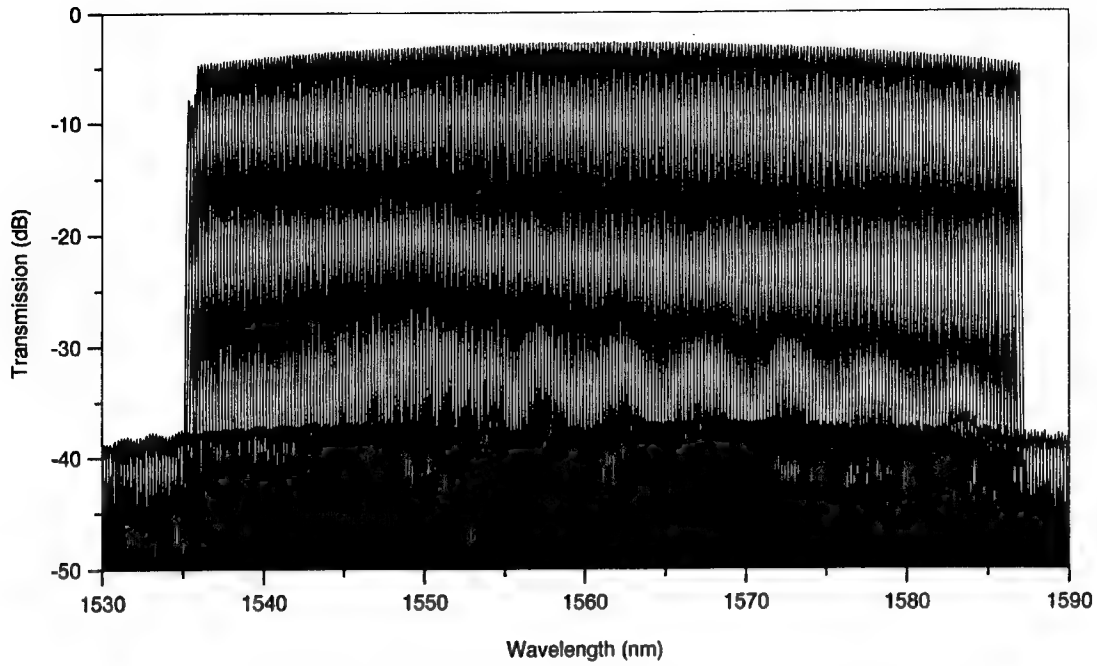
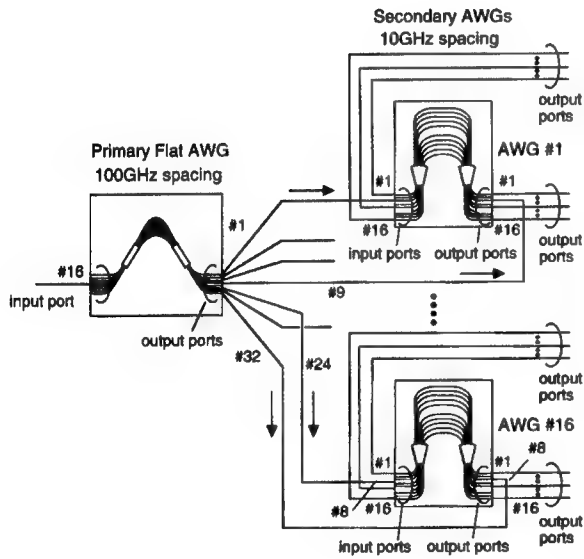Fig. 1 Demultiplexing properties of 256ch-25GHz spacing AWG

Fig. 2 Configuration of a cascaded
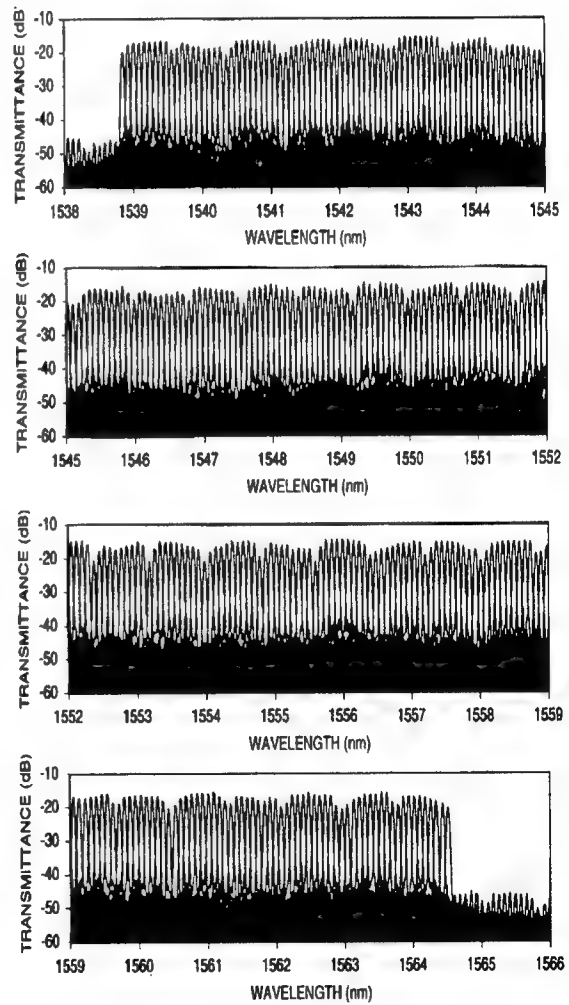AWG to realize 320ch-10GHz filter

Fig. 3 Demultiplexing properties of
320ch-10GHz AWG

Optical Monitoring Techniques for WDM Networks

Y. C. Chung
Korea Advanced Institute of Science and Technology
Department of Electrical Engineering
373-1 Kusong-dong, Yusong-gu, Taejon 305-701, Korea
(phone) 82-42-869-3456, (fax) 82-42-869-3410, (email) ychung@ee.kaist.ac.kr

I. Introduction:

Future optical networks are envisioned to be dynamically reconfigurable – the optical channels are added/dropped or cross-connected frequently in the optical layer using wavelength-division-multiplexing (WDM) technologies [1].   For the efficient operation and maintenance of these network, however, it is essential to monitor various parameters including the wavelength, optical power, optical signal-to-noise rations (OSNR's), and optical paths, etc.   In this paper, we review the current status of WDM monitoring techniques and introduce the relevant research activities at KAIST.

II. Wavelength Monitoring Techniques

Recently, there have been substantial efforts to develop the wavelength-monitoring techniques for WDM networks [2]-[7].   For example, it has been demonstrated that the wavelengths of multiple WDM channels could be monitored by using various types of tunable filters such as a PZT-tuned Fabry-Perot filter, an acousto-optic tunable filter, and a temperature-tuned etalon filter [2]-[4].   However, these techniques not only require elaborate tuning mechanisms, but also have insufficient resolution.   To avoid these tuning mechanisms, it has been proposed to use diffraction gratings such as a fiber Bragg grating (FBG) or an arrayed waveguide grating (AWG) with a photodiode array [5]-[6].   However, these techniques could be quite expensive, as they require a large number of photodetectors to cover a wide bandwidth at high resolution.   Another monitoring technique utilized pilot tones and a fixed etalon filter [7].   However, due to the pilot tones, the performance of this technique could be impaired by the cross gain modulation of EDFA and stimulated Raman effect [8]-[9].   We will review these techniques and discuss their advantages and disadvantages.

III. OSNR Monitoring Techniques

To monitor the performance of WDM networks, it is essential to measure the OSNR of each channel. Previously, it has been demonstrated that the OSNR could be measured by linearly interpolating the ASE noise level at the carrier wavelength [10]-[11].   However, in a dynamically reconfigurable WDM network, each channel may traverse through different route and different number of optical amplifiers. Thus, in this network, the OSNR could not be monitored accurately by the conventional linear interpolation technique.   To overcome this problem, we have recently developed new techniques based on (1) the receiver noise characteristics and (2) the polarization extinction ratio of each WDM signal [12]-[13].   We will discuss the current status of these techniques and future research directions.

IV. Optical Path Monitoring Technique

The WDM transport network requires reliable monitoring techniques not only for optical performance

but also for channel identification. In particular, for the proper management of these networks, it is essential to monitor the optical paths of WDM signals in the optical cross-connects (OXC's). Recently, several techniques have been proposed for this purpose [14]-[17]. These techniques utilized low-frequency tones in the range of 0.1 ~ 5 kHz. However, these low-frequency tones could propagate to the next node and accumulate in the amplified WDM network. In addition, the low frequency tones could generate the "ghost tones" due to the slow dynamic properties of EDFA's [8]. To avoid these problems, it has been proposed to erase the pilot tones at the outputs of OXC's using voltage-controlled attenuators [15]. However, these techniques could not be used for the channel identification within the entire network. To overcome this problem, we have proposed to monitor the optical paths in the OXC's using dual high-frequency tones (>100 kHz). The two tones were used to identify the originating node and individual channel, respectively. Thus, unlike the previous techniques, the proposed technique could monitor the optical paths not only within the OXC, but also within the entire network and reduce the required number of pilot tones considerably.

V. Summary

For the efficient operation of WDM network, it would be desirable to monitor the key parameters in the optical layer. Thus, various techniques have been proposed to monitor the wavelengths, optical powers, OSNR's, and optical paths in the DWDM networks. In this paper, we reviewed the current status of these technologies and discussed future directions. Although some of these technologies are promising, it appears that most of them are still in their early stages and should be improved further for the practical deployment in the rapidly evolving DWDM network.

VI. References

[1] N. Antoniades et al., *IEEE Photon. Tech. Lett.*, vol. 9, no. 9, pp. 1274-1276, 1997.
[2] C. Miller et al., *Lightwave*, pp. 71-75, Mar. 1999.
[3] St. Schmid et al., *Tech. Dig. OFC'97*, Dallas, TX, Feb. 1997, paper TuC.
[4] S. K. Shin et al., *Tech. Dig. OFC'98*, San Jose, CA, Feb. 1998, paper WJ7.
[5] K. Otsuka et al., *Proc. ECOC'97*, Edinburgh, UK, Sept. 1997, vol 2, pp. 147-150.
[6] M. Teshima et al., *J. Lightwave Technol.*, vol. 14, pp. 2277-2285, 1996.
[7] K. J. Park et al., *Tech. Dig. OFC'99*, San Diego, CA, Feb. 1999, paper FJ3.
[8] Y. Sun et al., *IEEE J. of Select. Topics in Quantum Elect.*, vol. 3, pp. 991-1007, 1997.
[9] H. S. Chung et al., *Tech. Dig. OFC2000*, Baltimore, MD, Mar. 2000, paper WK7.
[10] K. Asahi et al., *Tech. Dig. OFC '98*, San Jose, CA, Feb. 1998, Paper ThO2.
[11] H. Suzuki et al., *Electronics Lett.*, vol. 35, pp. 836-837, 1999.
[12] S. K. Shin et al., *Tech. Dig. OFC2000*, Baltimore, MD, Mar. 2000, paper WK6.
[13] D. K. Jung et al., *Tech. Dig. OFC2000*, Baltimore, MD, Mar. 2000, paper WK4.
[14] C. K. Chan et al., *IEEE Photon. Technol. Lett.*, vol. 10, pp. 899-901, 1998.
[15] K. W. Chu et al., *Tech. Dig. OFC'99*, San Diego, CA, Feb. 1999, paper FJ5.
[16] E. Kong et al., *Proc. CLEO/Pacific Rim'99*, Seoul, Aug. 1999, paper FT4.
[17] S. Zhong et al., *Tech. Dig. OFC2000*, Baltimore, MD, Mar. 2000, paper WK5.

Simple and low-cost silicon Fabry-Perot filter for WDM channel monitoring

Giuseppe Cocorullo[a,b], Francesco G. Della Corte[a], Mario Iodice[a], Ivo Rendina[a]

[a]IRECE – National Research Council, via Diocleziano 328, 80124, Napoli, Italy

[b]DEIS, University of Calabria, 87036, Rende, Cosenza, Italy

WDM networks are becoming increasingly complex as the number of wavelengths (channels) carried on a single fiber increases. Channels are added and dropped at various sites, and exchanged between two of more optical networks. Optical channel monitoring in a WDM system implies measurement and tracking of the wavelength of all channels. This information can be used for network elements control, network maintenance, and system performance monitoring. At this aim, various tunable filters at the wavelength of 1300 and 1550 nm have been demonstrated[1]. They are key components in WDM apparatus as well as in a wide range of fiberoptic sensors and measurement applications. So far, a variety of approaches ranging from the Pockels effect in LiNbO$_3$, current injection in semiconductor, electrooptic effect in liquid crystals and most recently microelectromechanical activated devices have been exploited. In almost all these proposals the filter linewidth is larger than a few nanometers and further degrades with tuning. However, for most applications, including the dense WDM systems, filters linewidths narrower than 0.5nm and free spectral range of tens of nanometers are required.

In this paper we propose a simple and low–cost solution for tracking the frequency of WDM channels, based on the thermooptic tuning of Fabry–Perot silicon optical filters. The fabricated structures exhibit, thanks to a suitable coating stack on both cavity sides, high finesse and narrow bandwidth. Moreover, the free spectral range is large compared to the channel spacing, allowing the monitoring of one carrier frequency at a time. By means of a heater we change the cavity refractive index and move the transmission peaks, thus scanning the WDM frequency set. In particular, in a preliminary prototype realized by using a 100-µm-long silicon cavity we demonstrate the possibility to resolve up to seven 50-GHz-spaced channels, with a crosstalk of −10 dB, at wavelengths around 1550 nm. More channels are easily resolvable by using shorter cavities.

In particular, commercial silicon wafers with nominal thickness of 100±10 µm, giving rise, for $\lambda = 1.55$ µm, to a theoretical *free spectral range* (FSR) $\Delta f \approx 432.3$ GHz, or about 3.45 nm, and with both sides polished to obtain a very good optical quality, were used as etalons. Using the experimental setup which is described later in this section, we checked the surfaces characteristics measuring the spectral response of the wafer itself before realizing the coating stack,. The measured spectrum is practically identical to the theoretical one, so verifying the high surface optical quality. The measured FSR results to be a little bit smaller (3.27 nm) than the expected one, so indicating a real wafer thickness of 105 µm. Then, we realized on both surfaces of a similar wafer, by means of e-beam evaporation from solid sources, alternated $\lambda/4$ layers of silicon dioxide SiO$_2$ (refractive index $n_{low} \approx 1.44$) and amorphous silicon a:Si ($n_{high} \approx 3.48$). The thickness of such layers are $L_{low} \approx 270$ nm and $L_{high} \approx 110$ nm respectively, for a central wavelength $\lambda = 1.55$ µm. The layer thickness and refractive index were checked by means of alpha-step and ellipsometric measurements. The deposition process guarantees uniformity, low roughness and good parallelism of the multi-layer mirrors.

The spontaneous emission ASE of an Erbium Doped Fiber Amplifier (EDFA) was used as broadband light source in the 1550 nm region. The spontaneous ASE emission of the EDFA extends in the range 1500-1600 nm, but is acceptably uniform between 1540 and 1560 nm. Its power level is about +3 dBm. A 62.5/125 multi-mode optical fiber brings the light from the EDFA output connector to the filter under test, which is firmly mounted over a Peltier cell. A second 62.5/125 multi-mode optical fiber collects the light transmitted through the filter and guides it to an Optical Spectrum Analyzer (OSA) for spectrum measurements. Both fiber end-facets are a few millimeters distant from the filter surfaces, so minimizing the undesired interference effects in the air gap. This choice implies a collected power reduction, but the high OSA sensitivity (−70 dBm) allows to overcome this problem. The input and the output fiber holder and the Peltier cell are mounted on three micro-positioning stages, allowing a proper alignment of the optical system. The Peltier cell is electrically connected to a constant current generator, so permitting a fine temperature control. The temperature is checked by a calibrated thermistor fixed on the Peltier. A first filter was made with a single coating SiO$_2$-a:Si pair on each side. The measured FSR is 421.2 GHz, which corresponds to 3.37 nm, and indicates a cavity length $L = 102.6$ µm. The measured 3-dB bandwidth is 66.25 GHz (0.53 nm) and it is relatively larger than the theoretical one. The global finesse calculated from these two parameters is 6.5, which is about 2.5 times lower than the theoretical one. The finesse reduction implies also a contrast reduction, which goes from 19 dB of the simulated curve, to 15 dB of the experimental one. This fact can be easily

explained, as previously discussed, referring to imperfection of the filter and of the coating layers surfaces (i.e., roughness and non-parallelism) and to further absorption into the coating layers.

In fig.1 are reported the experimental and the calculated transmission spectra of a silicon filter whose mirrors are made of two SiO_2-a:Si pairs. The comparison between theoretical and experimental data shows that the e-beam evaporation can produce coating layers of good quality. The FSR is 408.7 GHz, corresponding to 3.27 nm and indicating a cavity length of about 105 µm. The bandwidth of this filter is reduced to 30 GHz, or 0.24 nm, and the corresponding finesse is about 13.7. The maximum contrast is 22 dB. The calculated spectrum shows, as expected, a smaller bandwidth and consequently a higher finesse of about 45, and a contrast of 28 dB. In this case too, the real filter performance is penalized by several factors connected to the coating layer fabrication. However, even with a non-ideal optical characteristics, this filter shows

Fig.1 Experimental (solid line) and calculated (dashed line) transmission spectrum of a 4-layer-

very interesting features. A more accurate coating fabrication, that is a larger number of pairs or a higher coating films quality, would produce higher finesse structures. For instnce, sputtering or PECVD deposition of SiO_2, Si_3N_4, and a:Si would furnish layers with low absorption and low defect density.

A very important feature of such a filter is the possibility to tune it, that is to move the transmission spectrum with respect to the wavelength axis. We verified this fact, heating the filter under test by means of the Peltier cell and measuring the transmitted spectrum at different temperatures. In fig.2 are reported several spectra of the second filter above described, and acquired at various Peltier cell temperature. It is evident how the resonance peak, which at room temperature is at ~ 1550.5 nm, moves toward higher wavelength values by increasing the temperature. For a heating of about 32 °C the resonance moves at values beynd ~ 1553 nm. For further temperature increases the resonance peak goes out of the observation window and another peak appears at the left side, coming from lower wavelength region. It is possible to conclude that by means of a moderate heating, from room temperature to about 55 °C, we can tune the filter in a range which is determined by the filter FSR. In this interval,

which is about 3.0 nm wide, we resolved at least seven 50-GHz-spaced independent channels, accepting a crosstalk between two adjacent channels of about −10 dB[1]. Moreover, during the tuning, the resonance peak shape does not change and the passband bandwidth remains at about 0.24 nm over the entire tuning range. Wider wavelength ranges can be unambiguously explored using filters with larger FSRs, i.e., with shorter cavity lengths.

References

1. G. Livescu, "Channel monitoring in WDM networks: a system perspective", *1998 OSA Technical Digest Series*, Vol. 4, pp.43-45.
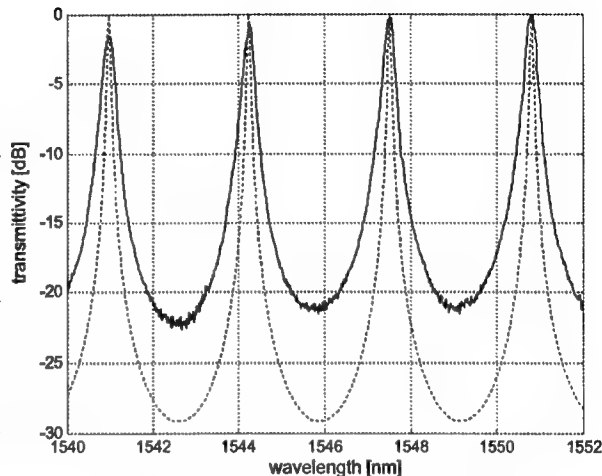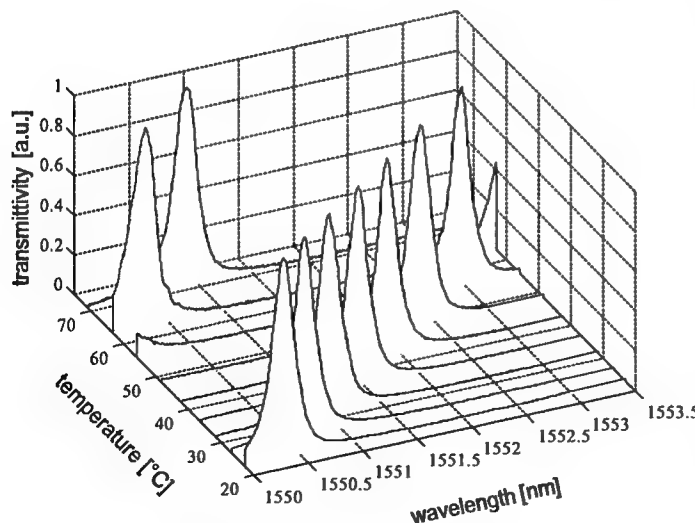
Fig.2 Thermal tuning of a 4-layer coated FP filter

Optical Switch Fabric Design for large fabrication tolerance

Xiao Lin, Qiang Wang, Yan Wang, Daniel C. Lee, Wei Chen, Ting Li and Yung Jui Chen

Dept. Electrical Engineering
University of Maryland, Baltimore County
5200 Westland Blvd.
Baltimore, MD 21227
Tel: (410) 455-3511
Fax: (410) 455-6500
Email: xilin@gl.umbc.edu

Summary

Optical cross-connect switch (OXC) are key components in advanced wavelength division multiplexed (WDM) networks. Integrated optical switches have been reported using several mechanisms and materials. We have demonstrated waveguide-type thermooptic switches which employ silica-based planar lightwave circuits (PLC's). The crosstalk of OXC, caused by a lot of reasons, is an important parameter which influences the system performance [1,2]. One of the reasons is the coupling ratio (CR) of a 3dB coupler in a switch unit. Due to the fabrication limitations, it is hard to obtain exact CR as designed. In this paper, we propose a scheme to achieve low crosstalk even with the variation of CR.

The design of our optical switch fabric is a strictly non-blocking matrix switch using dilated double-layer architecture [3]. The general architecture of a 4×4 OXC is shown in Fig. 1(a).

By using the dilated double layer switch architecture, there is always only one signal passing through a switch unit. It ensures that there is no first-order crosstalk by this switch architecture [4]. Every switch unit consists of a 2x2 cross-bar switch as shown in Fig. 1(b), for the Thermal Optical (TO) switch type.

The crosstalk of the switch unit is influenced by the directional coupler's CR as shown in Fig. 2(a). From the figure, the crosstalk of a switch unit in cross state degrades to −15 dB, if CR has 10% variation. Coupling Spacing (CS) and Coupling Length (CL) as shown in Fig. 1(b) of the directional coupler determine the CR. The formula 1 shows the relation between CL and CR from the experiment result. *CL_offset* is related to the coupling efficiency by the bending waveguides connected with the straight CL. *Eff_CL* is defined as the effective CL. CR is equal to 50%, when $CL = Eff\_CL - CL\_offset$.

$$CR=(1-cos(2\pi(CL+CL\_offset)/(4*Eff\_CL)))/2 \qquad (1)$$

The effective CL is only determined by CS as shown in formula 2. It behaves exponentially to the CS by BPM simulation as shown in Fig. 2(b). By the calculation, CR changes 10% with 0.1 um variation of CS, when CS should be 5um exactly. Although CL and CS of every 3dB coupler are fixed by the photomask design, CR is sensitive to the fabrication variation. For example, CS of directional coupler may vary within sub micron during waveguide etching process.

$$Eff\_CL=eff\_CL_0*exp(CS/\gamma), \text{ where } eff\_CL_0 \text{ and } \gamma \text{ are process dependent parameters} \qquad (2)$$

Fig. 3 shows the histogram of CR of all 3dB couplers in a 2-inch square area on one wafer. The variation of CR is about 15%, which means crosstalk of some switch units may be worse than -15 dB as mentioned before. Fig 3 also shows the histogram of CR among 10 different wafers. From these testing results, the variation of CR directly influences the crosstalk of thermal optical switch.

In order to lower the crosstalk of the switch, we can either improve the fabrication process of the directional couplers, for example to make CS as accurate as possible, or we can change the architecture of the switch design. The dilated double layer architecture is to lower the crosstalk level to the second order. The second-order crosstalk happens when two signals with the same wavelength cross the middle two-stage switch units. If all the switch units are designed in the same way, the degradation of crosstalk in single switch unit due to the variation of CR will cause the double degradation in second-order crosstalk. Since all the second-order crosstalk is from the middle two-stage switch units, we intentionally use different CL of switch unit in stage 2 and stage 3. For stage 2, we use shorter CL design which is related to the crosstalk tolerance. And for stage3, longer CL is used. Due to fabrication variation, the effective CL within a wafer is different from the designed CL. In our proposed design, the different CLs in stage 2 and 3 will compensate each other for lower crosstalk. Fig. 4 shows the simulation result of the second order crosstalk with different ΔCL, where ΔCL= CL-of-stage3 − CL-of-stage2. The second order crosstalk of the proposed design is not as good as ideal CR case, if CR is within 5% variation, But it maintains certain crosstalk level. We see that the second order crosstalk begins to drop in the proposed design, when CR is larger than 5% variation. For example, the crosstalk of a ΔCL =200 um design (ideal CL=1300um) is 6 dB less than of

ΔCL =0 design, when CR varies within ±7.5% which is reasonable within one wafer and among wafers. From another point of view, the proposed design can tolerate more CR variation than the original design within certain crosstalk limitation. For example, with the requirement of crosstalk level under –40 dB, the original design only can tolerate 10% CR variation. But the design of ΔCL=200 um can tolerate 15% CR variation. The range of ΔCL is determined by the crosstalk requirement and the variation of CR.

In summary, we have reported that the different CL design in the middle two stage switch units extends tolerant range of the fabrication of switch fabric under certain crosstalk limitation.

References:
1. Chungsheng Li, Frank Tong: 'Crosstalk Penalty in a All-Optical network Using Dynamic Wavelengh Routers.' OFC'94, pp.174 ~176.
2. Chungsheng Li, Frank Tong: 'Crosstalk and interference Penalty in All-Optical Networks Using Static Wavelength Routers', Journal of Lightwave Technology, vol. 14, No. 6, 1996, pp.1120~1126
3. C.-C. Lu and R. A. Thompson, "The Double-Layer Network Architecture for Photonic Switching," Lightwave Technology, vol. 12, no. 8, 1482~1489, (1994)
4. J. E. Midwinter, "Space-division Switching" Photonics in Switching, vol II (Academic, London, 1993)
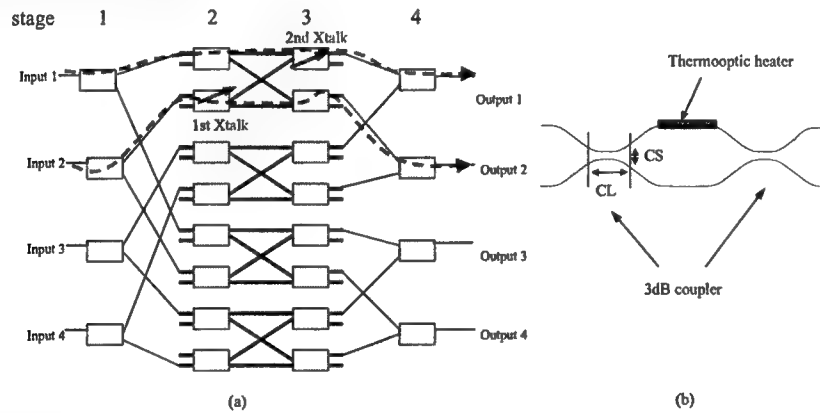
Fig. 1 (a) The architecture of the non-crosstalk 4x4 OXC design (b)Single-MZI switching unit configuration, CL is the coupling length.
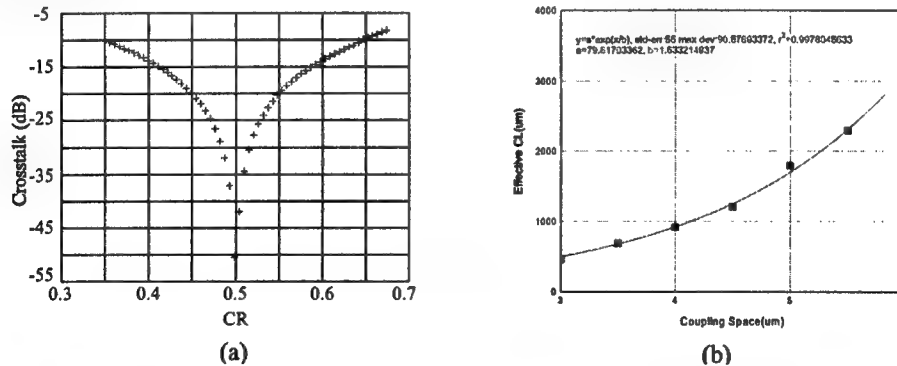

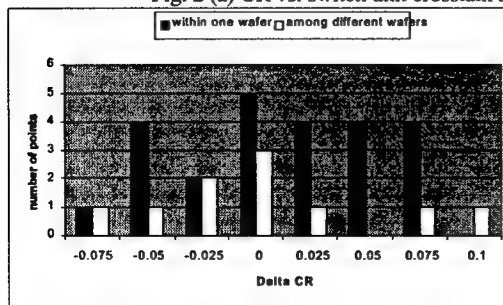Fig. 2 (a) CR vs. switch unit crosstalk in cross-state (b) effective CL vs. CS

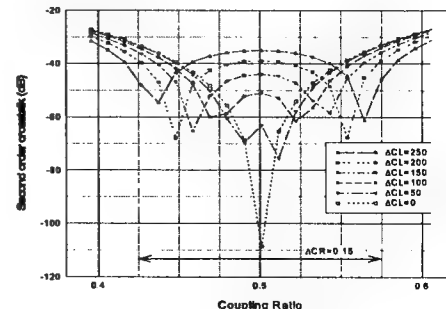Fig. 3 the variation of CR within one wafer and among different wafers

Fig. 4 The second order crosstalk vs. the CL difference between switches in stage 2 and 3.

Beyond-tera-bit-per-second-capacity optical core networks

Naoya Henmi

Networks Development Laboratories, NEC Corporation

1753, Shimonumabe, Nakahara-ku, Kawasaki, Kanagawa 211-8666, Japan

Tel.: +81 44 435 5632; Fax.: +81 44 435 5697

e-mail: n-henmi@cw.jp.nec.com

Abstract: Promising candidates for applying optical technologies to next-generation networks include optical self-healing for the transport function and an ultra-large-scale optical-switch fabric for the grooming/multiplexing function have been summarized.

1. Introduction

The tremendous growths of Internet traffic and the continually increasing demand for multimedia services have generated a need for increased transmission capacity and switching-systems throughput in next-generation broadband-data core networks. Wavelength division multiplexing (WDM) offers easy and cost-effective capacity-expansion by means of optical amplifier repeaters, and it has been widely applied to relieve congestion in public-transport networks. With regard to increasing switching throughput, however, the ultra-high-throughput optical switching systems under research can only be produced by using complicated optical-signal processing and large-capacity optical-data buffering, and the optical switching systems seems to be a long way off. The introduction of optical-switch fabrics into ultra-high-throughput switching systems therefore appears to be a more immediately promising approach to reducing size and total power consumption.

This paper presents our general views on next-generation beyond-Tb/s optical networking, including optical self-healing transport network technology for next-generation transport networks and ultra-high throughput optical-switch fabric technology for Tb/s-throughput switching systems.

2. Necessary functions for next-generation optical core networks

According to our vision, a beyond-Tb/s-capacity optical core should have two functions: 1) a transport function for supporting the data transportation with a reliable self-healing function and cost-effective WDM resource usage; and 2) a grooming/multiplexing function, which sorts the various services by type and destination to wide bandwidth paths for simple and cost-effective transportation. From a technical standpoint, it is practical to limit optical technologies' application to an optical self-healing for the transport function and an ultra-large-scale optical switch fabric for the grooming/multiplexing function.

Figure 1   Scenario for Introducing Optical Self-Healing Transport Network

3. Optical self-healing transport network

Figure 1 shows a scenario for introducing the self-healing function into transport networks.[1] WDM point-to-point systems are already in commercial application use with SONET/SDH protection capability. Due to the strong demand for large-transmission bandwidths in the use of the Internet and multimedia-related traffic, however, a new transport network that possesses a bandwidth expansion capability and a
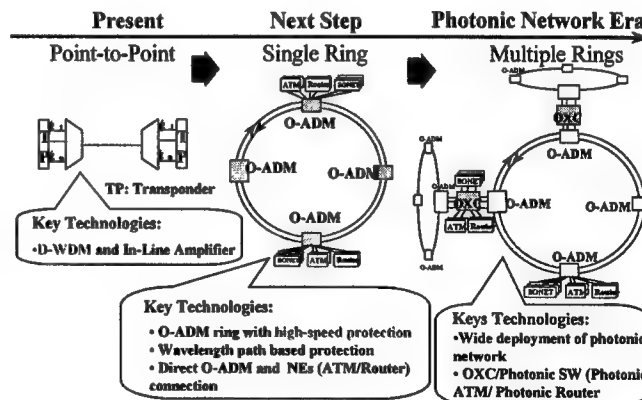
flexible/open interface. WDM optical networks have the capability to accommodate multi-Gb/s and bit-rate/format-independent demands as WDM channels, so they are very promising if they have self-healing functionality.

There are two approaches to producing optical self-healing networks. One is to configure a physical-mesh topology network with optical cross-connects (OXCs), and the other is to configure a physical ring topology network with optical ADMs (O-ADMs or WDM ADMs). Ring-topology-based optical self-healing networks[1] are preferred as a first step because 1) O-ADM is more economical than OXC, 2) protection speed in ring topology is much faster, and 3) O-ADM is more transparent to data bit-rate and format. Eventually though, in photonic networks of the future, multiple optical self-healing rings will be connected by emerging large-scale OXC/photonic nodes.[2]

4. WDM Self-healing ring-transport network

From the viewpoints of application requirements supported, available monitoring technology (e.g., availability of network protection and network management), and cost-effectiveness (e.g., number of wavelengths needed and/or required network resources for a fully logically meshed demand pattern), the BWPSR (bi-directional wavelength path-switched ring) is the best alternative. It is based on bi-directional, wavelength-based protection and a wavelength-based protection-trigger self-healing ring network. We have developed a prototype of BWPSR-based WDM ring network, and confirmed the network's protection speed is as fast as that of SONET/SDH ring networks

5. Ultra-large-scale switching systems with optical SW fabric

In beyond-Tb/s-capacity optical networks, the Tb/s-throughput grooming/multiplexing function plays an important role in making the network simple and cost-effective. State-of-the-art electronics technology can not easily produce a Tb/s-throughput switch fabric that is non-optical, and this incapability seems to be a prime first target for the applications of optical technologies.

Figure 2 shows an image of an ultra-high-throughput switching system with an optical SW fabric. For better network resource utilization, a Tb/s-throughput optical switch is used for WDM optical path grooming/multiplexing (OLXC), ATM SW capacity expansion, and IP-router capacity expansion.

We have developed a prototype of a photonic node by using our proposed WD/SD optical switch fabric, optical

Figure 2　Photonic Node with an ultra-high capacity optical switch fabric

semiconductor amplifier gate switches, and super-cell switching technologies. At present, the prototype has ATM cell handling capability, but we plan to expand the handling capability of the optical channel (OCh) and the IP.

5. Conclusion

This paper described the necessary functions of next-generation optical core networks. We believe that promising candidates for applying optical technologies to next-generation networks include optical self-healing for the transport function and an ultra-large-scale optical switch fabric for the grooming/multiplexing function. We have developed the prototypes of a WDM self-healing network and a photonic node. Fundamental technologies have been confirmed by evaluating the prototypes, and we found that cost-effectiveness is one of the main issues to be addressed in the near future. It is hoped that, with advanced and cost-effective optical-switching technologies, photonic networks will be able to support beyond-Tb/s networking in the near future.

[References] 1) N. Henmi et. al., EURESCOM P615, "OADM-workshop", p.36, 1998; 2) Y. Maeno et. al., WE1D, vol.3, p.67, ECOC'97; 3) N. Henmi, Telecom Forum 1999, in Geneva
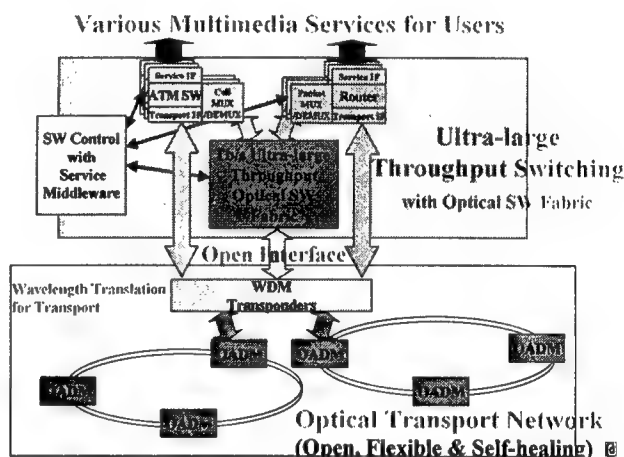
Burst mode optical data switching in WDM networks

Brian W. Meagher
Telcordia Technologies, 331 Newman Springs Road, Red Bank, NJ 07701
brian@research.telcordia.com
Xiaohui Yang
University of Maryland, Baltimore County, 5200 Westland Blvd., Baltimore, MD 21227
Jim Perreault and Ray McFarland
Laboratory for Telecommunications Sciences, Adelphi, MD 20783

Introduction   There is tremendous activity in burst mode routing and control traffic for next generation internet (NGI). For many applications it is desirable that data be transported from one point in a network to one or more other points in the least possible time. For some applications the time sensitivity is so important that minimum delay is the overriding factor for all protocol and equipment design decisions. A number of schemes have been employed to meet this requirement, including both signaling based and equipment intensive solutions. This paper compares several means available for providing burst mode switching capabilities in a WDM optical network, and reports some test results on a novel hybrid optical network switch.

The Need For Speed In order to appreciate the impetus for designing burst mode switching networks it is useful to consider the delays that are encountered in data networks. It takes 20.5 milliseconds for light to travel from San Francisco to New York City in a straight line through an optical fiber, without considering any intervening equipment or a realistic route. Many transmission protocols require that data packets traverse the network only after a circuit has been established. The circuit setup phase in TCP/IP, for example, involves three network traversals (sending a SYN packet, responding with an ACK, and completing the procedure with another ACK) before any data packets can be sent. While this helps ensure reliable data transport it also guarantees a minimum network delay of more than 80 milliseconds before data can be received. For some applications, such as periodic transmission of sensor data, this may be an unnecessary overhead to impose.

Reducing the Bottleneck One way to mitigate the impact of network setup time on packet latency is to pipeline the signaling messages. Two methods for accomplishing these timesavings are presented in Ref. 1, which discusses Cut-at-Confirm and Cut-at-Setup. Both of these methods allow the first packet delay to be reduced from two round-trip times to one and one half round trip times. The scheme has been implemented and is currently undergoing field testing.

Signaling Based Burst Mode Transmission One paradigm for providing a burst mode switching capability using conventional equipment is to send a signaling packet prior to the actual data packet transmission, and transmitting the data while the setup is in progress. An interesting description of a system that uses this paradigm is presented in Ref. 2. This system uses a dedicated wavelength for signaling control information, and a Burst Storage Unit in order to buffer packets when necessary. An implementation friendly link scheduling algorithm is used in order to insure efficient utilization of the WDM channels.

A Hybrid Approach Another system that uses pipelined signaling with data transmission to optical burst switching was constructed for use in our optical testbed. The system includes Network Interface Units (NIU) and Optical Crossbar Switches (OXBS). In this system data packets, which originate as groups of cells in a conventional ATM over SONET OC-12 network, are transformed into optical bursts at the NIU. The bursts travel through one or more OXBS units and exit the optical network at another NIU. The destination NIU reformats the transmission back into its original SONET format and passes it on to another ATM network. The OXBS has input ports and output ports that may be connected in a one-to-one or one-to-many configuration, accommodating both point-to-point and multicast operation. Several of these units were built for a U. S. government project and have been evaluated at Telcordia Technologies.

The design of this system uses ATM/SONET interfaces to receive packets on an inbound link to an NIU. The packets are placed in a fast memory buffer, and a request to the OXBS is sent over a dedicated

signaling wavelength. The request is encoded in an OC3 ATM/SONET cell which tells the OXBS to establish a connection after a few microseconds. The OXBS can then pass further setup information to downstream OXBSs, requesting connections on the path to the final NIU. Data frames are sent through the network over these connections in 8B/10B encoding, which allows for simpler encoding and easier synchronization.
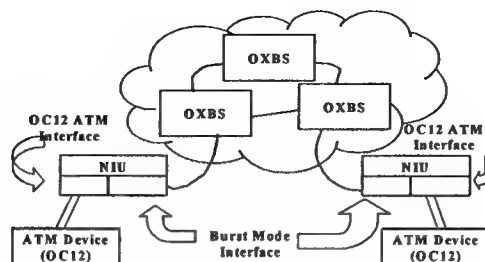
Since the efficient utilization of the OXBS requires a very fast optical switch, a characterization of the switching speed was performed. The OXBS uses semiconductor optical amplifier technology for the crosspoint switching elements. The trace below shows that both the rise and fall times were shorter than
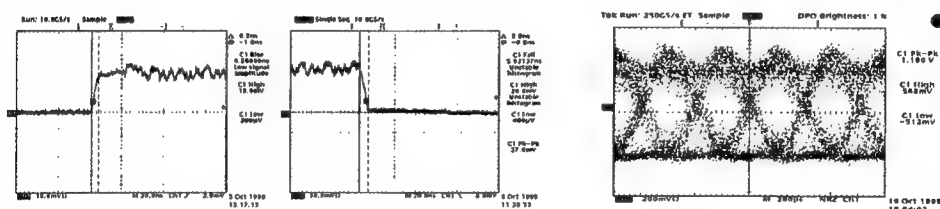
9 nanoseconds, indicating that a very efficient design was employed. A short switching time is very important for handling fine grain packets such as TCP ACK packets, which are only 40 bytes long. Also shown is an eye diagram of a OC48 signal after passing through the OXBS.

Pure Burst Mode Transmission The alternative to signaled data transmission is data switching using header information. An example of this type of network is described in Ref.3, and was demonstrated at OFC 2000. In this design a data packet is sent simultaneously with a header that contains routing information. The headers are carried along with the data, but out of band, using subcarrier multiplexing. At switch nodes inside the network, the optical signal is sampled just prior to entering a short fiber delay line. While most of the signal is being delayed, a fast packet processing engine determines the correct state for the switching fabric, based on the incoming header and a local forwarding table. The switch fabric is commanded to enter a new state just before the packet exits the delay line and enters the switch. This method provides the lowest possible latency for packet transmission and removes the onerous task of pre-calculating the arrival time of burst mode data packets.

Conclusion We have tested a novel hybrid system and constructed a burst mode optical networking testbed. There are several ways to accomplish burst mode transmission in a WDM optical network, including methods that rely on signaling in advance of data packet arrival and pure burst mode transmission of packets with no a priori indication. This paper discusses two designs from the literature and also reports on a novel hybrid system that was evaluated. Finally, a testbed that offers true optical burst mode capability is reported. This study provides a foundation for evaluating results of various methods that provide burst mode capability in WDM optical networks.

References
[1] Wei, J., "The Role of DCN in Optical WDM Networks", OFC2000, 2000.
[2] Turner, J. S., "WDM Burst Switching for Petabit Data Networks", OFC2000, 2000.
[3] Chang, G. K., et al, "A Proof-of-Concept, Ultra-low Latency Optical Label Switching Testbed Demonstration for Next Generation Internet Networks", OFC2000, 2000.

ALL OPTICAL REGENERATION

J.C. Simon (1), L. Billès (2), and L. Bramerie (2)

(1) Université de Rennes 1/ENSSAT, 6 rue de Kerampont, F22305 LANNION, FRANCE (simon@enssat.fr)
(2) France Télécom BD /FTR&D/DTD/RTO, 2 av. Pierre Marzin F22307 LANNION FRANCE

Abstract: All-optical signal regeneration techniques are presented: fiber and semiconductor based devices are addressed, and some 3R signal regeneration schemes are reviewed.

Introduction

Record terabit/s point-to-point transmission systems over more than 2000 km have recently been reported [1], based on dispersion managed non-linear transmission techniques, without need for any regeneration device, except for simple linear optical amplifiers. However, if terrestrial photonic networks featuring dynamic routing capability are considered, more sophisticated regeneration schemes could be necessary in order to compensate for signal quality discrepancies between high data rate WDM channels which could be routed at different times over variable distances. Although classical optoelectronic regenerators constitute an attractive solution for single channel, single data rate transmission, it is not clear whether they could be a cost effective solution in a tremendously growing data bandwidth scenario. All optical regenerators, based on components which can process low as well as high bit rates signals could be an interesting alternative. In this summary, we briefly review 2R (reshaping repeater) and 3R (retiming, reshaping repeater) optical regeneration schemes for high speed optical signal processing, based on different technologies such as fibers or semiconductors

1 Main signal degradations:

Main signal degradations in fiber systems arise from amplified spontaneous emission (ASE) due to optical amplifiers, pulse spreading due to group velocity dispersion (GVD), which can be corrected through passive dispersion compensation schemes, polarisation mode dispersion (PMD), and finally non-linear effects due to Kerr non-linearity contributing to signal distortion and jitter above 10 Gbit/s.

2 Basic principle of optical regeneration:

2.1 2R regeneration:

If time jitter is negligible, simple amplification and reshaping processes are usually sufficient to maintain signal quality over long distances by preventing from noise and distortion accumulation. A 2R regenerator mainly consists of a linear optical amplifier followed by a data-driven non-linear optical gate (NLOG) which modulates a "clean" (low noise) CW laser light source. If the gate transmission versus signal intensity characteristics yields a kind of thresholding and limiting behaviour, then signal extinction ratio can be improved and ASE amplitude noise partly reduced. In addition, the accumulated chirp can be wiped off.

2.2 3R regeneration:

When jitter accumulation is also a problem, e.g. owing to cross-phase modulation (XPM) in WDM systems, or pulse edge distortions due to finite response time of non-linear analog signal processing devices (e.g. wavelength converters), then 3R regeneration might be necessary. Fig. 1 shows the basic structure of an optical 3R regenerator [2], which mainly consists of an optical amplifier, a clock recovery block providing an unjittered short pulse clock stream, which is then modulated by a data driven non-linear optical gate block.

Figure 1: Principle of optical 3R regeneration
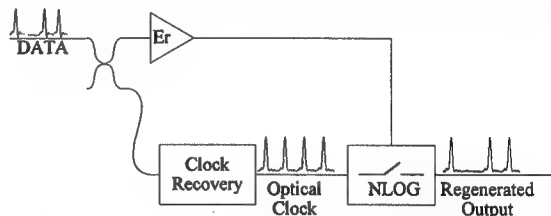
Let's now review some recent approaches for these different building blocks.

3 Regenerator main building blocks.

The core of an optical regenerator is a non-linear gate featuring signal extinction ratio enhancement and noise reduction.

3.1 Fibre based gates:

Kerr-shutter [3] and non-linear optical loop mirror (NOLM) [4] are probably the first studied gates for regeneration applications. The ultra fast response of Kerr non-linearity is a major advantage of these devices for high speed signal processing. Using a Kerr-shutter, a 40 Gbit/s optical regenerator has been reported [3]. But the weak silica fiber non-linearity requires typical peak power x length products of 0.5 W x km. Long fibre lengths (several km) and polarisation sensitivity to incoming signal are drawbacks for WDM field deployment. Recently, a new polarisation insensitive gate based on self phase modulation spectrum filtering was reported [5], with a good limiting behaviour.

3.2 Semiconductor based optical gates:

Although not as fast as fibre based devices, these gates are much more compact. One can distinguish between " active

devices ", i.e. that require an electrical power supply like semiconductor optical amplifier (SOA) based devices, and " passive devices ", like saturable absorbers [6].

Among active semiconductor gates, work has been focused on bistable lasers [7] and mostly on SOA based devices . First reported SOA based optical gates were Sagnac interferometer incorporating one SOA as the non-linear element [8,9]. However this gates are much better suted for high speed OTDM demultiplexing [10] than for 3R regeneration which requires a gate with a well shape rectangular window when switching data pulses are somewhat large. Other high speed and well shaped optical gates are SOA-based Mach-Zehnder or Michelson interferometers [11,12], which can be data driven with polarisation independence up to 40 Gbit/s, with excellent performances [13]. Main features of interferometric non-linear gates are signal extinction ratio enhancement and noise variance reduction. 100 Gbit/s optical logic gate based on an ultrafast nonlinear interferometer (UNI) using an SOA in a birefringent interferometer was reported [14], while feasibilility of data regeneration at 40 Gb/s with this gate was reported [15].

3.3 Clock recovery:

For optical 3R regeneration, a synchronous unjittered short pulse stream clock has to be recovered from incident signal. Many solutions meeting these requirements have been reported, which cannot all be reviewed here. We only focus on polarisation independent and potentially ultrahigh speed schemes for RZ formats. All-optical clock recovery through optical injection of mode-locked lasers, either in semiconductor [16] or Erbium doped fibre [17] could yield low jitter, short pulse clocks. Phase locked loop techniques using a high speed non-linear optical element as phase comparator [18], could also yield good performance above 100 GHz. Recently, a self-pulsating laser clock recovery was demonstrated at 40 GHz [19,20].

4 Some recent results on optical regeneration:

We shortly review here some recent results on polarisation independent regeneration schemes for data rates above 10 Gbit/s. Although 2R regeneration looks very attractive because of its simplicity and bit rate flexibility, it is not clear whether it could be used above 10 Gb/s because it would require devices with very short transition time response.

4.1. 3R regeneration:

" All-electronic " signal processing is rapidly progressing, with recent demonstration of a 40 Gbit/s optoelectronic repeater using InP-HEMT technology [21]. Several 3R optical regenerator architectures have also been demonstrated. All optical fibre devices were first reported, and have shown now 20 [22], and 40 Gbit/s [3] operation capability. On the semiconductor technology side, hybrid regenerator structure using optoelectronic clock recovery stage and all optical SOA based non-linear interferometric gates have been demonstrated (with BER assaisment) at 10 [23], 20 [24,25] and 40 Gb/s [26]. Cascadability feasability of up to 1000 regenerators in the recirculation loop has been reported [27] with multistage interferometric gates (cascaded non-linear gates improve signal regeneration [28]).

Finally, InP electro-optic modulators have successfully been used for polarisation insensitive in-line amplitude and phase synchronous modulation of soliton signals up to 40 Gb/s, enabling error-free transmission over more than 20 000 km [29].

5. Conclusion:

High speed WDM photonic networks will probably require signal regenerators. Although significant progress has been achieved these two last years, it is not yet clear to-day whether all building blocks of a 3R all optical regenerator will be as easily integrated as for an electronic device, with cost effective targets, particularly in a dense WDM context. This means that optical signal processing solutions should yield superior or not otherwise available functionalities, such as bit rate flexibility, for example.

References

/1/ C.G Gyaneshwar et al. : OFC'2000, Baltimore, USA, TuJ7-2

/2/ M. Jinno: JLT, 1994, vol. 12, n° 9,. pp.1648-1659.

/3/ W.A. Pender et al.: Electron. Lett., 1996, vol. 32, n° 6, pp. 567-569

/4/ J.K. Lucek et al.: Optics Letters, 1993, vol. 18, n° 15, 1993, pp. 1226-1228.

/5/ P.V. Mamyshev : ECOC'98, 20-24 September 1998, Madrid, Spain, pp. 475-476.

/6/ T. Otani et al. :OFC'2000, Baltimore, USA, ThP3

/7/ W. Pieper et al.:, OFC'96, San Jose, 25-29 Feb. 1996, PD35 ; K. Nonaka et al:, 1995, PTL, vol. 7, n° 1, pp. 29-31

/8/ M. Eiselt et al: Electron. Lett., 1993, vol. 29, n° 1

/9/ J.P. Sokoloff et al:, PTL, 1993, vol. 7, n° 5, pp. 787-790

/10/ I. Glesk et al: Electron. Lett., 1994, vol. 30, n° 4

/11/ C. Joergensen et al: IEEE J^al of sel. topics in QE, 1997, vol. 3, n° 5, pp. 1168-1179

/12/ C. Janz :OFC'2000, Baltimore, USA, ThF6

/13/ K. Tajima et al.:Electron. Lett., 1999, 35, N° 23

/14/ K.L. Hall et al: OFC'98, San Jose, paper PD5

/15/ I.D. Phillips et al., Electron. Lett., 1998, vol. 34 n° 24

/16/ E. Lach et al: ECOC'96, Oslo, paper ThB1.6

/17/ L.E. Adams et al: Electron. Lett., 1995, vol. 31, n° 20

/18/ O. Kamatani et al.:, Electron. Lett., 1994, vol. 30, n° 10

/19/ C Bornholdt et al. : ECOC 99, Nice, France, PD3-5

/20/ W. Maho et al. :OFC'2000, Baltimore, USA, ThF2

/21/ M. Yoneyama et al: Electron. Lett., 1997, vol. 33, n° 23

/22/ S. Bigo et al: OFC'97, Dallas, Texas, USA, PD22

/23/ D. Chiaroni et al : OFC'98, San Jose, Paper PD15.

/24/ L. Billes et al. : ECOC'97,Edimburgh,UK, vol. 2

/25/ B. Lavigne et al :OFC'2000,Baltimore,TuF7

/26/ S. Fischer et al. : Electron. Lett., 1999, 35, N° 23

/27/ B. Lavigne et al. :OFC'99,SanDiego,Ca., TuJ3

/28/ L. Billès et al: OAA'95, Davos, 1995, pp. 59-62

/29/ O. Leclerc et al.: Electron. Lett., 1999, vol. 35, N°9

Superior Performance of Nonlinear Optical Loop Mirrors Using Semiconductor Optical Amplifiers with Robust Transparency

J.M.Tang, P.S.Spencer, P.Rees and K.A.Shore
School of Informatics, University of Wales, Bangor,
BANGOR, LL57 1UT, UK.
Tel: +44(1248)382618; Fax: +44(1248)361429; e-mail: alan@sees.bangor.ac.uk

1. Introduction

Nonlinear Optical Loop Mirrors based on Transparent Semiconductor Optical Amplifiers (TSOA-NOLMs) exhibit fast switching with a recovery time of the order of a few picoseconds, cascadable switching functionalities, low cross-talk between adjacent channels and low noise figures [1,2]. When an SOA is biased such that the optical gain exactly compensates the linear waveguide loss, the SOA is, in general, not transparent to an injected intense pump pulse since Two-Photon Absorption (TPA) and Ultrafast Nonlinear Refraction (UNR) respectively absorb the pulse energy and broaden its spectral width [3]. In a TSOA-NOLM, following the passage of the pump pulse, the SOA may be considered to be transparent to the probe pulse if the carrier density is immediately restored to the value existing prior to the arrival of the pump pulse. Hence the output energy of the probe probe pulse is independent of the time delay between the probe and pump pulses. The transparency carrier density is, however, significantly dependent upon the pump pulse power [1]. Furthermore, due to the small net optical gain in a TSOA-NOLM, a high pump pulse power is usually required to achieve a specific switching output energy. Therefore, both the strong pump power dependence of the transparency carrier density of SOAs and the requirement of high switching powers would seriously limit the utilisation of TSOA-NOLMs in practice.

The pump power dependent transparency carrier density of an SOA was measured [1] using a pump-probe configuration, and in that work the switching characteristics of a TSOA-NOLM were also reported. In this paper, calculations predict that long SOAs (>500μm) can be employed in TSOA-NOLMs to not only considerably reduce the pump power dependence of the transparency carrier density of the SOAs but also to significantly increase the transmission of the switches.

2. Results and Discussions

To simulate the pump power dependent transparency carrier density of SOAs, calculations are performed of a pump-probe configuration. An optical pulse model [4] that governs co-propagating strong pump and weak probe pulses in SOAs is adopted. Moreover, to compute the switching behaviour of TSOA-NOLMs, a comprehensive model [5] that determines the output properties of the Sagnac-interferometer devices using SOAs as the nonlinear elements is utilised. To accurately describe the optical gains of SOAs, a detailed material gain model [6] is employed here, from which the unsaturated optical gain, the differential gain coefficient and the carrier density linewidth enhancement factor can be computed as functions of optical pulse wavelength, carrier density and temperature.

The simulated dependence of the transparency carrier density on the input pump pulse energy is illustrated in Fig.1 for different SOA lengths. The behaviour of the transparency carrier density shows good agreement with experimental measurements [1]. In particular, Fig.1 also shows that the pump pulse power dependence of the transparency carrier density can be considerably decreased by employing long SOAs. Two-Photon Absorption (TPA) and TPA-induced carrier creation are dominant in determining the carrier density behaviour. When the pump pulse propagates along the SOA, these effects are gradually reduced because of the reduced pump powers. For a long device, the average optical gain per unit length experienced by the probe pulses after the arrival of the pump pulses is lower in comparison to that of the short SOA. A reduced dependence of the transparency carrier density is thus achieved.
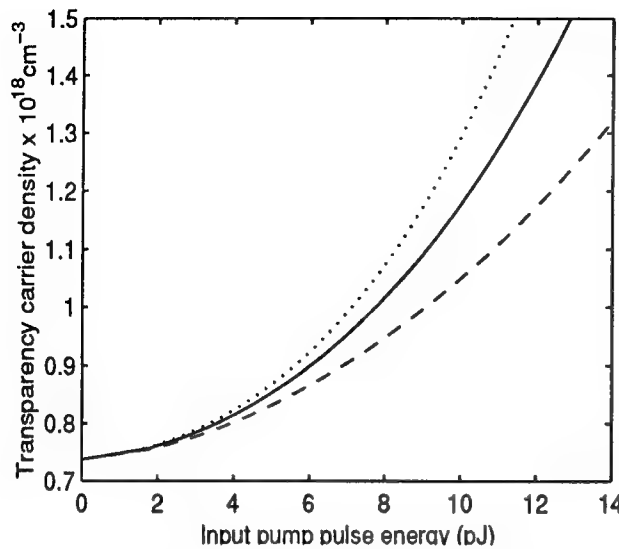
Figure 1: The transparency carrier density as a function of the input pump pulse energy for different SOA lengths. The SOA lengths for the dotted, solid and dashed lines are $125\mu m$, $250\mu m$ and $500\mu m$ respectively.
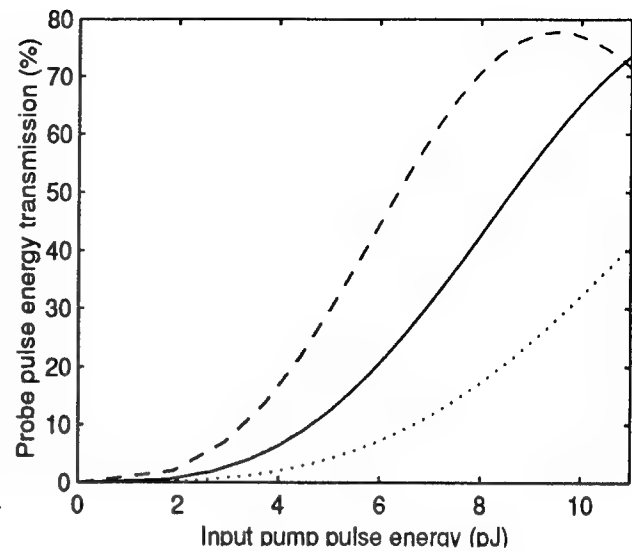
Figure 2: The probe pulse energy transmission versus the input pump pulse energy in a TSOA-NOLM. The SOA lengths for the dotted, solid and dashed lines are $125\mu m$, $250\mu m$ and $500\mu m$ respectively.

Fig.2 demonstrates the probe pulse energy transmission of TSOA-NOLMs (ratio between output and input probe pulse energies) as a function of the input pump pulse energy. It is shown that an increase in the transmission with increasing the pump pulse energy and the existence of transmission saturation at even stronger pump pulse energies. Again these features agree very well with experimental measurements [1]. It is interesting to note that long SOA devices can significantly enhance the probe pulse energy transmission. The features of the probe transmission in Fig.2 occur as a direct results of the inter play between phase and amplitude differences between two counter propagating signal pulses in the loop. A long SOA produces a large phase change and hence enhances significantly the probe pulse energy transmission.

In conclusion, an approach of utilising long SOAs in TSOA-NOLMs has been shown to reduce the pump power dependence of the transparency carrier density of the SOA and simultaneously enhance the probe pulse transmission of the device.

References
1   Y.-H.Kao, et al., *J. Appl. Phys.*, Vol.86, pp.4740-4747, Nov. 1999.
2   S.Diez, et al., *IEEE Photon. Technol. Lett.*, Vol.11, pp.60-62, Jan. 1999.
3   J.M.Tang and K.A.Shore, *IEEE J. Quantum Electron.*, Vol.34, pp.1263-1269, July 1998.
4   J.M.Tang and K.A.Shore, *IEEE J. Quantum Electron.*, Vol.35, pp.93-100, Jan. 1999.
5   J.M.Tang and K.A.Shore, *IEEE J. Quantum Electron.*, Vol.35, pp.1704-1712, Nov. 1999.
6   P.Rees, H.D.Summers, and P.Blood, *Appl.Phys.Lett.*, Vol.59, pp.3521-3523, Dec. 1991.

Optical Switches Based on The Generalized Mach-Zehnder Interferometer

L.W.Cahill[1] and F.P.Payne[2]

1) La Trobe University, Department of Electronic Engineering, Bundoora, Vic. 3083, Australia
2) Department of Engineering, University of Cambridge, Trumpington St, Cambridge CB2 1PZ, U.K.

Multimode interference (MMI) couplers have found wide application in integrated optical circuits. These couplers are based on self-imaging multimode waveguides and have been shown to be very effective in splitting and combining optical beams. Their advantages include compact size, ease of fabrication, low excess loss, good crosstalk performance and accurate splitting ratios.

Good power balance and stable relative phases of the MMI couplers make them ideal for incorporation into generalized Mach-Zehnder interferometer (GMZI) structures. GMZI wavelength-selective switches, variable-ratio power splitters and optimized switches have been reported [1]. However, the switching capability of these devices has been very limited so far. The purpose of this paper is to further investigate the switching possibilities of the GMZI and to propose a novel design for an optical GMZI switch.

The general layout of an NxN GMZI is illustrated in Fig. 1. Identical 4x4 MMI couplers are used as splitter and combiners. They are linked by N arms, each containing a phase shifter, either electro-optic or thermo-optic in nature.
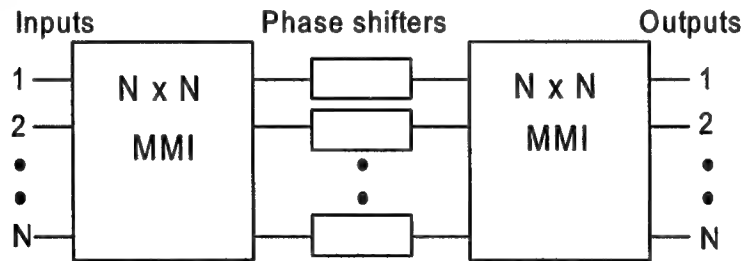
Fig 1. Structure of an NxN generalized Mach-Zehnder interferometer (GMZI).

The transfer matrix T for the NxN coupler ideally is given by

$$t_{mn} = a_{mn} \exp(j\phi_{mn}) \tag{1}$$

where a_{mn} is the (field) amplitude transfer coefficient, and the phase ϕ_{mn} is associated with imaging an input m to an output n [1].

The overall transfer matrix S of the generalized Mach-Zehnder interferometer can be written as follows

$$S = T\Lambda T \tag{2}$$

where Λ is the diagonal matrix representing the phase shifts in the arms, and T is the transfer matrix for the NxN couplers.

Since the phase shifting arms provide only N degrees of freedom, then only N of the total N! number of switching states can be produced by such a structure. The phase shifts required in the arms for each state, are given by

$$\Lambda = T^{-1}S_a T^{-1} \tag{3}$$

where S_a is one of the N allowable switching states.

However, for a switch to be useful, it needs to provide all possible switching states. For the case of the 4x4 switch, there are 4! = 24 separate states. The 4x4 GMZI can be modified, by adding some additional logic, to enable it to provide the complete range of switching states. A complete switch is shown in Fig 2.
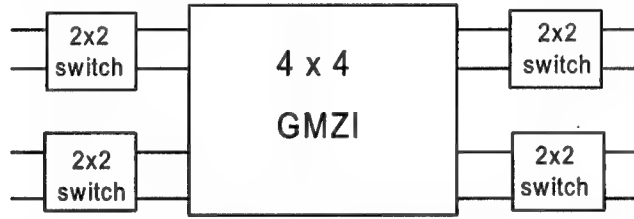

Fig 2. Proposed architecture for a 4x4 optical switch.

Thus by the addition of only four 2x2 switches (which could be 2x2 GMZI switches) all the switching states are achieved. The major advantages of this design are that the losses are uniform across the paths and that the switching states are achieved using only a very small number of phase shifters. External crossovers are avoided. The switch is rearrangeably non-blocking. However, it is possible to allocate the connections of the switch in such a way as to reduce the probability of rearrangement. The switch also has some fault-tolerant properties.

In summary, a brief outline of the switching capabilities of the GMZI has been given. This study has led to the design of a novel 4x4 switch. This type of switch has good loss uniformity and requires only a relatively small number of phase-shifting or switching elements.

REFERENCE
[1]   N.S.Lagali, M.R.Paiam, R.I.MacDonald, K.Worhoff, and A.Driessen, "Analysis of generalized Mach-Zehnder interferometers for variable-ratio power splitting and optimized switching, *IEEE. Lightwave Technol.* vol. 17, no. 12, pp. 2542 – 2550, December 1999.

Perfectly synchronized bit-parallel WDM data transmission over a single optical fiber

Deyu Zhou, Bing C. Wang,
Robert J. Runser, Ivan Glesk and Paul R. Prucnal

Dept. of Electrical Engineering, Princeton University, Princeton, NJ 08544
609-258-2041, 609-258-2158 (fax), deyuzhou@princeton.edu

We conducted perfectly synchronized bit-parallel WDM data transmission over a single optical fiber. The demonstrated technique is applicable to scenarios where bit-level synchronization among parallel WDM channels is required. In bit-Parallel WDM, each bit of a byte or a WORD is transported in a different wavelength over the optical fiber. Bit-parallel WDM data transmission is suitable for interconnecting computers since processors read and write data in a byte-wise fashion. Due to group velocity dispersion (GVD), however, different bit-parallel wavelengths do not arrive simultaneously at the receiver. The best accuracy of present methods [1, 2] for compensating the time skew is $3ps$ for $2.5km$ fiber, therefore $30ps$ for $25km$.

The bit-parallel WDM data is transmitted over a $27.5km$ Corning dispersion shifted fiber (DSF). The experimental setup of the demonstration consists of three parts: the input stage, the synchronization stage, and the output stage, as illustrated in Fig. 1. The input stage involves three narrow linewidth CW lasers (one tunable diode laser at wavelength $\lambda_1 = 1563.2nm$ and two DFBs centered at wavelengths $\lambda_2 = 1540.9nm$, $\lambda_3 = 1539.5nm$, respectively) and the DSF to introduce $140ps$ time skew. The narrow linewidth lasers are appropriately amplified with erbium doped fiber amplifiers (EDFAs) to provide equalized amplitudes among bit-parallel WDM channels and simultaneously modulated by an Li:NbO$_3$ modulator with an OC-48 non-return-zero formatted $2^{31} - 1$ pseudo-random bit sequence (PRBS). Using only one modulator with a rising time of $40ps$ gives an accurate timing alignment among all bit-parallel WDM channels and a $360ps$ flat overlapping range at the DSF input. In addition, imprinting the same data pattern on all wavelengths simulates the worst case scenario for nonlinear interactions among the different channels.

The synchronization stage uses an all optical switch: Terahertz Optical Asymmetric Demultiplexer (TOAD), with the bit-parallel WDM data entering the input port and a synchronous OC-48 picosecond pulse train entering the clock port. Upon incidence of a clocking pulse, the TOAD opens a small-switching window for all bits or WDM channels at the same temporal location determined by the timing of the clocking pulse. When the small switching window is placed in a $220ps$ time region (for our particular setup) where all bits overlap, the different WDM channels are aligned precisely in time. The output stage of the experiment uses an array waveguide grating (AWG) to demultiplex the different WDM channels exiting the output port of the TOAD. Optical filters are
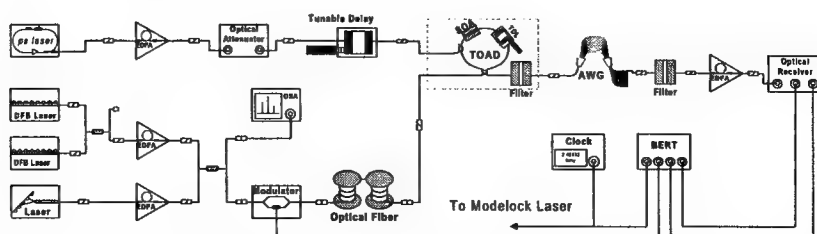

Fig. 1. A schematic diagram of perfectly synchronized bit-parallel WDM data transmission over a single optical fiber
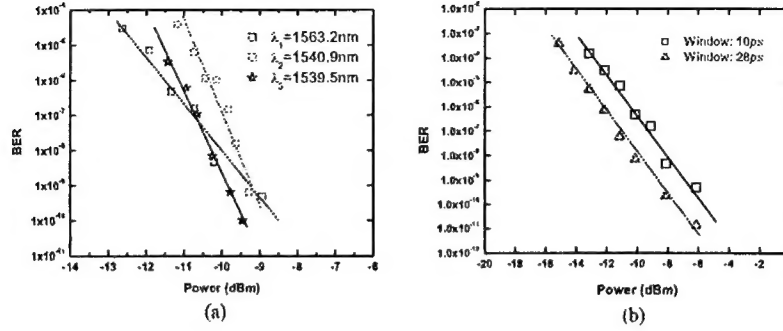
Fig. 2. (a) BER of all channels for bit-parallel WDM data ($\square - \lambda_1, \triangle - \lambda_2, and \star - \lambda_3$) at a switching window of 28ps, (b) BER of channel λ_1 at TOAD's switching windows of 10ps ($\square$) and 28ps ($\triangle$).

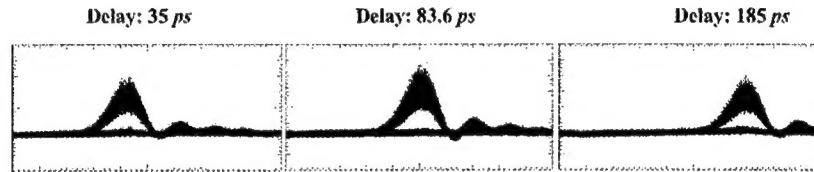**Delay: 35 ps**   **Delay: 83.6 ps**   **Delay: 185 ps**

Fig. 3. EYE diagrams of the channel λ_1 at different sampling locations. Here, the sampling time delay values are relative to the beginning of the range where all bit-parallel WDM channels overlap.

placed both before and after AWG to eliminate residual clocking pulses and amplifier spontaneous emission from both SOA and EDFAs. An OC-48 SONET receiver is connected to a bit error rate (BER) tester which measures the BER of each channel one at a time.

The BER measurements for each channel of the precisely aligned bit-parallel WDM data are shown in Fig 2(a) for a TOAD's switching window of 28ps. BER 10^{-10} is obtained for every channel with a $2^{31} - 1$ PRBS. A few dB power penalty is introduced when the switching window is reduced to 10ps as indicated in Fig. 2(b). Here powers in BER plots are the values measured at the input of the all optical switch. Wide open EYE diagrams at different overlap regions of the bit-parallel WDM channels are illustrated in Fig. 3 to indicate that good BER can be obtained at any location where all bit-parallel WDM data overlap. Here, EYE diagrams were obtained by using a 10GHz lightwave converter and a 35GHz digital sampling scope.

In conclusion, we have proposed and demonstrated a novel bit-level synchronization technique by perfectly synchronizing all bit-parallel WDM data transmitted over a 27.5km single fiber. By sampling temporally skewed bit-parallel WDM data at a common overlapping range with an all optical switch(TOAD), the bit-parallel WDM channels emerge aligned exactly in time. Error free transmission on all WDM channels was achieved. The working range, where TOAD samples all overlapping bit-parallel WDM channels, is 220ps for our particular experimental setup. For transmissions where the time skew exceeds 140ps, traditional dispersion compensation techniques must be employed to contain the time-skew within 220ps and to transmit longer distances.

References

1. O.H. Adamczyk, M. C. Cardakli, J.X. Cai, M.I. Hayee, C. Kim, and A.E. Willner, "Coarse and fine bit synchronization for wdm interconnections using two subcarrier-multiplexed control pilot tones", *IEEE Photonics Technol. Lett.*, vol. 11, pp. 1057–1059, 1999.
2. S. Shen and A. M. Weiner, "Demonstration of timing skew compensation for bit-parallel wdm data transmission with picosecond precision", *IEEE Photonics Technol. Lett.*, vol. 11, pp. 566–568, 1999.

Penalty-Free Polarization Insensitive Wavelength Conversion Using Bidirectional Four-Wave Mixing in a Single Semiconductor Optical Amplifier

J.M.Tang, P.S.Spencer and K.A.Shore
School of Informatics, University of Wales, Bangor,
BANGOR, LL57 1UT, UK.
Tel: +44(1248)382618; Fax: +44(1248)361429; e-mail: alan@sees.bangor.ac.uk

1. Introduction

Four-Wave Mixing (FWM) in Semiconductor Optical Amplifiers (SOAs) has been extensively investigated for a number of applications in optical communications. The strong polarization sensitivity of the mixing process is, however, a major issue in the utilization of the FWM technique in practical networks. Several schemes for polarization insensitive FWM in SOAs have been demonstrated [1-3], which utilise rather complex configurations involving several optical components. Recently, we proposed an extremely simple scheme [4] for polarization insensitive FWM, utilizing just one polarization insensitive SOA and one pump wave. Furthermore, employing two pump sources in the scheme, polarization insensitive and frequency-conversion frequency-interval independent FWM [5] can be also obtained.

In all the aforementioned configurations, polarization insensitive SOAs were employed to achieve the polarization insensitive FWM performance. In this paper, we will show that polarization insensitive FWM operation can also be realised, using a polarization sensitive SOA by modifying the configuration presented in Ref.4.

2. Polarization insensitive FWM scheme

The proposed polarization insensitive FWM configuration is illustrated in Fig.1, which employs one conventional SOA and a single pump source. A pump wave at frequency ω_p and a collinear signal wave at frequency ω_s are injected into a Polarizing Beam Splitter 1 (PBS1). After passing through the PBS1, these waves are split into clockwise and counter clockwise orthogonally polarized beams: a pump field and a copolarized component of the signal field propagate clockwise and the other two copolarized components of the pump and signal beams travel counter clockwise. The generated conjugate waves appear at both facets of the SOA. If the ratio of the powers between the forward and backward pump beams is adjusted in accordance with the optical gains of the SOA for the TE and TM modes, a polarization insensitive conjugate wave can be obtained after combining at the PBS2.

3. Performance analysis

The output conjugate frequency of interest in this scheme is $2\omega_p - \omega_s$, which can be obtained through nonlinear mixing between both co-propagating and counter propagating waves. Based on a space-averaged model [6], the conjugate waves generated by co-propagating pump and signal waves are

$$\widehat{\mathbf{E}}_{pf,sf,pf} = \widehat{\mathbf{x}} P_{pf} \sqrt{P_s} G_x^{\frac{3}{2}} cos\theta r(\omega_p - \omega_s) e^{-i[(2\omega_p - \omega_s)t - (2k_p - k_s)z]}, \tag{1}$$

$$\widehat{\mathbf{E}}_{pb,sb,pb} = \widehat{\mathbf{y}} P_{pb} \sqrt{P_s} G_y^{\frac{3}{2}} sin\theta r(\omega_p - \omega_s) e^{-i[(2\omega_p - \omega_s)t + (2k_p - k_s)z]}. \tag{2}$$

where $\widehat{\mathbf{x}}$ and $\widehat{\mathbf{y}}$ are unit vectors parallel to the TE and TM modes of the SOA; P_{pf}, P_{pb} and P_s are the input optical powers for the clockwise and counter clockwise pump as well as signal pulses; G_x and G_y are the SOA's gain for the TE and TM polarized waves; θ is the polarization direction of the signal pulse; r is the complex coupling coefficient. $k_j > 0$, j = p, s are wavenumbers.

The conjugate wave $\widehat{\mathbf{E}}_{pf,sf,pf}$ ($\widehat{\mathbf{E}}_{pb,sb,pb}$) polarized in the $\widehat{\mathbf{x}}$ ($\widehat{\mathbf{y}}$) direction does not suffer from the wave number mismatch effect [6], and travels clockwise (counter clockwise) along the loop.
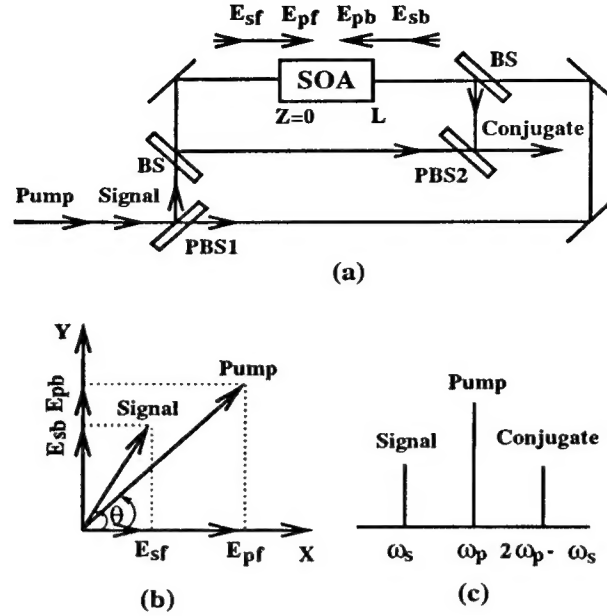
Figure 1: Polarization insensitive FWM scheme: (a) layout, (b) input states of polarization and (c) output spectrum. PBS: Polarizing beam splitter. BS: Beam splitter.

Meanwhile, conjugate waves with the same frequency can also be created through nonlinear mixing between the counter propagating waves. However, it is sufficiently accurate to neglect these conjugate waves for an SOA device longer than, say, ~1mm and a frequency detuning larger than a few hundred GHz [6]. If the ratio of the pump powers between the forward and backward pump beams is adjusted to satisfy

$$\frac{P_{pf}}{P_{pb}} = (\frac{G_y}{G_x})^{3/2} \tag{3}$$

then the output conjugate power from the PBS2 is

$$P_c = (P_{pf}^2 G_x^3 + P_{pb}^2 G_y^3)P_s r^2(\omega_p - \omega_s). \tag{4}$$

Hence a polarization insensitive conjugate power can be measured from the output port of PBS2. Eq.(4) indicates that the proposed scheme does not compromise the achievable conjugate power and signal to noise ratio. The significant advantages of the scheme also include extreme simplicity, efficient reduction in noise. Therefore, this approach would significantly broaden the potential applications of the technique.

References
1   J.P.R.Lacey, S.J.Madden, et al., IEEE Photon. Technol. Lett. **9**, 1355 (1997).
2   R.Schnabel, U.Hilbk, T.Hermes, et al., IEEE Photon. Technol. Lett. **6**, 56 (1994).
3   R.M.Jopson and R.E.Tench, Electron. Lett. **29**, 2216 (1993).
4   J.M.Tang, P.S.Spencer, and K.A.Shore, Appl. Phys. Lett., **75**, 2710, (1999).
5   J.M.Tang, P.S.Spencer, and K.A.Shore, Opt. Lett., **24**, 1605, (1999).
6   J.M.Tang and K.A.Shore, IEEE Photon. Technol. Lett. **11**, 1123 (1999).

AUTHOR INDEX

Antoniades, N.	ThC1.4		Manzalini, A.	ThC1.2
Beveridge, G.	ThC2.2		Martin, C.	ThC2.3
Billes, L.	FC4.1		McFarland, R.	FC3.2
Bonenfant, P.	WC1.2		Meagher, B.	FC3.2
Bramerie, L.	FC4.1		Medard, M.	FC1.4
Cahill, L.	FC4.3		Mitchell, J.	ThC2.5
Chang, G.-K.	WC1.4		Mouftah, H.	FC1.3
Chen, W.	FC2.4		Mysore, S.	ThC2.2
Chen, Y.	FC2.4		Nuss, M.	FC3.1
Chiaroni, D.	FC1.2		O'Reilly, J.	ThC2.5
Christele, B.	ThC2.3		Okamoto, K.	FC2.1
Chung, Y.	FC2.2		Payne, F.	FC4.3
Cocorullo, G.	FC2.3		Perreault, J.	FC3.2
da Silva, V.	ThC1.4		Prucnal, P.	FC4.4
Della Corte, F.	FC2.3		Qiu, J.	ThC2.3
Dotaro, E.	FC1.2		Rees, P.	FC4.2
Durrani, K.	ThC1.3		Rendina, I.	FC2.3
Ennser, K.	ThC1.4		Ringoot, E.	ThC2.3
Feuer, M.	ThC2.4		Rodriguez Moral, A.	WC1.2
Frigo, N.	ThC2.4		Runser, R.	FC4.4
Gibbons, T.	WC1.4		Shore, K.	FC4.2, FC4.5
Gladisch, A.	ThC1.2		Simmons, J.	WC1.1
Glesk, I.	FC4.4		Simon, J.-C.	FC4.1
Henmi, N.	FC2.5		Spencer, P.	FC4.2, FC4.5
Holmes, M.	ThC1.3		Stubbe, B.	ThC2.3
Iodice, M.	FC2.3		Tang, J.	FC4.2, FC4.5
Jourdan, A.	FC1.2		Tassent, M.	ThC2.3
Lam, C.	ThC2.4		Vaes, P.	ThC2.3
Lane, P.	ThC2.5		Van de Voorde, I.	ThC2.3
Le Sauze, N.	FC1.2		Vandewege, J.	ThC2.3
Lee, D.	FC2.4		Villa, R.	ThC2.2
Lehr, G.	ThC1.2		Wagner, R.	FC1.1
Li, T.	FC2.4		Wang, B.	FC4.4
Lin, C.	FC3.3		Wang, Q.	FC2.4
Lin, X.	FC2.4		Wang, Y.	FC2.4
Liu, C.	WC1.3		Wei, J.	WC1.3
Liu, K.	WC1.3		Wu, J.	FC1.3
Lu, X.	ThC2.1		Xin, W.	WC1.4
Lucky, R.	CPLE1.1		Yadlowsky, M.	ThC1.4
Lumetta, S.	FC1.4		Yang, X.	FC3.2
Maier, G.	ThC1.1		Zhou, D.	FC4.4